# A Study of the Dynamics of Diffractive Photoproduction at HERA

Paul Newman

February 1996

A thesis submitted to the University of Birmingham for the degree of Doctor of Philosophy in the School of Physics and Space Research.

# Abstract

A measurement is presented, using the H1 detector, of the differential cross-section, $\frac{d\sigma}{dM_X^2}$, for diffractive photoproduction processes in which the proton vertex is elastic, and the final state photon system has mass, $M_X < 27.1$GeV. The average $\gamma p$ centre of mass energy is 187GeV. Using the forward components of the detector, events are selected on the basis of a large gap in the pseudorapidity distribution of final state hadrons adjacent to the leading proton. By using a reconstruction method that is insensitive to any non-containment of parts of the final state in the photon direction, the cross-section is evaluated for values of $M_X$ down to those consistent with the exclusive production of the lowest lying vector meson states, $\rho(770)$, $\omega(783)$, and $\phi(1020)$. The total cross-section for the quasi-elastic production of one of these states, or for the non-resonant photon dissociation to $\pi^+\pi^-$ is found to be $18.2 \pm 0.8(stat) \pm 1.9(sys)\mu$b. The total cross-section for photon dissociation to the continuum of higher mass states in the measured kinematic range is $17.5 \pm 0.4(stat) \pm 2.4(sys)\mu$b. In the high mass region, the differential cross-section is fitted to the triple Regge form, $d\sigma/dM_X^2 \sim (1/M_X^2)^n$, and a value, $n = 1.00 \pm 0.02(stat) \pm 0.03(sys)$, is obtained.

By demanding activity in the pseudorapidity range, $5.5 \lesssim \eta \lesssim 7.5$, and that the largest rapidity gap in the main part of H1 is bounded by the forward edge in acceptance ($\eta \sim 5.5$), a limited measurement of the differential cross-section, $\frac{d\sigma}{dM_X^2}$, has been made for diffractive processes in which the proton dissociates to any state with mass, $m_p < M_Y \leq 10$GeV. The cross-section for such processes that are quasi-elastic at the photon vertex is found to be $5.5 \pm 0.4(stat) \pm 1.2(sys)\mu$b. An investigation of the double dissociative diffractive process, in which both $M_X$ and $M_Y$ are large, suggests that its cross-section is similar to that of single photon dissociation.

The acceptance of the H1 Forward Muon Trigger in its 1995 configuration is evaluated from simulations. For tracks passing through the first three double layers of drift cells, the acceptance is found to be $\sim 95\%$ for single muons generated in the range of polar angle, $7.5^o \lesssim \theta \lesssim 17.2^o$, with momentum, $p \gtrsim 2.9$GeV. For tracks that also traverse the iron toroidal magnet of the system and the three subsequent double layers, the acceptance is $\sim 93\%$ for muons in a similar range of polar angle, and with $p \gtrsim 6.0$GeV.

# A note on the author's contribution

Whilst this thesis is entirely written by myself, the work presented would not have been possible without the input of very many people from the H1 collaboration. Here, I wish to acknowledge specific contributions from a number of people. More general acknowledgements can be found at the end of this thesis.

The development of the experimental techniques described in chapter 5 was performed in collaboration with Andrew Mehta. The sub-triggers and Monte Carlo used were already in place before we commenced the work, having been used in a previous H1 analysis [25]. The invariant mass reconstruction method, and noise suppression techniques were developed by us, and have been used in the extraction of a cross-section for exclusive $\rho^0$ photoproduction [132]. The development of the loads for the Forward Muon Trigger, presented in chapter 6, is a responsibility that began with John Dowell, was passed to myself in 1994, and then on again to Paul Sutton in 1995. The loads described are the result of the work of all three people concerned. Little of the theoretical perspective offered in chapters, 2 and 3 is original. Instead it leans on a wealth of information to be found in original publications and review articles. Whilst I have tried to be careful to reference original work, many of the citations refer to more general sources that I have found to be useful. The measurement described in chapter 5 is my own work, as is the determination of Forward Muon Trigger acceptance, described in chapter 6. Unless indicated otherwise, all of the plots presented have been made by myself.

I am grateful to John Dainton, John Garvey and Ian Kenyon for proof-reading all or part of this thesis, and for making many helpful suggestions.

# A note on Units

In this work, a system of natural units will be used, whereby $\hbar = c = 1$

Between October 1992 and September 1995, this work was supported financially by the UK Particle Physics and Astronomy Research Council (P.P.A.R.C), formerly a part of the Science and Engineering Research Council (S.E.R.C).

*Dedicated to the memory of Arthur,*

*my grandfather.*

# Contents

# Introduction

The scattering of electrons from hadrons has historically been an important tool in the understanding of the constituents of matter. Electrons are particularly useful probes, since they are easily produced and accelerated, point-like and stable. Their interactions take place in the well understood and calculable electroweak sector of the Standard Model [1].

Early elastic electron-nucleus scattering experiments [2] demonstrated conclusively that the proton has a finite spatial extent on the scale of $10^{-15}$m, and measured the sizes and shapes of the charge distributions of nuclei from Hydrogen to Uranium. The earliest inelastic electron-nucleon scattering experiments [3] studied the electroproduction of resonances of isospin 3/2, decaying to $\pi N$ final states. Experiments at higher energies performed at SLAC[4], and later at DESY[5], observed excitations to a continuum of final states beyond the resonance region.

The resolution with which the target hadron is probed is measured by the square of the 4-momentum transferred, $Q^2$. In contrast to elastic $ep$ scattering, the SLAC and DESY experiments observed a scaling behaviour, such that other than the $1/Q^4$ term arising from the exchange photon propagator, there was no discernible dependence of the cross-section on $Q^2$ at fixed $Q^2/2M\nu$ [1], where $\nu$ is the energy transferred, and $M$ is the mass of the proton.

Such inelastic $ep$ interactions at large momentum transfer are termed *Deep-Inelastic Scattering* (DIS). They have been instrumental in the development of the modern picture of hadrons, as being composed of point-like spin-half *quarks*, with fractional electric charge, interacting with one another via the strong force, by the exchange of intermediate vector bosons, or *gluons*.

The total $ep$ cross-section is dominated by the limit, $Q^2 \to 0$, where the exchange photon is near to its pole. In this *photoproduction* limit, interactions may be interpreted as taking

[1] $Q^2/2M\nu$ may be identified as the Bjorken scaling variable, $x$, defined in equation 2.4.

place between an on-shell photon, and a proton. By factoring out a flux of photons associated with the electron, $ep$ collisions can be used to make measurements of cross-sections in the real $\gamma p$ system. At large centre of mass energies, the total $\gamma p$ cross-section is known to be dominated by contributions in which the photon converts to a hadronic state similar to a vector meson before reaching the target. Photoproduction processes therefore display similar characteristics to hadron-hadron collisions at high energy, including large elastic and other diffractive contributions, in which vacuum quantum numbers are exchanged.

Located at DESY in Hamburg, Germany, the Hadron Electron Ring Accelerator (HERA) is the most recent facility for the study of $ep$ collisions, and has been taking data since 1992. This thesis is concerned with a number of aspects of physics at HERA. Chapter 1 contains a brief description of the HERA accelerator, and a fuller review of the H1 experiment, which is built around one of the beam-crossing points. Challenging triggering problems arise from the high bunch-crossing repetition rate and large background levels, and the solutions that have evolved in H1 are stressed in particular. In chapters 2 and 3, theoretical issues relating to HERA physics are surveyed. Chapter 2 contains an introduction to DIS, and to the manner in which it is described in the gauge theory of the strong interaction, Quantum Chromodynamics (QCD). The phenomenology of electroproduction in the newly accessed low $x$ regime, and of photoproduction is discussed. Chapter 3 is devoted to a review of diffractive scattering. Regge's theory of the complex angular momentum plane is discussed, and predictions for HERA data are pointed out. One of the more exciting results to emerge from HERA to date is the observation of a class of events with diffractive topologies, but at large photon virtualities. In the final part of chapter 3, measurements of *deep-inelastic diffraction* are reviewed, and the present level of understanding of the partonic sub-structure of the diffractive exchange is discussed. Chapters 4 and 5 are concerned with measurements of cross-sections for diffractive photoproduction, using H1 data from the 1994 running period. In chapter 4, the experimental techniques used in the selection and kinematic reconstruction of diffractive events are described. In chapter 5, differential and total cross-sections are presented. Chapter 6 returns to detector issues, and is concerned with the trigger for the H1 Forward Muon Spectrometer. The mode of operation and field-programming of the device is described, and the acceptance is quantified. Physics processes to which the forward muon system is sensitive are identified, and the prospects for measurements of elastic and inelastic $J/\psi$ cross-sections with 1995 data are discussed.

# Chapter 1

# The H1 Experiment

## 1.1 Introduction

H1 is one of two detectors built around the HERA interaction points which are designed for the study of all aspects of electron-proton scattering. The first part of this chapter is devoted to a discussion of the HERA accelerator, and the remainder contains a more detailed description of the H1 experiment. After a brief review of the lay-out of the detector, the separate components of H1 are discussed in varying degrees of detail. A complete presentation of the design and performance of the detector can be found in [6]. This chapter concentrates on the components that are particularly relevant to the later parts of this thesis[1]. Several unprecedented challenges in event triggering are posed by the HERA collider, and emphasis is placed here on the design and mode of operation of trigger systems. A fuller description of the Forward Muon Spectrometer, and of the methods that it uses to reconstruct particle tracks, ends the chapter. The Forward Muon Trigger is the subject of chapter 6.

## 1.2 The HERA Accelerator

The HERA collider is the first example of the use of storage rings in the study of $ep$ collisions. Electrons[2] of around 30 GeV interact with protons at 820 GeV, giving a centre of mass energy equivalent to a 50 TeV electron beam incident on a stationary target, and

[1]During the winter shut-down between the 1994 and 1995 HERA running periods, a major upgrade of the backward (electron direction) region of H1 took place. Since the principal analysis in this thesis is concerned with 1994 data, the detector is described in its pre-upgrade configuration.

[2]Since the middle of the 1994 data taking period, HERA has been running with positron beams. Throughout this thesis, the beam lepton will be described as an electron, irrespective of its charge.

providing an extension of two orders of magnitude over fixed target experiments in the kinematic range covered in $x$ and $Q^2$. A further advantage of colliding beams is that the central range in pseudorapidity[3] in the $ep$ centre of mass frame covers a large solid angle in the laboratory, allowing for the first time detailed study of the hadronic recoil in DIS processes.

The HERA electron and proton beams are housed separately in a tunnel of 6.3km circumference, and are brought to collision at zero crossing angle. Conventional magnets are used to steer the electron beam, but fields well in excess of the magnetic saturation of iron are required to constrain the 820GeV protons. A field of 4.6T is achieved with a system of superconducting coils. Both superconducting, and warm RF cavities are used to accelerate the beams. Since the total $ep$ cross-section is small, large beam currents are required, and the accelerator operates in multi-bunch mode. Bunch-crossings occur in the interaction regions at 96ns intervals. The size of the proton beam dominates the longitudinal extent of the interaction region, which had an rms of approximately 10cm in the 1994 run. In that year, there were 153 colliding bunches of each type, and an additional 15 electron and 17 proton bunches were not brought into collision. These non-colliding bunches are known as pilot bunches, and are used to study and estimate background levels from beam interactions with residual gas in the beam-pipe (beam-gas)[4], and from collisions of stray protons with the beam-pipe walls and other apertures (beam-wall). The average luminosity in 1994 was $1.4 \times 10^{30}\mathrm{cm}^{-2}\mathrm{s}^{-1}$.

Located at the north and south interaction points of HERA are the multi-purpose detectors, H1 and ZEUS, both of which provide near hermetic coverage and are asymmetric in the beam direction, optimising the acceptance and measurement of scattered electrons in the electron direction, and of high multiplicities of final state hadrons in the proton direction.

Deep inelastic scattering of longitudinally polarised leptons from polarised targets has previously been used to study the spin structure of the nucleon. The present understanding is somewhat incomplete, with measurements [7] showing that the total helicity carried by charged partons is surprisingly small. The HERMES [8] experiment, located on the east side of HERA, is designed to further investigate the spin structure functions of the proton and neutron. The HERA electron beam can be polarised to a level of $\sim 80\%$, by making use of the fact that, over a period of time, synchrotron radiation leads to a natural transverse polarisation [9]. Spin rotators flip this to a longitudinal polarisation in advance of the HERMES target, and then back again afterwards. A polarised hydrogen,

[3] Pseudorapidity, $\eta$, is defined in equation 4.12.

[4] The gas pressure in the beam-pipe is around $10^{-9}$mbar. Even so, activity in the H1 detector from beam-gas sources alone occurred at rates of $\geq$ 10kHz for 'stable' running conditions in 1994.

deuterium or $^{3}$He target is placed in a storage cell at 20K, fed by a high intensity source of polarised atoms. The scattered lepton is detected in an electron spectrometer, consisting of drift chambers, proportional counters, and calorimetry.

On the west side of the accelerator, the HERA-B experiment is under construction. Fixed wire targets are introduced to the proton ring, with the aim of producing $b$-quarks, mainly through gluon-gluon fusion. The principal motivation for the experiment is the investigation of CP violation in the $B$ system, through the study of the process, $B^0 \rightarrow J/\psi K^0_S$. The triggering and reconstruction of lepton pairs from the $J/\psi$ decay, and the detection of pion pairs from the $K^0_S$ decay are therefore the main consideration in the design.

## 1.3 Overview of H1

The H1 apparatus is designed for the study of a wide range of aspects of the physics of electron-proton scattering. It must therefore provide comprehensive detection and measurement both of leptons and of hadrons, throughout the full solid angle about the interaction point. In addition, it must be capable of recognising processes originating from $ep$ interactions from amidst an overwhelming background of beam-gas and beam-wall interactions, and from cosmic sources. With a bunch-crossing repetition rate of 10.4MHz, fast pipelined triggering is necessary, which must also be able to identify uniquely the bunch-crossing in which an interaction took place. To enable complex decisions to be made, a multiple level trigger system is implemented. A final challenge is the digitisation of all detector information, and the reading out and writing to tape of over a quarter of a million electronic channels, spread over a large area of space, at rates of $\sim$ 10Hz.

The identification and measurement of the scattered lepton is paramount, particularly in the electron direction, where the final state lepton in DIS processes at moderate $Q^2$ is detected. The higher density of particle tracks requires that the parts of the detector in the proton direction be the most heavily instrumented. Hadronic calorimetry with high granularity and resolution is important for the detailed study of the hadronic final state. The calorimetry should be hermetic in order to measure imbalance in transverse energy, and detect charged current DIS events[5]. A magnetic field, and tracking chambers covering a large solid angle are necessary for the high resolution measurement of charged track momenta and multiplicity, and for particle identification using energy loss. Muon detectors are required for detection of the decays of heavy flavour particles, and for searches for a host of rare standard model and exotic processes. For the study of photoproduction

[5] For a discussion of neutral and charged current DIS processes, see section 2.1.1.

processes, in which the beam electron is scattered at very small angles, and for luminosity monitoring and measurement, further instrumentation is necessary downstream in the electron direction. Detectors that are sensitive to hadronic activity in the very forward direction facilitate the study of elastic and diffractive processes. Finally, strategically placed scintillators are required, to identify out of time particles, and hence to reject non *ep* background.

The main body of the H1 detector is depicted in figure 1.1. Nearest the interaction point are the central $\boxed{2}$, and forward $\boxed{3}$ tracking devices. The Backward Electromagnetic Calorimeter (BEMC) $\boxed{12}$ surrounds the beam-pipe in the backward direction. Labelled $\boxed{4}$ and $\boxed{5}$, the Liquid Argon (LAr) calorimeter is situated outside the trackers and the BEMC, and fills the space beyond the trackers in the proton direction. A superconducting coil $\boxed{6}$, of radius 3m, loops around the LAr calorimeter, providing a highly uniform solenoidal field of 1.15T throughout the tracking region. The iron return yoke of the magnet $\boxed{10}$ is instrumented to provide muon detection throughout the full solid angle, and is also used as a tail-catcher for uncontained hadronic showers. There are further muon chambers $\boxed{9}$ beyond the iron in the forward direction, with a toroidal magnet $\boxed{11}$ enabling a further measurement of the momentum of penetrating tracks at low angles to the beam-pipe.

As illustrated in figure 1.1, a right handed coordinate system is defined, with its origin at the nominal interaction point, the positive $z$ direction being that of the proton beam, and the positive $y$ direction being vertically upwards. In the corresponding set of spherical polar coordinates, $\theta = 0$ lies in the positive $z$ direction.

## 1.4 Triggering and Reconstruction

Efficient event triggering and data read-out are essential to the design of the HERA experiments. H1 has 270 000 electronic channels to be read out per event, with the additional constraint of a very high bunch-crossing frequency. Triggering and read-out systems are based on a VMEbus [10] standard. Most of the sub-detectors that comprise H1 have trigger systems, each of which typically sends eight bits of information, called *trigger elements* or *trigger bits*, to the first level of the central trigger (CTL1) [11] at each bunch-crossing [6].

The time interval between bunch-crossings at HERA (96ns) is short by comparison with

[6] In 1995, CTL1 received a total of 168 trigger elements per bunch-crossing.

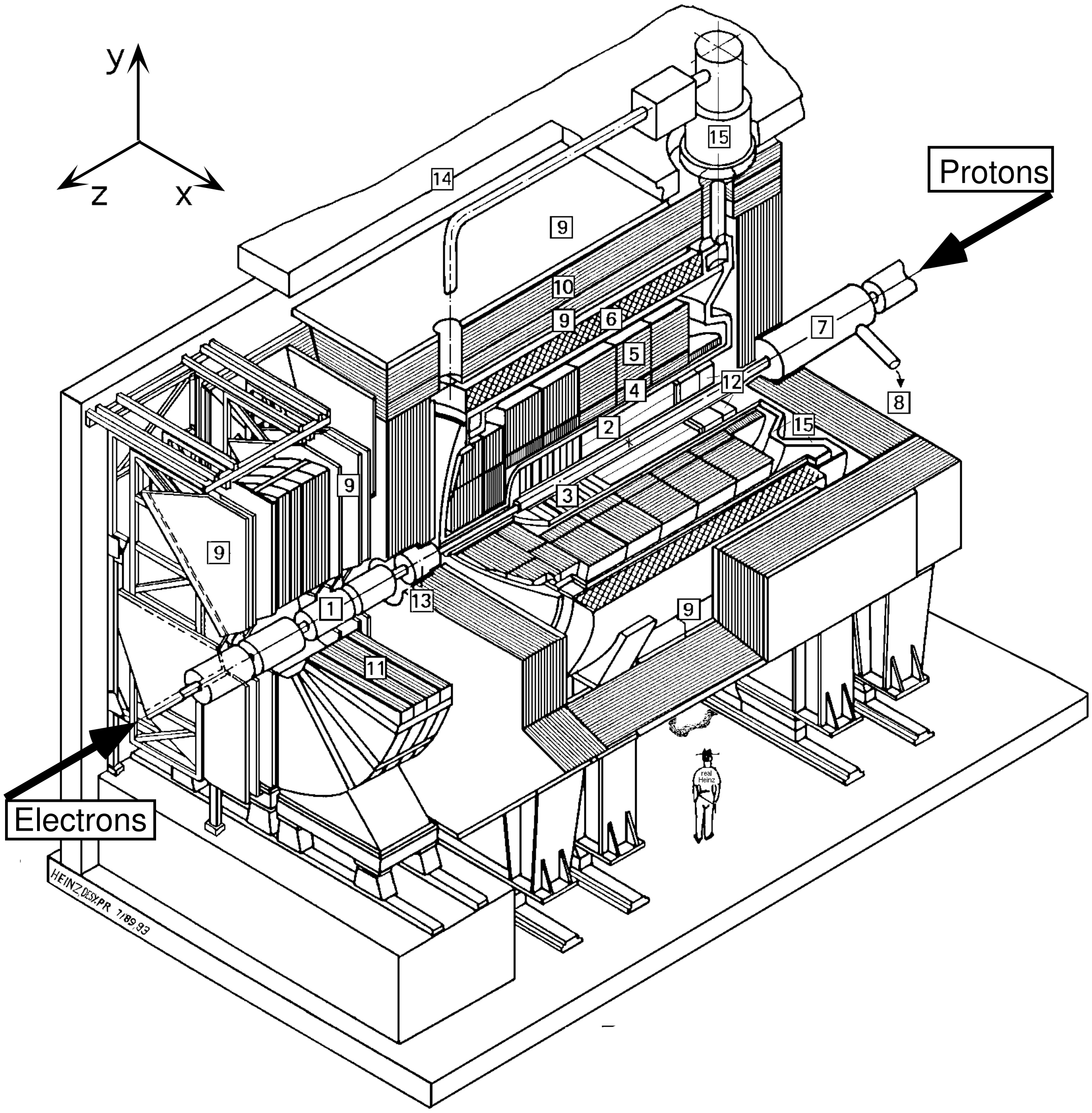


- 1 Beam-pipe and Beam Magnets
- 2 Central Tracking Detector
- 3 Forward Tracking Detector
- 4 Electromagnetic LAr Calorimeter
- 5 Hadronic LAr Calorimeter
- 6 Superconducting Solenoid
- 7 Compensating Magnet
- 8 Helium Cryogenics
- 9 Muon Chambers
- 10 Instrumented Iron Return Yoke
- 11 Forward Muon Toroidal Magnet
- 12 BEMC Calorimeter
- 13 Plug Calorimeter
- 14 Concrete Shielding
- 15 Liquid Argon Cryostat

Figure 1.1: *The H1 detector. The forward (+z) direction is defined to be that of the proton beam, and is towards the bottom left of the figure.*

the response and read-out times of the detector components [7]. For example, the maximum drift time in the cells of the Forward Muon Detector is $\sim 1.2\mu$s. Both the trigger, and the readout for the experiment are therefore pipelined.

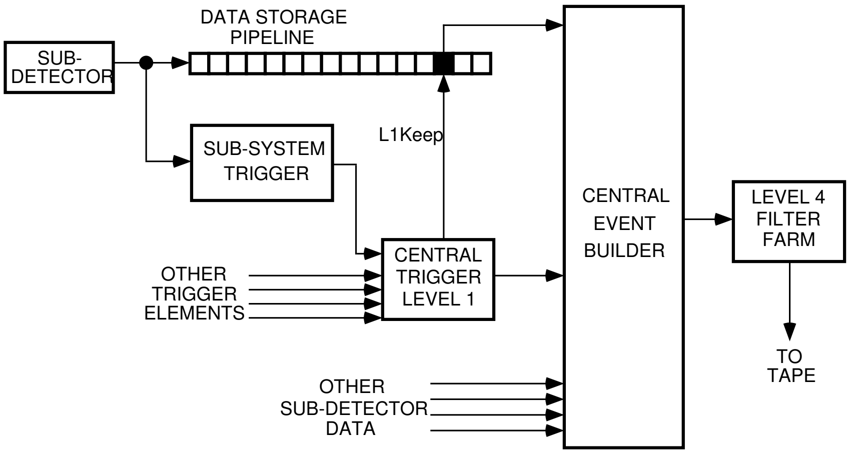


Figure 1.2: *A schematic illustration of the H1 trigger and read-out chain.*

Figure 1.2 illustrates the principal behind the H1 implementation of pipelining. Each sub-system trigger must process the information from a number of bunch-crossings simultaneously and sequentially, and the decision for a particular bunch-crossing is required to reach CTL1 within a fixed period (currently 22 bunch crossings). The full sub-detector information must be stored in memory for at least as long as it takes for the CTL1 decision to return ($\sim$ 24 bunch-crossings). Pipelining makes the first level trigger dead-time free, and it is therefore desirable that as much background rejection as possible is performed by CTL1.

Trigger elements arrive at CTL1 every 96ns, and are synchronised using variable delay lines that account for the differing latencies of the different sub-system triggers. CTL1 combines the information it receives from the full detector by searching for programmable combinations of trigger elements that constitute a *sub-trigger*. If a sub-trigger condition is satisfied, a scaler, corresponding to that sub-trigger, is incremented. Pre-defined *pre-scales* determine how many times a particular sub-trigger condition must be met before it results in the read-out of an event. Sub-triggers divide into two groups. Those designed for obtaining samples for physics analysis[8] must always contain a T0 signal[9] from at least one sub-system trigger, and are not pre-scaled if at all possible. Either because of high physics

[7] At the LHC, the situation will be even more extreme, with a bunch crossing interval of 25ns.
[8] There were around 65 physics sub-triggers in 1995.
[9] Most, but not all sub-system triggers have sufficient time resolution to provide information to the central trigger as to the precise bunch-crossing from which an event originates. Those that can are known as T0 triggers.

rates in the case of minimum bias photoproduction triggers, or because of high background rates in the case of some of the looser DIS and muon triggers, small pre-scales have to be applied, which merely result in a precisely known inefficiency factor for measurements. The second group of sub-triggers are constructed for monitoring purposes[10]. Some of these are designed to trigger on particular sources of background, to measure their rates. This class have very high pre-scales so that numbers of events can be counted without contributing to dead-time, and the occasional event is read-out for monitoring. A second class of monitor triggers are similar to particular physics sub-triggers, but have one or more of the conditions missing. Their pre-scales are generally lower than the background monitor triggers, but significantly higher than their physics partners, and they are used in the measurement of efficiencies of the sub-system trigger elements that they make redundant. After CTL1 has taken 1-2 bunch-crossings to combine the information from the different sub-system triggers, it sends an *L1Keep* signal to all branches, defined by the OR of all sub-triggers after application of pre-scales, stating whether or not each bunch-crossing should be read out further.

If the L1Keep signal is not set for a particular bunch-crossing, the information stored by each sub-detector simply falls off the end of the pipeline. Dead-time begins when a positive L1Keep signal is returned by CTL1, at which point, all pipelines are stopped, and the data that they contain are passed to front-end processors for zero-suppression. Upon an L1Keep signal, each trigger system also provides more detailed information to the central trigger. This can be[11] used by two further trigger levels that can make the decision to abort the building and readout of an event if it is identified as background. The level 2 trigger provides a signal after $20\mu$s, and level 3 can reject the event after $800\mu$s.

The requirement that the tracks in an event should point to a vertex in the nominal interaction region is the main criterion by which CTL1 selects events. From a background rate in excess of 10kHz, it is able to reduce the event rate to 30-40Hz, with dead-time of the order of 10%, and minimal losses to efficiencies for the majority of $ep$ interaction processes. After front-end processing, each sub-detector transfers its compressed data asynchronously, with an event tag, to a central event builder (CEB), over an optical fibre ring [12] (see figure 1.2). The front-end systems of all sub-detectors, and the CEB are sufficiently well buffered for the event building not to contribute significantly to dead-time. When all sub-detectors have sent their information to the CEB, dead-time ends, and the pipelines are once again freed. The reading out of an event costs the experiment 1-2ms of dead-time.

[10]There were around 40 monitor sub-triggers in 1995.

[11]During 1994 running, neither the level 2, nor the level 3 trigger levels were used.

Once the information from the different sub-systems has been pieced together by the CEB, events are passed to the level 4 stage of the trigger. This takes the form of a filter farm of 30 RISC (Reduced Instruction Set Computing) processors, running in parallel. A limited reconstruction of each event is performed, and fast and often complex on-line software cuts are applied, based on the full event information, and varying from level 1 sub-trigger to sub-trigger. The level 4 trigger rejects the bulk of remaining beam-gas and cosmic induced events, as well as those resulting from trigger noise. Events that pass the level 4 cuts are written permanently to tape at the rate of approximately 5-10 events per second, and are an average of 120kBytes in size. A small proportion of events rejected at the level 4 stage are still allowed through the filter, to monitor the effects of the cuts.

Although all data written to tape is permanently retained, further selection must take place before data sets are produced for physics analysis, and there is therefore a fifth level of selection off-line. A full reconstruction of each component of the detector is performed separately, after which detailed linking of charged particle track segments and energy clusters from the different sub-detectors gives an overall picture of the final state. Monitor sub-triggers are placed in data streams separate from physics sub-triggers. The fully reconstructed physics sub-triggers are subjected to further cuts, before being written, in a smaller format more convenient for analysis, to data summary tapes.

## 1.5 Calorimetry

Figure 1.3 summarises the four distinct components of the H1 calorimetry. The LAr (labelled EMC and HAC in the figure) and BEMC calorimeters are used in chapters 4 and 5 of this thesis for the measurement of the hadronic final state produced in photoproduction processes. Between these two detectors, full coverage in laboratory rapidity is available throughout the range, $-3.4 < \eta < 2.9$.

The remaining two calorimeters are not used in the analysis in this thesis. The plug calorimeter consists of nine 7.5cm layers of copper absorbing plates, with eight 40$\mu$m layers of silicon as sampling material. It is designed to close the gap in acceptance between the forward edge of the LAr and the beam-pipe, in order to minimise the transverse momentum that can escape in the forward direction. Its resolution is limited by its coarse sampling and by leakage, and is designed to be $\frac{\sigma(E)}{E} \sim \frac{1.5}{\sqrt{E}}$ [6] [12].

The instrumented iron uses the return yoke of the magnet as absorbing material, and

[12]Radiation damage to the silicon detectors of the plug calorimeter [13] has resulted in an increasingly poor signal to noise ratio, and the design resolution has never been reached.

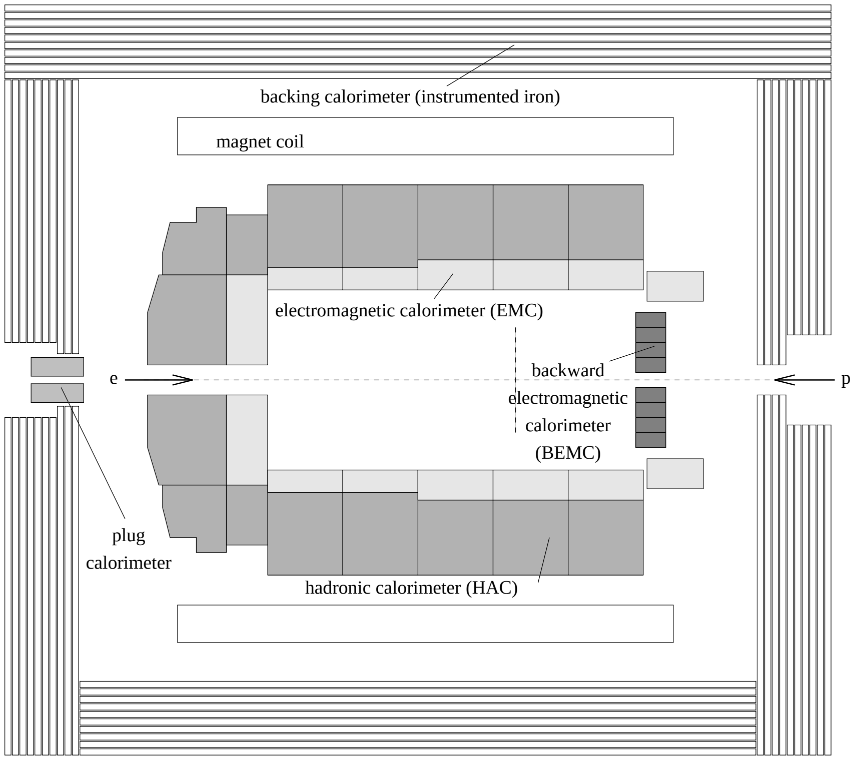


Figure 1.3: *$r - z$ projection of the H1 calorimeters, showing the four separate systems described in the text.*

limited streamer tubes [6] to detect the showers produced. Divided into barrel, front and back end-cap regions, the instrumented iron provides near $4\pi$ coverage. Apart from the detection of muons (section 1.9), it also acts as a 'tail-catcher', to detect components of hadronic showers not fully contained by the LAr and BEMC calorimeters, with resolution $\frac{\sigma(E)}{E} \sim \frac{1.0}{\sqrt{E}}$ [6].

### 1.5.1 The Liquid Argon calorimeter

The principal measurement of the hadronic final state, as well as that of scattered electrons in very high $Q^2$ ($\gtrsim 100\mathrm{GeV}^2$) DIS events, takes place in the LAr calorimeter [14]. It is designed to provide smooth and hermetic coverage in the range, $4^o < \theta < 154^o$, for the detection and energy measurement of all strongly and electromagnetically interacting particles. A single liquid argon cryostat is used, containing calorimeter stacks, structured in 8 wheels in $z$, each of which is divided into octants in $\phi$. This level of segmentation is a compromise between the minimisation of cracks, and practical considerations of handling. Liquid Argon is chosen for the sampling medium, because of its high atomic density, and its stability, homogeneity of response, and ease of calibration. The LAr is located inside the solenoidal magnet to minimise the dead material encountered by particles in their path to the calorimeter.

The electromagnetic part of the LAr uses 2.4mm thick plates of lead as absorbing material, sandwiching comparable thicknesses of sampling medium. Its thickness varies between 30 radiation lengths in the more forward part, and 20 radiation lengths in the central and backward regions. Except in the most backward wheel, the electromagnetic part of the LAr is entirely surrounded by the hadronic section. Reflecting the greater length of time taken for hadronic showers to develop in a medium, the plates in the hadronic LAr are each 16mm in thickness, and are made from stainless steel. The sampling cells are approximately 5mm thick, and the overall coverage varies between 4.5 and 8 interaction lengths. The orientation of the absorber plates in both parts of the LAr is such that the angle of incidence of a particle originating in the vertex region is always less than $45^o$. The cells are therefore stacked parallel to the beam in the forward and backward regions, and perpendicular to the beam in the central region.

The LAr contains around 45 000 read-out channels. Both for the electromagnetic and hadronic parts, the trigger combines and re-orders these into 256 *towers*, pointing to the interaction region. The energies and transverse energies in each tower are summed, towers are combined, and the final energy sums are discriminated against programmable thresholds that define the trigger elements sent to the level 1 trigger. Separate thresholds may be set for channels, towers and final sums. Acceptable rates have been achieved by setting final thresholds of less than 2GeV.

Off-line, noise is eliminated by removing signals from channels that are isolated from other activity. The non-compensating nature of the hadronic calorimeter results in losses at the 30% level, which are corrected using energy dependent weighting factors. The fine segmentation of the calorimeter, and the difference between the locations and shapes developed by electromagnetic and hadronic showers, allows a highly effective $e/\pi$ separation of less than $10^{-3}$. Measured in test beams [14], the resolution of the electromagnetic LAr system was found to be $\frac{\sigma(E)}{E} \sim \frac{0.12}{\sqrt{E}} \otimes 0.01$, with $E$ in GeV, and that of the hadronic part, $\frac{\sigma(E)}{E} \sim \frac{0.50}{\sqrt{E}} \otimes 0.02$. The overall energy scale for the electromagnetic system is known to 3%, from calibrations comparing the LAr energy measurement of the scattered electron in DIS, with measurements made in the tracking detectors. The hadronic scale is determined using $p_T$ balance in DIS events, and is presently known to 6%.

### 1.5.2 The Backward Electromagnetic Calorimeter

Filling the region between the beam-pipe and the backward part of the electromagnetic LAr, is the BEMC [15]. It is a conventional lead-scintillator sampling calorimeter, and its principal purpose is the triggering and energy measurement of the scattered electron in neutral current DIS events, with $5 \lesssim Q^2 \lesssim 100\mathrm{GeV}^2$. It is also used in the measurement of the hadronic final state in low-$x$ DIS and photoproduction processes. The angular range covered is $151 < \theta < 176^o$. In order to aid the spatial resolution for electrons, a Backward Proportional Chamber (BPC) is mounted directly onto the front surface of the BEMC (see figure 1.5), covering the region, $155 < \theta < 174^o$. The BPC consists of four planes of multi-wire proportional chambers (MWPCs), with the wires of alternate planes off-set from one another by $45^o$. It measures the impact position of particles entering the BEMC to 1.5mm. Proton beam-induced background is vetoed using the ToF device (section 1.8), which is located behind the BEMC in the $z$ direction[13].

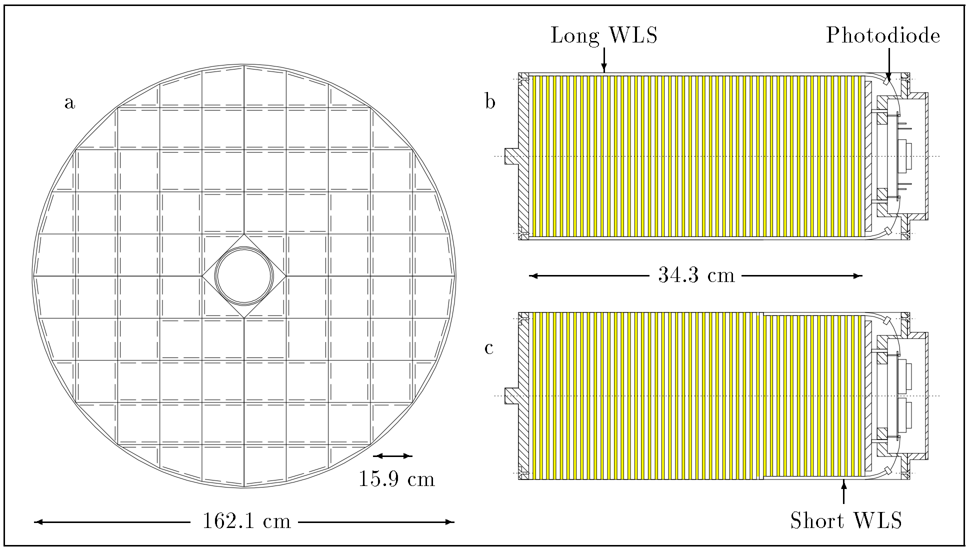


Figure 1.4: *The Backward Electromagnetic Calorimeter. (a) Cross-section in the beam direction, showing the layout of stacks. (b) and (c) Longitudinal views of a stack, showing the wavelength shifters (WLS) and photodiodes used for readout.*

Figure 1.4a shows a view of the BEMC in the $z$ direction. 88 calorimeter stacks are contained within a cylindrical barrel. Of these, 56 are square in cross-section and the

[13]During the winter shut-down prior to the 1995 run, the backward region of the H1 detector was upgraded. The BEMC was replaced by a high resolution lead-fibre *SPACAL* calorimeter [16], which is also able to fulfil the rôle of the Time of Flight Device. The BPC has been replaced with a drift-cell based tracker, giving improved spatial resolution and an additional measurement of electron momenta.

remainder, at the inner and outer extremes, have triangular and trapezoidal cross-section such as to make the most efficient use of the available space. In profile (figures 1.4b and c), each stack consists of 50 sampling layers, covering a total of 21.7 radiation lengths. 4mm depths of scintillator are sandwiched between 2.5mm sections of lead absorber. Atomic excitations of the scintillating material produce electromagnetic radiation in the ultra-violet region, which is shifted by a dye into the blue, and passed via wavelength shifters to photodiodes, by which stage its wavelength distribution is centred at around 500nm. 'Long' wavelength shifters collect the light from the full length of the stack, and in order to improve the reconstruction of the longitudinal profile of showers, light from the final 15 layers is also collected by broader 'short' wavelength shifters, which are connected to two photodiodes.

Each photo-diode corresponds to a read-out channel. The trigger sums the analogue signals to give a response for each stack at each bunch-crossing. Two thresholds are defined for the stacks, the lower of which is intended to be as low as possible within noise constraints (1.3GeV in 1994), and the higher of which was 2.3GeV in 1994. Any stack with energy greater than the higher threshold is combined with all adjacent stacks that are above the lower threshold to define a *cluster*. Pre-defined thresholds for cluster energies, and for the energy deposited throughout the entirety of the BEMC define the trigger bits that are sent to the level 1 trigger. In 1994, the cluster threshold was 4.3GeV in combination with a track trigger, or 7.7GeV for a stand-alone BEMC trigger.

Calibration of the BEMC is performed in data, using the kinematic peak technique[14], and gives an overall energy scale that is known to 1% for electrons. Test beam results [15], along with cross-checks using H1 data, show an electron energy resolution that is parameterised by $\frac{\sigma(E)}{E} \sim \frac{0.39}{E} \otimes \frac{0.10}{\sqrt{E}} \otimes 0.017$, where the first term arises from constant levels of noise in the electronics, the second term is due to sampling fluctuations, and the final term is generated mainly by leakage due to finite stack depth. The comparatively large stack cross-section of the BEMC means that the spatial position of a cluster is best measured by the BPC. Electron-hadron separation is performed off-line, based mainly on lateral shower profiles, and the isolation of clusters.

Since it only covers $\sim 1$ interaction length, the hadronic response of the BEMC is poor. Around 40% of hadrons fail to interact in passing through the detector, and since the minimal ionising signal is only $\sim 2\sigma$ above noise levels, they are not detected. The average pion deposits around 45% of its energy in the BEMC, and with detailed off-line corrections, measurements can still be made. The resolution for hadrons is of the order

[14]The energy spectrum of scattered electrons in DIS events has a pronounced peak near to the beam energy. Monte Carlo techniques are used to tune the energy measurement to the expected shape.

of $\frac{\sigma(E)}{E} \sim \frac{1.0}{\sqrt{E}}$ [6].

## 1.6 Tracking

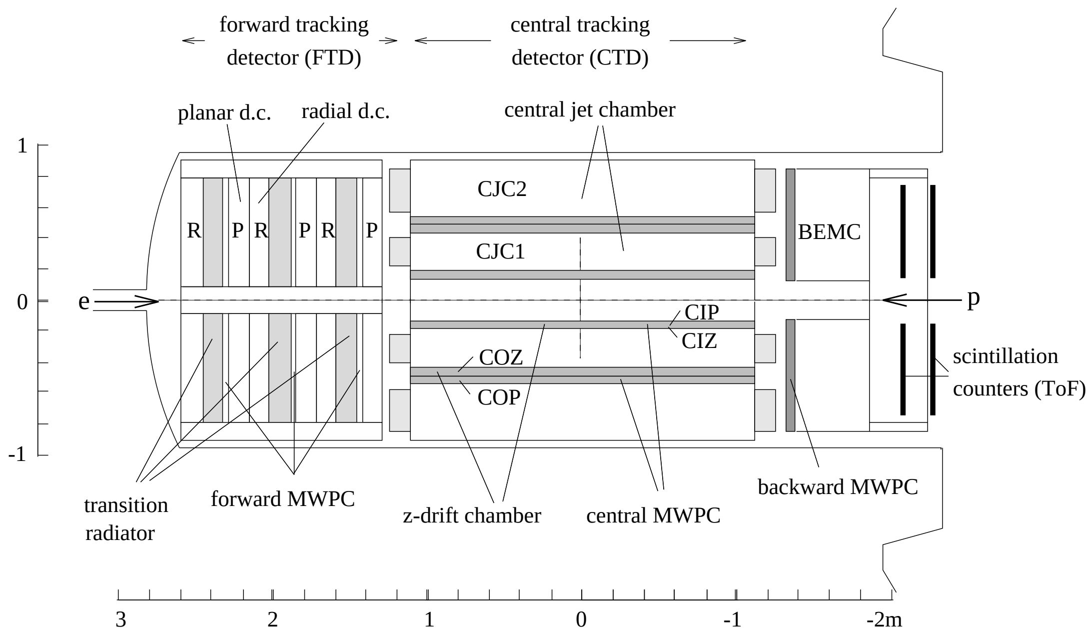


Figure 1.5: *The inner part of the H1 detector, showing the central and forward trackers, and the full inner-backward region. The BPC is labelled 'backward MWPC', and sits on the surface of the BEMC.*

The H1 particle tracking system divides into two distinct components; the central and forward trackers. The central tracker has a coverage in polar angle of $15 < \theta < 165^{\circ}$, whilst the forward tracker covers the region $7 < \theta < 25^{\circ}$. With the BPC (section 1.5.2) providing additional tracking information in the backward region, charged particle tracks can be reconstructed throughout the rapidity range, $-3.0 < \eta < 2.8$. An illustration of the full tracking region of H1 can be found in figure 1.5.

Both the forward and central trackers contain mixtures of drift chambers and MWPCs. The MWPCs have fast response times, and are used primarily as triggering devices. Their resolution is limited to the wire spacing, and more accurate measurements of hit coordinates can be made with drift chambers. Digitisation of all drift chamber information in H1 is performed with F1001 Flash Analogue to Digital Converters (FADCs) [6]. These have sampling frequencies of 104MHz, and hence, resolutions of the order of a few ns on the times of arrival of pulses. With drift velocities for electrons in the gas of around $5\mathrm{cm}\mu\mathrm{s}^{-1}$, hits can be located to $100 - 200\mu$m in the drift direction. Building multiple layers of drift cells allows detailed reconstruction of the trajectory of a charged particle, and staggering cells relative to one another resolves ambiguities as to which side of a central sense wire a particle passed through. The coordinate in the direction of the sense wire may be inferred by charge division to $1-2\%$ of the wire length, provided it is read out at both ends. Momentum measurement is possible from the bending of the track in the solenoidal field. Particle identification is performed from $dE/dx$ measurement, and with transition radiators.

### 1.6.1 The Central Tracker

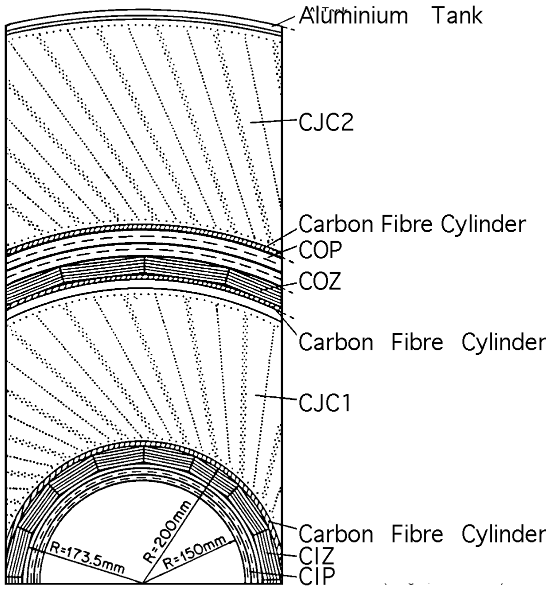


Figure 1.6: *A section in the $r-\phi$ plane of the Central Tracking Detector.*

A longitudinal profile of the central tracker can be seen in figure 1.5, and a cross-section is shown in figure 1.6. The main feature is two large concentric drift chambers, CJC1 and CJC2 [17], with wires strung parallel to the beam axis, such that the $r$ and $\phi$ coordinates are best measured. The CJCs have cells that are tilted by about $30^o$ from the radial direction, so that the drift direction for high momentum tracks is never far from perpendicular to the track direction, and so that tracks of all momenta are sampled a number of times. CJC1 has 30 cells with 24 sense wires each, and CJC2 has 60 cells, each of which contains 32 sense wires.

Along with hadron triggers from the LAr calorimeter, the CJC trigger [18] is principally responsible for triggering hard photoproduction events, both with and without a tagged electron, and other classes of events containing high $p_T$ tracks. Using 10 of the 56 layers in $r$, the trigger accepts tracks whose distance of closest approach to the origin in the $r-\phi$ plane it measures to be less than 2cm. Trigger elements are defined according to multiplicity and numbers of tracks of either sign.

The best measurement of the $z$ coordinates of central tracks is obtained from two thin layers of drift chambers (CIZ, COZ) [19], whose sense wires run perpendicular to the beam-pipe, and whose drift fields are such that ionisation drifts in the $z$ direction. The CIZ is located immediately inside CJC1, and the COZ lies immediately outside it. With this additional information on the $z$ coordinate of tracks, the design resolution on the momentum of charged tracks in the central tracker is $\frac{\sigma(p)}{p^2} \sim 3 \times 10^{-3}\mathrm{GeV}^{-1}$, with double track resolution of $\sim 2.5$mm.

The presence of any track pointing to the nominal vertex region is established in the majority of sub-triggers, using the *z-vertex T0* trigger element from the MWPCs in the central tracker (CIP, COP) [20]. The CIP detector is the innermost component of the central tracker, and the COP is located immediately inside CJC2. The mode of operation of the z-vertex trigger is described in section 1.6.3.

### 1.6.2 The Forward Tracker

As shown in figure 1.5, the forward tracker [21] is divided in $z$ into three very similar *supermodules*. Each supermodule consists, in increasing $z$, of twelve layers of planar drift chambers, a section of MWPCs, transition radiators and twelve layers of radial drift chambers.

The planar drift chambers are split into four sets, each of which has three layers of drift cells, with wires in the $r-\phi$ plane. The three layers in a set have sense wires offset from one another by 60° in azimuth, so that a space-point measurement can be made. The transition radiators consist of 400 closely spaced polypropylene films. When a charged particle crosses one of the boundaries in refractive index, it emits a soft X-ray with a probability proportional to the Lorentz factor, $\gamma$. This makes transition radiators particularly useful for $e-\pi$ separation. The photons are emitted at small angles to the direction of the track, and cause ionisation principally by the photo-electric effect in the gas of the subsequent radial drift chambers. The transition radiation is therefore observed as an enhancement in charge deposition in the first layers of the radial chambers. The radial chambers consist of 48 radially strung wires in each of twelve planes, the length of which increases with $z$. They provide an accurate measurement of the $\phi$ coordinate and a more limited extraction of the radial coordinate from charge division.

The MWPCs in the first supermodule are used with the CIP and COP in the z-vertex trigger. The *Forward Ray* trigger [22] uses all MWPCs in the forward tracker, with the CIP, to trigger forward going tracks using topological criteria. The trigger searches for 'rays' in each of 16 sections in azimuth and activates level 1 trigger elements when it finds a ray segment in three of the four modules used.

### 1.6.3 The z-Vertex Trigger

Most non-*ep* induced background can be removed by requiring the reconstruction of a vertex in the interaction region. The z-vertex trigger [23] is able to do this at the level 1 trigger stage, and is used as one of the main triggers in the analysis that follows. Signals from the double cylindrical MWPC layers of the CIP and COP are used, along with the double layer of the planar MWPC in the first supermodule of the Forward Tracker.

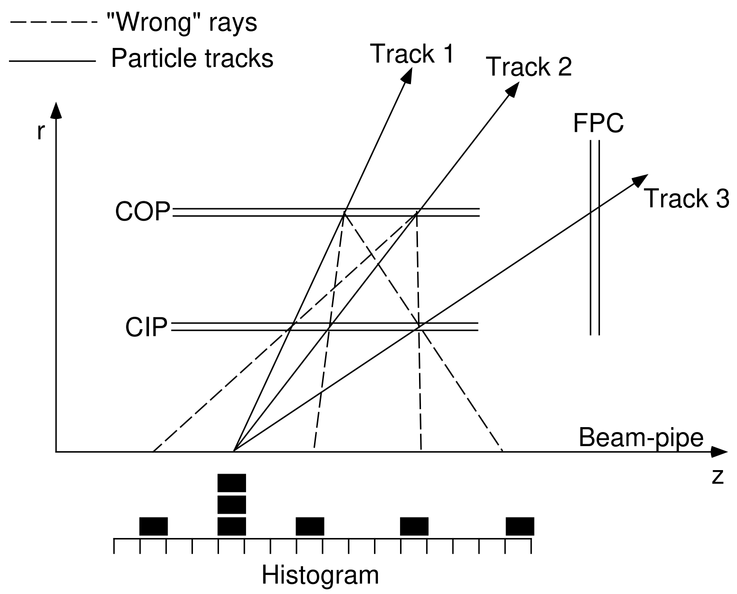


Figure 1.7: *An illustration of the mode of operation of the z-vertex trigger, showing a single segment in $\phi$ for a hypothetical event. By combining information from any two of the CIP, COP and the MWPCs in the first supermodule of the Forward Tracker, rays are defined, and extrapolated back to $r = 0$, where a histogram of the resulting positions in z is made. The three genuine tracks give entries in the same bin, whereas rays made from wrong combinations form a random pedestal.*

Figure 1.7 illustrates the principal on which the z-vertex trigger works. The detector is divided by the trigger logic into 16 segments in $\phi$. *Rays* are defined within each segment, corresponding to lines drawn through pairs of hits in any two of the three sets of chambers used. All possible rays are extrapolated to $r = 0$ and a histogram is logically built of the resulting positions in $z$, in 16 bins of 5.4cm. The histograms from different $\phi$ segments are summed and the combined histogram is used in a fully programmable way to define trigger elements to be sent to the first level trigger.

Rays corresponding to true tracks give entries in the bin of the histogram corresponding to the vertex position of the event, significant above a relatively flat background from wrongly identified rays. Background events with vertices outside the interaction region develop no peak, and only the pedestal is visible. A T0 trigger element is defined, and is set whenever there is at least one entry in the histogram. The T0 bit is efficient at recognising any activity whatsoever in the central region of the detector, and is used by most sub-triggers for bunch-crossing identification. Peak significance analysis on the histogram is performed on-line, to define further trigger elements and low multiplicity triggers are set in the case where there are few entries in the histogram, but they are all in the same bin.

## 1.7 The Luminosity System

The H1 detector is complemented with instrumentation along the beam-line in the electron direction, in the form of a photon detector, and a low angle electron tagger, both of which are illustrated in figure 1.8. This system fulfils the dual rôle of measuring luminosities [24], and triggering on and measuring the energy of electrons scattered at extremely low $Q^2$ ($< 10^{-2}\mathrm{GeV}^2$) for photoproduction analyses [25]. The luminosity system is used for both of these purposes in the analysis parts of this thesis.

### 1.7.1 The Electron Tagger and the Photon Detector

Electrons scattered at very small angles to the beam-line are deflected by the beam magnets through an exit window and hit the electron tagger at $z = -33.4$m. The electron tagger consists of 49 crystal calorimeters, covering 22 radiation lengths. Its acceptance is defined by the fields of the HERA magnets, and is highly sensitive to any change in the $x$ coordinate of the electron beam at the interaction point. The issue of the acceptance and resolution of the electron tagger is discussed in section 4.4.2.

Photons leaving the interaction point collinear with the electron beam leave the beam-pipe where it starts to bend, and enter the photon spectrometer. This consists of the

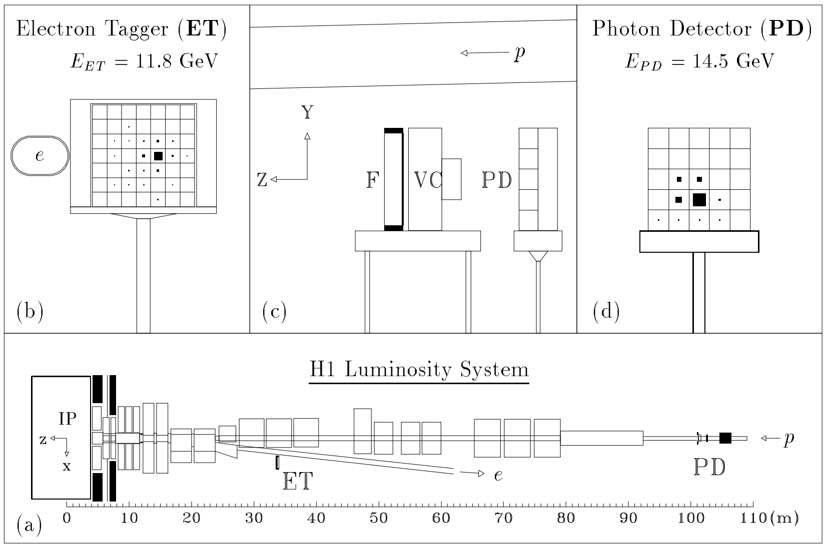


Figure 1.8: *A Bremsstrahlung event, detected in the luminosity system. a) Top view of the beam-line instrumentation, showing the electron tagger (ET) and photon detector (PD) in their positions relative to the interaction point (IP). b) $x - y$ projection of the electron tagger. c) Side view of the photon arm, consisting of a lead filter (F), a water Čerenkov counter (VC) and the main photon detector, (PD). d) $x - y$ projection of the photon detector.*

main photon detector, along with a lead filter for the removal of synchrotron radiation and a water Čerenkov counter, which provides a crude energy measurement, and removes out of time photon showers. The photon detector itself consists of 25 crystal calorimeters of the same design as those in the electron tagger and also covers 22 radiation lengths. It is situated at $z = -102.9$m.

### 1.7.2 Luminosity Measurement

The luminosity collected by the experiment can be measured by several different methods [26], from the radiative elastic process, $ep \to ep\gamma$. Near to the poles of both the electron and photon propagators, the elastic Bremsstrahlung process, whereby the electron radiates a photon in the electromagnetic field of the proton, dominates over inelastic reactions. Radiation from the initial and final state proton lines can be safely neglected, and at low virtualities, the proton is well approximated as being point-like. A precise calculation of the cross-section in QED is then possible, and in the highly relativistic limit and small angle approximation, the Bethe-Heitler formula [27] can be used to measure the luminosity, from the measured and acceptance corrected Bremsstrahlung rate, with a theoretical uncertainty of less than 0.5%. Due to the statistical limitations in using other processes, measurements based on the Bremsstrahlung process are the only ones that are currently competitive[15]. The errors on the measured luminosities are then dominantly systematic.

On-line, the luminosity is monitored in a way that is sensitive to instantaneous changes, by counting events with coincident signals in the electron tagger and the photon detector. In the very low $Q^2$ limit, the sum of the electron and photon energies from the Bremsstrahlung process is constrained,

$$E_e = E_{e'} + E_\gamma \tag{1.1}$$

such that the selection of events with $23 < E_\gamma + E_{e'} < 30$GeV yields a relatively pure sample. The additional requirements that $E_\gamma > 5$GeV and $E_{e'} > 5$GeV ensures that the sample is not corrupted by trigger thresholds or noise effects.

A more accurate luminosity measurement can be made off-line, with corrections for energy leakage from the edges of the electron detector. Residual background from the Bremsstrahlung of electrons from gas particles in the beam-pipe are subtracted statistically using pilot bunch information. A correction must also be made for the effect of *Proton Satellite Bunches*, which appear at 4.8ns intervals relative to the main bunch, and are due to protons escaping during pre-acceleration and injection. They can contain up to 10% of the total proton current. The error on the resulting luminosity measurement is $\sim 4\%$, limited by the dependence of the electron tagger acceptance on the beam-optics.

An alternative method gives the best luminosity measurement available. The Bremsstrahlung process is still used, but the measurement is based solely on the detection of the scattered photon. With a slightly higher energy cut of $E_\gamma > 8$GeV, the acceptance of the photon spectrometer for the Bremsstrahlung process is $\sim 98\%$, and is only weakly dependent on the beam optics. The absolute calibration and determination of resolution for the photon detector is performed by comparison of the photon energy spectrum with a Monte Carlo [28] based on the Bethe-Heitler formula, and including a full simulation of the HERA beam-line, and and the luminosity system.

The average luminosity is calculated using the formula,

$$\mathcal{L} = \frac{\mathcal{N}_{data}(\Delta t) - \mathcal{N}_{back}(\Delta t)}{\mathcal{A}_{BH}\ \Delta t} \tag{1.2}$$

where $\mathcal{A}_{BH}$ is the acceptance for the Bethe-Heitler process, as measured using the Monte Carlo. $\mathcal{N}_{data}(\Delta t)$ is the number of events collected in a time interval, $\Delta t$, and $\mathcal{N}_{back}(\Delta t)$ is

[15] At 1994 luminosities, typical Bremsstrahlung rates were $\sim 60$kHz.

the corresponding number of electron-beam-gas initiated events. $\mathcal{N}_{back}(\Delta t)$ is estimated from the number of detected events in the electron pilot bunches, and the ratio of total to pilot bunch currents,

$$\mathcal{N}_{back}(\Delta t) = \frac{I_{all}}{I_{pilot}} \mathcal{N}_{pilot}(\Delta t) \tag{1.3}$$

## 1.8 The Time of Flight Device and Other Scintillators

Scintillator based detectors have intrinsically good time resolution, and are essential for the removal of background at CTL1. The principal purpose of the Time of Flight hodoscope (ToF) [29] is the fast separation of $ep$ collisions in the interaction region from proton beam induced background originating upstream.

The ToF consists of two walls of plastic scintillator between the BEMC and the backward end-cap of the iron (see figure 1.5), detecting particles arriving from either direction,. The scintillator walls are sandwiched between layers of lead, whose purpose is the removal of synchrotron radiation. The device must operate in the 1.15T field of the magnet, so signals are amplified using high field photomultipliers. They are then discriminated in NIM logic and information with a time resolution of $\sim$ 2ns results. The signals are strobed against predefined *windows*, corresponding to signal and background time periods, before being sent to the level 1 trigger.

The principal of operation of the ToF is that particles originating upstream, associated with proton beam induced background, arrive at the scintillator a time $\sim |z|/c$ before a bunch-crossing, where $z$ is the location of the ToF relative to the interaction point. Particles associated with an $ep$ interaction arrive at a time $\sim |z|/c$ after the bunches are brought to collision. The timing discrimination therefore improves with $|z|$, but at the expense of angular coverage. The ToF is located at $z \simeq -2$m, which is just sufficient for the efficient separation of signal from background. Its geometrical coverage of $-3.5 \lesssim \eta \lesssim -2$ is similar to that of the BEMC. The efficiency of the device for minimally ionising particles has been measured to be $98 \pm 1\%$ from studies of independently triggered beam halo muons arriving nearly parallel to the proton beam.

Three main pieces of information are sent by the ToF to the Central Trigger for each bunch-crossing, all of which correspond to a coincidence of hits in both scintillator walls within the open period of a strobe window:-

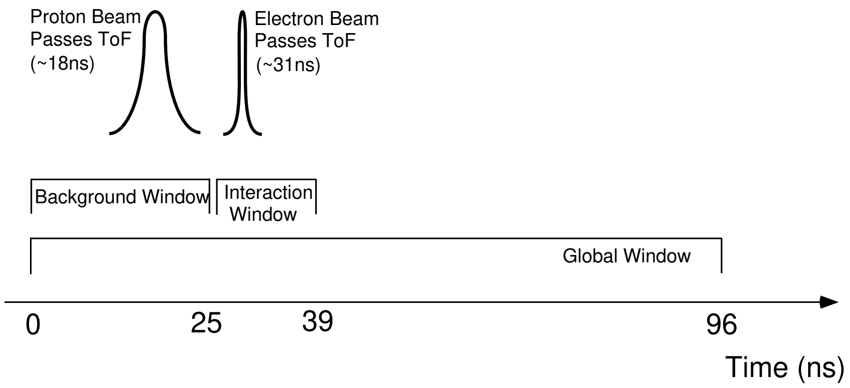


Figure 1.9: *An illustration of a 96ns cycle in the operation of the Time of Flight hodoscope. The Global window covers the full beam-crossing cycle. The Background Window is* $\sim$ 25ns *long and covers the period during which the proton beam, of 2-3ns in size, passes. Around 1ns after the end of the Background Window, the Interaction Window begins. This is* $\sim$ 13ns *long, and includes the point at which the electron beam, of negligible size, passes the device.*

**Global Signal** A pair of hits at any stage in the 96ns cycle.

**Background Signal** A pair of hits in the pre-defined background window.

**Interaction Signal** A pair of hits in the pre-defined interaction window.

Figure 1.9 shows how the three time windows are defined, relative to the times at which the electron and proton beams pass the device. Events triggered by the trigger element from the ToF interaction window are analysed in chapters 4 and 5.

Since the electron beam passes the ToF at similar times to particles from $ep$ interactions, signals in the Interaction Window are dominated by synchrotron radiation. A further Time of Flight device, similar to, but smaller than the one in the backward direction is placed 50mm from the beam axis, in the vicinity of the forward muon toroid ($z \simeq 7$m), and is known as the Forward ToF (FToF) [30]. The FToF is sensitive to particles arising from beam-gas and beam-wall interactions, as well as from secondary scattering of proton remnants in $ep$ interactions. Global, Interaction and Background signals are sent to the Level 1 trigger along similar lines to those of the ToF. Where both sets of scintillators are fired, the difference in timing between ToF and FToF signals separates $ep$ interactions from background arising from either beam.

H1 is instrumented with two further sets of scintillators. The 'Veto Wall' is situated backward of the iron return yoke, and consists of two double scintillator walls at $z = -6.5$m and $z = -8.1$m. Its purpose is the detection of hard penetrating background particles (almost exclusively muons), arriving with the proton beam. Again, information is sent to the level 1 trigger, allowing dead-time free removal of such background.

In the very forward direction, at $z = 26$m, the Proton Remnant Tagger (PRT) surrounds the beam-pipe. It consists of two layers of scintillator, sandwiched between lead shielding, and is used off-line for the identification, at very large rapidities ($6 \lesssim \eta \lesssim 8$), of particles originating from proton fragmentation. This makes the PRT very useful for diffraction analyses (see section 4.5.3).

## 1.9 Muon Detection

The outermost components of H1 are devoted to the detection of penetrating muon tracks. Surrounding the whole of the main body of the detector (see figure 1.3), the iron yoke of the magnet is interleaved with instrumented slits, containing a total of 16 layers of limited streamer tubes, comprising the central muon system. In the forward direction, the Forward Muon Spectrometer provides supplementary muon detection and measurements.

Reconstruction efficiency has been studied in the Central Muon System using samples of cosmic muons which are triggered, and whose momentum is measured by the central tracker. Efficiencies of around 90% are found for muons with momenta above a threshold of approximately 2GeV. The central muon trigger [31] uses 5 of the 16 layers. It divides the system into inner and outer forward and backward end-caps, as well as forward and backward barrel regions. The trigger logic searches for coincidences of signals from the layers in each of the 6 regions, requiring pre-programmed numbers of layers to show a track segment. Currently, a $\frac{3}{5}$ layer condition is required in all regions except for the front end-cap, where backgrounds are largest, and a $\frac{4}{5}$ layer coincidence requirement is set.

The very forward regions of the HERA detectors are subjected to the highest levels of activity, and are therefore a complicated environment in which to trigger and reconstruct particles. For this reason, H1 is instrumented with further muon detectors, in addition to the instrumented iron, in the form of the Forward Muon Detector (FMD) [32]. The resolution on momentum of muons at low polar angles, when measured in the main solenoidal field of H1, is poor, since the transverse motion with respect to the field lines is small. To provide an independent measurement, an iron toroidal magnet is included as part of the Forward Muon system.

The following sections contain a detailed description of the FMD. This serves to give an impression of how the reconstruction chain of a typical component of H1 works, and also provides the necessary background for chapter 6, which is concerned with the Forward Muon Trigger.

### 1.9.1 Overview of the Forward Muon Spectrometer

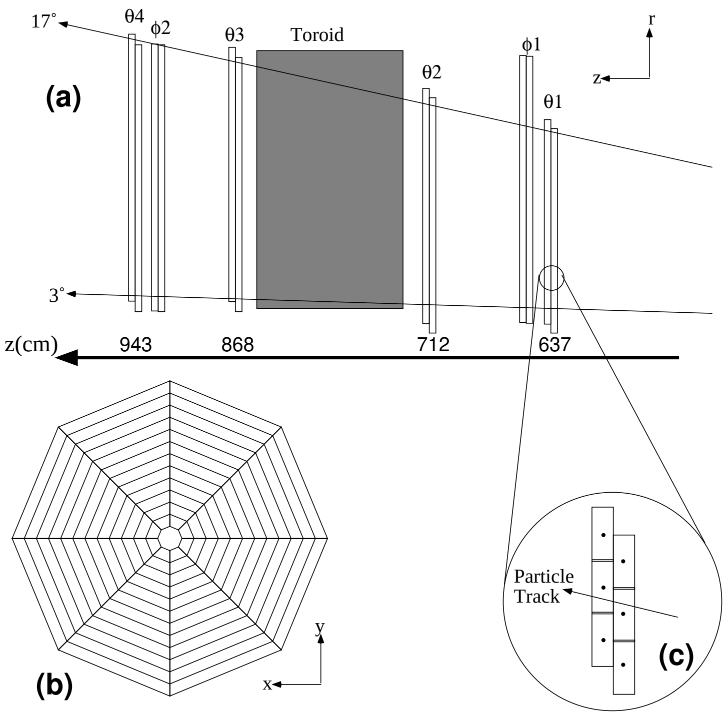


Figure 1.10: *Schematic overview of the Forward Muon Spectrometer. (a) The full system in $r-z$ projection. (b) A single $\theta$ layer in $x-y$ projection. (c) Distribution of drift cells within a layer in $r-z$ projection.*

The FMD is designed to provide identification and momentum measurement of muons produced at the vertex in the momentum range, $5 < p < 100$GeV, with polar angles, $3^o < \theta < 17^o$. Multiple Coulomb scattering sets the lower bound on the momentum measurement[16], and the upper limit is set by the degree to which a track can be bent in the magnetic field of the toroid. The muon signal from $ep$ interactions is very small by comparison with background levels. As well as the high incidence of secondary hadronic activity, there are also high rates of background muon tracks not originating from $ep$ interactions. Cosmic rays, and *beam-halo* muons, passing through the detector in time with, and almost parallel to the proton beam, are the main sources of muon background. Beam halo muons arise from proton beam-gas and beam-wall interactions, well upstream

[16]A muon loses an average energy $\sim$ 3GeV in the main body of H1, before reaching the FMD. An additional energy $\sim$ 1.5GeV, is lost in the iron toroid.

of the detector. Both beam-halo and cosmic muons are useful for calibrating the detector, and measuring misalignments [33] [34].

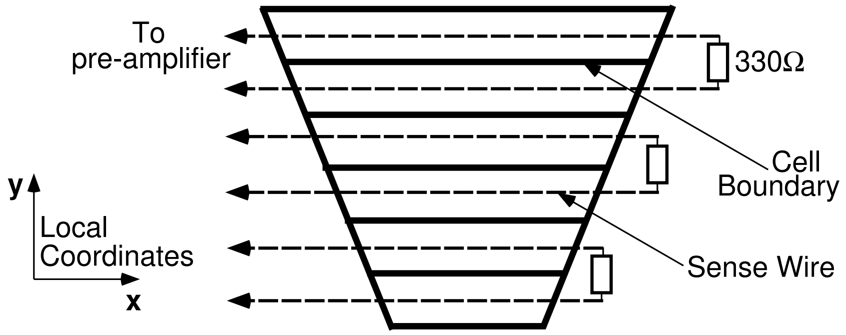


Figure 1.11: *A section of an octant of a $\theta$ layer, showing the location of the sense wires. The local coordinate system used within an octant is also illustrated. The local $x$ and $y$ coordinates are defined such that the origin is at the beam-pipe.*

The lay-out of the FMD in the $r-z$ plane is shown in figure 1.10a. Three pairs of planes, or *layers*, of drift chambers are located on either side of the toroidal magnet. Those layers labelled $\theta$ are designed to give an accurate measurement of the polar coordinate[17], and a more restricted measurement of $\phi$. The drift cells in the layers labelled $\phi$ are orthogonal to those in the $\theta$ layers, and are designed to be more sensitive to the $\phi$ coordinate. In azimuth, each pair of planes is divided into distinct octants, as shown for a $\theta$ layer in figure 1.10b. The number of drift cells per octant increases with distance from the interaction point, between 24 in $\theta 1$ and 40 in $\theta 4$. Within an octant, a local system of coordinates is defined, shown for a $\theta$ layer in figure 1.11, such that the origin in local $x$ and $y$ is at the beam-pipe, and the $y$ direction points radially outwards along the axis of symmetry of the octant. As shown in figure 1.10c, each layer consists of two planes of drift chambers, staggered from one another by half a cell. A muon track can therefore be sampled up to twelve times as it traverses the system.

The toroidal magnet is 1.2m thick, has inner radius 0.65m, and outer radius, 2.9m. Twelve rectangular coils, each with fifteen turns of water cooled copper tubing and carrying a current of 150A, provide a field of approximately 1.5T. The incident polar angle of charged tracks is deviated in the magnetic field by $\Delta\theta \sim 31^{\circ}/p$, where $p$ is the track momentum, measured in $GeV$. Multiple scattering is the limiting factor for the momentum resolution, except at very large momenta, where octant misalignments become important.

[17]All subsequent description of cell geometry refers to the $\theta$ layers.

### 1.9.2 The Forward Muon Drift Cells

Each drift cell has internal dimension in the local $y$ coordinate of 118mm. There are approximately 2mm of dead material between cells. The thickness of the cells in the $z$ coordinate is 19mm. The length in the local $x$ coordinate varies from 40cm for the innermost cells, to 240cm for the outermost. As illustrated in figure 1.11, each cell has a central sense wire, stretched in the local $x$ direction, such that the maximum drift distance is always 59mm. Pairs of adjacent sense wires are linked at one end by a 330$\Omega$ resistor. The other end of the sense wire is read out, via a pre-amplifier, and the cell through which a particle passed is determined by charge division.

The sense wire is held at a higher potential than the outer edges of the cells, and the resulting field is very uniform in the local $y$ coordinate except near to the sense wire, where it increases sharply. A minimally ionising particle passing through a cell causes primary ionisation of a small number of atoms. The liberated electrons drift towards the sense wire at a terminal velocity determined by collision rates with gas particles. In the final few hundred $\mu$m nearest to the sense wire, where the field increases, the electrons gain sufficient energy to cause secondary ionisation, and an avalanche of electrons ultimately develops. Since most of the ionisation takes place very near to the sense wire, a sharply rising pulse develops, which passes in both directions along the wire, to the pre-amplifiers.

Noble gases are generally chosen for drift cells, since they are more easily ionised than polyatomic gases. Small admixtures of polyatomic gases are also included, since their rotational and vibrational degrees of freedom allow absorption of photons from electromagnetic showers, limiting the lateral extent of the avalanche. The detailed choice of gas mixture and drift field is determined by the requirements that the mixture should be non-flammable, and that there should be a uniform drift velocity. If the drift velocity is too large, it limits the resolution, and if it is to small, triggering speed is compromised. A drift field of 450Vcm$^{-1}$, with a gas mixture of 92.5% argon, 5% carbon dioxide and 2.5% methane, provides a drift velocity, $v_{drift} \sim 5\text{cm}\mu\text{s}^{-1}$, which is stable against small variations in the field, or in pressure [35].

### 1.9.3 Reconstruction of Forward Muon Tracks

The pulses that are read out through the pre-amplifiers pass via coaxial cables to FADCs, which are remote from the detector. Here, the signals are digitised in 9.61ns time bins, with a non-linear 8-bit scale, designed to provide the most accurate measurement for small pulses. The FADCs have a 256 time-slice memory, which recirculates until a readout instruction is received from the central trigger. The full contents of the memory are then passed to front end processors, where information on drift times and deposited charge is extracted by the $Q - t$ algorithm.

The $Q - t$ algorithm [36] defines a hit as two successive rising digitisations above a pre-defined threshold. The start time of the pulse, and hence the drift time in the gas is defined as the intercept of the steepest part of the rising edge of the pulse with the pedestal. Knowledge of the drift velocity in the gas enables extraction of the location of the hit in the local $y$ coordinate to $330\mu$m[18]. As the pulses travel along the sense wires, they undergo dispersion in proportion to the total resistance that they encounter. Integrating the charge collected at either end of the sense wire in a fixed number of time bins from the start of the pulse determines which of the two possible cells was struck, and provides a measurement to better than 2% of the wire length of the local $x$ coordinate. There is still ambiguity as to whether a track passed above or below the central sense wire. This is resolved at the pair-finding stage of the reconstruction.

The FMD data is written to tape in its $Q - t$ed format. Off-line, the reconstruction [37] takes place as a three stage process. Pairs of hits within an octant from the two sub-planes of a layer are first combined. Multiple solutions are retained, except where a pair candidate has a separation in the local $y$ coordinate in excess of 3.4cm. Linking between the layers on the same side of the toroid to produce track segments is the next stage. Any segment must contain at least one pair of hits and an unpaired hit from the two distinct $\theta$ layers. All hits must be in the same, or adjacent octants. $\chi^2$ cuts are used to determine which of the possible segments to retain. The final stage is to link segments from before and after the toroid to produce final tracks. Initially, pre- and post-toroid segments are linearly extrapolated to the centre of the toroid, where the combination is rejected if the segments do not pass within 20cm of one another in the radial coordinate, and $30^o$ of one another in azimuth. For candidates that pass this cut, a momentum scan is performed, allowing for the field of the magnet, multiple scattering, and either charge of muon. The minimum $\chi^2$ of the scan with respect to the track momentum defines the final momentum measurement. If the $\chi^2$ is too large, does not contain a minimum, or any of the hits in the track can be used to give a better solution with other points, the track is rejected. The resolution is currently estimated [38] to be $\sigma(1/p)/(1/p) \sim 18\%$ for tracks at 5GeV, rising to 50% at 100GeV.

[18]This figure applies for 1995 conditions.

# Chapter 2

# HERA Physics

This chapter contains background information on the physics of $ep$ scattering, and discusses the main theoretical issues confronted with data from HERA. A brief review of DIS will be given, concentrating on the relevance of HERA data to the understanding of the dynamics of the previously unmeasured low $x$ regime. This is followed by a discussion of the *photoproduction* limit, in which $Q^2 \to 0$. Searches for rare standard model and exotic processes that can be carried out at HERA are reviewed in [39], and will not be covered here. A full discussion of diffractive physics and its relevance to HERA will be given in chapter 3.

## 2.1 Deep-Inelastic Scattering

### 2.1.1 Kinematics of Deep-Inelastic Scattering

The diagram shown in figure 2.1 defines the 4-vectors used in the discussion of the neutral current (NC) DIS process, $ep \to eX$. The description of the process is based on the assumption that the interaction proceeds via the exchange of a single point-like electroweak gauge boson, which couples to a single charged *parton* within the proton. The exchanged boson has 4-vector $q$, such that $q^2 \leq 0$

In electroweak theory, the neutral current can be mediated either by a photon, or by a $Z^0$ boson. Since the propagator term in the amplitude has the form,

$$T \sim \frac{1}{Q^2 + M^2} \tag{2.1}$$

where $M$ is the mass of the intermediate boson, $Z^0$ exchange does not become significant by comparison with photon exchange until $Q^2 \sim M^2_{Z^0} \sim 10^4\text{GeV}^2$. Throughout most of

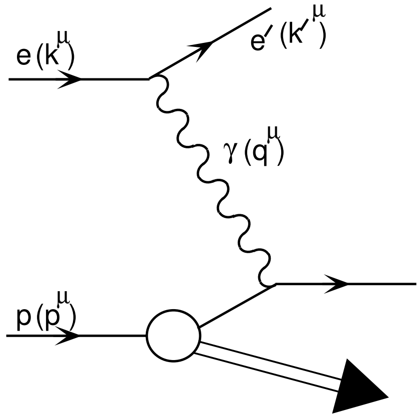


Figure 2.1: *The neutral current Deep-Inelastic Scattering process via photon exchange, in the lowest order of QED. The four-vectors used in the definitions of kinematic variables are shown.*

the accessible kinematic range, $Z^0$ exchange is therefore strongly suppressed, and contributes no more than 5% to the cross-section, even at the highest $Q^2$ points measured at HERA so far.

In the Charged Current (CC) DIS process, $ep \to \nu_e X$, the exchanged boson is a $W^{\pm}$, and the final state electron of figure 2.1 is replaced by a neutrino. Since the $W$ boson is also massive, CC DIS also occurs significantly only at the highest values of $Q^2$. CC events are characterised by a large imbalance in final state transverse momentum, facilitating the isolation of a sample of events with an unobserved final state neutrino, and the measurement of a CC cross-section [40].

The kinematics of the inclusive electromagnetic DIS process are described using combinations of the 4-vectors of figure 2.1 that are Lorentz scalars. The centre of mass energy of the $ep$ system,

$$s = (k + p)^2 \tag{2.2}$$

is $90\,200\mathrm{GeV}^2$ for the HERA beam energies[1]. The square of the 4-momentum transferred,

$$Q^2 = -q^2 = -(k - k')^2 \tag{2.3}$$

defines the virtuality of the exchanged photon, and provides a scale in the interaction. The dimensionless Bjorken scaling variable,

$$x = \frac{Q^2}{2p.q} \tag{2.4}$$

[1]This value applies for the 1994 beam configuration, of electrons at 27.5GeV and protons at 820GeV.

is interpreted as the fraction of the proton's momentum carried by the struck parton, provided that the parton is itself massless, and carries no transverse momentum. The deep inelastic regime may be defined as that region in which both $Q^2$ and $p.q$ are large, such that their ratio, $x$, is well defined. The second Bjorken scaling variable is defined as

$$y = \frac{p.q}{p.k} \tag{2.5}$$

In the target rest frame, $y$ describes the fraction of the electron energy taken by the exchanged boson. In the centre of mass frame of the electron-parton system, it specifies the angle at which the lepton is scattered, according[2] to $y = (1 + \cos\theta^\star)/2$.

The invariant mass of the hadronic final state (i.e. the complete final state excluding the scattered electron) is denoted $W$, so that

$$W^2 = (q + p)^2 \tag{2.6}$$

The quantities defined in equations 2.2 − 2.6 are not mutually independent. Neglecting the azimuthal degree of freedom, the kinematics of the inclusive scattering process at fixed $s$ can be completely described in terms of two independent variables. In the limit where the masses of the incoming particles are small by comparison with the centre of mass energy, the kinematic variables are related by

$$Q^2 = sxy \tag{2.7}$$

$$W^2 = Q^2\left(\frac{1-x}{x}\right) \tag{2.8}$$

### 2.1.2 The Born Cross-Section, and Structure Functions

The most general considerations of invariance under the discreet and continuous transformations of the Poincaré group allow the inclusive differential electromagnetic[3] cross-section $ep \to eX$ to be expressed, in lowest order of QED, in terms of two *Structure Functions*, $F_1(x, Q^2)$ and $F_2(x, Q^2)$, which are dependent upon the spatial distribution of electric charge within the proton[4]. The structure functions are related to the $ep$ cross-section by

$$\frac{d^2\sigma_{ep\to eX}}{dxdQ^2} = \frac{4\pi\alpha_{em}^2}{xQ^4}\left[xy^2F_1(x,Q^2) + (1-y)F_2(x,Q^2)\right] \tag{2.9}$$

From similar symmetry considerations, it can be shown that $F_1$ describes the photo-absorption cross-section for transversely polarised photons, $\sigma_T$, and $F_2$ is related to the

[2]This equality holds with $\theta^\star = 0$ defined by back-scattering of the electron.

[3]To describe the full neutral current, a third structure function, $F_3(x, Q^2)$ is added, which is parity violating, and describes $Z^0$ boson exchange.

[4]For a formal derivation, see for example [41]

sum of longitudinally and transversely polarised photon cross-sections, $\sigma_T + \sigma_L$ [42]. Equation 2.9 can therefore be re-expressed in terms of one structure function and the photo-absorption ratio,

$$R(x, Q^2) = \frac{\sigma_L(x, Q^2)}{\sigma_T(x, Q^2)} \tag{2.10}$$

as

$$\frac{d^2\sigma_{ep\to eX}}{dx dQ^2} = \frac{4\pi\alpha_{em}^2}{xQ^4}\left(1 - y + \frac{y^2}{2\,[\,1 + R(x, Q^2)\,]}\right) F_2(x, Q^2) \tag{2.11}$$

In order to decouple $R(x, Q^2)$ from $F_2(x, Q^2)$ in equation 2.11, it is necessary to measure the differential cross-section at a number of different centre of mass energies of the $ep$ system [43]. At fixed beam energies, this is in principal possible through the study of events with initial state QED radiation [44], though the sensitivity to $R$ is limited by the precision of the measurements. In lower energy experiments, the size of $R$ has been shown to be negligible[5] by comparison with that of $F_2$ except at the highest values of $y$ [45]. The inclusive cross-section can thus be described to good approximation by a single structure function, $F_2(x, Q^2)$. In HERA analyses to date, the value of $R(x, Q^2)$ has been assumed from previous measurement and evolved using QCD [46].

Equation 2.11 gives the *QED Born* cross-section, for the lowest order DIS process in $\alpha_{em}$. After small corrections for initial and final state electromagnetic radiation, this equation is used to extract $F_2(x, Q^2)$ from the experimentally measured differential cross-section. The structure function, $F_2(x, Q^2)$ has now been measured by H1 at 181 points in the $x - Q^2$ kinematic plane [47], in the range $5 \times 10^{-5} < x < 0.32$ and $1.5 < Q^2 < 5000\mathrm{GeV}^2$, some of which are shown in figure 2.2.

### 2.1.3 Scaling and the Quark Parton Model

The experimental observation [4] [48] that at fixed $x$, $F_2(x, Q^2)$ has little, if any dependence on $Q^2$ over a wide kinematic range, is known as *scale invariance* [49]. It can be understood in models, such as the Quark Parton Model (QPM) [50], that consider the proton as having a sub-structure of non-interacting point-like constituents, termed 'partons'. DIS processes are then treated as the incoherent elastic scattering of leptons from charged partons within the proton.

The point-like nature of the interaction in the QPM leaves no scale in the process, and leads automatically to scale invariance. The scaling is expected to hold wherever the

[5] This is an equivalent statement to the Callan Gross relation [45], $F_2 = 2xF_1$, and leads to the conclusion that the charged partons within the proton are spin half objects. The Callan Gross relation is violated to the extent that $R$ is non-zero.

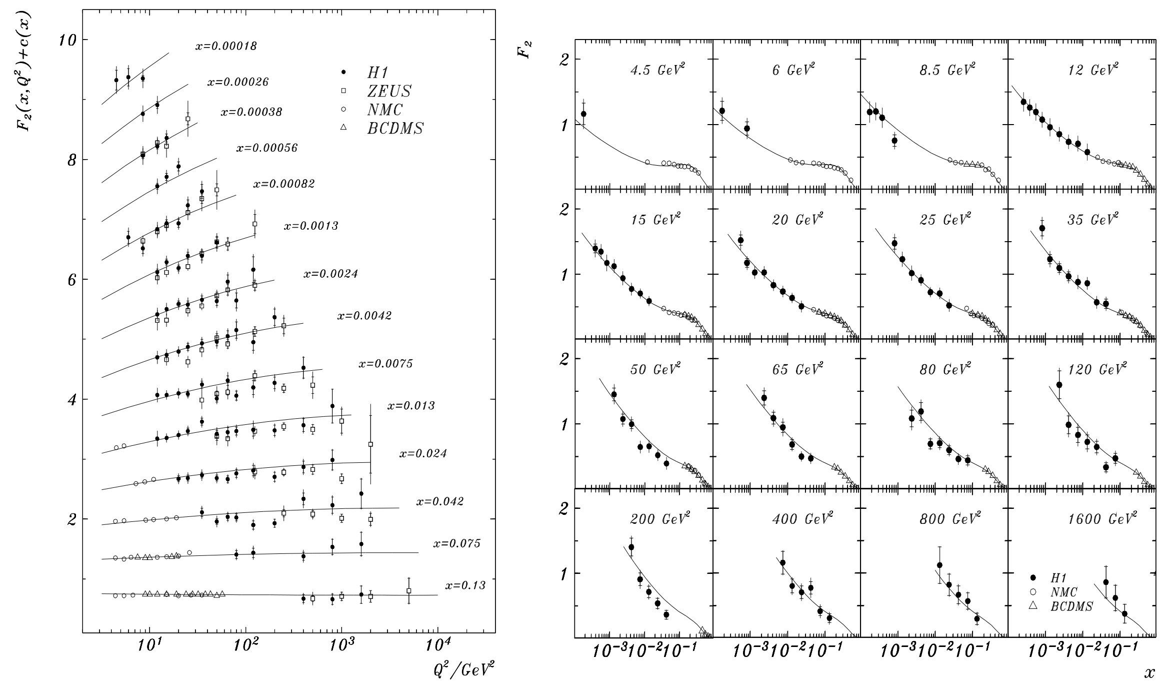


a) b)

Figure 2.2: $F_2(x, Q^2)$ *as measured at HERA, and in fixed target experiments, as a function of (a)* $Q^2$ *and (b)* $x$. *The curves shown represent a phenomenological fit performed by H1 in [47] . For clarity, an arbitrary vertical displacement is added to each point in (a),* $c(x) = 0.6(n - 0.4)$, *where* $n$ *is the* $x$ *bin number such that* $n = 1$ *for* $x = 0.13$.

partons can be considered as *stationary*; i.e. where the motion of the partons as bound constituents is negligible. For this reason, the model is formulated in the infinite momentum frame of the proton. It is, at first sight, surprising that the QPM can provide a good description of data. The partons concerned are never produced as free particles, but are always confined within hadrons, implying that very strong parton-parton interactions must exist. This appears hard to reconcile with the fact that the QPM requires bound quarks to be completely non-interacting. The low energy confinement property and the scale invariance observed in the deep-inelastic regime can be simultaneously understood in terms of the fast *running* of the coupling constant, $\alpha_s$, that is peculiar to the strong interaction. Figure 2.3 shows a measurement of $\alpha_s$ as a function of the main scale in the inclusive DIS process, $Q^2$. At low $Q^2$, the coupling constant becomes very large, and partons are strongly interacting, a property which is known as *infrared slavery.* However, in the high $Q^2$ limit, $\alpha_s(Q^2) \to 0$, and once $Q^2$ has reached moderately large values, the quarks within the proton can be considered to good approximation as being non-interacting. This high $Q^2$ behaviour is known as *asymptotic freedom.*

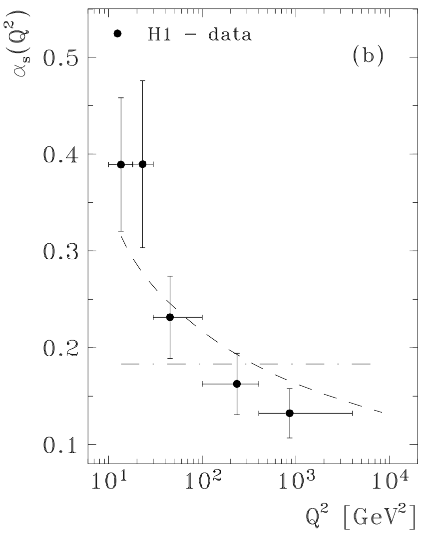


Figure 2.3: *A measurement of $\alpha_s$ as a function of $Q^2$ from an analysis of jet rates in DIS. The falling dashed curve is a prediction based on QCD in next to leading order. Taken from [51] .*

The observed $x$ dependence of the structure function (figure 2.2b) can be consistently described in parton models [52] in which the proton consists of three valence quarks, a sea of quark-antiquark pairs at low $x$, and gluons, responsible for binding the quarks and generating the strong final state interactions that restore the observed colour confinement. Since the photon couples only to charged objects, $F_2$ can be expressed as a sum of charge squared and momentum fraction weighted *Parton Density Functions*, $f_i(x, Q^2)$, for each quark flavour, expressing the probability of finding a quark of type $i$ carrying a fraction, $x$, of the proton's momentum.

$$F_2(x, Q^2) = x \sum_i e_i^2 \; f_i(x, Q^2) \tag{2.12}$$

where the sum is over all active quark flavours. The scaling property of the QPM implies that in the region of asymptotic freedom, the parton densities of equation 2.12 are a function solely of the singlet (valence) and non-singlet (sea) quark distributions in the proton, and are independent of $Q^2$, so that $F_2(x, Q^2) \rightarrow F_2(x)$.

Experimentally, gluons are observed to carry a significant fraction of the proton's momentum. The normalisation of the parton density functions should be given by momentum conservation, through the momentum sum rule,

$$\sum_i \int_0^1 dx\ x\ f_i(x) = 1 \tag{2.13}$$

such that the sum of all parton momenta is equal to the momentum of the proton. However, when only the charged partons that can couple to the photon are considered, around half of the proton momentum is unaccounted for. The remaining momentum must be carried by electrically neutral partons.

### 2.1.4 Scaling Violations

The QPM describes the proton as a distribution of asymptotically non-interacting charged partons, giving rise to scale invariance. Scaling is observed to hold exactly at values of $x \sim 0.1$, but away from this value, detailed measurements have shown that $F_2$ displays a slow evolution with $Q^2$ (see figure 2.2a). This reflects the fact that, even at large $Q^2$, $\alpha_s$ is still finite, and partons should really be regarded as weakly interacting. In order to fully understand violations of scaling in DIS data in general, and HERA data in particular, a theory that describes the interactions between partons is required.

Quantum Chromodynamics (QCD) is the gauge theory of the strong force. The QPM is equivalent to the zeroth order process in QCD, with higher order processes described by a perturbative expansion in orders of $\alpha_s$. Where the coupling constant is small, or equivalently the hard scale in the interaction, $Q^2$, is moderately large, the perturbative expansion is convergent [53], and predictions can be made. The study of $F_2(x, Q^2)$ is then a quantitative testing ground for QCD.

For a given order, $n$, of perturbation theory, a full expansion for $\frac{\partial F_2(x,Q^2)}{\partial \ln Q^2}$ would contain terms of order $\alpha_s^n \ln^m Q^2$ and $\alpha_s^n \ln^m 1/x$, with $m \leq n$. A full QCD expansion is not tractable, but different terms in the expansion dominate in different kinematic regions. Analytic treatments are possible under a number of different approximations, and the dynamics in each case are expressed in terms of evolution equations, relating parton distributions at one point in the kinematic plane to parton distributions at others. HERA data on $F_2(x, Q^2)$ provide an opportunity for detailed tests of the applicability of different evolution schemes over a very wide kinematic range.

## 2.2 Phenomenology in the Low $x$ Regime

The substantial rise in $F_2$ with decreasing $x$ in the newly accessed low $x$ regime (figure 2.2b), becoming more significant with increasing $Q^2$, is the most striking feature of the HERA DIS data. Various schemes for perturbative QCD evolution in which the rise can be explained have been proposed, and will be discussed in this section.

### 2.2.1 The DGLAP Evolution Mechanism

In the comparatively large-$x$ kinematic region accessed by fixed target experiments [54], the evolution equations variously ascribed to Dokshitzer, Gribov, Lipatov, Altarelli and Parisi (DGLAP)[55] describe the observed scaling violations well.

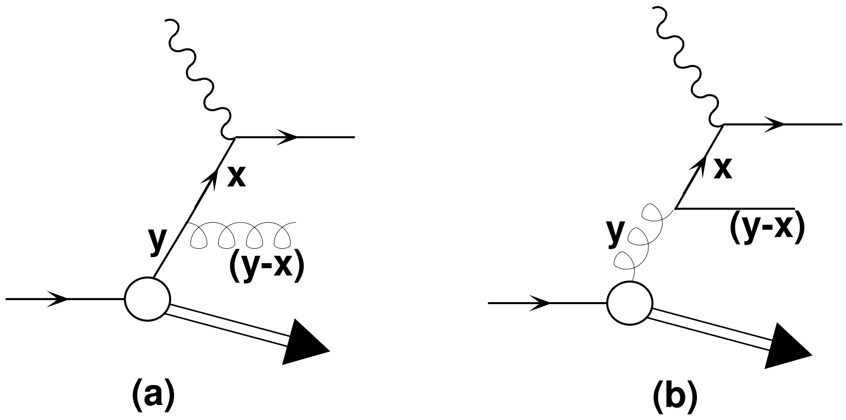


Figure 2.4: *Illustrations of the splitting functions, (a) $P_{qq}(x/y)$ and (b) $P_{qg}(x/y)$ The quark coupling to the photon with momentum fraction, $x$, originates from a parent quark or gluon with momentum fraction, $y$. The splitting functions express the probabilities that the parent parton will undergo each splitting, as a function of the ratio of momentum fractions, $x/y$.*

The quark density functions are split into a flavour non-singlet (valence) distribution and a flavour singlet (sea) distribution. The quark and gluon density functions are fitted or inserted by hand from existing data, at a moderately large starting scale, typically $Q_0^2 \sim 4\text{GeV}^2$, such that perturbation theory is valid. These distributions are then evolved to higher values of $Q^2$ by allowing partons to undergo QCD splitting processes, such as those depicted in figure 2.4. Quarks coupling to the photon from the non-singlet distribution are modified from those at the starting scale by the gluon Bremsstrahlung process $q \to qg$. Those from the singlet distribution are modified by both $q \to qg$ and $g \to \bar{q}q$. The gluon distribution is driven by the processes $q \to qg$ and $g \to gg$. The iteration of splitting processes such as those in figure 2.4 leads to a description of the low $x$ regime in terms of *ladder* diagrams such as that shown in figure 2.5a.

The result is three coupled integro-differential equations for the $Q^2$ dependence of the quark singlet and non-singlet, and gluon density functions, known as the DGLAP equations,

$$\frac{dq^{NS}(x,Q^2)}{d\ln Q^2} = \frac{\alpha_s(Q^2)}{2\pi}\int_x^1 \frac{dy}{y}\left(q^{NS}(y,Q^2)P_{qq}\left[\frac{x}{y}\right]\right) \tag{2.14}$$

$$\frac{dq^{S}(x,Q^2)}{d\ln Q^2} = \frac{\alpha_s(Q^2)}{2\pi}\int_x^1 \frac{dy}{y}\left(q^{S}(y,Q^2)P_{qq}\left[\frac{x}{y}\right] + g(y,Q^2)P_{qg}\left[\frac{x}{y}\right]\right) \tag{2.15}$$

$$\frac{dg(x,Q^2)}{d\ln Q^2} = \frac{\alpha_s(Q^2)}{2\pi}\int_x^1 \frac{dy}{y}\left(q^{S}(y,Q^2)P_{gq}\left[\frac{x}{y}\right] + g(y,Q^2)P_{gg}\left[\frac{x}{y}\right]\right) \tag{2.16}$$

where, for example, $P_{qq}(x/y)$ is a *splitting function*, describing the probability of a struck quark of momentum fraction, $x$, originating via a gluon Bremsstrahlung process, from a starting distribution quark with momentum fraction, $y$. The splitting functions have been calculated in leading order and next to leading order of QCD, and solving the DGLAP equations leads, via equation 2.12, to logarithmic dependences of the structure function on $Q^2$, such that $F_2$ falls with $Q^2$ at high $x$ and rises with $Q^2$ at low $x$. A physical interpretation of the $Q^2$ dependence is that the spatial resolution of the virtual photon increases with $Q^2$, such that more and more partonic structure is revealed. The splitting mechanisms then result in a net migration of partons from high $x$ to low $x$, at high $Q^2$.

The DGLAP evolution equations formally sum terms contributing to $F_2$ with maximum power of $\ln Q^2$, to all orders of perturbation theory. The reduction of the full expansion to sums of the terms in $\alpha_s^n \ln^n(Q^2)$ is known as the leading logarithm approximation (LLA($Q^2$)). The kinematic region of validity of DGLAP evolution is that in which perturbation theory is applicable, and all terms involving powers of $\ln(1/x)$ may safely be neglected;

$$\alpha_s \ll 1 \tag{2.17}$$

$$\ln\frac{1}{x} \ll \ln\frac{Q^2}{Q_0^2} \tag{2.18}$$

DGLAP evolution is thus expected to be valid for large $Q^2$ and intermediate to large $x$. Parameterisations based solely on DGLAP evolution, for example, those of Martin, Roberts and Stirling[56], have been successful in the description of all HERA data to date, provided that parton distributions at the starting scale show a rise with decreasing $x$ in the low $x$ region. An equally successful phenomenological fit to HERA and fixed target data is obtained by Glück, Reya and Vogt (GRV)[57]. A modified approach to DGLAP evolution is taken in an attempt to generate the parton distributions throughout the kinematic plane from a starting point representing the valence structure only, at a very low starting scale of $Q_0^2 = 0.3\text{GeV}^2$. Even at the lowest values of $x$, the GRV parameterisation is able to describe HERA data well, though a small admixture of valence gluons are required and since $\alpha_s$ must be large at the starting scale, the use of the standard perturbative approach of DGLAP evolution is generally considered to be questionable.

In the low $x$ limit, the dynamics of parton distributions are governed principally by the behaviour of the gluon distribution, $g(x, Q^2)$ (see section 2.2.5). The non-singlet quark distribution can safely be neglected, and the singlet quark distribution is driven by the rapidly rising gluon distribution. Under such circumstances, predicting the behaviour of $F_2(x, Q^2)$ reduces to predicting the behaviour of the gluon distribution. Ball and Forte have noted [58] that in the double limit of large $Q^2$ and small $x$, the DGLAP evolution equations can be reduced to a wave-like equation for $xg(x)$, which is analytically soluble, and specifies the behaviour of $F_2$ in the region, depending on the boundary conditions imposed by constraining the gluon distribution at the starting scale. Provided only that the starting gluon distribution is soft (i.e. $g(x, Q_0^2) \sim x^{-1}$ as $x \to 0$), the resulting low $x$ behaviour of the gluon distribution is always similar, and yields a scaling behaviour for $F_2$ in the two variables, $\sigma = \sqrt{\ln \frac{1}{x} \ln^2 Q^2}$ and $\rho = \sqrt{\ln \frac{1}{x} / \ln^2 Q^2}$. In the double asymptotic limit of large $\sigma$ and large $\rho$, $\ln[xg(x)]$ is predicted to be linear in $\sigma$, with a slope that is independent of $\rho$, and flat in $\rho$ at fixed $\sigma$, up to corrections of order $1/\rho$ and $1/\sigma$. In the double limit, the gluon distribution, $xg(x)$, is predicted to grow faster than any power of $\ln 1/x$ but slower than $1/x$. H1 data for $F_2$, rescaled to remove sub-asymptotic contributions, exhibit these scaling properties to within present experimental errors [59]. The BFKL mechanism of section 2.2.2 implies a steeper gluon distribution at the starting scale. Such hard boundary conditions would destroy the double scaling property.

### 2.2.2 The BFKL Evolution Mechanism

Terms in $\alpha_s^n \ln^n(1/x)$ in an expansion for $F_2$, not described by the DGLAP equations, are expected to become relevant to the description of QCD dynamics at sufficiently low $x$, though it is not clear whether the appropriate limit is reached in the HERA regime. In the LLA($1/x$), the leading term in $1/x$ is considered at each order of perturbation theory. Balitski, Fadin, Kuraev and Lipatov (BFKL) assume that the low $x$ region is dominated by the splitting $g \to gg$, such that figure 2.5a is a typical diagram contributing to $F_2$. The (scale dependent) gluon density function, $g(x, Q^2)$, is related to the non-integrated gluon distribution of the proton, $f(x, k^2)$ by

$$xg(x, Q^2) = \int_0^{Q^2} \frac{dk^2}{k^2} f(x, k^2) \tag{2.19}$$

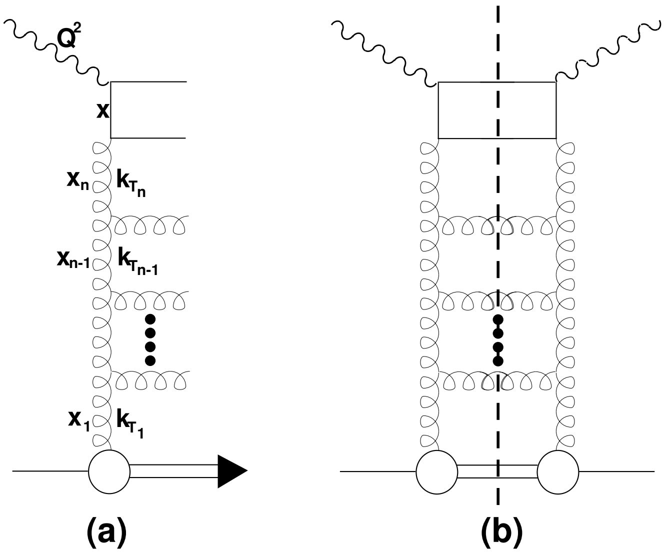


Figure 2.5: *(a) A* ladder *diagram contributing to the structure function, $F_2(x, Q^2)$ at low $x$. In DGLAP evolution, the ladder is, in general, composed of both quarks and gluons, and there is strong ordering in transverse momentum, $k_T$, and weak ordering in longitudinal momentum, $x$, of partons along the ladder. In the BFKL scheme, gluons only contribute. The strong ordering in $k_T$ is replaced by strong ordering in $x$. The Double Leading Logarithm Approximation of section 2.2.3 implies strong ordering in both quantities. The BFKL equation is formed by summing squared amplitudes such as that in (b).* Cutting *along the dotted line reveals the final states of (a).*

where $k$ describes the transverse momenta of gluons along the chain in figure 2.5a. By summing squared amplitudes, such as that in figure 2.5b, for all possible gluon insertions[6], the *BFKL* or *Lipatov* equation[60] is obtained:

$$x\frac{\partial f}{\partial x} \equiv K_L \otimes f \tag{2.20}$$

where the symbol $\otimes$ implies integration over $x$ and $k_T$. $K_L$ is the *Lipatov kernel*, corresponding to a sum over terms of form $\alpha_s^n \ln(1/x)^n$, and hence expressing evolution in $x$. The BFKL equation can be solved analytically at fixed $Q^2$, and leads via equation 2.19 to the prediction that for the gluon dominated low $x$ regime,

$$F_2(x, Q^2) \sim x^{-\lambda} \tag{2.21}$$

where

$$\lambda = \frac{12\alpha_s}{\pi}\ln 2 \tag{2.22}$$

[6]Relating inclusive cross-sections (figure 2.5a) to elastic amplitudes (figure 2.5b) in this way is a widely used technique, the validity of which follows from Unitarity via the Optical Theorem. For $F_2$, the relevant amplitude is that of forward virtual Compton scattering. Such ideas are expanded in section 3.3.1.

giving[7] $\lambda \sim 0.5$. Using the BFKL equation, the structure function at low $x$ is then predicted from the measured structure function at higher $x$ and the same $Q^2$.

The LLA in $1/x$ is valid in the kinematic regime where

$$\alpha_s \ll 1 \tag{2.23}$$

$$\ln \frac{Q^2}{Q_0^2} \ll \ln \frac{1}{x} \tag{2.24}$$

where $Q_0^2$ is a moderate scale $\gtrsim 1\mathrm{GeV}^2$. The BFKL equation is thus applicable to the region of the kinematic plane where both $x$ and $Q^2$ are comparatively small.

### 2.2.3 The Double Leading Logarithm Approximation and the GLR Equation

The observed rise in $F_2$ with decreasing $x$ cannot continue indefinitely, or unitary would ultimately be violated. It is usually assumed that the rising gluon distribution is eventually damped, in the large $Q^2$, very low $x$ limit, by the recombination process, $gg \rightarrow g$. Recombination is expected to become important where parton densities become so high that gluons can no longer be considered to be independent.

For sufficiently large $Q^2$ and small $x$, terms in $\ln(Q^2)$ and $\ln(1/x)$ are both important to the behaviour of $F_2$. An appropriate framework in which to describe this region is offered by the Double Leading Logarithm Approximation (DLLA), which formally sums all terms of the forms $(\alpha_s \ln Q^2)^n$, $(\alpha_s \ln 1/x)^n$ and $(\alpha_s \ln Q^2 \ln 1/x)^n$.

The nature of the ordering in transverse momentum, $k_T$, and longitudinal momentum, $x$, of partons in low $x$ ladder diagrams such as that of figure 2.5a, is dependent upon the evolution scheme used. The LLA($Q^2$) of DGLAP evolution implies strong ordering in parton virtuality, and weak ordering in $x$, such that in figure 2.5a,

$$x \leq x_n \leq x_{n-1} \leq x_1 \tag{2.25}$$

$$Q^2 \gg k_{T_n}^2 \gg k_{T_{n-1}}^2 \gg k_{T_1}^2 \gg Q_0^2 \tag{2.26}$$

The LLA($1/x$) of the BFKL equation relaxes the strong ordering in $k_T$ in favour of ordering in $1/x$ such that

$$x \ll x_n \ll x_{n-1} \ll x_1 \tag{2.27}$$

$$Q^2 \geq k_{T_n}^2 \geq k_{T_{n-1}}^2 \geq k_{T_1}^2 \geq Q_0^2 \tag{2.28}$$

[7]Problems with low $k_T$ cut-offs (validity of perturbation theory) and high $k_T$ cut-offs (Energy - momentum conservation) may modify the effective value of $\lambda$ such that it falls to around 0.3 - 0.4. See for example [61].

The DLLA has strong ordering in both $k_T$ and $1/x$.

The evolution equation of Gribov, Levin and Ryskin (GLR) [62] can describe the necessary saturation of the parton densities within the framework of the DLLA. If $\alpha_s$ is kept fixed, the GLR equation predicts an asymptotic gluon density at low $x$ and large $Q^2$ of the form,

$$xg(x) \sim e^{2\left[\frac{3\alpha_s}{\pi}\ln\left(\frac{1}{x}\right)\ln\left(\frac{Q^2}{Q_0^2}\right)\right]^{\frac{1}{2}}} \tag{2.29}$$

Recombination effects are expected to be small in the kinematic domain of HERA, since gluon densities should not be sufficiently large [63]. However, interest in GLR evolution is sustained by the possibility of the existence of localised regions of high density, or *hotspots* [64].

### 2.2.4 The Hadronic Photon and the Regge Limit

In the limit as $Q^2 \to 0$, no form of perturbative description is valid. $ep$ collisions are therefore generally divided into two distinct classes according to the virtuality of the exchanged photon. The high $Q^2$ DIS regime is traditionally viewed in terms of a point-like virtual photon probing the partonic structure of the proton target. Interactions in the photoproduction regime of vanishing $Q^2$ are well known to resemble hadron-hadron collisions (section 2.3.2). This behaviour is understood in terms of the photon fluctuating to a hadronic state before interacting with the proton (section 2.3.3). The appropriate language with which to discuss photoproduction is then that of soft collisions between a proton and a quasi-real hadronic photon. At sufficiently small momentum transfers, $t$, hadron-hadron cross-sections are best described in the framework of Regge phenomenology (section 3.2). Such an approach is equally applicable to photoproduction interactions, wherever the photon interacts through its hadronic component.

A sharp division between the perturbatively calculable and incalculable is unphysical, and the hadronic interpretation of the photon has been extended to describe low $x$ electroproduction. At low $x$, large longitudinal distances are involved in the interaction[8], and even at large $Q^2$, the photon may dissociate to a hadronic system at distances of $\sim 100$fm in advance of the target in the proton rest frame at HERA [65]. In the Aligned Jet Model [66], the photon splits to a $q\bar{q}$ pair with a probability that is proportional to $1/Q^2$, which are aligned along the $\gamma^\star p$ interaction axis with little relative $p_T$. By the nature of the splitting, one of the quark pair can in general be considered to be 'fast' and

[8] By the uncertainty principle, distance scales follow a $1/x$ behaviour.

undergoes little further evolution, whilst the second 'slow' parton undergoes substantial QCD development before being absorbed on the target.

In the Regge theory based model of Abramowicz, Levin, Levy and Maor (ALLM) [67], $F_2$ is related to the total photoproduction cross-section through [68]

$$\sigma_{\gamma p}^{tot}(W_{\gamma p}) \sim \lim_{Q^2 \to 0} \frac{4\pi^2 \alpha_{em}}{Q^2} F_2(x, Q^2) \tag{2.30}$$

where $W_{\gamma p}$ is the invariant mass of the $\gamma p$ system at the specified values of $x$ and $Q^2$. The divergence at $Q^2 = 0$ is controlled by including an effective propagator mass for the photon, reflecting its finite spatial extent when interacting hadronically. The valence and sea components of the structure function are related to the pomeron ($\alpha_{I\!P}$) and reggeon ($\alpha_{I\!R}$) components of the total $\gamma p$ cross-section (see section 3.3.2), such that

$$\sigma_{\gamma p}^{tot}(W^2) = A_{I\!P} W^{2(\alpha_{I\!P}(0)-1)} + A_{I\!R} W^{2(\alpha_{I\!R}(0)-1)} \tag{2.31}$$

$$F_2(x, Q^2) = A_{sea} x^{1-\alpha_{I\!P}(0)} + A_{val} x^{1-\alpha_{I\!R}(0)} \tag{2.32}$$

The virtual photon at low $x$ has been observed to display similar characteristics [69] [70], to those of the real photon. A direct comparison, using H1 data, between photoproduction processes and DIS at low $x$, in terms of hadronic final state energy flows and rates of diffractive processes is presented in [71]. Even at relatively large values of $Q^2$, the DIS data display similar topologies and proportions of diffractive events to those of the photoproduction sample.

Treatments of DIS in which the hadronic photon picture is used to complement the traditional point-like photon treatment (eg [72]), will be instrumental in understanding the manner in which QCD dynamics approach the non-perturbative limit at low $x$ and low $Q^2$. Regge theory, and its application to $\gamma p$ interactions, will be discussed in detail in chapter 3.

### 2.2.5 The Gluon Density of the Proton at low $x$

The dynamics of the low $x$ region are principally dependent upon the behaviour of the gluon density, $xg(x)$. Although the photon does not couple directly to gluons, various methods have been used to infer the gluon density function from DIS data.

Phenomenological fits to $F_2(x, Q^2)$, based on DGLAP, or mixed DGLAP and BFKL evolution, with assumptions for functional forms of the gluon, and singlet and non singlet

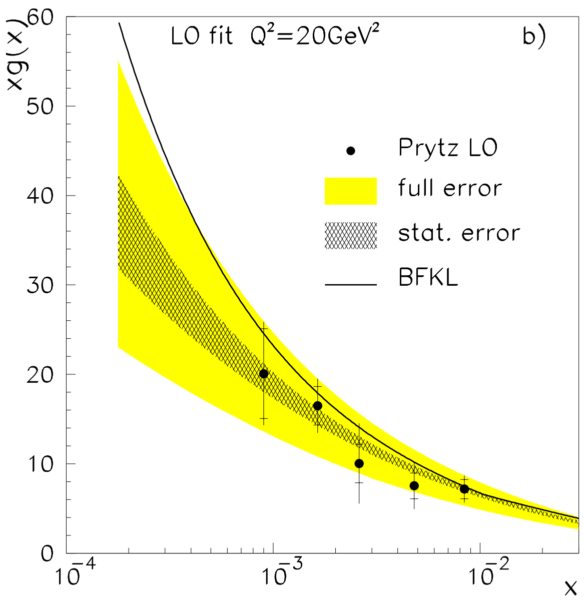


Figure 2.6: *The gluon density, $xg(x)$ of the proton at $Q^2 = 20\mathrm{GeV}^2$, as extracted in [59] in the LLA($Q^2$) approximation. The points are extracted from $F_2$ data, using the Prytz method described in the text. The shaded area shows the results of a QCD fit using DGLAP evolution, and the solid line is the result of a mixed fit, where DGLAP evolution is used for $x > 10^{-2}$ and BFKL evolution is used for $x < 10^{-2}$.*

quark distribution functions at the starting scale, have been used to estimate $xg(x)$ to next to leading order in QCD [59].

Under certain approximations to the evolution equations, the gluon density can be extracted from the measured $F_2(x, Q^2)$, and its derivatives with respect to $x$ and $Q^2$. For example, the method due to Prytz [73], achieves this in the DGLAP framework, by assuming that the low $x$ quark distribution coupling to photons is dominated by the splitting, $g \to \bar{q}q$. By Taylor expanding the splitting function, $P_{qg}(x/y)$ about $x/y = 1/2$, a prediction for the gluon distribution is obtained.

$$\frac{\partial F_2(\frac{x}{2}, Q^2)}{\partial \log Q^2} \simeq \frac{10}{27} \frac{\alpha_s(Q^2)}{\pi} xg(x) \tag{2.33}$$

which gives an approximation that is good to $\sim 20\%$, with the principal source of error being the neglect of separate evolution of the singlet quark distribution. A measurement of $xg(x)$, extracted by this method is shown in figure 2.6. Fuller details, along with other methods of extracting gluon densities based on derivatives of $F_2$, can be found in [59].

The gluon density can also be measured from studies of photon-gluon fusion events, where the hard sub-process is $\gamma^\star g \to q\bar{q}$ (see section 6.4.2). In leading order of QCD, such processes give rise to a two-jet final state configuration. The gluon density in leading order can be unfolded from the observed rate of such events, after statistical subtraction of background from the QCD Compton process, $\gamma^* q \rightarrow gq$, which also yields a two jet final state. A measurement of $xg(x)$ based on photon-gluon fusion rates is presented in [74].

All of the methods of measuring the gluon density described above give consistent results for HERA data to within errors, and a strong rise with decreasing $x$ is common to all measurements. It can be seen from figure 2.6 that the gluon density rises by a factor $\sim 3$ between $x = 10^{-2}$ and $x = 10^{-3}$.

Whilst the data are not yet sufficiently accurate to discriminate between evolution schemes, the form of the gluon distribution is consistent with the BFKL prediction of equation 2.21, with a weak constraint on the hardness of the $x$ dependence, $0.2 \lesssim \lambda \lesssim 0.5$. Since the DGLAP equations evolve the structure function in $Q^2$ only, they do not directly predict $x$ dependencies, and the gluon density at low $x$ depends upon that assumed at the starting scale. As discussed in section 2.2.1, a number of parameterisations based solely on DGLAP evolution provide a good description of DIS data.

### 2.2.6 Concluding Remarks

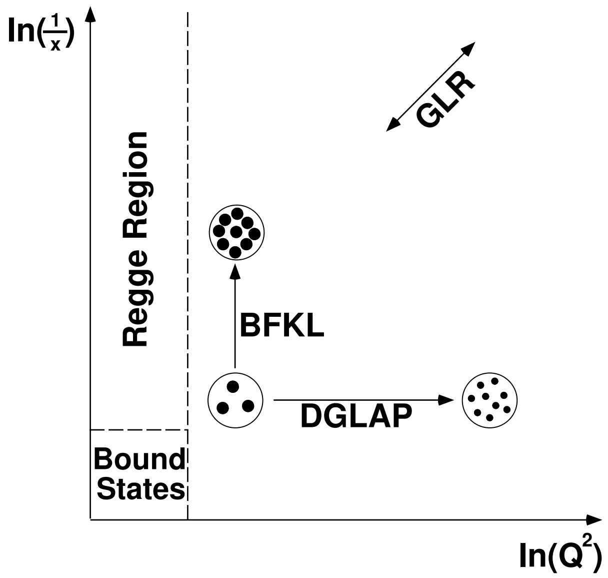


Figure 2.7: *A schematic illustration of the $x - Q^2$ kinematic plane, and the various evolution schemes that may describe the dominant dynamics in different regions.*

A brief review has been given of the phenomenology of the HERA low $x$ regime, and of the different possible approximations to a full perturbative QCD expansion that may apply in different regions of $x - Q^2$ space. The kinematic limits of applicability for each scheme are not well defined, though figure 2.7 gives a qualitative picture of how the approximations fit together.

At present, HERA data is equally well described by the DGLAP mechanism, or by a mixture of BFKL and DGLAP evolution [59]. Future measurements of $F_2(x, Q^2)$ may enable more exacting tests, and determine whether BFKL dynamics are visible at the values of $x$ reached at HERA. The final states produced in DIS are also sensitive to the dominant dynamics at low $x$ [75], but they will not be discussed here.

## 2.3 Photon Physics

*"...fifty years of conscious brooding have brought me no closer to the answer to the question, 'What are light quanta?' Of course, today, every rascal thinks he knows the answer, but he is deluding himself!"* A.Einstein, 1951

### 2.3.1 Introduction

Since the differential $ep$ cross-section contains a propagator term of the form $1/Q^4$, HERA physics is dominated by very low $Q^2$ electroproduction, usually termed *photoproduction*. By factoring out the photon flux using the Weizsäcker-Williams approximation (see section 5.2.1), cross-sections for the scattering of real photons from the proton can be extracted from those measured in $ep$ interactions at vanishing $Q^2$. HERA thus offers an excellent arena for the study of the photon at high energy[9].

The understanding of photons, as the interacting quanta of the electromagnetic force, dates back to the earliest years of Quantum Mechanics. Quantum Electrodynamics (QED) is the modern theory of photons and their interactions with matter. The essential ingredient of QED is that photon couplings must be modified by corrections in a power series in $\alpha_{em}$, to account for interactions of the photon with the electromagnetic field of the vacuum. QED is the most successful theory that we have, having been tested with extreme precision in a variety of different experiments over a very wide range of energy. For

[9] A typical real photon originating from the electron beam at HERA has a laboratory energy of around 15GeV, giving a $\gamma p$ centre of mass energy ($W_{\gamma p}$) of around 200GeV. In terms of hadron-hadron collisions, only data for $pp$ and $\bar{p}p$ collisions exist at such energies.

example, QED predicts that the Landé $g$-factor of leptons, identically 2 in Dirac theory, is subject to small corrections due to vacuum interactions. $g$-factors can be obtained experimentally by measurement of spin precession frequencies when a particle is subjected to a uniform external magnetic field. The $g$ factor for the electron has been measured to a precision of one part in $10^{11}$ using a low temperature trapping device [76], whilst that of the muon has been extracted to one part in $10^8$ in a muon storage ring at CERN [77]. In both cases, the measured value is correctly predicted by QED. Indeed there is no experimental evidence for any departure from QED predictions for photon interactions, based solely on the electrical and magnetic properties of interacting particles, and of the vacuum.

### 2.3.2 The Hadronic Behaviour of Photons

At sufficiently high photon energies ($> 2m_e$), the $e^+e^-$ pairs generated in QED photon splittings may materialise as real particles. This is the most trivial example of the photon interacting in a *resolved* way, rather than through its bare state. As experiments reached GeV scales, photons were still generally treated as point-like quanta, with all physical detail revealed being assumed to be associated with the target. However, it increasingly became apparent [78] that photon-hadron interactions showed broadly similar characteristics to hadron-hadron collisions, but with cross-sections reduced by a factor $\sim \alpha_{em}$. Soft collisions, typical of peripheral strong interactions, yielding entirely hadronic final states of low $p_T$ were observed to dominate. At high energies, the total cross-section for photon interactions with nuclei, $\gamma A \to X$, where $A$ denotes the atomic number of the target nucleus, ceases to scale linearly with $A$, as would be expected for a point-like electromagnetically interacting photon. Instead, it follows a lesser power of $A$ [79], indicating that processes in which the photon interacts strongly, near to the surface of the nucleus are dominant. This phenomenon is known as nuclear shadowing. The exclusive yield of final state hadrons with identical quantum numbers to the photon (i.e. vector mesons) was also significantly larger than would be expected for a bare photon.

### 2.3.3 The Vector Dominance Model

The observation that the photon may behave in a similar way to hadrons led to the idea of a two component state vector:

$$|\gamma\rangle = \sqrt{Z_3}\,|\gamma_B\rangle + \sqrt{\alpha_{em}}\,|h\rangle \tag{2.34}$$

where $|\gamma_B\rangle$ is the bare photon, interacting only electromagnetically, $|h\rangle$ undergoes conventional strong interactions, and $(1-Z_3)$ expresses the probability that the photon behaves hadronically. At HERA energies, interactions between real photons and hadronic matter are expected to be heavily dominated by the hadronic component.

Any hadronic manifestation of the photon must have the same quantum numbers as the bare state, $J^{PC} = 1^{--}$, and zero charge, strangeness and baryon number. This has been confirmed experimentally in the study of quasi-elastic photon interactions [80]. The Vector Dominance Model (VDM), first formulated by Sakurai [81], provides a description of the hadronic component of the photon. The state, $|h\rangle$, is treated as a superposition of the three vector mesons known at the time, $\rho(770)$, $\omega(783)$, and $\phi(1020)$, roughly[10] in the ratio 9:1:2. The model is built from three principles:

- When interacting, $|h\rangle$ is a superposition of vector mesons, with relative contributions proportional to $g/m_v$, where $g$ is the coupling of the vector meson to the photon, and $m_v$ is the mass of the vector meson.
- Any photon surviving an interaction as a hadron remains a superposition of vector mesons.
- As predicted by unitarity, the optical theorem (see section 3.3.1) relates the forward elastic (diffractive) cross-section to the total (absorptive) cross-section.

The VDM has been *generalised* [83] to include other vector mesons ($\rho'(1450)$, $J/\psi(3097)$, $\Upsilon(9460)$ ...), and further *extended* [84] to a continuum of unbound states with appropriate quantum numbers ($\pi^+\pi^-$, $\pi^+\pi^-\pi^0$, $\bar{K}K$, $\bar{N}N$ etc.). It has proved successful in giving at least a phenomenological description of high energy processes involving photons. For example, the VDM predicts for the total $\gamma p$ cross-section [85]

$$\sigma_{tot}^{\gamma p} \simeq \frac{\pi\alpha_{em}}{\gamma^2}\sigma_{tot}^{\rho p} \simeq \frac{1}{206}\sigma_{tot}^{\rho p} \simeq \frac{1}{206}\sigma_{tot}^{\pi p} \tag{2.35}$$

where $\gamma$ is an effective coupling of the photon to the $\rho$ meson, with a correction for $\omega$ and $\phi$ contributions. The final equality follows from use of the additive quark model [86], in which coupling strengths are determined by numbers of valence quarks. This relation between the total $\gamma p$ and $\pi p$ cross-sections is demonstrated to hold approximately in section 3.3.1.

[10]These ratios are asymptotic predictions based on the SU(3) flavour wave-functions of the vector meson states. There are strong corrections in the photoproduction regime, mainly due to interference between the $\omega$ and $\phi$ states [82].

### 2.3.4 The Structure of the Photon

The partonic structure of the photon has been measured [87] in $e^+e^-$ colliders, by studying interactions in which a virtual photon associated with one of the beams probes a real photon radiated from the other. A structure function, $F_2^\gamma(x_\gamma, Q^2)$, analogous to that of the proton can be defined. The photon's structure function is observed to differ from those of conventional hadrons, in that it does not fall rapidly with increasing $x$, but is relatively flat for most values of $x_\gamma$. This can be qualitatively understood in terms of the evolution processes that take place during the fluctuation of the photon to a hadronic object. Any resolved manifestation of the photon must originate from the point-like QED process, $\gamma \to q\bar{q}$, whilst any subsequent development of the $q\bar{q}$ pair is a consequence of QCD. The relative transverse momentum squared, $p_T^2$ of the $q\bar{q}$ pair provides a scale for QCD processes, which defines the coupling strength in the same way that $Q^2$ did in figure 2.3. Where $p_T$ is small, the coupling strength is large, the $q\bar{q}$ pair interact strongly with one another, and the resonant $1^{--}$ states of the VDM are ultimately built, in a perturbatively incalculable way. However, the process $\gamma \to q\bar{q}$ gives rise to a wide spectrum in relative $p_T$, reaching into the regime where the coupling strength becomes small and the $q\bar{q}$ pair are asymptotically free. At high $p_T$, the resolved photon no longer behaves in the way predicted by the VDM. Instead, the perturbative scale ensures little QCD development, and a significant fraction of photon interactions take place at large values of $x_\gamma$. The result is a harder overall structure function than is the case for conventional mesons.

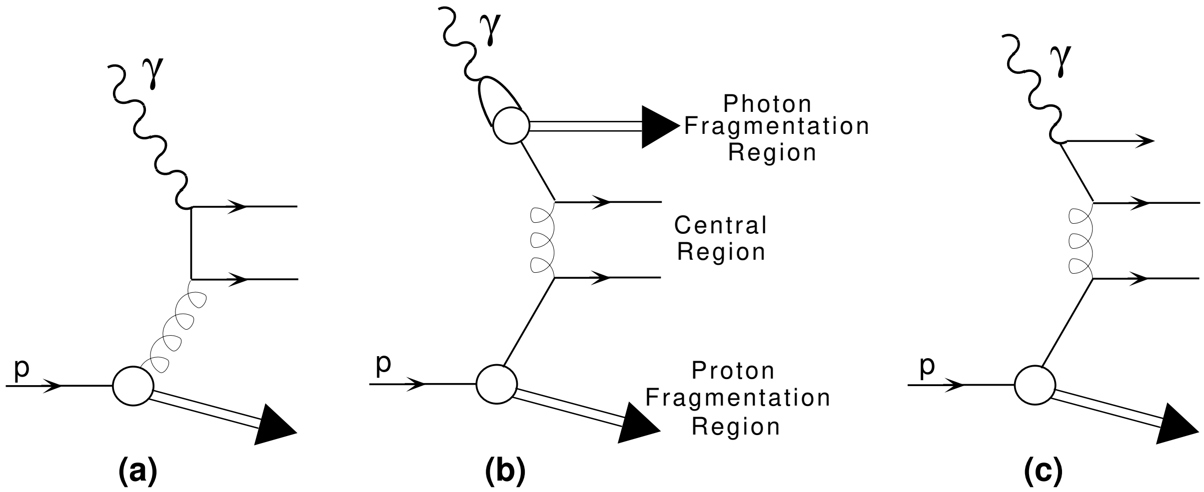


Figure 2.8: *Examples of (a) Direct, (b) VDM Resolved and (c) Anomalous resolved photon couplings in hard photoproduction processes at HERA. Resolved couplings are characterised by the presence of a photon remnant.*

The resolved structure of the photon is often divided into two components, such that equation 2.34 is extended to

$$|\gamma\rangle = \sqrt{Z_3}\,|\gamma_B\rangle + \sqrt{\alpha_{em}}\,|h\rangle + \sqrt{\alpha_{em}}\,|h_{anom}\rangle \tag{2.36}$$

where $|h\rangle$ describes a structure typical of bound-state mesons, as expected in the VDM, and the additional term, $|h_{anom}\rangle$ denotes the *anomalous*, perturbative part of the photon structure. The definition of the boundary in $p_T$ between the VDM and anomalous components is somewhat arbitrary. Examples of direct, resolved and anomalous photon couplings at HERA are shown in figure 2.8.

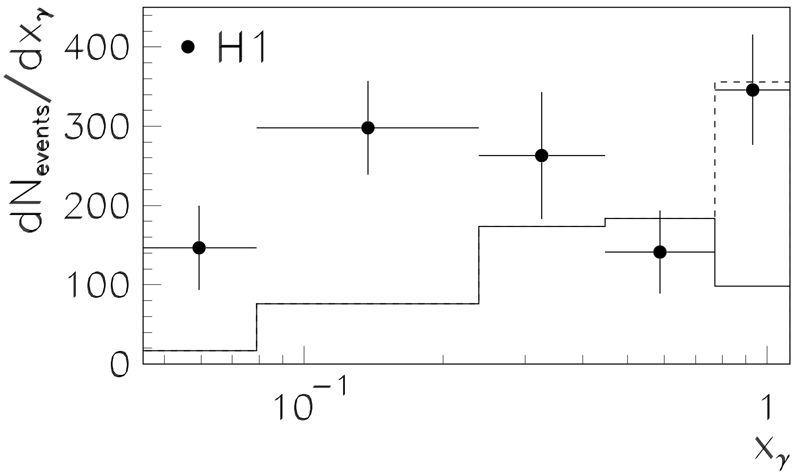


Figure 2.9: *The distribution in $x_\gamma$ of a sample of two jet photoproduction events, taken from [88] . The dashed line shows a Monte Carlo prediction for the direct photon contribution. The full line is a prediction for quark induced resolved processes, based on measurements in two-photon experiments, and corresponding to the sum of the VDM resolved, and anomalous resolved contributions. The gluon distribution of the photon is inferred from the difference between the points and the sum of the two quark-based Monte Carlo predictions.*

The partonic structure of the photon can be investigated at HERA through the study of the photoproduction of high $p_T$ jets. The jets are interpreted as originating from hard scattering processes between a single parton from the proton and a single parton from the photon. Jet cross-sections are then sensitive to the parton distributions of the photon, via unfolding methods in which parton-parton cross-sections, calculated in QCD, are convoluted with the measured parton distributions of the proton. In contrast to photon-photon scattering experiments, hard photoproduction events can be induced by gluons as well as quarks. By comparing parton densities measured in photon-photon experiments with jet-jet cross-sections in photoproduction, measurements of the gluon density of the photon have been made at HERA[88]. The distribution of the fractional momentum, $x_\gamma$, carried by the parton from the photon entering the hard scattering in events with two centrally produced jets is shown in figure 2.9. Contributions from direct, resolved quark and resolved gluon induced interactions are clearly observed.

## 2.4 Summary

Both through cross-section measurements, and analyses of final states, data from HERA provide the most detailed testing ground, in the widest kinematic range yet, for the understanding of QCD. Detailed measurements of the partonic structures of the proton and photon have already been made. The structure function, $F_2(x, Q^2)$, has been observed to display a sharp rise in the newly accessed low Bjorken-$x$ regime, which has been shown to be principally generated by an equally sharp rise in the gluon density function. Both fixed target, and HERA data for $F_2$ can be well fitted, using parameterisations based on evolution in $Q^2$ or mixed evolution in $Q^2$ and $1/x$. No evidence has yet been found for saturation of the gluon distribution.

Future measurements at H1 and ZEUS will extend the kinematic range of measurement of $F_2$ to lower values of $Q^2$ at fixed $x$[11], and with increased statistics, to values of $Q^2$ close to the kinematic limit[12] of $s \sim 10^5\mathrm{GeV}^2$. $\alpha_s(Q^2)$ decreases by at least a factor of two in the accessible kinematic regime, and at the highest $Q^2$, non-perturbative effects are truly negligible. The possibility of running the accelerator at different beam energies may allow measurements of the longitudinal structure function of the proton, $F_L(x, Q^2) = \frac{R(x,Q^2)}{1+R(x,Q^2)} F_2(x, Q^2)$, and the HERMES experiment will obtain information on the spin structure of the nucleon.

The study of interactions of the hadronic photon with protons has been possible using the $Q^2 \to 0$ limit of $ep$ collisions. Measurements have been made that allow, for the first time, an extraction of gluon densities for the photon. These too will be improved by the collection of larger luminosity samples, and better understanding of systematic errors.

This chapter has given a broad overview of the main aspects of proton and photon physics that are accessible at HERA. In the following chapter, a more detailed discussion of the third major area of interest in HERA physics, that of the structure of the pomeron, is presented.

[11]The SPACAL extends the H1 upper limit in $\theta$ of acceptance for the scattered electron from $\sim 173^\circ$ to $\sim 176^\circ$.

[12]At this value of $Q^2$, the spatial resolution is $\sim 10^{-18}$m.

# Chapter 3

# Diffraction

## 3.1 Introduction

The study of hadron-hadron interactions at low momentum transfers has been one of the central themes in the development of particle physics. In the absence of any hard scale, perturbative QCD is not applicable, and the phenomenological models that have been instrumental in the development of the field very often still give the best descriptions available. A consistent description of peripheral strong interactions is offered by Regge theory, in which scattering processes are described in terms of the exchange of virtual mesons. The interpretation in the framework of Regge theory of elastic scattering at high energies has long been problematic, in that none of the known mesons can be used to describe observed cross-sections. The introduction of a vacuum or *diffractive* exchange, known as the pomeron, to describe total, elastic, and low mass inelastic cross-sections has proved highly successful[89], though the nature of the object exchanged is not determined. The observation of high $p_T$ diffractive jet production [90][91] supports a partonic interpretation, though the parton distributions are not well constrained.

Interactions consistent with a diffractive interpretation have been observed throughout the $Q^2$ range at HERA, and the hermetic coverage offered by the detectors has allowed the final states produced to be fully contained. Diffractive photoproduction is relevant to the understanding of the high energy hadronic nature of the photon in the VDM. In diffractive DIS, the hard scale provided by the virtuality of the photon probe facilitates a study of the deep-inelastic structure of the exchange.

In this chapter, the ideas that lie behind Regge theory are surveyed[1]. The application

[1]Regge theory is the theory of the complex angular momentum plane. No attempt at a detailed description of its formalism is offered here, though it can be found, for example, in [92].

to the cases of elastic, total, and diffractive dissociation cross-sections is then discussed, concentrating on the specific case of the $\gamma p$ system. Finally, recent measurements of the diffractive contribution to the proton structure function, and of the partonic structure of the pomeron are briefly reviewed. The additional constraints on the nature of the diffractive exchange that can be obtained in the study of jet production and final state energy flows will not be considered here.

## 3.2 Hadron-Hadron Interactions

### 3.2.1 Soft Strong Interactions

Figure 2.3 showed the dependence of the strong coupling constant, $\alpha_s$, on the main DIS scale, $Q^2$. In hadron-hadron interactions, the appropriate scale for QCD is also set by the momentum transferred. At large momentum transfer, corresponding to hard interactions, the coupling constant is small, making perturbative QCD in low order applicable for calculations. At low momentum transfer, the coupling constant becomes large, such that a perturbative expansion is no longer appropriate. In this non-perturbative regime, the phenomenological approach of Regge theory [93] gives the best description of hadronic cross-sections that we have.

It is the size of $\alpha_s$ in long range interactions that gives rise to the confinement of strongly interacting particles inside hadrons. At low momentum transfers, the sub-structure of hadrons is not resolved, and the residual strong interaction takes place between composite hadrons, rather than between the quarks and gluons that compose them. The confinement aspects of QCD can be incorporated in a picture in which the peripheral strong interactions that take place between composite hadrons are not viewed in terms of single gauge boson exchange, but as being due to the exchange of groups of coloured partons, comprising virtual hadrons that are net colour singlets.

### 3.2.2 $s$ and $t$ Channel Processes

The general two-body scattering process, $AB \rightarrow CD$ can be discussed in terms of two independent invariants. It is convenient to work in terms of the Mandelstam $s$ and $t$ variables, defined by

$$s = (A + B)^2 = (C + D)^2 \tag{3.1}$$

$$t = (A - C)^2 = (B - D)^2 \tag{3.2}$$

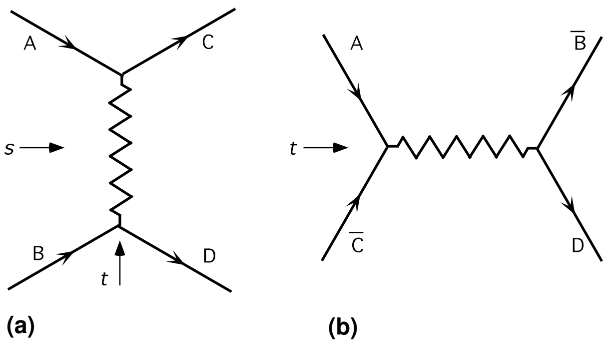


Figure 3.1: *Diagrammatic representation of a) a generalised $s$ channel process, and b) the equivalent $t$ channel crossed process.*

where $A, B, C$, and $D$ denote the 4-vectors of the initial and final state hadrons. The variable, $s$, is the square of the centre of mass energy of the interaction, and $t$, which is negative, gives the square of the 4-momentum transferred between the interacting particles, $A$ and $B$.

In field theories, interactions are described in terms of intermediate states, occurring either as exchanges or as resonances. For the purposes of this discussion, the generalised $s$ *channel* process, $AB \rightarrow CD$, will be defined as the exchange case, shown in figure 3.1a. Using crossing symmetry, the related $t$ *channel* process, $A\bar{C} \rightarrow \bar{B}D$ of figure 3.1b, can be described with the same amplitude, though the two processes take place in physically disconnected regions of $s$ and $t$ space. The amplitudes for the two processes are identical, provided that $s$ of figure 3.1a is replaced by $t$ for figure 3.1b, and vice versa. i.e.

$$T_{AB\rightarrow CD}(s,t) = T_{A\bar{C}\rightarrow \bar{B}D}(t,s) \tag{3.3}$$

The existence, and approximate mass of the $\pi$ meson was anticipated by Yukawa [94] in an attempt to understand the limited range of the nuclear force in terms of the exchange of massive particles. Since the uncertainty principle relates the range, $r$, and mass, $m$, of the exchanged particle, according to $r \sim 1/m$, a model in which only the lightest mesons are considered is able to describe only the long-range, highly peripheral components of an interaction.

In field theoretic formulations of exchange ideas, for example, the One Particle Exchange model [95], where single $\pi$ exchange is treated in a similar way to photon exchange in QED, the amplitude for an exchange must contain a propagator term, of the form

$$T(s,t) \sim \frac{g^2}{m_\pi^2 - t} \tag{3.4}$$

where $g$ is the magnitude of the coupling of the propagator to the external particles, and there is a singularity, or *pole* in the unphysical, $t > 0$, region of the $s$ channel diagram where $t = m_\pi^2$. The amplitudes for peripheral $s$ channel processes, where $\pi$ exchange is dominant, are well described, via equation 3.3, in terms of a continuation of the amplitude for the resonance production of $\pi$ mesons in the crossed $t$ channel process.

### 3.2.3 Regge Trajectories and $s$-Channel Amplitudes

The modern generalisation of Yukawa type models is Regge Theory. A complete description of the short, as well as long range parts of an amplitude should sum contributions from all possible exchange particles with appropriate quantum numbers. Such particles may be viewed as angular momentum excitations of the lowest lying state, such that the angular momentum and mass-squared of contributing exchange particles are simply related by a *Regge trajectory.* In the original Regge theory of non-relativistic potential scattering [93], and its generalisation to relativistic particle physics [96] [92], angular momentum is treated as a continuous complex variable, $\alpha(t)$, with physically observable $t$ channel resonances occurring only at physical values of spin, such that $\mathcal{R}e[\alpha(t)]$ is an integer or half integer. Stable hadrons have pure real values of $\alpha(t)$, whilst unstable hadrons have an imaginary component that is related to their decay width. Bound states therefore lie near to the real axis of $\alpha(t)$. In general, the locus of a trajectory is found to be a linear path in spin$-$mass squared space[2], such that the trajectory in the $t$ channel, or at small $|t|$ in the $s$ channel can be written

$$\alpha(t) = \alpha(0) + \alpha' t \tag{3.5}$$

As an example, the trajectory for which the $\rho$ meson is the lowest lying state is shown in figure 3.2.

$t$-channel amplitudes may be computed by decomposition into partial waves of different angular momentum

$$T(s,t) \simeq \sum_{l=0}^{\infty} (2l+1)\ T_l(t)\ P_l(\cos\theta) \tag{3.6}$$

where $T_l(t)$ is the amplitude for the $l$th partial wave, and $P_l(\cos\theta)$ is the Legendre polynomial for angular momentum, $l$. In continuing the amplitude to describe the $s$-channel, where $\cos\theta > 1$, equation 3.6 may be re-expressed as a sum over poles of the form of equation 3.4 for each partial wave. When expressed in terms of contributing Regge

[2]The linearity of trajectories can be qualitatively understood in terms of QCD, if mesons are modelled as a simple pair of massless quarks connected by a rotating string. See for example [97].

trajectories, the pole in the $l$th partial wave may be written

$$T_l(t) \simeq \frac{\beta(t)}{l - \alpha(t)} \tag{3.7}$$

where $\alpha(t)$ denotes the trajectory exchanged, and the residue function, $\beta(t)$ describes the coupling of the pole to the external particles. In the asymptotic limit where $s \to \infty$ and $t/s \to 0$, the leading dependence on $s$ of the contribution to the amplitude of a trajectory, $\alpha(t)$, is given by[3]

$$T(s,t) \sim \beta(t) \left(\frac{s}{s_0}\right)^{\alpha(t)} \tag{3.8}$$

where $s_0$ defines the energy scale on which $s$ must be large, typically taken to be $\sim 1\mathrm{GeV}^2$. For a process that is dominated by the exchange of a single trajectory, the differential cross-section can then be expressed as

$$\frac{d\sigma}{dt} \sim \frac{1}{s^2} |T(s,t)|^2 \tag{3.9}$$

$$\sim f(t) \left(\frac{s}{s_0}\right)^{2\alpha(t)-2} \tag{3.10}$$

Despite being essentially a phenomenological model, with no real basis in QCD, Regge theory is able to provide accurate predictions for the $s$ and $t$ dependencies of a wide range of hadronic interactions at low momentum transfer, over many orders of magnitude in $s$ [100]. Consider, for example, the charge-exchange reaction, $\pi^- p \to \pi^0 n$, and its $t$ channel crossed equivalent, $\pi^- \pi^0 \to \bar{p} n$. The leading trajectory appropriate to these amplitudes is that of the $\rho$ meson, which is shown in the *Chew-Frautschi* [96] plot of figure 3.2. The linear trajectory constructed through the $t$ channel resonances extrapolates well through the $t < 0$ exchange points at low $|t|$, measured directly in the s channel process. The cross-section for $\pi^- p \to \pi^0 n$ is well described by the form, 3.10, with $\alpha(t) = \alpha_\rho(t)$

### 3.2.4 $t$ Dependences and Shrinkage

Using the low $|t|$ parameterisation of equation 3.5, the $s$ channel cross-section of equation 3.10 may be expressed as

$$\frac{d\sigma}{dt} \sim f'(t) \left(\frac{s}{s_0}\right)^{2\alpha(0)-2} \left(\frac{s}{s_0}\right)^{2\alpha' t} \tag{3.11}$$

If the dependence of the propagator couplings on $t$ is small, then at large $s$, the $t$ dependence must be dominated by the final term of equation 3.11. Since $t$ is negative, and

[3]There are many reasons, independently of Regge theory, to expect the scattering amplitude to have the leading behaviour of equation 3.8. See, for example [98].

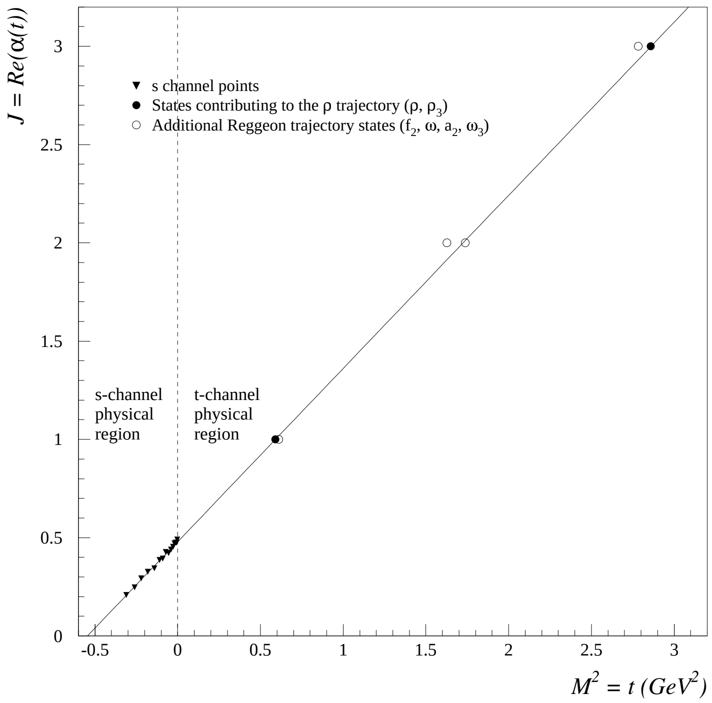


Figure 3.2: *Chew-Frautschi plot of the $\rho$ trajectory, $\alpha_\rho(t)$. The data shown with triangles at negative $t$ are measured in the charge exchange reaction, $\pi^- p \rightarrow \pi^0 n$, and are taken from [99] . The line drawn is $\alpha(t) = 0.480 + 0.881t$, fitting through the natural G-parity,* $\mathrm{J^{PC}} = 1^{--}$ *states, $\rho$ and $\rho_3$ (closed points). An extrapolation of the trajectory at positive $t$ fits well through the points at negative $t$. Related states with positive parity or negative G-parity, that are added to the $\rho$ trajectory to form the more general exchange-degenerate leading meson trajectory, the* Reggeon, *$\alpha_{I\!R}(t)$, are shown as open points.*

$\alpha'$ must be positive, $d\sigma/dt$ falls sharply at large $s$, from a maximum at $t = 0$. Regge theory thus predicts that as the centre of mass energy increases, the forward ($t \rightarrow 0$) peak becomes sharper, or *shrinks*. A physical interpretation of this fact is that as $s$ increases, more and more partial waves of higher and higher angular momentum contribute to the scattering process. The Legendre polynomials that describe each partial wave have faster variations with $\cos\theta$ as the angular momentum increases, and hence, stronger dependences on $t$. The forward peak, which is the only place where all partial waves add more or less coherently, must therefore become more pronounced as the centre of mass energy increases.

Shrinkage of hadron-hadron cross-sections is an experimentally well observed phenomenon [100]. The fast variation of cross-sections with $t$ at fixed $s$ is found to be well described at low $|t|$ by an exponential parameterisation. Equation 3.11 may be re-expressed as

$$\frac{d\sigma}{dt} \sim f'(t)\left(\frac{s}{s_0}\right)^{2\alpha(0)-2} e^{2\alpha'\ln\left(\frac{s}{s_0}\right)t} \tag{3.12}$$

$$\sim \left(\frac{d\sigma}{dt}\right)_{t=0} e^{bt} \tag{3.13}$$

where $b$ ($\sim 5-10$) is known as the *slope parameter*,

$$b \sim b_0 + 2\alpha' \ln\left(\frac{s}{s_0}\right) \tag{3.14}$$

and describes a logarithmic shrinkage of the forward peak for a process with centre of mass energy.

## 3.3 Diffractive Scattering

### 3.3.1 The Pomerančuk Trajectory

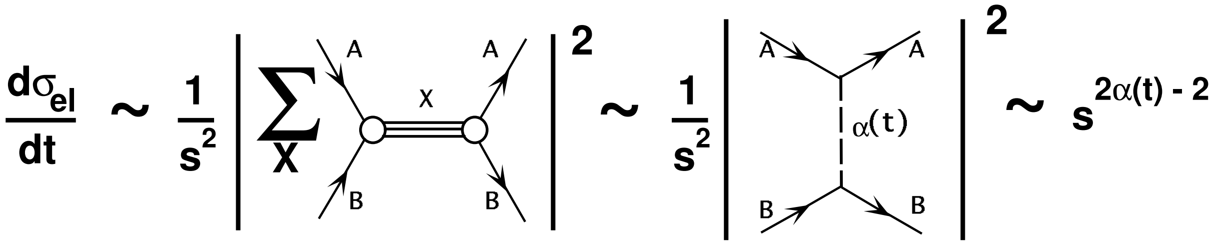


Figure 3.3: *A diagrammatic representation of a general elastic cross-section in terms of a leading Regge trajectory, $\alpha(t)$, and its physical interpretation as a sum over $t$ channel intermediate states, $X$.*

Equation 3.10 gives the Regge prediction for the $s$ and $t$ dependences of a general hadronic cross-section, in terms of the leading trajectory that contributes to the exchange. An application of this is to the case of the elastic cross-section, $AB \to AB$. Figure 3.3 shows a diagrammatic representation of the required leading trajectory for the elastic process, in terms of a coherent sum over possible intermediate states, $X$.

Elastic and total cross-sections are closely related by the *Optical Theorem*:

$$\sigma_{tot}^{AB} \sim \frac{1}{s}\mathcal{I}m(T_{el}^{AB})_{t=0} \tag{3.15}$$

$$\sim s^{\alpha(0)-1} \tag{3.16}$$

where the second equality follows from 3.8, and from the fact that the elastic amplitude is almost pure imaginary. A diagrammatic demonstration of the optical theorem can be found in figure 3.4. The total cross-section may be represented as a squared incoherent sum over a complete set of final states, which in turn is related, via the closure of the set, to an elastic amplitude. The dashed line in the diagram following the second equality of figure 3.4 illustrates where an elastic amplitude, proceeding through a given intermediate state, $X$, must be cut, in order to obtain the original amplitude of the first diagram. The final equality follows by the same definition of the trajectory as that used in figure 3.3.

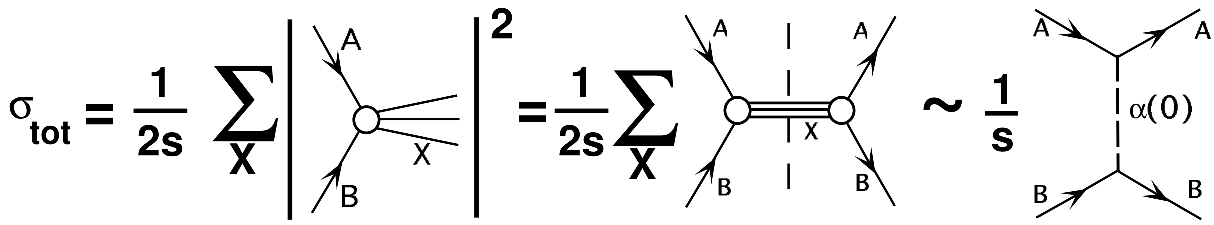


Figure 3.4: *A diagrammatic representation of the Optical Theorem. The $s$ dependence of a total cross-section is related to the elastic amplitude at $t = 0$.*

Experimentally, a clear picture has emerged [89], in which total and elastic cross-sections for hadron–hadron collisions display a slow rise with $\sqrt{s}$ at high centre of mass energy. In the Regge picture, from equations 3.10 and 3.16, this would require that the leading trajectory mediating high energy elastic scattering has an intercept,

$$\alpha(0) \sim 1 + \epsilon \tag{3.17}$$

with $\epsilon$ small and positive. However, all meson trajectories have $\alpha(0) \lesssim 0.5$. This apparent contradiction is resolved by the introduction of a *vacuum* or *Pomeron* trajectory, $\alpha_{I\!P}(t)$, to describe total and elastic cross-sections at high energies. Such a trajectory must carry the quantum numbers of the vacuum if it is to mediate elastic scattering, and must couple equally to particles and anti-particles, if the Pomerančuk theorem [101],

$$\sigma(AB) \underset{s\to\infty}{\longrightarrow} \sigma(\bar{A}B) \tag{3.18}$$

for all hadrons, $A$ and $B$, is to be satisfied.

The $t < 0$ part of the pomeron trajectory is well measured in $pp$ and $p\bar{p}$ interactions, and is generally taken to have a linear[4] form [102], similar to

$$\alpha_{I\!P}(t) = 1.085 + 0.25t \tag{3.19}$$

[4]At high $|t|$, in the exchange process, the trajectory ceases to be linear, and a quadratic term is often added. This behaviour can be understood in terms of interference between the leading trajectory exchange and multiple pomeron exchanges [92]. In fact, the raw $t$ dependence of an elastic process at fixed $s$ looks like a classical diffraction pattern, with the position of the first minimum giving information on the spatial extent of the target hadron.

This differs from all meson trajectories, not only in that its intercept is greater than unity, but also in that meson trajectories universally have slopes, $\alpha' \sim 1$. Interactions described by the exchange of the pomeron trajectory are termed diffractive.

If elastic cross-sections are described by the exchange of the pomeron trajectory, then the cross-section for the process, $AB \to AB$, may be written (from 3.10, and corresponding to the final diagram of figure 3.3) as

$$\frac{d\sigma_{el}^{AB}}{dt} = \frac{\beta_{A\mathbb{P}}^2(t)\beta_{B\mathbb{P}}^2(t)}{16\pi}\ s^{2\alpha_{\mathbb{P}}(t)-2} \tag{3.20}$$

where $\beta_{i\mathbb{P}}(t)$ is the coupling strength of the pomeron to the external particle, $i$. Equation 3.20 is valid in the Regge limit, where $s \to \infty$ and $t/s \to 0$.

Where the centre of mass energy is large, the diffractive exchange dominates both elastic and total cross-sections. The total cross-section of equation 3.16 is given, as in the final diagram of figure 3.4, by

$$\sigma_{tot}^{AB} = \beta_{A\mathbb{P}}(0)\beta_{B\mathbb{P}}(0)\ s^{\alpha_{\mathbb{P}}(0)-1} \tag{3.21}$$

Though the introduction of the pomeron trajectory is an effective tool in the phenomenological description of total and elastic cross-sections at large centre of mass energies, there are no established poles corresponding to resonance production of pomeron states in the $t$ channel. By extrapolation of the measured $s$ channel trajectory, 3.19, one might expect to find a pole in the form of a $\mathrm{J}^{\mathrm{PC}} = 2^{++}$ state at a mass of around 1900MeV. It is often assumed that the pomeron trajectory is associated with multiple gluon exchange, and if this is the case, then the pole might be expected to have a valence gluon structure. A recent candidate for such a state is presented in [103].

### 3.3.2 Phenomenology of Total Cross Sections

The interpretation of diffractive scattering as being due to the exchange of $t$ channel physical states implies that the pomeron can be considered as a distinct entity, or quasi-hadron, the properties of which are portable between the collisions of different types of hadron. The part of the amplitude expressing the propagator should then factorise, and the pomeron should be considered as a universal object to all forms of hadron scattering. The ideas of universality and factorisation will be discussed further in section 3.6.

In [105], Donnachie and Landshoff fit the centre of mass energy dependence of the total cross-section for $pp$ and $\bar{p}p$ scattering from $\sqrt{s} \sim$ 5GeV to $\sqrt{s} \sim$ 2000GeV, using a

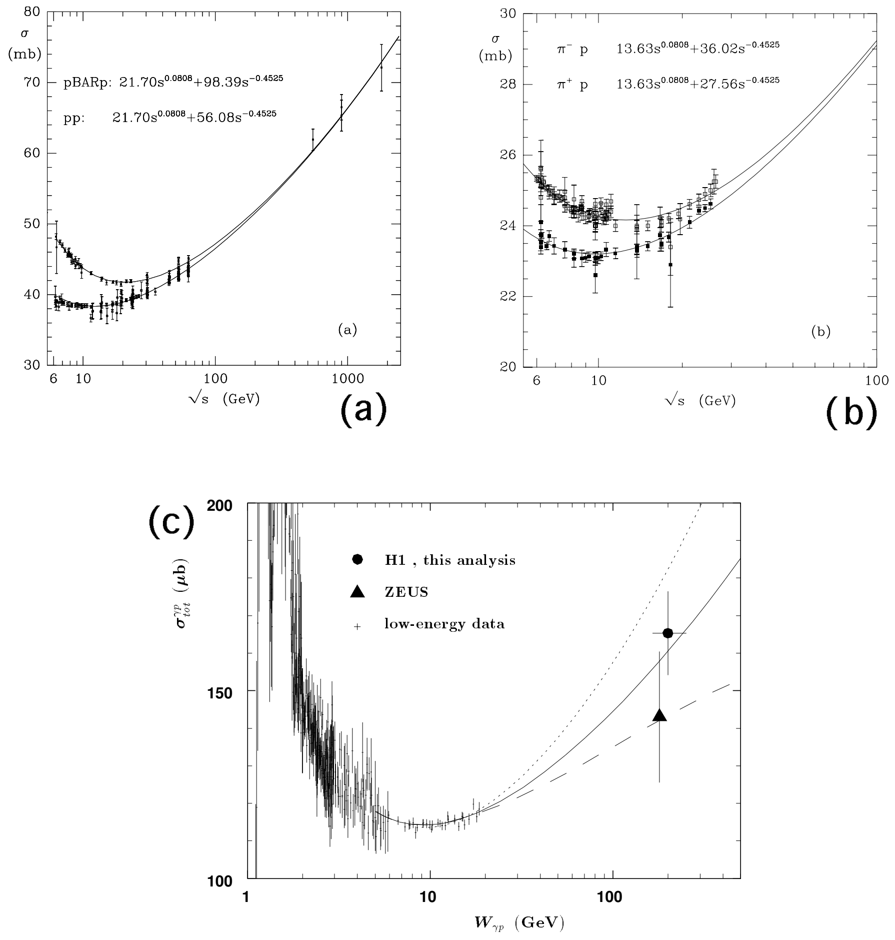


Figure 3.5: *Donnachie Landshoff fits to the centre of mass energy dependence of the total cross section for a) $pp$ and $\bar{p}p$ scattering [104] , b) $\pi^- p$ and $\pi^+ p$ scattering [104] , and c) $\gamma p$ scattering [25] . The high $s$ points in the $\bar{p}p$ case are from the Tevatron. Those in the $\gamma p$ case are from HERA. In c) the solid line is the Donnachie Landshoff fit, whilst the broad dashed curve represents the ALLM parameterisation of section 2.2.4.*

simple sum of two Regge amplitudes; the pomeron, and the exchange degenerate *reggeon*, introduced in figure 3.2. The fit used is (see equation 3.16)

$$\sigma_{tot}(s) = A_{I\!P} s^{\alpha_{I\!P}(0)-1} + A_{I\!R} s^{\alpha_{I\!R}(0)-1} \tag{3.22}$$

with the normalisations, $A_{I\!P}$, $A_{I\!R}$, and trajectory intercepts, $\alpha_{I\!P}$ and $\alpha_{I\!R}$ as free parameters. The Pomerančuk theorem is satisfied by keeping $A_{I\!P}$ fixed in the $pp$ and $\bar{p}p$ cases. The result of the fit is shown in figure 3.5a, with the trajectory intercepts found to be[5]

$$\alpha_{I\!P}(0) = 1.08 \tag{3.23}$$

$$\alpha_{I\!R}(0) = 0.55 \tag{3.24}$$

Constraining these values for the intercepts, the fit is performed to $\pi^- p$, and $\pi^+ p$ data (figure 3.5b), and $\gamma p$ data (figure 3.5c), with only the normalisations for the pomeron and reggeon terms as free parameters. From the results for the amplitudes and intercepts of the fits, the following conclusions may be drawn:

- All hadronic cross-sections can be described via the optical theorem, over a large range of energy, with a universal pomeron / reggeon model. The reggeon has the larger coupling to hadrons, and consequently dominates at low centre of mass energies. However, the reggeon contribution falls approximately as $s^{-1/2}$, such that at large centre of mass energies, the pomeron term ($\sim s^{0.08}$) dominates, and the cross-section starts to rise slowly with $s$.
- In accordance with the Pomerančuk theorem, at large centre of mass energies, the couplings to charge conjugates are equal, such that $\sigma(pp) \underset{s\to\infty}{\longrightarrow} \sigma(\bar{p}p)$ and $\sigma(\pi^+ p) \underset{s\to\infty}{\longrightarrow} \sigma(\pi^- p)$
- The ratio of the strengths of pomeron exchange for $\pi p$ to $pp$ is approximately 2:3, which is an example of the *additive quark rule*, and indicates that the pomeron coupling strength to hadrons is in proportion to the number of valence quarks[6].
- The total $\gamma p$ cross-section is $\sim \frac{1}{200}$ times that for $\pi p$, as predicted by vector dominance in equation 2.35

In light of the total photoproduction cross-section data from H1 and ZEUS (figure 3.5c), Regge inspired models, such as those of Donnachie and Landshoff, and of ALLM, are generally found to be successful for the description of $\gamma p$ collisions [25].

[5]The rise of the total cross-section where the leading pomeron trajectory dominates goes approximately as $s^{0.08}$. Asymptotically, unitarity, in the form of the Froissart bound [106] dictates that total cross-sections can rise no faster than $\ln^2 s$, though the problem is not relevant at HERA energies. It is generally assumed that the effective intercept, $\alpha_{I\!P}(0)$ falls very slowly with energy because of multiple pomeron exchange (cuts), such that the Froissart bound is ultimately satisfied.

[6]Further evidence for the fact that the pomeron coupling strength depends on numbers of valence quarks has been found in the analysis of exclusive diffractively produced final states in $pp$ collisions at the ISR [107].

### 3.3.3 Diffractive Processes in $\gamma p$ interactions

The truly elastic reaction, $\gamma p \rightarrow \gamma p$ is an $\mathcal{O}(\alpha_{em}^2)$ process, and has a very low cross-section. However, the reaction $\gamma p \rightarrow Vp$, where $V$ is any vector meson, occurs at around 10% of the total photoproduction cross-section [25]. This is an $\mathcal{O}(\alpha_{em})$ process, and within the framework of the VDM of section 2.3.3, may be considered to be elastic. In Regge theory, the VDM elastic process is expected to have the same $s$ and $t$ dependences as conventional hadron-hadron elastic scattering. A diagram of such a quasi-elastic $\gamma p$ reaction is shown in figure 3.6a.

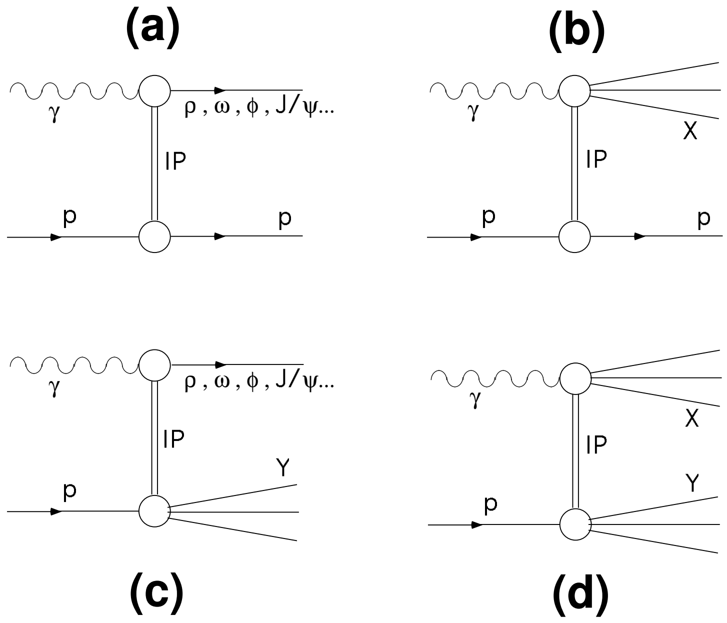


Figure 3.6: *Diffractive interactions proceeding by single pomeron exchange, occurring in $\gamma p$ collisions. a) The quasi-elastic reaction $\gamma p \rightarrow Vp$. b) Single photon dissociation $\gamma p \rightarrow X(1^{--})p$. c) Single proton dissociation $\gamma p \rightarrow VY(\frac{1}{2}^+)$. d) Double dissociation $\gamma p \rightarrow X(1^{--})Y(\frac{1}{2}^+)$. In each case, the symbol, $I\!P$ is used to denote the exchange of the leading pomeron trajectory.*

So far, diffraction, or pomeron exchange, has been discussed in terms of its relevance to elastic scattering, and through the optical theorem, to total cross-sections. In fact, diffraction also exists as an inelastic process, in which one or both of the interacting hadrons *dissociates* to an unbound state in a high mass continuum, which must still have identical quantum numbers to the incident particle. Figures 3.6b-d show the three distinct classes of dissociative diffraction that can occur with single pomeron exchange in $\gamma p$ collisions. In all cases, no colour is exchanged.

In [25], a measurement is presented of the relative contributions of each of these processes to the total $\gamma p$ cross-section at HERA energies. All four processes contribute significantly, and around 45% of the total cross-section is found to be diffractive in the form of one of these diagrams. The principal concern of this thesis is the measurement of cross-sections for the reactions of figures, 3.6a and 3.6b. A restricted evaluation of cross-sections for the reactions of figures 3.6c and 3.6d is also performed.

## 3.4 Diffractive Dissociation

### 3.4.1 Triple Regge Dynamics

Regge theory offers predictions, in terms of trajectories, for the dynamics of dissociative diffraction, and of inclusive processes in general. Feynman[108] predicted that high energy inclusive reactions of the form $AB \to CX$ should scale in an analogous way to Bjorken scaling in DIS, such that cross-sections should be functions of the transverse and longitudinal momenta of the particle, $C$, but not of the centre of mass energy. A version of the optical theorem for such inclusive processes was proposed[109], formalising this statement by relating the inclusive reaction $AB \to CX$ to the theoretically much simpler three-body elastic scattering process, $AB\bar{C} \to AB\bar{C}$.

Provided that the amplitude, $T_{AB\to CX}$ retains its analytic form on exchanging the outgoing particle, $C$, for an incoming $\bar{C}$ with reversed 4-momentum, the physical region of $AB \to CX$ can be described in terms of the unphysical region of the hypothetical three-body cross-section, $AB\bar{C} \to X$.

$$T_{AB\to CX}(p_C, X) = T_{AB\bar{C}\to X}(-p_C, X) \tag{3.25}$$

Mueller's version of the optical theorem then relates the cross-section for $AB\bar{C} \to X$ to the three-body forward elastic amplitude in a similar way to equation 3.15

$$\sigma_{tot}(AB\bar{C} \to X) \sim \frac{1}{s}\mathcal{I}m\left(T_{AB\bar{C}\xrightarrow{X}AB\bar{C}}\right)_{t=0} \tag{3.26}$$

or formally,

$$\frac{d^2\sigma_{AB\to CX}}{dM^2dt} \simeq \frac{\pi}{s^2}Disc_{M^2}\left(T_{AB\bar{C}\to AB\bar{C}}\right) \tag{3.27}$$

where $M$ is the mass of the inclusive final state, $X$.

$$M^2 = (A + B + \bar{C})^2 \tag{3.28}$$

The term, $Disc_{M^2}$ is the discontinuity across the $M^2$ cut only of the elastic amplitude, constraining the intermediate state through which the elastic reaction proceeds to have mass, $M$. The Mueller optical theorem is illustrated in figure 3.7.

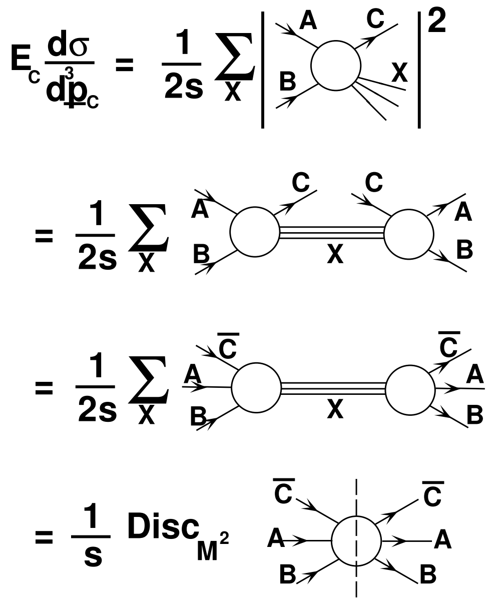


Figure 3.7: *A representation of the idea behind the Mueller Optical Theorem, relating the inclusive cross-section for $AB \rightarrow CX$ to the three-body elastic amplitude, $AB\bar{C} \rightarrow AB\bar{C}$, passing through an intermediate state of mass, $M$.*

Regge expansions are possible for equation 3.27 in various different regions of phase space. Where the particle, $C$, lies in the fragmentation region of $A$ or $B$ (i.e. it can be regarded as a fragment of one of the incident particles), the three-body forward scattering amplitude is dominated by Regge exchanges between the $A\bar{C}$ system and $B$. In the special case where $C$ is isolated in rapidity to the extent that it alone defines the fragmentation region, the process can be pictured in an analogous way to DIS, but with a Regge exchange rather than a photon, as in the first diagram of figure 3.8.

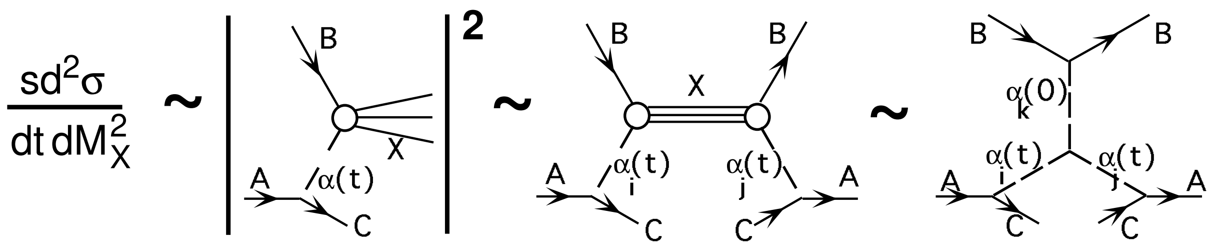


Figure 3.8: *Diagrammatic representation of the triple Regge amplitude, which is that shown in the final diagram, and can be used to calculate the inclusive cross-section, $AB \rightarrow CX$, shown in the first diagram.*

The region of phase space where $s \gg M^2 \gg t$ is known as the triple Regge region. In this limit, the inclusive cross-section is given in Regge theory by [110]

$$\frac{d^2\sigma_{AB\to CX}}{dM^2dt} \simeq \frac{1}{4}\sum_{i,j}\beta^i_{AC}(t)\beta^j_{AC}(t)\left(\frac{1}{M^2}\right)^2\left(\frac{s}{M^2}\right)^{\alpha_i(t)+\alpha_j(t)-2}\sigma^{tot}_{iB\to jB}(M^2,t) \tag{3.29}$$

where the labels refer to those in figure 3.8, and the sum is over all contributing trajectories. $\beta^i_{AC}$ are the Reggeon couplings as in equation 3.20. $\sigma^{tot}_{iB\to jB}(M^2,t)$ is the cross-section for the Reggeon hadron interaction, $iB \to X$, with the mass of the state, $X$, constrained to be $M$. This cross-section is related, by the Mueller optical theorem, to the amplitude for the forward scattering $iB \to jB$, via an intermediate state of mass, $M$, as shown in the second diagram of figure 3.8. The Reggeon-hadron scattering itself contains a large centre of mass energy ($M^2$), so it too can be treated with a Regge expansion,

$$\sigma^{tot}_{iB\to jB}(M^2,t) = 8\pi\sum_k g_{ijk}(t)\beta^k_{BB}(0)\left(\frac{M^2}{s_0}\right)^{\alpha_k(0)-1} \tag{3.30}$$

where $g_{ijk}$ is the triple Reggeon coupling at the centre of the last diagram of figure 3.8. The overall differential cross-section in the triple Regge region is then given, from equations 3.29 and 3.30, by

$$\frac{d^2\sigma}{dM^2dt} \simeq \frac{2\pi}{s^2}\sum_{i,j,k}\beta^i_{AC}(t)\beta^j_{AC}(t)\beta^k_{BB}(0)g_{ijk}(t)\ \ s^{\alpha_i(t)+\alpha_j(t)}\ \ (M^2)^{\alpha_k(0)-\alpha_i(t)-\alpha_j(t)} \tag{3.31}$$

Equation 3.31 extends the applicability of Regge descriptions of processes, from the exclusive two body case, to the general inclusive process, $AB \to CX$, where $C$ takes up the full fragmentation region of $A$.

### 3.4.2 The Triple Pomeron Amplitude and Feynman Scaling

It has been demonstrated that in the triple Regge limit, the Reggeon that couples to the particle, $B$, in the last diagram of figure 3.8, is dominantly the pomeron, and in the specific case of diffractive dissociation, $AB \to AX$, the two Reggeons coupling to the particle $A$ must also be pomerons. The cross-section, 3.31 then reduces to the triple pomeron amplitude, given differentially in $M_X^2$ and $t$ by

$$\frac{d^2\sigma}{dM_X^2dt} \simeq \frac{\beta^2_{A\mathbb{P}}(t)\beta_{B\mathbb{P}}(0)g_{\mathbb{P}\mathbb{P}\mathbb{P}}(t)}{16\pi s^2}\left(\frac{s}{M_X^2}\right)^{2\alpha_{\mathbb{P}}(t)}(M_X^2)^{\alpha_{\mathbb{P}}(0)} \tag{3.32}$$

Writing, as discussed in section 3.3.1

$$\alpha_{\mathbb{P}}(t) = 1 + \epsilon + \alpha'_{\mathbb{P}}t \tag{3.33}$$

one obtains

$$\frac{d^2\sigma}{dM_X^2\,dt} \simeq \kappa(t)s^{2\epsilon+2\alpha' t}\left(\frac{1}{M_X^2}\right)^{1+\epsilon+2\alpha' t} \tag{3.34}$$

where $\kappa$ contains all the couplings of equation 3.32.

With $\epsilon$ small and a peripheral $t$ distribution, diffractive dissociation cross-sections are expected to show approximate Feynman scaling in $s$, as discussed in section 3.4.1, and are predicted to display an approximate $1/M_X^2$ dependence. These properties have been demonstrated experimentally for $pp$ and $\bar{p}p$ interactions (eg [111]) and once in a photoproduction experiment [112]. All available experimental data support the hypothesis that both elastic and dissociative diffractive processes are dominated by the exchange of a single pomeron trajectory, defined in equation 3.19. Figure 3.9 shows a measurement of the differential cross-section $d^2\sigma/dtdM_X^2$ for diffractive $pp$ collisions at the CERN ISR. In the triple Regge region defined by the large dissociation masses beyond the resonance region, the $1/M^2$ dependence is clearly observed. Such dissociative cross-sections also display very little dependence on centre of mass energy.

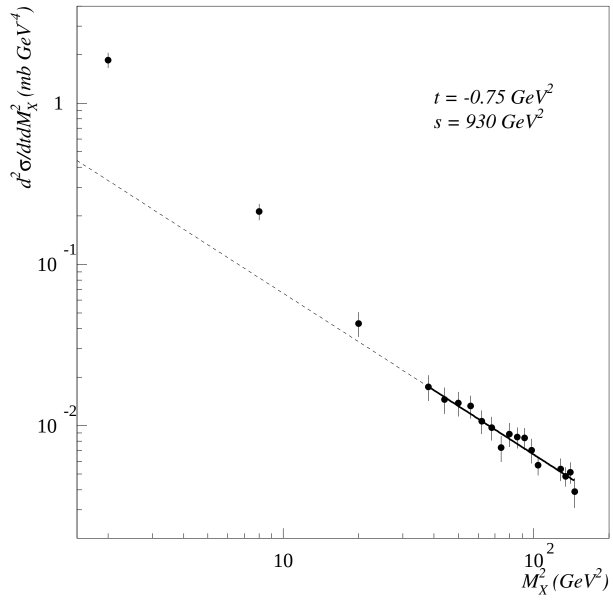


Figure 3.9: *A measurement of the invariant mass spectrum from the reaction $pp \to pX$ at $s = 930\mathrm{GeV}^2$ and $t = 0.75\mathrm{GeV}^2$. The spectrum shows a strong elastic and resonant peak at low masses, and a high mass continuum. The line drawn is $A/M^2$, which fits the data well in the triple Regge region. The dashed line is the continuation of the triple Regge region fit, which falls well short of the data at low masses. The data are taken from [113]*

.

Experimentally, diffractive dissociation has been shown to display a strong forward peak, with a fast exponential fall off with $t$, as was the case for elastic scattering (equation 3.13). In the small $t$ limit, equation 3.34 may be expressed in terms of a slope parameter, such that

$$s\frac{d^2\sigma}{dtdM_X^2} \sim \left(\frac{s}{M_X^2}\right)^{\alpha_{I\!P}(0)} e^{bt} \tag{3.35}$$

with

$$b \sim b_0 + 2\alpha' \ln\left(\frac{s}{M_X^2}\right) \tag{3.36}$$

giving a logarithmic shrinkage in $s/M_X^2$. The low $t$ exponential dependence has been extensively tested in $pp$, $\bar{p}p$, $\pi p$, and $Kp$ interactions[114]. It is found that at fixed $s$, the slope parameter falls to roughly half of its elastic value by the triple Regge region, and has very limited dependence on $M_X^2$ thereafter. Shrinkage in diffractive dissociation has been demonstrated in comparisons of $\bar{p}p$ data from the ISR and the SPS[115].

### 3.4.3 Further Scaling Properties of Diffraction

In the ansatz of factorisation of the diffractive vertex, there are further relationships between elastic, total and dissociative cross-sections. From equations 3.20, 3.21 and 3.32, and ignoring any $t$ dependence of couplings, the reactions, $AB \to AB$, $AB \to X$ and $AB \to AX$ are related by

$$\begin{aligned} M_X^2 \frac{\frac{d^2\sigma}{dtdM_X^2}}{\sigma_{tot}} &= \frac{\beta_{AI\!P}\, g_{I\!PI\!PI\!P}}{16\pi}\left(\frac{s}{M_X^2}\right)^{\epsilon+2\alpha' t} \\ &\simeq constant \end{aligned} \tag{3.37}$$

$$\begin{aligned} M_X^2 \frac{\frac{d^2\sigma}{dtdM_X^2}}{\frac{d\sigma_{el}}{dt}} &= \frac{g_{I\!PI\!PI\!P}}{\beta_{BI\!P}}\left(\frac{1}{M_X^2}\right)^{\epsilon+2\alpha' t} \\ &\simeq constant \end{aligned} \tag{3.38}$$

Equation 3.37 states that, neglecting the finite sizes of $\epsilon$ and $\alpha'$, diffractive dissociation cross-sections scale to total cross-section. Furthermore, the constant formed by the ratio of the two has no dependence on the dissociating particle, but only on the target. Equation 3.38 expresses a similar scaling behaviour of the dissociative to the elastic cross-section. In this case, the ratio is independent of the nature of the target hadron. These scaling properties have been tested for a number of different hadrons [114], and for photons[112] incident on proton targets, and are found to hold to within experimental accuracies of $\sim 10\%$.

Crossing symmetry and analyticity can be used to make a further connection between elastic and dissociative cross-sections in the form of the first moment Finite Mass Sum Rule (FMSR) [116]. This expresses the fact that the behaviour of the differential cross-section in the low mass resonance region must, on average, be the same as that in the smooth high mass region, provided that the cross-sections are expressed in terms of the fully crossing symmetric variable,

$$\nu = M_X^2 - M_0^2 - t \tag{3.39}$$

where $M_0$ is the mass of the incident hadron. Formally, the FMSR is expressed as

$$|t| \frac{d\sigma_{el}}{dt} + \int_0^{\nu'} d\nu \; \nu \frac{d^2\sigma_{diss}}{dt\, d\nu} = \int_0^{\nu'} d\nu \; \nu \; \frac{d^2\sigma_{diss}}{dt\, d\nu}\bigg|_{triple\; Regge\; region} \tag{3.40}$$

where $\nu'$ can take any value beyond the resonance region. The FMSR is found to hold for $pp \to Xp$ to within a few percent [117]. Its interpretation in the photoproduction case, $\gamma p \to Xp$, is interesting in that the choice of $M_0$ has implications to the interpretation of the VDM of section 2.3.3. In a strict application of the VDM, one might expect $M_0 \sim M_\rho$, whereas the massless nature of the photon would imply that even in the resolved case, $M_0 = 0$. A detailed test for photoproduction is described in [112], where it is found that the FMSR is strongly violated for $M_0 = 0$, and holds approximately for $M_0 = M_\rho$. If the incoming particle is considered to have mass, $M_\rho$, for resolved interactions and to be massless where the photon dissociates directly from its bare state, then the FMSR can be satisfied exactly when there is a fraction $\sim 25\%$ of direct photon interactions.

## 3.5 The BFKL Pomeron

The pomeron that has been discussed thus far is a highly non-perturbative object, that provides a good description of all aspects of long range diffractive scattering and total hadronic cross-sections.

The diagram of figure 2.5b, used in the calculation of squared amplitudes contributing to the proton structure function at low $x$, such as figure 2.5a, in itself constitutes a pomeron-like object. It is purely perturbative, and describes the exchange of gluon ladders. The $x$ dependence of equation 2.21 can be expressed in Regge language[7] to give a trajectory

[7]The value of $\lambda$ in equation 2.21 is related to the BFKL Pomeron trajectory of equation 3.41 by $\lambda = \alpha_{I\!P} - 1$.

with little $t$ dependence, and an intercept of around 1.4.

$$\alpha_{\mathbb{P}'}(t) \sim 1.4 + 0t \tag{3.41}$$

This trajectory defines the *BFKL* or *hard* pomeron. It differs from the trajectory of the soft pomeron (equation 3.19), both in the $t$ dependence, and in that the intercept is larger. Any measurement that suggests an increase in the pomeron intercept, or that shows a high-$t$ tail in diffractive processes would therefore be indicative of a contribution from the BFKL pomeron. A further signature is the absence of any shrinkage in the $t$ dependence.

If the total DIS cross-section, $\sigma_{tot}^{\gamma^\star p}$, is plotted as a function of the $\gamma^\star p$ centre of mass energy, $W_{\gamma^\star p}$, then equation 3.21 predicts that the high energy behaviour should follow

$$\sigma_{tot}^{\gamma^\star p} \sim W_{\gamma^\star p}^{2[\alpha_{\mathbb{P}}(0)-1]} \tag{3.42}$$

Plotting the $F_2$ data in this way [118] clearly indicates that the effective value of $\alpha_{\mathbb{P}}(0)$ increases from a value entirely consistent with the soft pomeron at $Q^2 = 0$, to a considerably larger value, as the perturbative region of high $Q^2$ is reached. As can be inferred from the duality expressed in equations 2.31 and 2.32, this is a reflection in Regge language of the rise of the low-$x$ structure function with decreasing $x$. As was discussed in section 2.2, this rise is consistent with the BFKL prediction, but it can also be generated in perturbative QCD with DGLAP evolution alone.

It is often suggested [119] that the onset of BFKL dynamics may most clearly be observed in terms of a contribution to diffractive processes from a pomeron of a form similar to 3.41, wherever a hard scale is present in the interaction. The large mass of the charm quark provides a hard scale in elastic $J/\psi$ photoproduction (see section 6.4.1). The $\gamma p$ centre of mass energy dependence of the cross-section is found to be stronger than that expected for the exchange of a soft pomeron [120][121], but once again, perturbative models that do not require the BFKL mechanism [122] can generate such a behaviour, given an appropriate gluon distribution for the proton. In exclusive $\rho$ meson electroproduction, the finite values of $Q^2$ provide a scale. ZEUS report [69] a centre of mass energy dependence that is significantly stronger than that expected for a conventional pomeron, but H1 find it to be entirely consistent with the soft prediction[8] [123]. There is also a suggestion of shrinkage in the H1 results, and no evidence for a tail in the $t$ distribution is found.

[8]The H1 and ZEUS data points are in agreement to within one standard deviation.

# 3.6 Deep-Inelastic Diffraction

## 3.6.1 Kinematics of Deep-Inelastic Diffraction

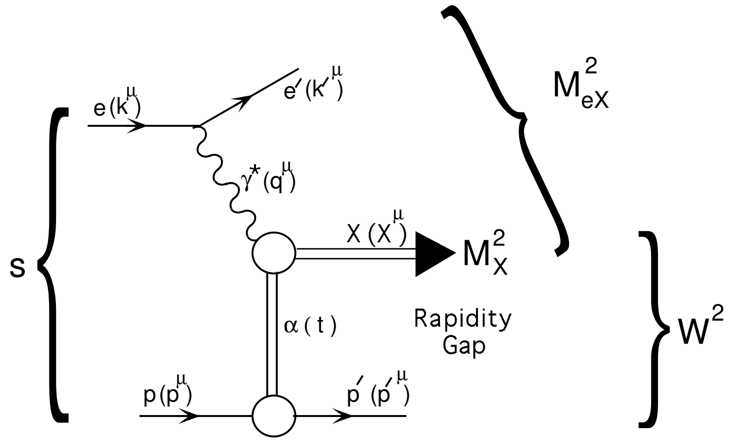


Figure 3.10: *Diagram representing the Inclusive Deep-Inelastic Diffractive Scattering process, under the assumption of factorisation and pomeron exchange dominance. The three final state invariants discussed in the text are shown as $M_X^2$, $M_{eX}^2$ and $W^2$.*

The observation at HERA[124] of a class of DIS events with a large rapidity gap adjacent to the proton direction is once again suggestive of the exchange of the vacuum trajectory. Such events can be interpreted within the dual frameworks of Regge theory and QCD, as a further manifestation of diffractive dissociation, but with a highly virtual photon, effectively probing the structure of the diffractive exchange. Figure 3.10 shows the interpretation of such events in terms of the exchange of the pomeron trajectory, $\alpha(t)$.

In diffractive DIS, the conventional description of the kinematics of DIS, as discussed in section 2.1.1 must still apply. Additional invariants are defined in terms of the 4-vectors of figure 3.10 as follows:

$$M_X^2 = X.X \tag{3.43}$$

$$W^2 = (\gamma^\star + p)^2 \tag{3.44}$$

$$M_{eX}^2 = (X + k')^2 \tag{3.45}$$

$$t = (p - p')^2 \tag{3.46}$$

$$= (\gamma^\star - X)^2 \tag{3.47}$$

$$x_{I\!P} = \frac{\gamma^\star.(p - p')}{\gamma^\star.p} \tag{3.48}$$

$$\beta = \frac{Q^2}{2\gamma^{\star}.(p-p')} \tag{3.49}$$

$$\tag{3.50}$$

Under the assumption of pomeron exchange, $\beta$ is the analogue of the scaling variable, $x$, for the pomeron, giving the fraction of the pomeron's longitudinal momentum that is carried by the parton coupling to the photon. $x_{I\!P}$ is a $y$-type variable, giving the projection of the pomeron momentum onto the proton[9]. Just as $y$ describes the fraction of the electron beam momentum taken by the photon in the $Q^2 \to 0$ limit, $x_{I\!P}$ can be interpreted as the fraction of the proton momentum that is carried by the pomeron as $t \to 0$. Neglecting the azimuthal degree of freedom, the deep-inelastic diffractive process can be entirely specified in terms of four independent variables, for example, $\beta$, $Q^2$, $x_{I\!P}$ and $t$.

### 3.6.2 The Diffractive Structure Function

By analogy with the definition of the proton structure function (equation 2.11), a diffractive structure function[10] may be defined in terms of the four degrees of freedom as

$$\frac{d^4\sigma^D(ep \to epX)}{d\beta\, dQ^2\, dx_{I\!P}\, dt} = \frac{4\pi\alpha_{em}^2}{\beta Q^4}\left(1 - y + \frac{y^2}{2}\right) F_2^{D(4)}(\beta, Q^2, x_{I\!P}, t) \tag{3.51}$$

where the photo-absorption ratio, $R$, has been set to 0. If the diffractive vertex factorises, then the structure function should separate between terms involving variables describing the lower end of the pomeron exchange in figure 3.10, and terms involving variables describing the upper end, such that

$$F_2^{D(4)}(\beta, Q^2, x_{I\!P}, t) = f_{I\!P/p}(x_{I\!P}, t)\; F_2^{I\!P}(\beta, Q^2) \tag{3.52}$$

Previous experiments that have studied diffraction have generally measured kinematic variables by the detection of a leading final state proton. In fixed target experiments, the recoiling target is detected, and in colliding beam experiments [90], Roman Pot detectors[11] are inserted into the beam-pipe well downstream of the vertex, to detect and measure the energy of intact protons scattered at low $t$. Such instrumentation is yet to be used in H1 analyses[12], and all kinematics must be obtained from the scattered electron and/or the

[9] Note that $x = \beta x_{I\!P}$.

[10] The structure function is well defined irrespective of the dynamics assumed for the exchange.

[11] Roman Pots are movable vacuum-tight inserts to the beam-pipe, housing detector elements, which are able to detect particles deflected at very small angles to the beam. Several Roman Pots are generally installed, so that a particle's momentum can be sampled more than once.

[12] Two stations of a Forward Proton Spectrometer have now been installed [125]. Scintillating fibre hodoscopes are used to detect the scattered proton.

diffracted hadronic final state. The quantity, $t$, can then only be determined, via equation 3.47, as the total $p_T^2$ of the final state. Except in the special case of the quasi-elastic production of vector mesons, where the tracks from the resulting low multiplicity decays may be measured with sufficient resolution, $t$ is very poorly reconstructed. Inclusive HERA measurements of diffractive processes to date have been integrated over $t$, leaving three degrees of freedom. A three dimensional structure function, $F_2^{D(3)}(\beta, Q^2, x_{I\!P})$ can then be defined, in an analogous way to $F_2^{D(4)}$ in equation 3.51. The factorisation statement of equation 3.52 reduces to the separation of the $x_{I\!P}$ dependence from the $\beta$ and $Q^2$ dependence.

If factorisation holds, the soft non-perturbative dynamics at the proton vertex, parameterised by the pomeron flux factor, $f_{I\!P/p}$, are given by Regge theory. By considering a single Regge amplitude of the form of equation 3.8 for the process, $ep \rightarrow Yp$, where $Y = e + X$, one obtains

$$\frac{d^2\sigma}{dt dM_{eX}^2} \sim \left(\frac{s}{M_{eX}^2}\right)^{2\alpha(t)-2} \tag{3.53}$$

which is valid at fixed mass, $M_{eX}$, of the system, $eX$, and where $M_{eX}^2$ provides a scale. Since $x_{I\!P} \equiv M_{eX}^2/s$, at fixed $M_{eX}$, equation 3.53 may be written

$$\frac{d^2\sigma}{dt dx_{I\!P}} \sim \left(\frac{1}{x_{I\!P}}\right)^{2\alpha(t)-1} \tag{3.54}$$

Various Regge theory motivated parameterisations for the pomeron flux factor exist [127], all of which follow the behaviour of equation 3.54 and are similar to

$$f_{I\!P/p}(x_{I\!P}, t) \sim f(t)\left(\frac{1}{x_{I\!P}}\right)^{2\alpha(t)-1} \tag{3.55}$$

The quantity, $F_2^{D(3)}(\beta, Q^2, x_{I\!P})$ has been measured by H1 [126] and by ZEUS[128]. The H1 results are shown in figure 3.11. The factorisation property is demonstrated by the fact that a universal fit of the three-dimensional structure function to the triple Regge form, $A/x_{I\!P}^n$, provides a satisfactory description of the data to within experimental accuracy, throughout the $\beta - Q^2$ space. Via equation 3.55, the fit yields a value for the $t$ integrated effective pomeron intercept of[13]

$$\bar{\alpha}_{I\!P} = 1.10 \pm 0.03(stat) \pm 0.04(sys) \tag{3.56}$$

Assuming a peripheral $t$ dependence of the form 3.35, with any slope parameter, $b > 1$, the integration over $t$ causes no more than a 4% deviation of $\bar{\alpha}_{I\!P}$ from the intercept, $\alpha_{I\!P}(0)$.

[13]In [128], ZEUS report a higher value, but not the $1.3 \leftrightarrow 1.4$ that would be indicative of hard pomeron dominance.

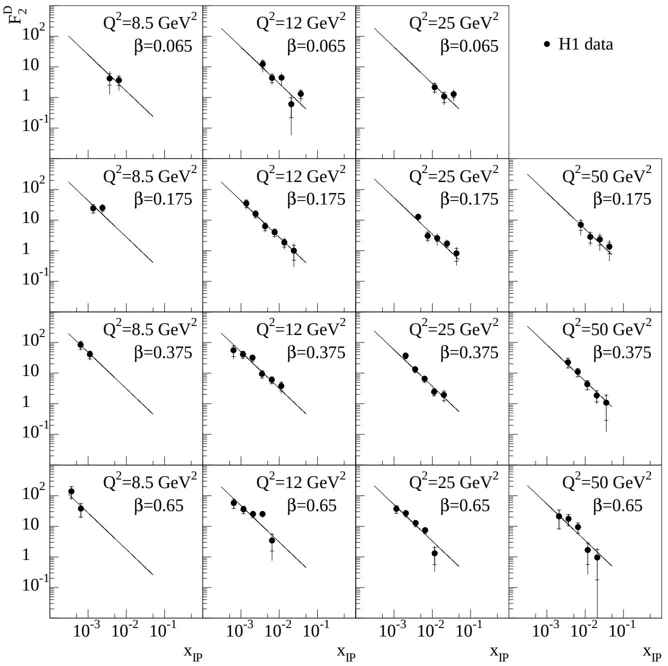


Figure 3.11: *A measurement of the three-dimensional diffractive structure function, $F_2^{D(3)}(\beta, Q^2, x_{I\!P})$ as a function of $x_{I\!P}$, in different bins of $\beta$ and $Q^2$ as presented in [126] . A universal fit (shown) to the form $A/x_{I\!P}^n$ gives a good description of the data throughout the $\beta - Q^2$ plane.*

The fact that the intercept is found to be very different from that of the leading meson trajectory ($\sim 0.5$) indicates clearly that the exchange is diffractive. There is no evidence for BFKL pomeron exchange, though a small contribution is not excluded.

### 3.6.3 The Partonic Structure of Diffraction

Insofar as the factorisation statement of equation 3.52 holds, the quantity, $F_2^{I\!P}(\beta, Q^2)$, may be interpreted as a structure function, measuring the partonic content of the mediator of the exchange in diffractive DIS. Equation 3.56 would indicate that that object is the universal pomeron of soft hadronic physics. Irrespective of the normalisation of the flux factor, $f_{I\!P/p}$, $F_2^{I\!P}(\beta, Q^2)$ is proportional to the quantity,

$$\tilde{F}_2^D(\beta, Q^2) = \int_{x_{I\!P_{low}}}^{x_{I\!P_{high}}} F_2^{D(3)}(\beta, Q^2, x_{I\!P})\, dx_{I\!P} \qquad (3.57)$$

obtained by integration of $F_2^{D(3)}$ over any fixed range in $x_{I\!P}$. The $\beta$ and $Q^2$ dependence of $\tilde{F}_2^D(\beta, Q^2)$, as obtained by integration of $F_2^{D(3)}(\beta, Q^2, x_{I\!P})$ over the full measured range in [126], is shown in figure 3.12. $\tilde{F}_2^D$ broadly displays $Q^2$ scale invariance, indicative of a partonic sub-structure, with the suggestion of $\log Q^2$ scaling violations. The $\beta$ dependence is inconsistent with that of conventionally bound mesons[14], but can be described by either a flat or a hard structure. There is no reason not to expect some QCD evolution to take place, so the extreme hard case of a $\beta(1-\beta)$ dependence, where two partons share the whole of the pomeron momentum, is unrealistic. The data are consistent with a pomeron valence structure consisting of a simple gluon pair, with a developing parton sea due to QCD splitting at low $\beta$.

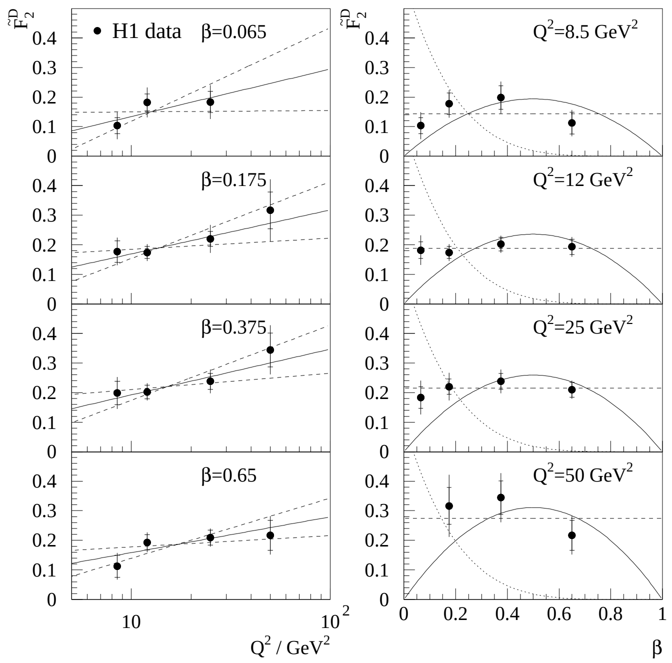


Figure 3.12: $\tilde{F}_2^D(\beta, Q^2)$, *as measured in [126] . The left hand plots show the dependence of the pomeron structure function on* $Q^2$ *in different bins of* $\beta$*, with best fits to a* $\log(Q^2)$ *behaviour shown as solid lines. The right hand plots show the* $\beta$ *dependence, in different bins of* $Q^2$*. The solid line is the form,* $\beta(1-\beta)$*, expected in models of the pomeron consisting of two hard gluons sharing the pomeron's momentum. The falling dotted line is* $(1-\beta)^5$*, which is a soft behaviour based on counting rules.*

The fact that $\tilde{F}_2^D$ continues to rise with $\log Q^2$ up to large values of $\beta$ (the bottom $Q^2$ dependence plot of figure 3.12), is indicative of a gluon dominated structure[15]. Several authors[129] have attempted to fit the measured pomeron structure function using standard DGLAP evolution, in order to determine valence and sea quark, and gluon densities at starting scales of $Q_0^2 \sim 4\text{GeV}^2$. The common conclusion is that the data are best fitted with a hard ($\beta \simeq 1$) gluon dominated structure at the starting scale. The confidence with

[14] This is probably unsurprising, since the measured pomeron must be well off shell.

[15] For the proton, which has a quark valence structure, $\frac{\partial F_2}{\partial \ln Q^2}$ becomes negative at around $x = 0.15$ (see figure 2.2).

which this assertion can be made is currently limited by the experimental accuracy of the results.

Large distance scales are involved in diffractive DIS, and an alternative approach is offered by the Aligned Jet Model (section 2.2.4). Unitarity requires that the absorption of partons on the proton must be *shadowed* by an elastic parton scattering process, yielding a rapidity gap. Much of the observed dynamics can be reproduced with simple non-perturbative arguments in this model [130]. Other non-perturbative approaches to the hadronic final state in DIS [131] seek to explain large rapidity gaps in statistical terms, as arising from large numbers of soft colour interactions, taking place along with a basic photon-gluon fusion mechanism.

## 3.7 The Present Picture

In this chapter, an extensive survey of diffractive physics has been presented. It is apparent that a large fraction of HERA physics may be discussed in terms of Regge theory, and that data are becoming available that distinguish between hard and soft diffractive dynamics.

The total and elastic cross-sections in the $Q^2 \rightarrow 0$ regime have been shown to be well described by the universal soft pomeron of hadron-hadron physics. Since no hard scale is present, this comes as no surprise, though such measurements are also relevant to the understanding of the hadronic nature of the photon. Where hard perturbative scales are present in an interaction, diffractive processes may provide the best indication as to whether or not BFKL dynamics are applicable in the HERA domain. The $W_{\gamma^* p}$ dependence of the total $ep$ cross-sections at large $Q^2$ can be explained by the introduction of the hard pomeron, and the elastic $J/\psi$ cross-section is also suggestive of a hard contribution. In both cases, perturbative treatments that do not use BFKL evolution are also able to generate the observed behaviour. Measurements of the differential diffractive dissociation cross-section at large $Q^2$ continue to support factorisation of the diffractive vertex. Results from H1 and ZEUS differ as to the pomeron intercept that is measured in diffractive DIS, and this is also the case for $\rho^0$ electroproduction.

Already, the study of deep-inelastic diffraction has yielded information on the structure of the pomeron. With increased statistics and a better understanding of systematic effects in the future, it is hoped that a full partonic interpretation will emerge. It is apparent that the introduction at HERA of the hard scale supplied by the photon virtuality to diffractive processes, throws up a number of questions relating to the interplay between the VDM, Regge theory, and QCD, and ultimately, to the relationship between perturbatively calculable, and incalculable strong interactions.

# Chapter 4

# Event Selection and Kinematic Reconstruction

## 4.1 Introduction

This chapter contains a discussion of the experimental techniques used in the subsequent extraction of diffractive photoproduction cross-sections. First, the kinematic variables describing diffractive processes at vanishing $Q^2$ are reviewed. The Monte Carlo models that are used to correct the data are surveyed, and the triggers used in collecting minimally biased samples of photoproduction events are discussed, and their efficiencies studied. There follows a description of the cuts applied in the isolation of samples of diffractive events, and in the reduction of sources of background. The method used to reconstruct invariant masses of diffractively produced states is introduced, and finally, further corrections that must be made in order to obtain fully corrected cross-sections are described. This chapter serves as a preamble to chapter 5, where the measured cross-sections are presented.

## 4.2 Nomenclature and Kinematic Variables

The measurements presented in this, and the following chapter, relate to the four diffractive photoproduction sub-processes defined by the diagrams in figure 3.6. Shorthand notations will be used to distinguish the different processes. The quasi-elastic process (figure 3.6a) will be referred to as EL, single photon dissociation (figure 3.6b) will be termed GD, single proton dissociation (figure 3.6c) PD, and double dissociation (figure 3.6d) DD. Non-diffractive processes will be referred to as ND.

For the purposes of this analysis, the EL process is defined as the elastic production of one of the lowest lying vector meson states, $\rho$, $\omega$ and $\phi$. This is a working definition, based on the simplest version of the VDM, which is not unambiguous. Any process in which the photon fluctuates into a hadronic state in advance of the target, and that hadronic state remains intact after the interaction, may be considered to be elastic. By the present definition, the exclusive production of vector mesons with higher masses than the lowest lying states ($\rho'(1450)$, $J/\psi$ ...), and the possibility, expressed through the extended version of the VDM [84], that the photon may fluctuate to a continuum of more complex, and ultimately unbound states, are incorporated in the definition of the GD process. Non-resonant photon dissociation to a $\pi^+\pi^-$ final state contributes to the low mass part of the invariant mass spectrum at the level of approximately 15% of the rate for elastic $\rho^0$ production [132]. The resonant and non-resonant processes are experimentally indistinguishable, and the direct process, $\gamma p \to \pi^+\pi^- p$ is included in the EL category in this measurement.

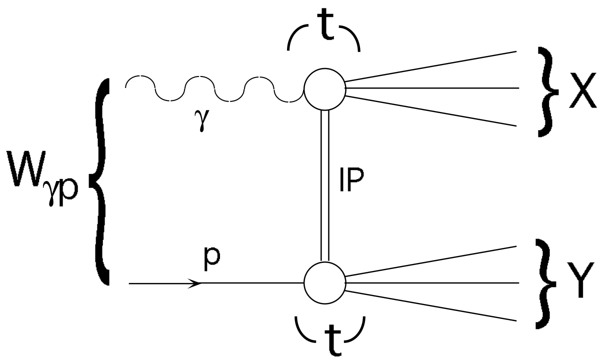


Figure 4.1: *Diagram illustrating the kinematic variables used to describe a generalised diffractive photoproduction process in the framework of single pomeron exchange. The state, $X$ has invariant mass, $M_X$, and the state, $Y$, has mass, $M_Y$.*

Figure 4.1 illustrates the invariants that will be used to discuss all four of the diffractive sub-processes. The diagram is essentially that of the DD process (figure 3.6d), but for the purposes of this discussion, the process may be either elastic or inelastic at either vertex. Then, for example, in the case of the EL process, $X$ in figure 4.1 is a vector meson state, and $Y$ denotes an intact proton. In the following definitions of invariants, the particle symbols are used to denote their four-vectors, and the electron and proton masses are neglected.

In the $Q^2 \to 0$ limit, the square of the centre of mass energy of the $\gamma p$ system,

$$W_{\gamma p}^2 = (\gamma + p)^2 \tag{4.1}$$

may be expressed in terms of the $y$ variable of equation 2.5, as

$$W_{\gamma p}^2 = ys \tag{4.2}$$

where $s$ is the squared centre of mass energy in the $ep$ system. Since the electron is scattered at very small angles in the photoproduction limit, $y$ describes the ratio of the photon to the electron beam energy.

$$y = \frac{E_\gamma}{E_e} \tag{4.3}$$

$W_{\gamma p}$ may then be obtained from the energy of the final state electron, using

$$W_{\gamma p} = \sqrt{s\left(1 - \frac{E_{e'}}{E_e}\right)} \tag{4.4}$$

Invoking energy and momentum conservation, the variable, $y$, may also be obtained from the full hadronic final state, $h$, according to

$$y = \frac{(E - p_z)_h}{2E_e} \tag{4.5}$$

In the case of the EL and GD processes, the final state proton continues intact, and close to the $+z$ direction, so that its contribution to $(E - P_z)_h$ may safely be neglected. $y$ can therefore be calculated from a knowledge of $E - p_z$ of the dissociating photon system, $X$, alone. Where the proton dissociates, such an approximation continues to be valid in the laboratory frame, to well within the experimental resolution.

The square of the four-momentum transferred between the proton and the photon defines the invariant mass of the propagator, generically referred to here as a pomeron,

$$t = (p - Y)^2 = I\!P^2 \tag{4.6}$$

such that the invariant masses of the diffractively produced final state systems may be expressed as

$$M_X^2 = (\gamma + I\!P)^2 \tag{4.7}$$

$$M_Y^2 = (p - I\!P)^2 \tag{4.8}$$

The measurement presented in these chapters is principally concerned with the quantity, $M_X$, which is obtained from the reconstructed invariant mass of all particles detected in the photon fragmentation region.

The variable,

$$\xi = \frac{M_X^2}{W_{\gamma p}^2} \tag{4.9}$$

is often found in the literature[1]. As expressed in equation 3.54, the contribution to the differential cross-section in $\xi$, of a Regge trajectory $\alpha(t)$, goes approximately as $\frac{d\sigma}{d\xi} \sim \left(\frac{1}{\xi}\right)^{2\alpha(0)-1}$. Since the pomeron intercept is significantly larger than that of other trajectories, processes yielding large rapidity gaps are dominantly diffractive at small values of $\xi$. At larger values, contributions from the exchange of other Regge trajectories (e.g. the pion) become important. Previous measurements of diffractive processes have therefore generally been subject to an upper kinematic limit in $\xi$. Typically, only data with $\xi < 0.05$ or $\xi < 0.1$ have been considered. The analogue of $\xi$ for the dissociating proton system, $Y$, is

$$\xi_{Y} = \frac{M_Y^2}{W_{\gamma p}^2} \tag{4.10}$$

The discussion that follows frequently refers to the rapidity of a particle,

$$\mathrm{y} = \frac{1}{2} \ln \left( \frac{E + p_z}{E - p_z} \right) \tag{4.11}$$

Where the mass of the particle is unimportant, true rapidity reduces to pseudorapidity, expressed[2] as

$$\eta = -\frac{1}{2} \ln \left( \tan \frac{\theta}{2} \right) \tag{4.12}$$

where $\theta$ is the polar angle of the particle with respect to the beam axis.

## 4.3 Monte Carlo Models

Corrections to the data for detector inefficiencies and smearing are made using two Monte Carlo models, based on the PHOJET [133] and PYTHIA [134] event generators. The two generators are designed to describe both direct and resolved photoproduction processes, throughout the range of transverse momenta occurring in the interaction. Where there is a hard sub-process, perturbative QCD is used to calculate cross-sections. However, the bulk of photoproduction events contain no hard scale, and the minimally biased parts of both models are based on Regge phenomenology. Different mechanisms are used by the

[1] $\xi$ is closely related to other variables that are commonly used in the description of diffractive dissociation. The Feynman variable, defined as $x_{F} = p_{z_{p'}}/p_p$ relates the longitudinal momentum of an intact final state proton to the beam momentum, such that, in the limit that $t$ and the proton mass may be neglected, $\xi = 1 - x_{F}$. The variable, $x_{I\!P}$, defined in equation 3.48 reduces to $\xi$ in the limit where $Q^2 \to 0$ and $t$,$m_p$ may be neglected.

[2] This differs from the usual definition by a factor of $-1$. This is a consequence of the H1 coordinate system, in which the proton beam defines the $+z$ direction.

two generators to achieve smooth transitions between the soft and hard regimes. Both Monte Carlos produce diffractive events of all four types in figure 3.6, as well as non-diffractive events. In the following sections, a brief overview is given of the manner in which the PHOJET and PYTHIA generators produce soft diffractive event distributions.

### 4.3.1 The PYTHIA Event Generator

The PYTHIA Monte Carlo uses the results of the fits of Donnachie and Landshoff (section 3.3.2) to describe the centre of mass energy dependence of the total $\gamma p$ cross-section, with $\alpha_{I\!P}(0) = 1.081$, and $\alpha_{I\!R}(0) = 0.453$. The various transitions between the different diffractive sub-processes are treated in such a way as to achieve smooth dependences, and to avoid double counting of event types. Quasi-elastic events are generated in the ratio $\rho : \omega : \phi = 13 : 1.5 : 1$, using the optical theorem of equation 3.16 and the assumed total cross-section, according to the approximation

$$\frac{d\sigma_{EL}}{dt} = \frac{\sigma_{tot}^2}{16\pi}\, e^{B_{EL}t} \tag{4.13}$$

with a slope parameter $B_{EL} \sim 11\mathrm{GeV}^{-2}$ at HERA energies. $\rho$ mesons produced in elastic processes are taken to be transversely polarised, and so decay with a $\sin^2\theta^\star$ distribution in their rest frame, where $\theta^\star$ is measured relative to their direction of flight in the $\gamma p$ centre of mass frame. Other vector meson states are treated similarly.

Dissociative diffractive events are generated using approximations to the triple Regge formalism of section 3.4.2. A critical pomeron is assumed, such that $\alpha_{I\!P} \equiv 1$, and $d\sigma/dM^2 \sim 1/M^2$. The resulting dissociative cross-sections are given by

$$\frac{d\sigma_{GD}}{dt\; dM_X^2} = \frac{g_{I\!PI\!PI\!P}}{16\pi}\, \beta^2_{\gamma I\!P}\, \beta_{pI\!P}\, \frac{1}{M_X^2}\, e^{B_{GD}t}\, F_{GD}(M_X^2, s) \tag{4.14}$$

$$\frac{d\sigma_{PD}}{dt\; dM_Y^2} = \frac{g_{I\!PI\!PI\!P}}{16\pi}\, \beta^2_{pI\!P}\, \beta_{\gamma I\!P}\, \frac{1}{M_Y^2}\, e^{B_{PD}t}\, F_{PD}(M_Y^2, s) \tag{4.15}$$

$$\frac{d\sigma_{DD}}{dt\; dM_X^2\; dM_Y^2} = \frac{g^2_{I\!PI\!PI\!P}}{16\pi}\, \beta_{pI\!P}\, \beta_{\gamma I\!P}\, \frac{1}{M_X^2}\, \frac{1}{M_Y^2}\, e^{B_{DD}t}\, F_{DD}(M_X^2, M_Y^2, s) \tag{4.16}$$

The factors $F_{GD}$, $F_{PD}$, and $F_{DD}$ are functions that are designed to modify equations 4.14–4.16 in kinematic regions where triple Regge predictions are not strictly valid. They contain free parameters which are extracted in fits to $pp$ and $p\bar{p}$ data. Their effect is to suppress production near to kinematic boundaries, to enhance the low mass part of the single dissociation cross-sections, and to suppress DD events where the two diffractively produced states overlap in rapidity space. The triple pomeron coupling and couplings of the pomeron to the external particles are constrained by low energy data. The $t$ dependences of the single dissociation processes are weakly mass dependent, and are given by equations 3.35 and 3.36, with $\alpha' = 0.25\text{GeV}^{-2}$. The slope parameter, $B_{PD}$, for PD is taken to be approximately one unit larger than that for GD at the same final state mass, and both are typically around half of the value for the elastic process. The slope parameter for double diffraction has a logarithmic dependence on the square of both dissociation masses, and is typically around 2 $\text{GeV}^{-2}$. The range in $t$ is governed by mass dependent kinematic limits. GD events are generated starting at a threshold of $M_X = M_\rho + 0.2\text{GeV}$. Light dissociating states with $M_X < M_\rho + 1\text{GeV}$ decay isotropically to a two body final state. Resonances, such as the $\rho'(1450)$ are therefore not generated explicitly, but are treated in an averaged manner. Higher mass dissociating systems are treated as strings stretched along the $\gamma p$ interaction axis, with particles produced in the string development distributed in a longitudinal phase space with limited transverse momentum. (see section 4.5.1 for a justification of this).

### 4.3.2 The PHOJET Event Generator

In the PHOJET Monte Carlo, the total cross-section is once again modelled in terms of a superposition of Pomeron and Reggeon components. The effective pomeron and reggeon intercepts used are determined in fits, using the PHOJET model, to $pp$ and $p\bar{p}$ data. $\alpha'_{I\!P}$ is taken to be $0.25\text{GeV}^{-2}$.

The elastic cross-section is treated in a similar way to the PYTHIA case, with the ratio of vector mesons once again constrained to be $\rho : \omega : \phi = 13 : 1.5 : 1$. The differential elastic cross-section is given by

$$\frac{d\sigma_{EL}}{dt} = \frac{1}{16\pi}\, \beta^2_{\gamma I\!P}\, \beta^2_{pI\!P} \left(\frac{s}{s_0}\right)^{2(\alpha_{I\!P}(0)-1)} e^{b_{EL}t} \tag{4.17}$$

Diffractive dissociation to states with masses not sufficiently large for triple Regge dynamics to apply[3] are treated, through the extended VDM of section 2.3.3, as quasi-elastic processes, though they are still included in the GD category. For simplicity, this region is treated as a single effective resonance, normalised to the triple Regge and the elastic kinematic regions via the FMSR of section 3.4.3. The differential cross-section in the low mass dissociation region is assumed to exhibit the Regge behaviour of equation 4.17, with mass dependence entering only through revised couplings and through the slope parameter, which evolves smoothly from the elastic to the triple Regge regions. The states produced in elastic and low mass dissociation processes are taken to be transversely polarised, and decay to two or three particle final states, with specified angular distributions.

The high mass diffraction dissociation region is modelled with a triple Regge amplitude,

[3]The low mass dissociation region is defined by $M_\rho + 2M_\pi < M_X < \sqrt{5}\text{GeV}$ in the model.

but with a mass dependence $d\sigma/d\nu \sim 1/\nu$. $\nu = M_X^2 - M_0^2 - t$, is the crossing symmetric variable used in the FMSR, and $M_0 = M_\rho$. The cross-section for high mass diffractive dissociation takes the form,

$$\frac{d\sigma_{GD}}{dM_X^2\ dt} = \frac{1}{16\pi}\,\beta_{\gamma I\!P}\,\beta_{pI\!P}^2\,g_{I\!PI\!PI\!P}\,\left(\frac{s}{s_0}\right)^{2(\alpha_{I\!P}(0)-1)}\left(\frac{s_0}{\nu}\right)^{\alpha_{I\!P}(0)}\,e^{b_{GD}t} \tag{4.18}$$

with the PD and DD cross-sections treated similarly. Dependences on $t$ are expressed through slope parameters ($b_{GD}$ etc.), similar in magnitude to those in the PYTHIA case. The pomeron couplings are obtained from fits to $pp$ and $p\bar{p}$ data.

Multi-particle final states are generated by considering colour flow topologies arising from various Pomeron and Reggeon cuts. Reggeon cuts produce single colour strings, whilst pomeron cuts yield two strings, which fragment independently of one another.

## 4.4 Selection of Minimally Biased Photoproduction Events

### 4.4.1 Data Samples

The data used in this analysis were collected in two short dedicated runs during 1994, one with the usual interaction point ($z \simeq 5$cm), and one with the interaction point shifted by $\sim 65$cm in the proton ($+z$) direction. In the nominal vertex case, samples collected with two different triggers are analysed. The first, hereafter described as the *z-vertex* trigger, requires a coincidence of a signal ($E_{e'} > 4$GeV) from the electron tagger trigger element of the luminosity system (section 1.7.1), and a T0 signal, indicating activity in the central part of the detector, from the z-vertex sub-system trigger (section 1.6.3). Studies have shown that the minimum requirement for the z-vertex T0 trigger bit is a single central track, originating from the vertex region, with a threshold of $p_T \sim 200$MeV. The second trigger used will be described as the *ToF-IA* trigger. It requires a coincidence of trigger elements from the electron tagger and from the interaction time window of the ToF (section 1.8). It is efficient for the detection of particles leaving the interaction region in the backward direction, close to the beam-pipe. For the shifted vertex data, only the sample collected with the ToF-IA trigger is analysed. Both of the sub-triggers used also contain vetoes, rejecting events in which signals are detected in the background time windows of the ToF and FToF scintillators. The overall sample sizes before any cuts are 28,157 events in the z-vertex triggered sample, 72,844 events in the nominal vertex ToF-IA sample, and 49,213 events in the shifted vertex ToF-IA sample.

The three distinct data samples are treated separately, and results are combined at the end of the analysis chain. The data used are taken from all runs for which the detectors needed for the analysis, and other main components of the H1 were fully operational, and for which background levels were tolerably low. The nominal and shifted vertex data samples were collected in different run ranges, and are therefore completely independent. The nominal vertex ToF-IA and z-vertex samples were collected in the same run period, and would be fully independent only if there were no events appearing in both samples. Although the two triggers are sensitive to events with differing topologies, approximately 8% of events with large $M_X$ in the nominal vertex ToF-IA sample also appear in the z-vertex sample. Because of this small correlation between the two nominal vertex measurements, only one of them can be considered wherever results are combined.

### 4.4.2 Electron Tagger Acceptance

The electron tagger is used in order to trigger, and measure the energy of the scattered electron emitting the photon. As discussed in section 1.7.1, its acceptance is sensitive to the beam optics. A method exists [25] for the extraction of the acceptance for inclusive photoproduction, for a given beam configuration, to an accuracy of $\sim 5\%$. The electron tagger acceptance for the Bremsstrahlung process, $\mathcal{A}_{BH}(y)$ is obtained in the same way as is done for the off-line luminosity calculation (section 1.7.2), with $y$ measured from the photon arm of the luminosity system alone. A simulation of Bremsstrahlung events is tuned to the data, by variation of the simulated beam tilt, until the electron energy spectrum of the luminosity tagger is duplicated. To account for the fact that the $Q^2$ dependences in the Bremsstrahlung and inclusive photoproduction cases are different, the acceptance for the photoproduction case, $\mathcal{A}_{\gamma p}(y)$, is calculated with the same simulation, now tuned to the beam optics, but with generated photoproduction events. The result is an integrated tagger acceptance, $\int \mathcal{A}_{\gamma p}(y)\, dy$ accurate to $\sim 3-5\%$ depending on the data sample. In the period spanning this measurement, there were three distinct periods of beam optics. The electron tagger acceptance functions for each period, calculated using the method described above, are shown in figure 4.2a. For the calculation of overall electron tagger acceptances, an average of the three functions shown, weighted to the total luminosity in each period, is used. The systematic error on the resulting acceptance is conservatively estimated to be 5%.

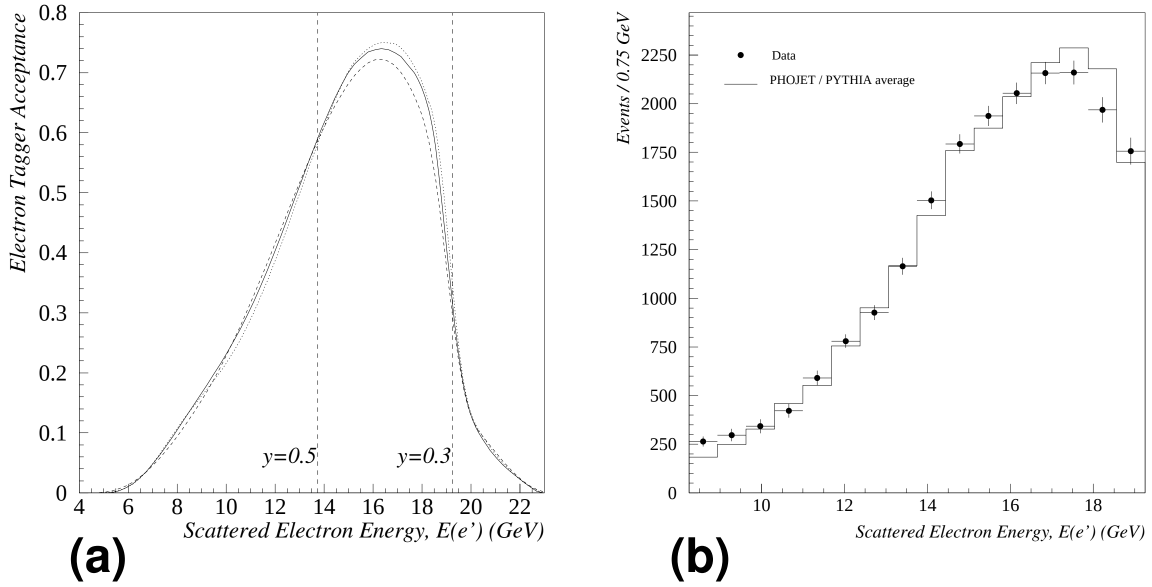


Figure 4.2: *(a) The efficiency of the Electron tagger as a function of the energy of the scattered electron, for the three different periods of beam optics spanning the measurement. Effects due to the tagger trigger efficiency, and due to the fiducial cut,* $|x_{ET}| < 65$mm, *are included. (b) The measured* $E_{e'}$ *spectrum in the electron tagger for the nominal vertex ToF-IA sample, compared to an average of the predictions of PHOJET and PYTHIA. The data are corrected for beam gas background.*

### 4.4.3 Removal of Background

Cuts are applied to the three data samples, to remove events from background sources and events for which the scattered electron energy is poorly measured.

To remove background from the Bremsstrahlung process, it is required that the energy measured in the photon detector of the luminosity system, $E_{PD} < 2$GeV.

Where the scattered electron is detected near to the boundaries of the electron tagger, there is a high probability that part of the electron shower is not contained. A cut on the local $x$ coordinate in the electron tagger, of the centre of gravity of the electron cluster, $|x_{tag}| < 6.5$cm, is applied, rejecting events in which the energy deposit is within 1.5cm of the edge of the detector.

For events in which the scattered electron energy is small, there is a large background from electron beam-gas interactions, and from off-momentum electrons travelling with the electron beam. At large energies of the scattered electron, the tagger acceptance becomes small (figure 4.2a). The analysis was therefore restricted to the range, $0.3 < y < 0.5$, or, equivalently, through equation 4.2, $164 < W_{\gamma p} < 212$GeV. Figure 4.2b shows a control plot for the scattered electron energy, after cuts on $x_{tag}$ and $E_{PD}$.

After cuts associated with the scattered electron, the resulting samples are still heavily contaminated with beam induced background. Since the electron beam, and particles associated with its interactions, pass the ToF device during its interaction window, the ToF-IA triggered data are contaminated with background from the electron beam. The z-vertex triggered data contains background associated with both beams. At the level 5 stage of the triggering process (section 1.4), z-vertex triggered data are subjected to cuts against beam-gas background, and are accepted only if

$$\sqrt{y_h^2 + \left(\frac{2(p - p_z)}{3p}\right)^2} \quad > \quad 0.12 \tag{4.19}$$

$$y_h \quad > \quad 0.03 \tag{4.20}$$

where $y_h$ is obtained using the hadronic definition of equation 4.5, and $p_z$ and $p$ are momentum variables for the hadronic final state observed in the detector. These cuts are highly effective in removing background, but also result in small losses in signal for low mass diffractive events. Corrections for these losses are described in section 4.7. Data obtained with the ToF-IA trigger are allowed to by-pass the level 5 beam gas cuts. Instead, cuts on the energy deposited in the calorimeters are made for the removal of beam gas events at the analysis stage. For the nominal vertex ToF-IA sample, the total energy deposited in the LAr and BEMC calorimeters is required to be greater than 1GeV. This cut is relaxed to 0.2GeV for the shifted vertex data, but the additional requirements that there should be at least 0.1GeV in the BEMC alone, and that there should be at least one BPC hit, are introduced.

A further effective requirement that is normally used in the removal of beam-gas background is that there should be a vertex reconstructed in the region of the bunch-crossing point. The probability that a diffractive event has a reconstructed vertex depends on the kinematic variables, $y$ and $M_X$. At the values of $y$ considered in this analysis, tracks produced in events of type EL or for the low $M_X$ part of the GD spectrum, are generally backward of the acceptance region of the central tracker, and a vertex is rarely reconstructed. For higher dissociation masses, the existence of a reconstructed vertex becomes considerably more likely. Figure 4.3 shows control plots for the position in $z$ of the reconstructed vertex in the three samples, after subtraction of beam-gas background. It is clear that the requirement of a reconstructed vertex would be catastrophic to the acceptance at low $M_X$ in the ToF-IA samples. Consequently, a cut is applied, whereby if a vertex is reconstructed in the ToF-IA data, it is required to be within 30cm of the

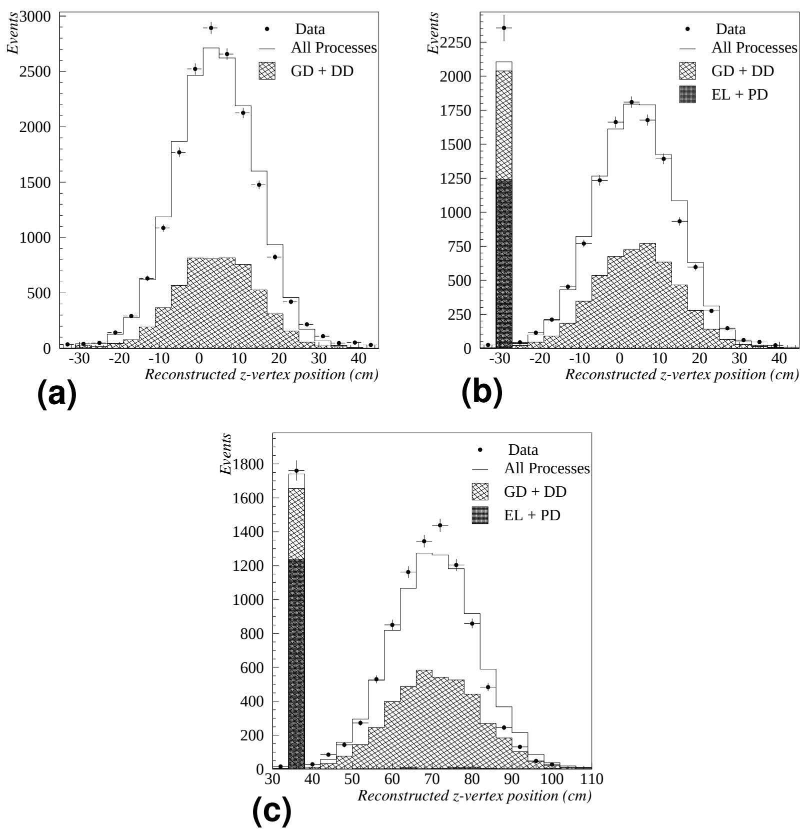


Figure 4.3: *Control plots, showing the z-vertex distributions for a) The z-vertex sample. b) The nominal vertex ToF-IA sample. c) The shifted vertex ToF-IA sample. Events for which no vertex was reconstructed are shown in b) in the bin at $z = -30$cm, and in c) at $z = 35$cm. The Monte Carlo histograms are averages of the PHOJET and PYTHIA models. The shaded regions correspond to EL processes, and PD events in which the proton dissociation mass is less than 10GeV. The cross-hatched region corresponds to the GD process, and DD where the proton dissociation mass is less than 10GeV.*

nominal value for the run. Where no vertex is reconstructed, the event is retained. For the z-vertex sample, in which a vertex has already been required at the trigger level, it is demanded that a vertex within 30cm of the nominal value is also reconstructed for the event.

Finally, events in which recognised noise patterns are found in the LAr calorimeter data are rejected.

### 4.4.4 Trigger Element Efficiencies

The final state energy flows of the four diffractive sub-processes are dependent on the kinematic variables, $y$, $M_X$ and $M_Y$. The fraction, $y$, of the electron beam energy carried by the interacting photon, defines the centre of mass energy of the $\gamma p$ collision according to equation 4.2, and hence describes the boost of the colliding system relative to the laboratory frame. The region of good acceptance of the electron tagger restricts the analysis to the case where the $\gamma p$ system is strongly boosted in the forward direction. The regions of rapidity populated by final state hadrons depend on the masses, $M_X$ and $M_Y$, of the diffracted systems on both the photon and proton sides.

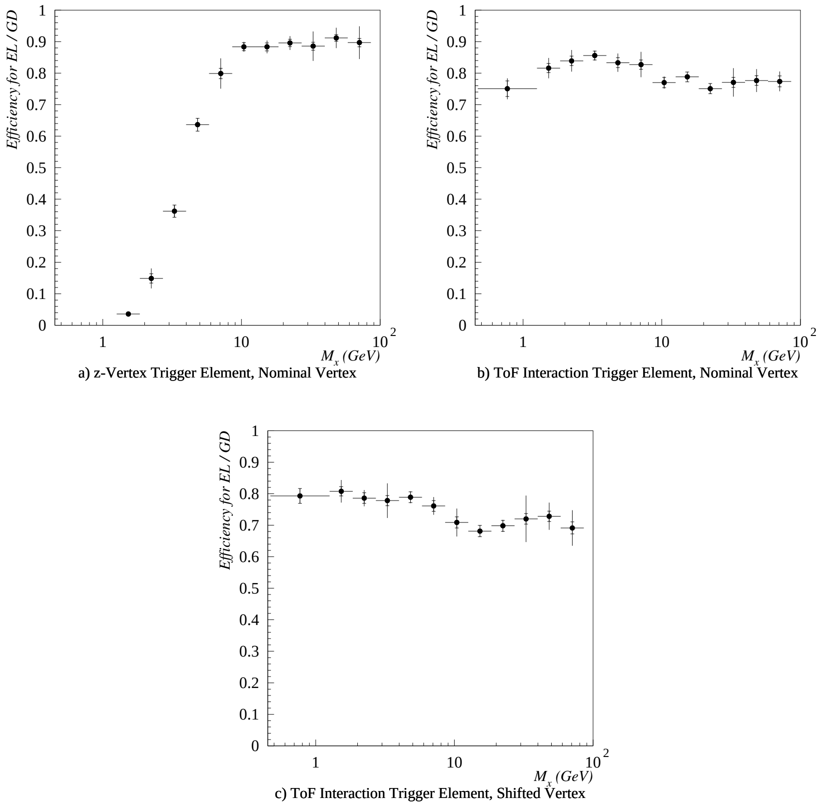


Figure 4.4: *Trigger element efficiencies for events of types GD and EL, in the range, $0.3 < y < 0.5$. The points plotted are the averages of results obtained with the PHOJET and PYTHIA Monte Carlos. The inner error bars are statistical. The outer error bars represent the statistical errors added in quadrature to a systematic error, equal to half of the difference between the efficiencies obtained with each Monte Carlo on its own. For the overall sub-trigger efficiencies, these values must be convoluted with the efficiency of the electron tagger, which is 0.61 ± 0.03 when averaged over the y range.*

The acceptance of the z-vertex trigger is particularly sensitive to the extent of the frag-

| | *z-vtx NOMINAL* | | *ToF-IA NOMINAL* | | *ToF-IA SHIFTED* | |
|---|---|---|---|---|---|---|
| | *Phojet* | *Pythia* | *Phojet* | *Pythia* | *Phojet* | *Pythia* |
| ND | 95.9 ± 0.3 | 95.5 ± 0.2 | 63.2 ± 0.6 | 68.5 ± 0.5 | 54.7 ± 0.6 | 62.4 ± 0.5 |
| GD | 59.6 ± 0.7 | 65.6 ± 0.9 | 78.3 ± 0.6 | 81.2 ± 0.7 | 72.3 ± 0.6 | 76.7 ± 0.8 |
| PD | 7.9 ± 0.7 | 13.0 ± 1.4 | 85.1 ± 0.9 | 85.8 ± 1.5 | 88.4 ± 0.8 | 86.7 ± 1.4 |
| DD | 65.0 ± 1.0 | 55.0 ± 1.7 | 77.7 ± 0.8 | 84.7 ± 1.2 | 71.1 ± 0.9 | 81.0 ± 1.3 |
| EL | 0.2 ± 0.1 | 0.2 ± 0.1 | 84.5 ± 0.7 | 83.0 ± 1.1 | 86.9 ± 0.7 | 85.7 ± 1.0 |

Table 4.1: *Monte Carlo estimates of the overall efficiencies of the z-vertex trigger element with nominal vertex, and the ToF-IA trigger element with both shifted and nominal vertex positions. The errors quoted are statistical.*

mentation region of the photon. At relatively large $M_X$, tracks are produced in the central region of laboratory rapidity, and the z-vertex trigger element is efficient. At small values of $M_X$, activity in the central trackers is rarely observed. Figure 4.4a shows the results of a Monte Carlo study of the efficiency of the z-vertex trigger bit, as a function of $M_X$, for GD and EL events in the range, $0.3 < y < 0.5$. A threshold behaviour is observed, with full efficiency reached at $M_X \simeq 10$GeV. A similar study of the acceptance as a function of $M_X$, for events of types DD and PD, yields very similar results. The acceptances are slightly improved in the case where the event is inelastic at the proton vertex, since at large $M_Y$, parts of the dissociating proton system may be observed in the central parts of the detector. The z-vertex trigger element can only be used for the study of diffractive processes yielding final states at relatively large $M_X$.

Since the ToF device is located in the very backward region of the detector ($-3.5 < \eta < -2.0$), the ToF-IA trigger element is efficient for the detection of backward-going hadrons throughout a large part of the photon fragmentation region, even in the range of $y$ considered. Figure 4.4b shows the acceptance of the ToF-IA trigger bit, with nominal vertex, for GD and EL events, as a function of $M_X$. Figure 4.4c shows the same thing for the shifted vertex case. The efficiency is found to be large, throughout the range in $M_X$. Once again, very similar results are obtained in studies of efficiencies for PD and DD events. In the shifted vertex case, the larger coverage of the photon fragmentation region results in a slight enhancement in the efficiency for the EL and PD processes.

Monte Carlo estimates for the overall ToF-IA and z-vertex trigger bit efficiencies for each of the five photoproduction sub-processes are shown in table 4.1. The ToF-IA trigger element has high efficiency for all four diffractive sub-processes, as well as for non-diffractive photoproduction. The z-vertex trigger element is efficient only for non diffractive events, and for GD and DD events where $M_X$ is large.

## 4.5 Selection of Diffractive Photoproduction Events

### 4.5.1 Final State Rapidity Distributions

Diffractive events are characterised by large gaps in the rapidity distributions of final state hadrons, indicating the absence of any colour string connecting the photon and proton fragmentation regions. At the mean centre of mass energy of this measurement, $\langle W_{\gamma p}\rangle = 187\mathrm{GeV}$, the $\gamma p$ centre of mass is boosted forwards relative to the laboratory frame, by approximately two units of rapidity. The detector thus provides better coverage of the photon fragmentation region than it does that of the proton. In general, at least part of the final state photon system, $X$, is observed in the detector, though at low $M_X$, it is restricted to the very backward region. By contrast, except where $M_Y$ is large ($\gtrsim 10\mathrm{GeV}$), no evidence of the diffracted proton system is visible in the main detector. Diffractive events of all four types thus tend to have a rapidity gap that extends to the forward edge of the LAr calorimeter.

In non-diffractive events, colour is generally exchanged, and the proton and photon fragmentation regions are connected by a colour string, giving rise to a hadronic plateau of low but detectable activity. The separation in rapidity of adjacent energy clusters in the calorimeter falls off exponentially, and the most forward cluster observed in the LAr calorimeter is typically very near to the edge of its acceptance.

### 4.5.2 $\eta_{max}$ Cuts

A cut in the variable, $\eta_{max}$, defined as the most forward track, BPC hit, or calorimeter deposit passing noise cuts, has previously been used in the isolation of clean samples of diffractive events. Figure 4.5a shows a control plot of the $\eta_{max}$ distribution for the ToF-IA nominal vertex data. The strong peak at large $\eta_{max}$ is dominated by non-diffractive events, and the peak at low $\eta_{max}$ is dominated by events of types EL and PD. There is a relatively flat region in between the two peaks, which contains predominantly GD and DD events. A simple cut at around $\eta_{max} = 2$ has been used in previous studies of diffraction at HERA [124].

The rapidity, $\eta_0^\star$ of the undecayed state, $X$, produced in the dissociation of the photon, is given, in the centre of mass of the $\gamma p$ system, by (see for example [92].)

$$\eta_0^\star = \ln \frac{M_X}{W_{\gamma p}} \tag{4.21}$$

If the decay products of the state, $X$, have an isotropic distribution in the centre of mass of

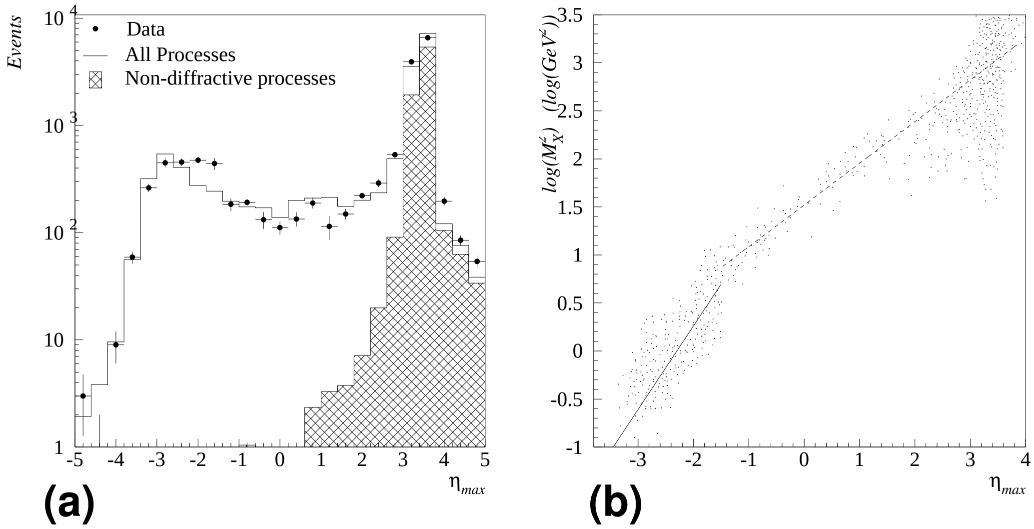


Figure 4.5: *(a) Control plot, comparing an average of PHOJET and PYTHIA predictions to the $\eta_{max}$ distribution of all data collected in the nominal vertex ToF-IA sample. The most forward energy deposition or track in the LAr and BEMC calorimeters, central and forward trackers, and the BPC defines $\eta_{max}$. The shaded histogram shows the non-diffractive contribution in the Monte Carlo. (b) The correlation between $\eta_{max}$ and $\log(M_X^2)$ for the same data. The dashed line shows the prediction of the multi-peripheral model described in the text, and given by equation 4.26 . The solid line is the prediction for an isotropic decay of the diffractively produced state in its centre of mass, expressed in equation 4.23 . The final state masses are reconstructed using the method described in section 4.6 .*

the diffracted system, the resulting rapidity distribution is expected to be approximately Gaussian, with a half width, $\Delta\eta$, that has little dependence on $M_X$. The maximum pseudorapidity reached by the dissociating photon system is therefore expected to depend logarithmically on $M_X$ at fixed $W_{\gamma p}$,

$$\eta^{\star}_{max} \sim \ln \frac{M_X}{W_{\gamma p}} + \Delta\eta \tag{4.22}$$

Elastic and low mass dissociating states decay to low multiplicity final states, with angular distributions that fill the available phase space. Provided that the most forward extent of the photon fragmentation region is contained within the acceptance of the main detector components, the variable, $\eta^{\star}_{max}$ of equation 4.22 corresponds to the measured $\eta_{max}$ plotted in figure 4.5a, apart from the boost between frames.

Figure 4.5b shows a scatter plot of log $M_X^2$ against $\eta_{max}$, for the full data sample obtained with the nominal vertex ToF-IA trigger. For values of $M_X < \sqrt{5}$GeV, below the triple

Regge region, the line,

$$\eta_{max} = \ln M_X - 2.3 \tag{4.23}$$

is superimposed on the scatter plot, corresponding to the prediction of equation 4.22, boosted to the laboratory frame with $\langle W_{\gamma p} \rangle = 187$GeV, and with $\Delta\eta = 0.7$units. Such a parameterisation gives a reasonable form for the average behaviour of the data.

At larger dissociation masses, corresponding to the triple Regge region, the distribution of final state hadrons is well known [135] to be limited in $p_T$. Multiperipheral models [136] have proved successful in the description of rapidity distributions of the decay products of $X$ at large masses. In such models, the cross-section is treated as an incoherent sum of cross-sections for chains of soft exchange processes, very similar to those occurring in long range hadronic interactions. Each final state particle in the chain is produced at low $p_T$ with respect to its neighbours.

Multiperipheral models give rise to a flat rapidity distribution for the dissociating photon system, spanning several units of rapidity, centred at $\eta_0$, with a half width at half maximum, $\Delta\eta_{HWHM}$, proportional to the log of the mass of the dissociating system

$$\Delta\eta_{HWHM} \simeq \ln\left(\frac{M_X}{\langle\mu\rangle}\right) \tag{4.24}$$

where $\langle\mu\rangle$ is a hadronic mass scale. From equations 4.21 and 4.24, the maximum pseudorapidity reached by the final state hadrons arising from the fragmentation of the photon state is given, in the $\gamma p$ centre of mass, by

$$\eta^{\star}_{max} \sim \ln\left(\frac{M_X^2}{\langle\mu\rangle\, W_{\gamma p}}\right) \tag{4.25}$$

For $M_X > \sqrt{5}$GeV, the line,

$$\eta_{max} = \ln M_X^2 - 3.5 \tag{4.26}$$

is superimposed on the scatter plot of figure 4.5b, and gives a good description of the average behaviour of the data at large $M_X$. Inserting this parameterisation in equation 4.25, with $\langle W_{\gamma p}\rangle = 187$GeV, gives $\langle\mu\rangle = 1500$MeV, after boosting between frames.

The plateau in the $\eta_{max}$ distribution in figure 4.5 is to be expected. From equation 3.34, the $M_X$ dependence is given approximately in the triple Regge region by $dN/dM_X^2 \sim 1/M_X^2$. Equation 4.26 implies that $dM_X^2/d\eta_{max} \sim M_X^2$. Then

$$\begin{aligned} \frac{dN}{d\eta_{max}} &= \frac{dN}{dM_X^2}\,\frac{dM_X^2}{d\eta_{max}} && (4.27)\\ &\sim \frac{1}{M_X^2}\,M_X^2 && (4.28)\\ &\sim const && (4.29) \end{aligned}$$

An $\eta_{max}$ cut is effective in isolating a diffractive sample, once the relatively flat dependence on $\eta_{max}$ of figure 4.5a is established in data, but severely limits the kinematic range of the sample obtained. From equation 4.26, a cut in the region of $\eta_{max} \sim 2$ restricts the resulting sample to $M_X \lesssim 15\text{GeV}$.

### 4.5.3 The Forward Detector Selection

In order to extract a sample of diffractive events extending to larger values of $M_X$ than is possible with a standard $\eta_{max}$ cut, use must be made of detectors that are sensitive to energy flow at higher values of rapidity than those covered by the main calorimeters and trackers. Since $|t|$ must be small for diffractive events, the intact final state proton in the GD and EL processes is scattered at very large rapidities ($\eta_{lab} \gtrsim 8$). Setting $M_X < 46\text{GeV}$ in equation 4.26, such that $\xi < 0.05$, leads to an approximate upper limit for diffractive events of $\eta_{max} \sim 4$. Diffractive events of types GD and EL are therefore expected, irrespective of $M_X$, to display an absence of hadronic activity in the region $4 \lesssim \eta_{lab} \lesssim 8$.

In the case of diffractive events of types DD and PD, the system $X$ is still confined to $\eta_{lab} \lesssim 4$. Using similar arguments, based on the multiperipheral model, for the dissociating proton system as were used for the photon fragmentation region, the minimum rapidity reached by the decayed system, $Y$, is given by

$$\eta^{\star}_{min,Y} \simeq \ln\left(\frac{W_{\gamma p}\,\langle\mu\rangle}{M_Y^2}\right) \tag{4.30}$$

Taking $\langle W_{\gamma p}\rangle = 187\text{GeV}$, and $\langle\mu\rangle = 1500\text{MeV}$, and boosting to the laboratory frame, one obtains, for large $M_Y$,

$$\eta_{min,Y} \sim 7.8 - \ln M_Y^2 \tag{4.31}$$

From equation 4.31, it can be seen that even for comparatively small values of $M_Y$, events of types PD and DD give rise to final state hadrons throughout a large part of the region, $4 < \eta_{lab} < 8$, that is expected to be devoid of activity in the EL and GD cases. Detectors that are sensitive to energy flow close to $\eta_{lab} = 8$ are therefore effective, not only in the isolation of diffractive events, but also in the separation of GD and EL events from diffractive events in which the proton dissociates.

In this analysis, the Forward Muon Detector (FMD) (section 1.9.1) and the Proton Remnant Tagger (PRT) (section 1.8) are used for the detection of final state hadrons at high rapidity. A final state particle may interact with the walls of the beam-pipe, a collimator, or quadrapole magnet, and produce a shower of secondary particles, some of

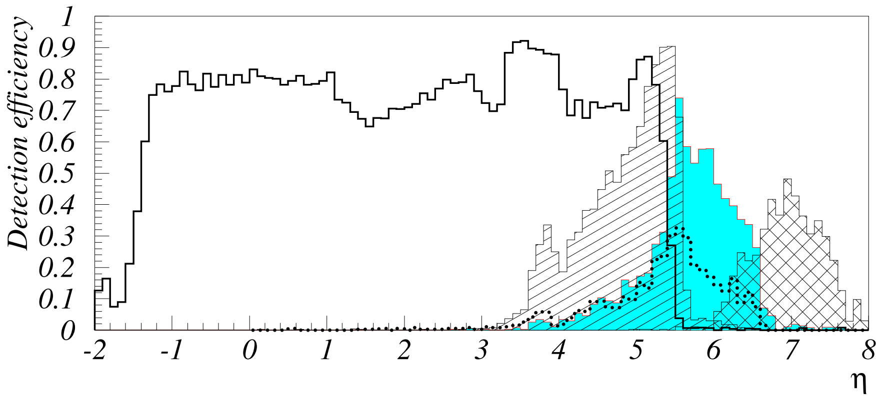


Figure 4.6: *The results of a study of single particle detection efficiencies as a function of rapidity, for forward detector components, using the MEPS Monte Carlo [137] . Particles may be detected either directly, or indirectly via secondary scattering from the beam-pipe, or other material in the forward direction. The open histogram shows the efficiency for the LAr calorimeter, the shaded histogram is that for the FMD, and the cross-hatched pattern is that for the PRT. With typically large particle multiplicities in the region covered, the efficiency per event of these detectors alone, is around 90% at large $M_Y$. The Plug calorimeter, shown with a diagonal pattern, is not used in this analysis, due to noise problems. The dotted histogram shows the efficiency for the Front End Cap of the Instrumented Iron, which is also not used, since it is not well described by Monte Carlo simulations. The plot is taken from [33] .*

which have sufficient transverse momentum to be observed in the forward components of the detector. For this reason, the FMD and PRT are sensitive to particles at larger rapidities than would be expected from their geometric acceptances. Figure 4.6 shows single particle detection efficiencies for various forward components of H1, as a function of rapidity. The combined detection efficiency of the FMD and the PRT for a single particle is greater than 30% throughout the range, $5.5 < \eta < 7.5$. Since non-diffractive, PD and DD events typically give rise to many final state particles in this region, the absence of activity in the FMD and PRT is a powerful tool for the isolation of a sample of EL and GD events.

The level of activity in the PRT is quantified by counting the number of scintillator layers that fire for each event. Noise levels are sufficiently low for this to provide a clean signal, requiring negligible correction. During the data taking period for this measurement, the post-toroid layers of the FMD suffered from a large flux of synchrotron radiation, originating from the electron beam. This source of background heavily dominates the signal in all three post-toroid layers, making them unusable as a tag of forward activity. However, synchrotron radiation is almost entirely absorbed in the iron toroid, leaving the pre-toroid layers more or less free of beam induced background. The only significant noise in the pre-toroid layers is generated in the readout electronics, at the rate of approximately 0.005 hits per cell per event. Since this source of noise has a random distribution, reconstruction to the level of pairs of hits within a layer, is found to be sufficient to reduce the noise contamination to acceptable levels. The pairing algorithm (section 1.9.3) has been extended so that it can recognise tracks originating from secondary scattering in the beam-pipe that enter the system at large polar angles. Any compatible pair of hits within 9cm in the local $y$ coordinate are accepted as a track segment.

### 4.5.4 Response of the Forward Detectors

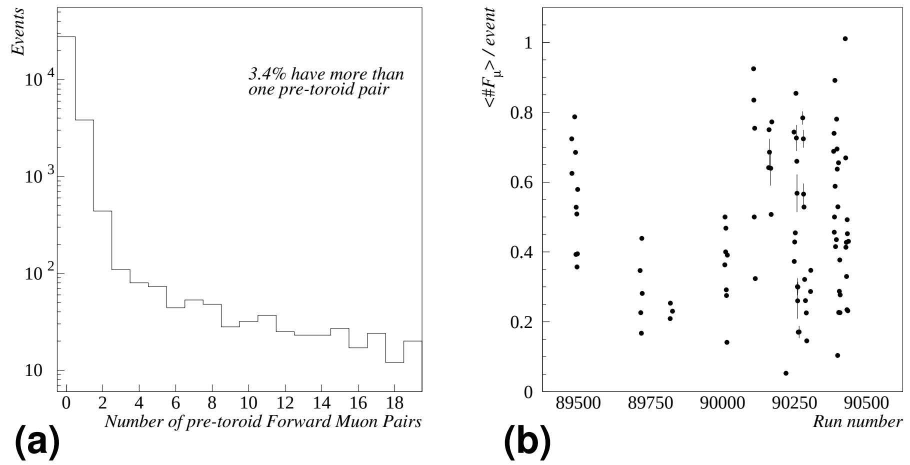


Figure 4.7: *(a) Noise distribution per event in the Forward Muon Detector, as extracted from randomly triggered events distributed uniformly throughout the run period spanning the measurement. (b) The stability of the noise level in the Forward Muon detector, as measured using randomly triggered events. The mean number of reconstructed pre-toroid pairs per event is plotted against the run number. The level generally falls steadily throughout each machine fill, which typically covers several runs.*

Approximately 1% of all events written to tape during standard data taking are triggered on random bunch-crossings, in which both the electron and proton bunches are filled, but where no trigger elements are required to fire. Residual noise levels in the FMD and the PRT have been quantified by studying the level of activity in the detectors in such randomly triggered events, from the same run range as was used for the measurement. The noise level in the PRT is found to be negligible ($\sim 5 \times 10^{-3}$ hits per event), but even after pairing hits, there is a significant residual noise signal for the pre-toroid layers of the FMD. Figure 4.7a shows the distribution of the number of FMD pairs, reconstructed as discussed in section 4.5.3, for the randomly triggered events. Approximately 20% of the events have a single pre-toroid pair; an unacceptable level of noise. In light of this fact, at least two pre-toroid FMD pairs are required as a signal for forward activity. 3.4% of randomly triggered events still fail this criterion, and a correction is made to the measured cross-sections to account for this.

The stability of the FMD noise level has also been investigated (figure 4.7b), by plotting the mean number of pre-toroid pairs per randomly triggered event for each run. The noise level is seen to depend on beam currents and background conditions. No systematic trends in the noise level are observed, nor are there any runs with anomalously high background.

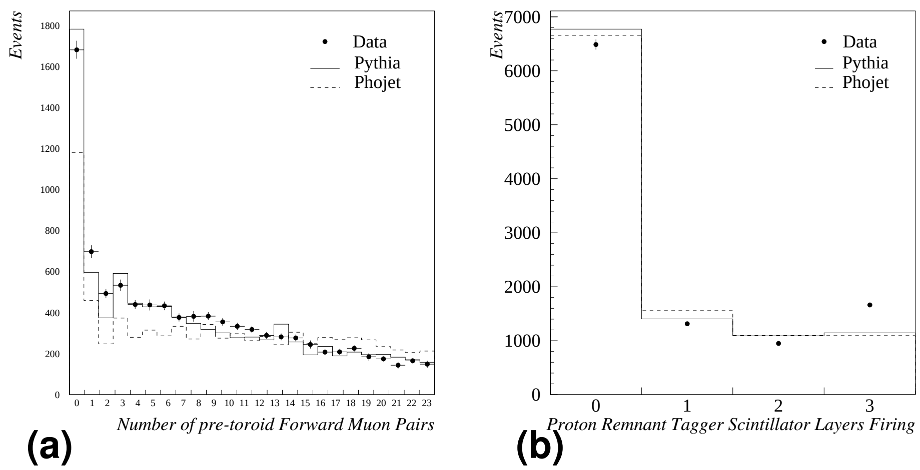


Figure 4.8: *Control plots for (a) The Forward Muon Detector and (b) The Proton Remnant Tagger signals, with the nominal vertex ToF-IA data. A cut of* $\eta_{max} > 3.15$ *is applied to suppress diffractive events. Each Monte Carlo event has a random trigger event superimposed, such that noise effects are also simulated.*

The response of the forward detectors has been studied in the data samples, and compared to the predictions of the PHOJET and PYTHIA Monte Carlos. Noise effects are included in the simulation, by adding the signals from a randomly triggered event to each Monte Carlo event. The version of the detector simulation used includes a detailed description of the forward detectors and their environment, including the forward beam-pipe, and collimators in the region. The comparison of forward detector activity in Monte Carlo and data, with a cut of $\eta_{max} > 3.15$ to suppress diffractive events, is shown in figure 4.8. The PYTHIA model is found to give a significantly better description of the activity in the FMD than does PHOJET. Both Monte Carlos give an acceptable description of the

PRT activity. The Monte Carlo simulation has been further tested using data, by cross-calibrating the efficiencies of different forward detectors [33]. The agreement between data and Monte Carlo for the FMD, PRT and LAr calorimeter efficiencies was found to be better than 5%.

### 4.5.5 Selection of Diffractive Events that are Elastic at the Proton Vertex

The selection of diffractive events of types GD and EL is based on the absence of activity in the FMD and the PRT. An $\eta_{max}$ cut using information from the main detector components is still applied, but with the forward detector cuts, it can be relaxed from $\eta_{max} < 2$ in previous analyses, to $\eta_{max} < 3$. In the parameterisation of equation 4.26, this corresponds to an extension in the accessible kinematic range from $M_X \lesssim 15$GeV to $M_X \lesssim 26$GeV.

To summarise, the following *forward* cuts are defined for the reduction of minimally biased photoproduction samples to diffractive samples in which there is a leading final state proton.

- Number of pre-toroid FMD pairs $\leq 1$
- Number of PRT scintillators giving a signal $= 0$
- From the main detector, $\eta_{max} < 3.0$

After all cuts, 1,358 events remain in the z-vertex triggered sample, 3,718 in the nominal vertex ToF-IA sample, and 3,237 in the shifted vertex ToF-IA sample.

### 4.5.6 Selection of Diffractive Events that are Inelastic at the Proton Vertex

From equations 4.26 and 4.31, it can be seen that, even for relatively small values of $M_X$ and $M_Y$, it is quite possible for DD events to contain only very small rapidity gaps. This makes DD events with large dissociation masses very difficult to distinguish from non-diffractive events. Where a large rapidity gap does exist, its location depends strongly on the values of $M_X$ and $M_Y$. The measurements of cross-sections for diffractive processes that are inelastic at the proton vertex are therefore restricted, in this analysis, to small values both of $M_X$, and of $M_Y$. A consequence of this is that the z-vertex triggered sample cannot be used.

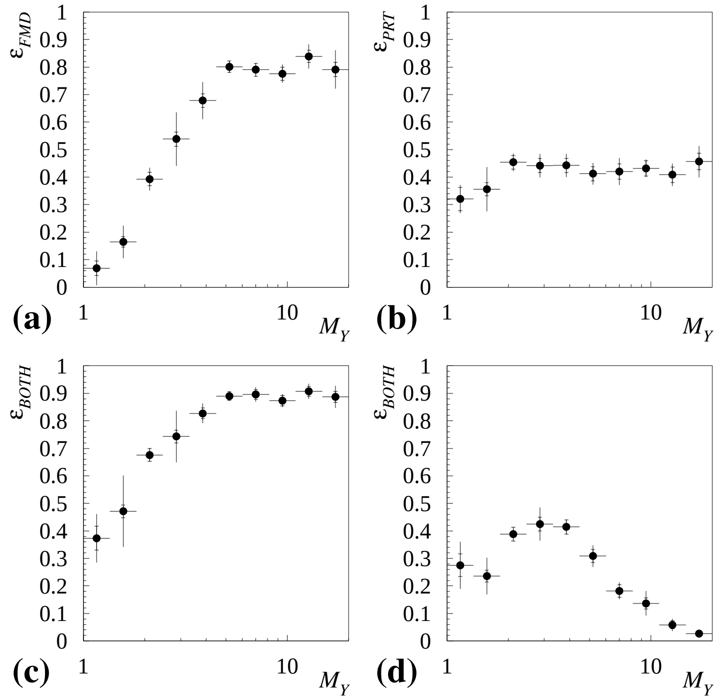


Figure 4.9: *Monte Carlo estimates of Forward detector efficiencies for PD and DD events, as a function of the mass of the dissociating proton system, $M_Y$, for nominal vertex running. (a) The Forward Muon Detector. (b) The Proton Remnant Tagger. (c) Combined use of the Forward Muon Detector and the Proton Remnant Tagger. (d) The combined efficiency of both detectors, but with the additional requirement that the largest rapidity gap in the Liquid Argon calorimeter should be adjacent to its forward edge. In each case, an average of the PHOJET and PYTHIA models is shown. The inner error bars are statistical. The outer error bars show the statistical error added in quadrature to a systematic error equal to half of the difference between the two models.*

The dissociating proton system in PD and DD events may be detected in the forward detectors down to very low proton dissociation masses, $M_Y$. Figures 4.9a and 4.9b show the results of a Monte Carlo study of the efficiency for the detection of the dissociating system in the FMD and PRT, as a function of $M_Y$. Since its single particle acceptance region extends to $\eta \sim 7.5$, the efficiency of the PRT is relatively flat, and covers the masses of the lowest lying proton excitations. The efficiency of the FMD shows a threshold behaviour, reaching saturation at $M_Y \sim 5$GeV. Figure 4.9c shows the combined efficiency of the two detectors.

A large proportion of events of types PD and DD give rise to a signal in the forward detectors, distinguishing them from events in which the proton does not dissociate. However, non-diffractive events also give rise to activity at high rapidity, and a large gap must be required elsewhere in the event, if a clean sample of PD and DD events is to be obtained. Figure 4.6 shows that the acceptances of the FMD and PRT, and of the LAr calorimeter overlap little in rapidity space. At $M_Y = 10\text{GeV}$, equation 4.31 predicts that the minimum laboratory rapidity reached by the fragments of the proton is approximately 3.3, which lies at the limit of the acceptance of the LAr calorimeter for primary tracks, and well inside its acceptance for secondary scattered particles. Requiring that the largest rapidity gap in the main parts of the detector extends to the forward edge of the LAr calorimeter provides a method of distinguishing PD and DD events at low $M_Y$, from non-diffractive events. In the ND case, secondary scattering usually means that the most forward part of the LAr calorimeter is the most active. Table 4.2 shows the combined efficiency of the FMD and the PRT for ND events, as well as overall efficiencies for the PD and DD processes, where $M_Y < 10\text{GeV}$, and $M_Y > 10\text{GeV}$. The efficiencies are quoted with and without the additional requirement that the largest gap in the final state rapidity distribution in the main detectors should be adjacent to the forward edge of the LAr calorimeter. Figure 4.9d shows the combined FMT and PRT efficiency for the PD and DD processes as a function of $M_Y$, with the same additional requirement.

Although the central gap cut results in a significant decrease in efficiency for PD and DD events at all masses, and almost zero efficiency for $M_Y > 10\text{GeV}$, such a cut is highly effective in the removal of non-diffractive events. Reflecting the range of acceptance of this cut, measurements in this thesis of cross-sections for processes in which the proton dissociates are corrected to $M_Y < 10\text{GeV}$.

To summarise, the cuts used in the isolation of a sample of diffractive events that are inelastic at the proton vertex are

- A forward detector signal either from the FMD or the PRT or both.
- The largest rapidity gap in the main detector must extend to the forward edge of the acceptance.

After all cuts to isolate events of types PD and DD, the sample size for the nominal vertex ToF-IA triggered data is 1033 events, and that for the shifted vertex ToF-IA triggered data is 814 events.

| | *All Events* | | *Central Gap* | |
|---|---|---|---|---|
| | *PHOJET* | *PYTHIA* | *PHOJET* | *PYTHIA* |
| *Nominal Vertex* *PD, DD* $M_Y < 10\text{GeV}$ | $66.5 \pm 1.0$ | $74.5 \pm 1.4$ | $27.7 \pm 0.9$ | $32.7 \pm 1.6$ |
| *Nominal Vertex* *PD, DD* $M_Y > 10\text{GeV}$ | $92.3 \pm 1.1$ | $87.6 \pm 2.2$ | $4.3 \pm 0.8$ | $7.3 \pm 1.7$ |
| *Nominal Vertex* *ND* | $94.4 \pm 0.3$ | $89.5 \pm 0.3$ | $0.5 \pm 0.1$ | $0.5 \pm 0.1$ |
| *Shifted Vertex* *PD, DD* $M_Y < 10\text{GeV}$ | $67.1 \pm 1.4$ | $72.0 \pm 1.5$ | $31.0 \pm 1.3$ | $37.8 \pm 1.6$ |
| *Shifted Vertex* *PD, DD* $M_Y > 10\text{GeV}$ | $92.4 \pm 1.6$ | $88.0 \pm 2.1$ | $3.5 \pm 1.1$ | $8.1 \pm 1.8$ |
| *Shifted Vertex* *ND* | $94.1 \pm 0.3$ | $90.3 \pm 0.3$ | $1.0 \pm 0.1$ | $0.6 \pm 0.1$ |

Table 4.2: *A Monte Carlo study of the combined efficiency of the Forward Detectors for PD, DD and ND events. The PD and DD events are split into low and high dissociation mass samples at* $M_Y = 10\text{GeV}$*. The first two columns show the efficiencies of the simple requirement that there should be activity in the forward detectors. The final two columns show the efficiencies with the additional requirement that the largest rapidity gap in the LAr calorimeter should extend to the Forward edge of its acceptance. The errors quoted are statistical.*

## 4.6 Reconstruction of Invariant Masses

At the centre of mass energies and dissociation masses that are considered in this analysis, the decayed system, $X$, never extends as far as the forward edge of the detector, but particularly at low masses, there are losses in the backward ($-z$) direction. A method of reconstructing invariant masses that is relatively insensitive to such losses has therefore been devised.

The invariant mass of the diffracted system is given in terms of the total 4-vector, $p_h$, of the hadronic final state associated with the photon, by

$$M_X^2 = E_h^2 - p_{x_h}^2 - p_{y_h}^2 - p_{z_h}^2 \tag{4.32}$$

Since the incident photon in the $\gamma p$ interaction at $Q^2 \simeq 0$ is collinear with the beam axis, the overall transverse momentum of the state, $X$, is zero. Equation 4.32 can then be written

$$M_X^2 = (E_h + p_{z_h})(E_h - p_{z_h}) \tag{4.33}$$

For a particle that is lost in the backward direction, $E \simeq -p_z$ so that the term, $(E_h + p_{z_h})$ is insensitive to such losses, whilst the term, $(E_h - p_{z_h})$ is maximally affected. Using equation 4.5, equation 4.33 may be re-expressed as

$$M_X^2 = 2yE_e\,(E_h + p_{z_h}) \tag{4.34}$$

The value of $y$ is then obtained from equation 4.3 using the energy measurement of the tagged electron, and $(E_h + p_{z_h})$ is measured from the full hadronic final state observed in the BEMC and LAr calorimeters, as well as the central and forward trackers, which provide more accurate momentum determination for charged tracks.

To avoid double counting of energy where a track is to be taken, the part of the calorimeter in a cylinder of radius 30cm about the extrapolated track is masked off. If the energy counted in the resulting cylinder is greater than twice that of the track, then the energy in the calorimeter cylinder is taken. Otherwise the track is used, under the assumption that it is a pion. A control plot for the number of charged tracks in each event with this reconstruction method is shown in figure 4.10a.

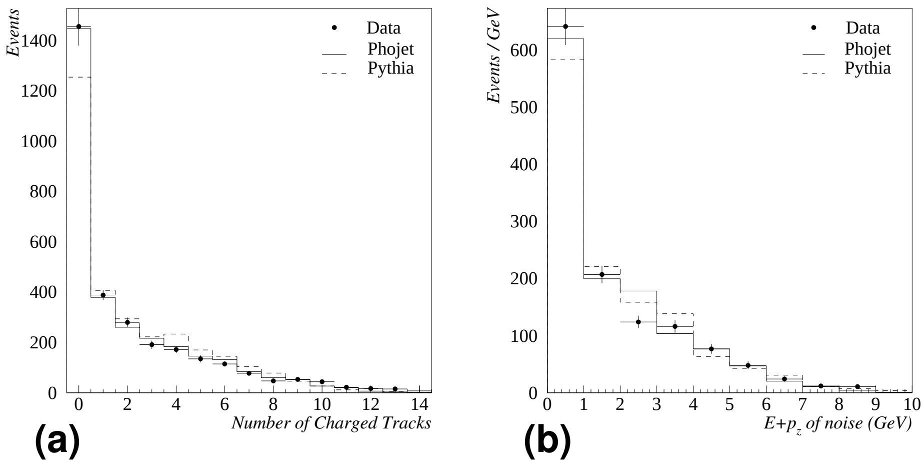


Figure 4.10: *(a) Control plot for the multiplicity of charged tracks used per event in the shifted vertex ToF-IA analysis. (b) Control plot for the $(E + p_z)$ of the LAr clusters that are taken to be noise and are not used in the reconstruction of $M_X$, in the nominal vertex z-vertex analysis.*

At low masses, the value of $M_X$, reconstructed by this method, can still be seriously affected by small amounts of noise in the forward part of the LAr calorimeter. A noise suppression technique has therefore been developed, whereby isolated low energy clusters in the forward direction, compatible with noise, are not considered in the invariant mass reconstruction. All clusters with energies greater than 700MeV are taken. For smaller energy deposits than this, a sphere of radius 30cm about the cluster is defined. If the energy in the resulting sphere is found to be less than 500MeV, the cluster is considered to be isolated, and is not used. If the energy in the sphere is greater than 500MeV, the cluster at the centre is used in the $M_X$ determination, irrespective of its energy. In the more backward region of the LAr calorimeter, the activity is highest in most events, and since $(E + p_z)_h$ is no longer maximal, the presence of noise is no longer catastrophic to the measurement of the final state mass. Where the polar angle of a cluster, $\theta > 40^o$, the threshold at which a cluster is automatically taken is relaxed from 700MeV to 300MeV. The energy required to be in the 30cm sphere for a cluster to be considered as non-isolated is changed from 500MeV to 100MeV. An example of a control plot for the $E+p_z$ of clusters that are considered to be noise by this algorithm is shown in figure 4.10b.

Scatter plots showing reconstructed masses plotted against generated masses, from a study using the PHOJET Monte Carlo, with $M_X$ reconstruction using equations 4.32 and 4.34 with noise suppression, are shown in figure 4.11. Particularly at low masses, a considerable difference in the resolution on $M_X$ is observed. Defining the resolution in $M_X$ to be given by the width, and the shift to be the mean of the $\delta$ distribution, where $\delta$ is defined as

$$\delta = \frac{M_X^{gen} - M_X^{rec}}{M_X^{gen}} \tag{4.35}$$

the remaining shifts and resolutions implicit in the $M_X$ reconstruction method have been estimated using both Monte Carlo models. With the cuts that are applied to each data sample, and both for the proton-elastic and proton-inelastic measurements, similar results are obtained. For the low mass states leading to more isotropic decay distributions, the resolution is $\sim$ 30%. At larger dissociation masses, such that the decay of the state, $X$ is limited in $p_T$, the resolution improves to $\sim$ 20%. These figures are sufficiently good for the mass distributions to be measured in six bins per decade of $M_X$, with bin sizes remaining larger than resolutions throughout.

The remaining level of losses in the $M_X$ determination is quantified as the shift in the mean of the $\delta$ distribution from zero. The proportional shift is more or less constant throughout the $M_X$ range, being approximately 7% in the nominal vertex case, and approximately 11% for shifted vertex. Accordingly, the reconstructed masses are multiplied by a universal factor of 1.07 for nominal vertex, and 1.11 where the vertex is shifted.

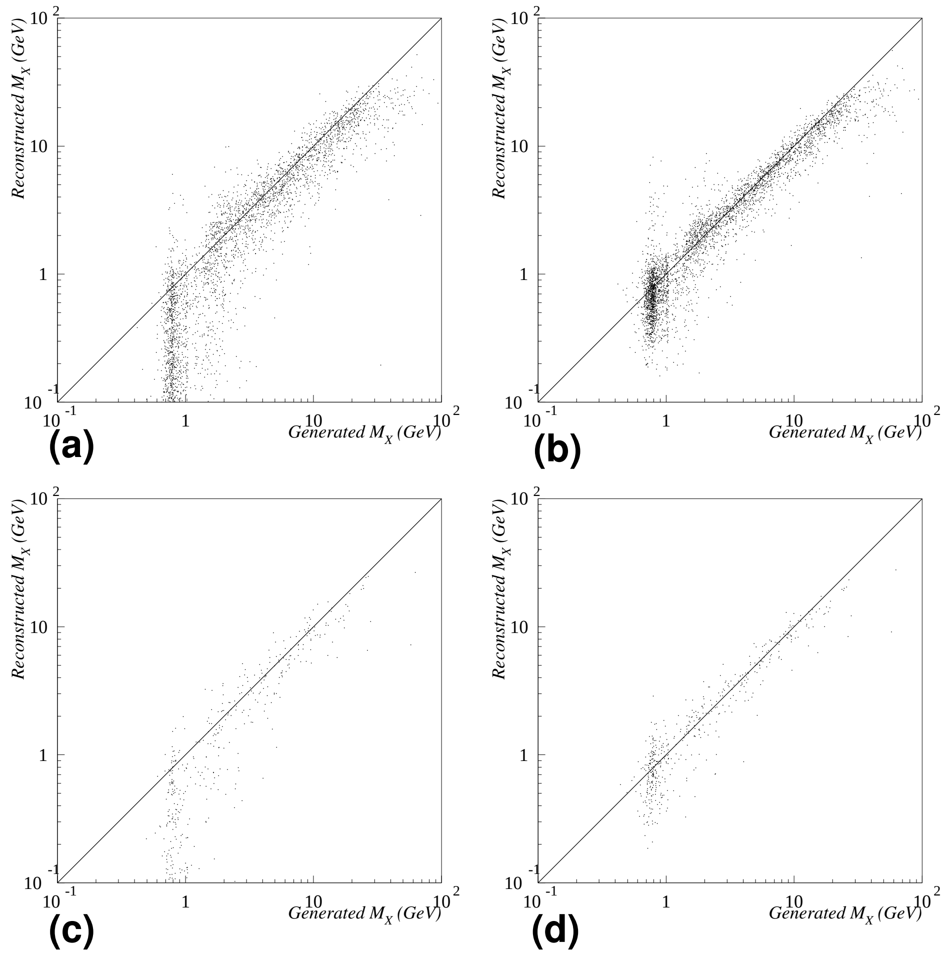


Figure 4.11: *Scatter plots of reconstructed versus generated $M_X$, using the PHOJET Monte Carlo with shifted vertex. (a) EL and GD events using equation 4.32 . (b) EL and GD events using equation 4.34 . (c) PD and DD events using equation 4.32 . (d) PD and DD events using equation 4.34 . In all cases, the same cuts as are applied in the final analysis are used.*

## 4.7 Further Corrections to the Data

After all cuts, the ToF-IA samples still contain a significant fraction of electron beam-gas background, whilst the z-vertex triggered data is comparatively pure. The pilot bunches, described in section 1.2 are used to estimate the remaining level of contamination with background from beam-gas interactions. All triggered events from bunch-crossings corresponding to pilot bunches are written to tape, and are treated in the same way throughout the trigger and reconstruction chain, as events from normal bunch crossings. Using the ratio of total to pilot bunch currents (equation 1.3), the resulting numbers of events passing cuts, that originate from the pilot bunches can be scaled to measure the contribution from beam induced background. In all cases, beam gas background is statistically subtracted on a bin by bin basis from the data samples. The resulting corrections to the z-vertex sample are negligible. In the ToF-IA samples, there is a correction at the 20% level in the very low mass part of the spectrum, where events of types EL and PD are heavily dominant. Only very small corrections are required for $M_X \gtrsim 2$GeV.

Using the pilot bunch method to subtract beam-gas background neglects second order effects for which both beams are required. For example, a proton beam-gas event depositing hadronic activity in the main parts of the detector may coincide with the detection of an off-momentum or gas-scattered electron in the luminosity tagger. For the ToF-IA triggered data, such background is negligibly small, since an interaction of a proton from the beam, with a near stationary gas particle in the vertex region, has a very low probability of producing a backward going track that will trigger the ToF. This has been verified by studying a monitor sub-trigger that requires a hit in the ToF interaction strobe, but does not require a scattered electron in the luminosity tagger. No events corresponding to proton pilot bunches are found in the monitor trigger sample. The situation for the z-vertex triggered data is somewhat more complicated, since the probability of a proton beam-gas induced event giving a central track is no longer negligible. However, proton beam-gas events give rise to significant activity at large rapidity, and the forward detector cuts applied in the GD and EL measurements remove almost all of this source of background.

Corrections must also be made for losses caused by cuts at the level 4 and level 5 stages of the trigger. As discussed in section 1.4, 1% of level 4 rejects are written to tape in a separate stream. None of the events written to the level 4 monitor tape during the run period of the measurement pass the off-line cuts imposed in the data selection, and so no correction is needed. The beam gas cuts applied to the z-vertex sample, at the off-line level 5 stage of the trigger, are stated in equations 4.19 and 4.20. The losses to the z-vertex sample, due to these cuts were estimated using the PHOJET and PYTHIA Monte Carlos. Corrections at the level of 10% are applied on a bin by bin basis for the level 5 losses, which affect both the GD and the DD measurements.

The effect of noise in the forward detectors is accounted for with a 3.4% correction, as discussed in section 4.5.4. In the case of the PD and DD measurements, the result of the noise is that a 3.4% fraction of GD and EL events are misidentified as having a dissociating final state proton system. A correction based on the measured GD and EL cross-sections is made. A correction of 7% for inefficiencies of the ToF-IA trigger bit, not described in the Monte Carlo simulation is applied to the ToF-IA samples.

# Chapter 5

# Diffractive Cross Section Measurements

## 5.1 Uncorrected Mass Distributions

After all cuts, the Monte Carlos models are compared to the data samples, in order to test the level to which the physics and detector simulations are able to describe the data. Figure 5.1 shows uncorrected mass distributions for the two ToF-IA samples, after cuts used to isolate diffractive events, both where the proton vertex is elastic, and inelastic. In all cases, clear elastic peaks and relatively smooth higher mass continua are visible. The description by the Monte Carlos of the higher $M_X$ parts of the spectra is always good. In the elastic and resonance regions, the Monte Carlo spectra show some deviations from those of the data, indicating small, but not surprising inadequacies in the event generators or detector simulations. For all acceptance corrected measurements, systematic errors, defined by half of the difference between the PHOJET and PYTHIA model predictions are applied. To within such errors, the Monte Carlo description of the data is sufficiently good at all values of $M_X$, for the PHOJET and PYTHIA models to be used to correct the data for acceptance and smearing.

## 5.2 The Cross-Section $\frac{d\sigma(\gamma p \to Xp)}{dM_X^2}$

### 5.2.1 Extraction of Differential Cross-Sections

The differential cross-section, $\frac{d\sigma}{dM_X^2}$, for diffractive events containing a leading final state proton, is extracted separately in the three largely independent samples. An $ep$ cross-

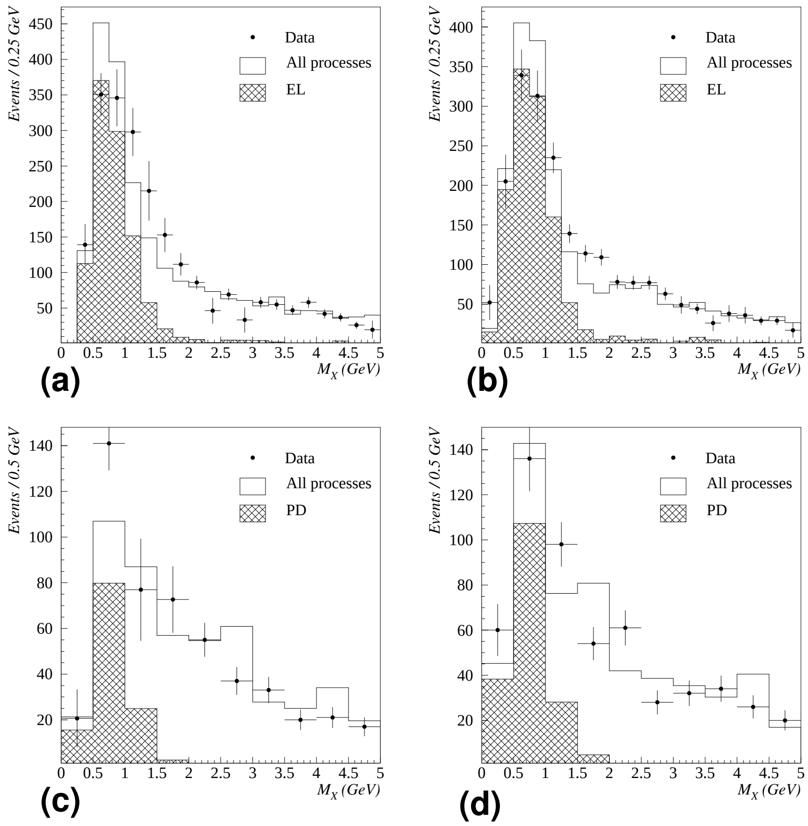


Figure 5.1: *Comparison of Monte Carlo predictions to uncorrected mass distributions at the low end of the mass spectra, after the cuts described in sections 4.5.5 and 4.5.6. PHOJET / PYTHIA averages are always used. The open histograms show the Monte Carlo predictions, after cuts, for all processes combined, and the cross-hatched histograms show those for the quasi-elastic processes at the photon vertex. (a) Nominal Vertex ToF-IA sample, GD, EL selection. (b) Shifted Vertex ToF-IA sample, GD, EL selection. (c) Nominal Vertex ToF-IA sample, DD, PD selection. (d) Shifted Vertex ToF-IA sample, DD, PD selection.*

section is obtained in each mass bin, using

$$\frac{d\sigma(ep \to epX)}{dM_X^2} = \mathcal{K}\,\frac{(\mathcal{N} - \mathcal{N}_{back})}{\mathcal{A}\,.\,\mathcal{L}\,.\,\mathcal{W}} \tag{5.1}$$

where $\mathcal{N}$ denotes the number of measured events per bin, and $\mathcal{N}_{back}$ is the estimate of the number of background events from beam-gas interactions and from the PD, DD and ND processes. $\mathcal{A}$ is the Monte Carlo estimate of the average acceptance for the bin. The effect of smearing of events between bins, due to the finite resolution on $M_X$, is also accounted for with this correction. $\mathcal{L}$ is the integrated luminosity of the measurement, and $\mathcal{W}$ is the width of the bin in $M_X^2$. Implicit in the bin width factor is also a correction for the fact that the bin centre does not correspond to the average value of $M_X$ for the data in the bin. The correction is made by modelling the data with the FMSR (section 3.4.3) and is at the 2% level. The factor, $\mathcal{K}$ accounts for all of the corrections to the data, discussed in section 4.7. An integration over $t$ is implicit in the measurement.

In order to measure a $\gamma p$ rather than an $ep$ cross-section, it is necessary to estimate the flux of quasi-real photons, $F(y, Q^2)$, emitted from the electron beam. The equation,

$$\frac{d^2\sigma^{ep}(s)}{dydQ^2} = \sigma^{\gamma p}(ys)(1+\delta_{RC})F(y, Q^2) \tag{5.2}$$

is used, where $\delta_{RC}$ is the QED radiative correction factor, and the $\gamma p$ cross-section is assumed to be independent of $Q^2$. The photon flux is given by the Weizsäcker -Williams formula [138], with modern refinements [139],

$$F(y, Q^2) = \frac{\alpha_{em}}{2\pi Q^2}\left(\frac{1+(1-y)^2}{y} - \frac{2(1-y)}{y}\frac{Q^2_{min}}{Q^2}\right) \tag{5.3}$$

with

$$Q^2_{min} = \frac{(m_e y)^2}{(1-y)} \tag{5.4}$$

In the measured range of $0.3 < y < 0.5$, the resulting flux, integrated over $y$ and $Q^2$ is calculated analytically, and found to be

$$F = \int F(y, Q^2)dydQ^2 = 9.03 \times 10^{-3} \tag{5.5}$$

The mean value of $W_{\gamma p}$ averaged over the photon flux dependence was found to be $\langle W_{\gamma p}\rangle =$ 187GeV. The value of $\delta_{RC}$ is taken to be $+1 \pm 1\%$ for the z-vertex trigger, and $-1 \pm 1\%$ for the ToF-IA trigger, as was the case in [25].

Corrections for inefficiencies of the detector, and losses due to analysis cuts, are made with an average of the acceptance calculations using the PHOJET and PYTHIA Monte Carlos. The resulting acceptances for the GD and EL processes are shown for the three data samples in figure 5.2. Residual background from other photoproduction processes is also estimated for each bin, using an average of predictions from the two Monte Carlos. In order to normalise the background to the measured processes, the relative sizes of the cross-sections for the five photoproduction sub-processes are taken to be in the ratios

$$ND : GD : PD : DD : EL = 0.5 : 0.125 : 0.075 : 0.2 : 0.1 \tag{5.6}$$

which is consistent with previous measurement [25]. The resulting estimates of the fraction of non-diffractive and proton dissociative background that remains in each of the proton-elastic samples after all cuts are shown in figure 5.3. Only bins for which overall acceptances, including those of the electron tagger, are greater than 35%, and backgrounds are less than 35%, are considered for the measurements.

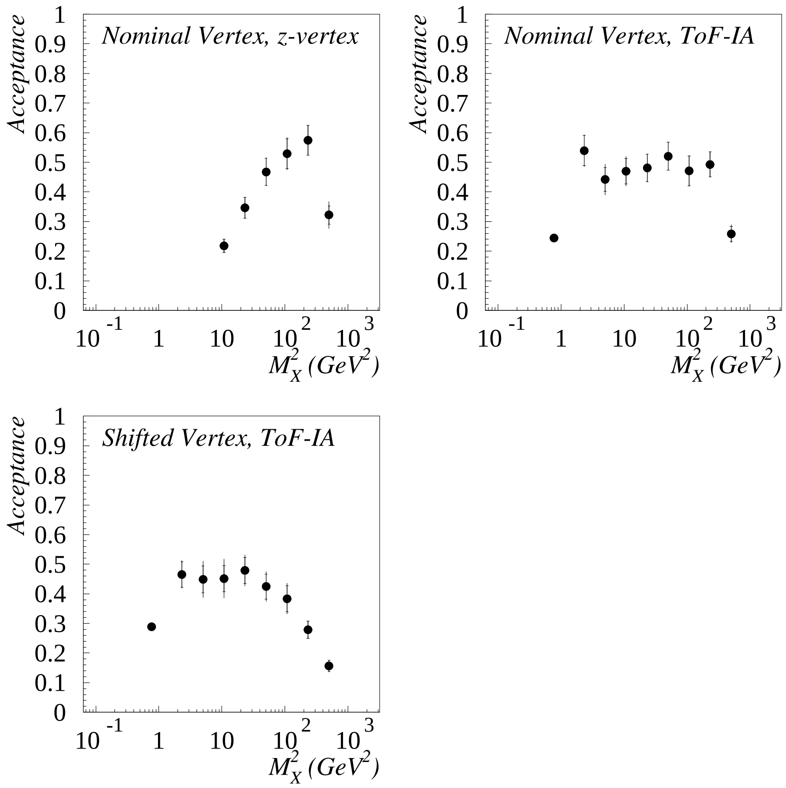


Figure 5.2: *The acceptance in each bin of $M_X$ for the GD and EL processes in each data sample. The points are averages of those obtained with the PHOJET and PYTHIA Monte Carlos. The inner error bars show the statistical errors. The outer error bars are the statistical errors added in quadrature to a systematic error equal to half of the difference between the values obtained using the two models. The acceptance of the electron tagger is included in the plots, and contributes a constant factor of* $0.61 \pm 0.03$, *irrespective of the value of* $M_X$.

The luminosities for the three samples are determined using the off-line calculation based only on the photon arising in Bremsstrahlung events, discussed in section 1.7.2. After corrections for pre-scale factors, the integrated luminosities are found to be $24.7 \pm 0.4\text{nb}^{-1}$ for the nominal vertex ToF-IA sample, $24.0 \pm 0.4\text{nb}^{-1}$ for the nominal vertex z-vertex sample, and $23.8 \pm 1.3\text{nb}^{-1}$ for the shifted vertex ToF-IA sample. The error in the nominal vertex case is dominated by the understanding of the calibration of the photon arm of the luminosity system. The larger error on the shifted vertex luminosity measurement reflects the lower level of pilot bunch statistics collected in the shorter shifted vertex run period, and required for the statistical subtraction of beam-gas background.

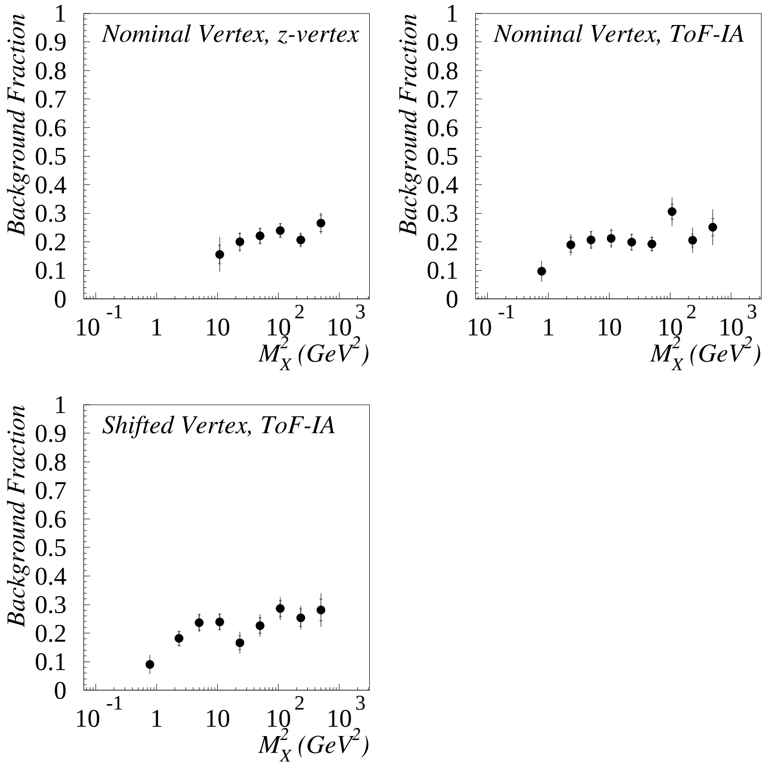


Figure 5.3: *The proportion of background that is subtracted in each bin in the proton-elastic measurement, due to contamination with events of types PD, DD and ND. The inner error bars are statistical; the outer error bars reflect the model dependence added in quadrature to the statistical error.*

### 5.2.2 Evaluation of Errors

There are two contributions to the statistical error on each measured point, arising from the finite sample size and from the finite size of the pilot bunch samples used to make beam-gas subtractions. These are added in quadrature to give an overall statistical error.

Systematic effects are considered on a bin by bin basis for each sample, by the variation of important parameters by equal amounts in either direction, about the central value assumed in the measurement. The systematic error assigned is then taken to be equivalent to half of the difference between the points obtained with the two shifts. The sources of systematic error that have been considered are listed below.

BEMC Calorimeter Energy Scale

The main purpose of the BEMC calorimeter is the detection and measurement of scattered electrons in DIS processes. The response for hadronic showers is considerably less well known than that for electromagnetic showers, and a 20% uncertainty in the hadronic energy scale is applied.

Liquid Argon Calorimeter Energy Scale

An uncertainty of 6% is assigned to the hadronic energy scale of the LAr calorimeter.

Uncertainty on Track Measurements

A 3% variation is made in the momentum scale of track measurements.

Model dependence of Acceptance Corrections

Half of the difference between the acceptances obtained using the PHOJET and PYTHIA models is taken as a systematic error.

Subtraction of Beam Gas Background

A systematic error resulting from the subtraction of beam-gas background is formed by shifting the number of events that are subtracted by 25% in either direction.

Subtraction of Background from Other Processes

Since the cross-section for the DD process is not well measured, its background subtraction can potentially give rise to a large systematic effect. To account for this possibility, the relative size of the DD cross-section, assumed in equation 5.6, is varied by 50% in either direction, mainly at the expense of the ND fraction. Smaller variations in the fractions of the other processes are also made.

Definition of the GD Process

The dissociation mass spectrum for the GD process is assumed by both Monte Carlos to begin at $M_{X_0} \sim 1$GeV. A systematic error is formed by taking a 20% variation in this figure.

Assumptions on Dissociation Mass Spectra

Both PHOJET and PYTHIA assume a distributions in $M_X$ and $M_Y$ beyond resonance regions similar to $d\sigma/dM^2 \sim 1/M^2$. GD and DD processes in the Monte Carlos are reweighted at all masses by $(1/M_X^2)^{\pm 0.15}$, and a systematic error is assigned accordingly. A further error is formed by reweighting PD and DD events by factors $(1/M_Y^2)^{\pm 0.3}$.

Assumption of $t$ dependences

The Monte Carlos have exponential $t$ distributions, $e^{bt}$, with slope parameters, $b \sim 11$ for EL, $b \sim 5$ for GD and PD, and $b \sim 2$ for DD. Systematic errors are formed by varying $b$ by $\pm 2$ units for EL, $\pm 1$ unit for GD and PD, and $\pm 0.5$ units for DD.

Monte Carlo Statistics

Statistical errors due to the limited Monte Carlo sample sizes available are included in the systematic errors.

The sources of error discussed above affect the measurement in ways that vary from bin to bin. Systematic effects due to errors in the luminosity measurement, and the calculation of the acceptance of the electron tagger, shift all points by a constant factor.

Luminosity Measurement

The errors on the luminosities for the three samples result in systematic errors on each measured point of 1.7% for the nominal vertex ToF-IA sample, 1.8% for the nominal vertex z-vertex sample, and 5.4% for the shifted vertex ToF-IA sample.

Acceptance of the Electron Tagger

As discussed in section 4.4.2, a figure of 5% is assumed for the systematic error on the acceptance of the electron tagger, averaged over the different periods of beam optics, and the measured range in $y$.

### 5.2.3 Combination of Measurements

Figure 5.4 shows a comparison of the differential cross-sections measured in the three different samples. For the most part, they agree to within the level of statistical errors. Due to the small correlation between the two nominal vertex samples, discussed in section 4.4.1, only one of the nominal vertex measurements can be used in combining to a final point. The two ToF-IA measurements are therefore combined to make the final points, and the results obtained with the z-vertex sample provide a cross-check.

Points are obtained from combinations of the separate measurements, $\{x_i \pm \sigma_i\}$, such that the best value is given by

$$\bar{x} = \frac{\sum \frac{x_i}{\sigma_i^2}}{\sum \frac{1}{\sigma_i^2}} \tag{5.7}$$

and the weight given to each measurement is in proportion to the inverse of the statistical variance. The statistical error on the best value, $\bar{x}$, is then given by

$$\sigma^2(\bar{x}) = \frac{1}{\sum \frac{1}{\sigma_i^2}} \tag{5.8}$$

To evaluate the systematic errors on the averaged points, the full measurement and combination of points is made with each systematic shift imposed, and each systematic error

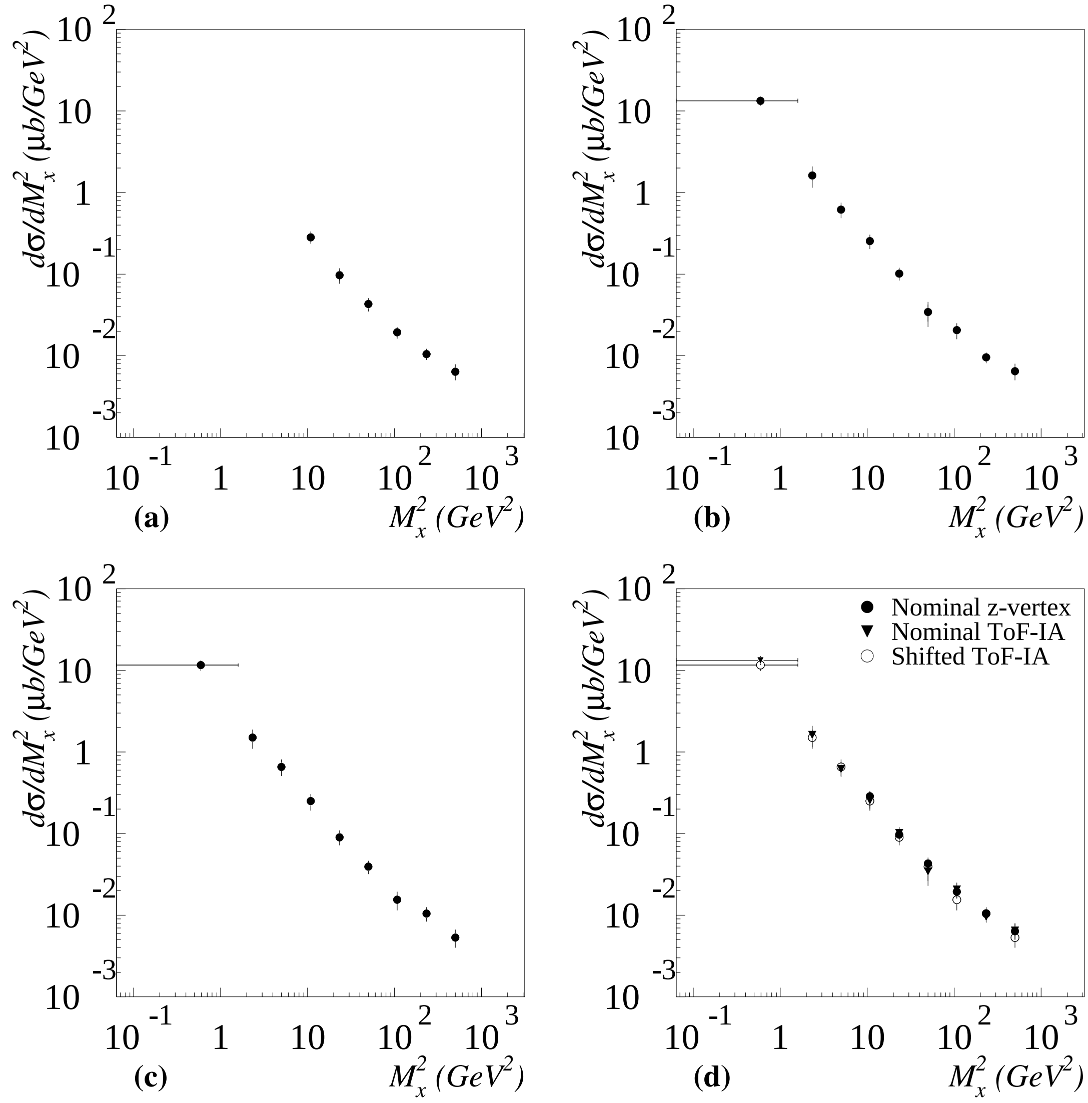


Figure 5.4: *Comparison of points measured for the differential cross-section,* $\frac{d\sigma}{dM_X^2}$*, for diffractive processes in which the proton remains intact, using the three different data samples. a) The nominal vertex z-vertex sample. b) The nominal vertex ToF-IA sample. c) The shifted vertex ToF-IA sample. d) Points from all three samples superimposed. In each case, the first bin is dominated by the EL process, and is plotted at the* $\rho$ *mass, with error on the* $M_X$ *value equal to the bin width. The mass dependence in the remaining bins is assumed to be smooth, and the value is plotted at the centre of the bin in* $\log M_X^2$*, with no error in* $M_X$*.*

is obtained from the resulting shifts in the averaged points, $\{\bar{x}\}$. Combining the measurements in this way leads to a significant decrease in statistical errors, with systematic errors on the averaged points comparable to those in the separate samples.

| *BIN* | $M_X^2$ (GeV$^2$) | *Bin Width* (GeV$^2$) | $\frac{d\sigma}{dM_X^2}$ ($\mu$bGeV$^{-2}$) | *Stat Error* ($\mu$bGeV$^{-2}$) | *Sys Error* ($\mu$bGeV$^{-2}$) |
|---|---|---|---|---|---|
| 1 | 0.593 | 1.58 | 12.3 | 0.5 | 1.4 |
| 2 | 2.33 | 1.83 | 1.51 | 0.08 | 0.37 |
| 3 | 5.01 | 3.92 | 0.646 | 0.031 | 0.112 |
| 4 | 10.8 | 8.50 | 0.252 | 0.014 | 0.045 |
| 5 | 23.3 | 18.3 | 0.0973 | 0.0068 | 0.0138 |
| 6 | 50.1 | 39.5 | 0.0386 | 0.0029 | 0.0058 |
| 7 | 108 | 84.9 | 0.0176 | 0.0013 | 0.0036 |
| 8 | 233 | 183 | 0.00976 | 0.00056 | 0.00126 |
| 9 | 501 | 394 | 0.00601 | 0.00037 | 0.00125 |

Table 5.1: *Details of the final points measured, and of the statistical and systematic errors. The first bin is quoted at the $\rho$ mass. The remainder are quoted at the bin centres in* $\log M_X^2$.

The differential cross-section, obtained by this method of combination, is shown in figure 5.5. Full details for each bin are given in table 5.1. The systematic error on the first point is dominated by the beam gas subtraction (6.9%) and uncertainty in modelling (5.7%). The fractional systematic error on the second point is significantly larger than that on any of the others. The dominant sources are the BEMC energy scale (16.4%) and the assumption of the lowest $M_X$ value for the GD process (11.5%). At larger $M_X$, the systematic error is dominated by the background subtraction of other processes ($\sim 10\%$), the $M_X$, $M_Y$ and $t$ dependences assumed by the Monte Carlos ($\sim 10\%$ combined), and the model dependence ($\sim 5\%$).

The possibility of unforeseen systematic effects is investigated by performing the measurement in two different ranges of $\gamma p$ centre of mass energy. For $0.3 < y < 0.4$, or $0.4 < y < 0.5$, the points are stable to $\sim 10\%$, which is at the level of the statistical errors. No systematic trends in the changes to the points are observed in either range. The sensitivity of the results to the multiplicative factors of 1.07 and 1.11, applied in the $M_X$ reconstruction (section 4.6) has also been studied. If the factor is entirely removed, none of the final points change by amounts that are larger than the statistical error.

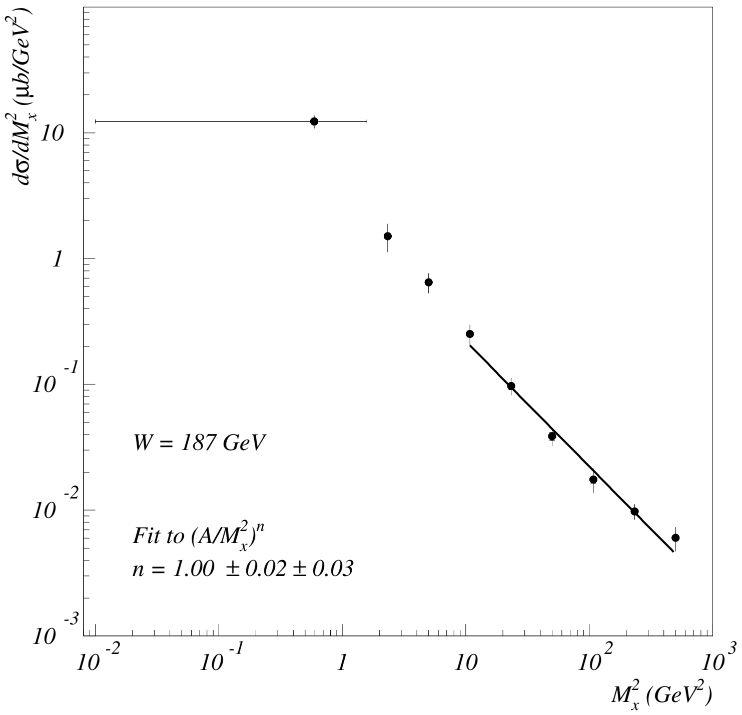


Figure 5.5: *The final points obtained for the cross-section, $\sigma(\gamma p \rightarrow Xp)$, by combination of results from the three samples. For bins such that $M_X^2 > 7.3\mathrm{GeV}^2$, a fit to the form, $\frac{d\sigma}{dM_X^2} = (A/M_X^2)^n$ is made. This is based on the triple Regge prediction of equation 3.34 , with experimental integration over $t$.*

### 5.2.4 The Mass dependence of Diffractive Dissociation

From equation 3.35, at fixed centre of mass energy, the differential cross-section for the GD process at large $M_X$ may be approximated as

$$\frac{d\sigma}{dM_X^2} \sim \left(\frac{1}{M_X^2}\right)^n \tag{5.9}$$

where $n$ is an effective value for the pomeron trajectory in the measured kinematic range. $n$ takes a lower value than the intercept of the trajectory, $\alpha_{I\!P}(0)$, due to the finite values of $t$ at which the measurement takes place. Integrating equation 3.35 over $t$ with $\alpha' = 0.25\mathrm{GeV}^{-2}$ and $4 < b < 8\mathrm{GeV}^{-2}$ sets the limits

$$n + 0.07 < \alpha_{I\!P}(0) < n + 0.13 \tag{5.10}$$

For $M_X^2 > 7.3\mathrm{GeV}^2$, by which stage the triple Regge limit is reached, the final points are fitted to the form of equation 5.9. A value is obtained for the $t$ averaged trajectory of

$$n = 1.00 \pm 0.02(stat) \pm 0.03(sys) \tag{5.11}$$

The principal sources of systematic error on this measurement arise from the BEMC and LAr energy scale uncertainties (1.9% and 1.2% respectively), the model dependence (0.8%) and the assumed $M_X$ dependence used in the Monte Carlo models (0.7%). The $\chi^2$ of the fit was 3.82, with 4 degrees of freedom.

The values obtained separately for the averaged trajectory in each of the three individual samples are

$$n = 1.01 \pm 0.03(stat) \pm 0.03(sys) \quad \text{(Nominal Vertex ToF–IA)} \tag{5.12}$$
$$n = 0.99 \pm 0.04(stat) \pm 0.03(sys) \quad \text{(Shifted Vertex ToF–IA)} \tag{5.13}$$
$$n = 1.01 \pm 0.03(stat) \pm 0.04(sys) \quad \text{(Nominal Vertex z–vertex)} \tag{5.14}$$

When the data are divided into two ranges in $y$, the measurement of $n$ is also found to be stable to within statistical errors.

## 5.3 The Cross-Section $\frac{d\sigma(\gamma p \to XY)}{dM_X^2}$

In figure 4.9d, the acceptance of the cuts used in the selection of diffractive events in which the proton dissociates was shown to be small. The result is that the measurement of cross-sections for the DD and PD processes is substantially less accurate than that for GD and EL. Additionally, the requirement that none of the dissociating proton system is observed in the main components of the detector restricts the analysis to comparatively low values of $M_Y$. Attempts to select DD events at higher $M_Y$ by searching for large rapidity gaps in the main calorimeter, closed at both ends by hadronic activity, have proved fruitless, since the gaps tend to be small and the resulting topologies are often indistinguishable from those of non-diffractive events. The differential cross-section for diffractive events in which the proton dissociates is measured and corrected to $M_Y < 10$GeV. The low $M_X$ part of this cross-section may be interpreted in terms of the PD process, whilst the higher $M_X$ part corresponds to DD. The method of extracting a $\gamma p$ cross-section is identical to that used in the case where the proton vertex is elastic, and is described in section 5.2.1.

All of the systematic errors considered in the measurement of the GD and EL cross-sections also apply to the measurement where the proton dissociates. Since the acceptance corrections are large, the systematic errors are dominated by Monte Carlo uncertainties, in the form of the $M_X$, $M_Y$ and $t$ dependencies, as well as the PHOJET / PYTHIA model dependence and the statistical Monte Carlo error.

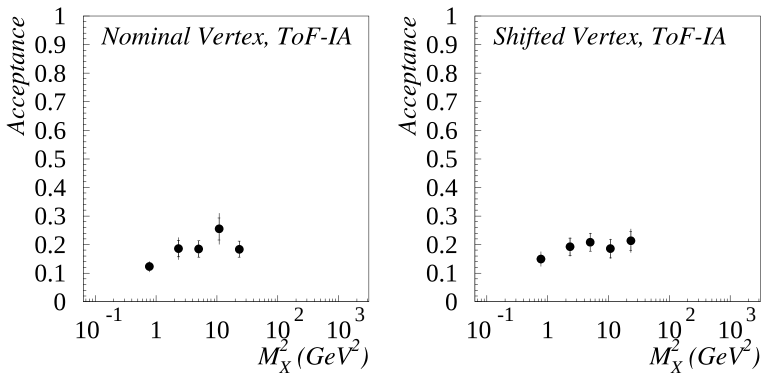


Figure 5.6: *The overall acceptance, including that of the electron tagger, for the proton dissociation measurement in each $M_X$ bin for the two ToF-IA samples. The points are averages of those obtained with the PHOJET and PYTHIA Monte Carlos. The inner error bars show the statistical errors. The outer error bars are the statistical errors added in quadrature to a systematic error equal to half of the difference between the values obtained using the different models.*

The backgrounds from the GD, and EL processes are relatively well understood, and are less than 10% at all values of $M_X$. Non-diffractive background is less well understood, and becomes increasingly important with decreasing rapidity gap size. The measurement is therefore restricted to small values of $M_X (< 5.8\text{GeV})$, under which circumstances, the rapidity gap between the systems $X$ and $Y$ is kinematically forced to be large. At such values of $M_X$, only the two ToF-IA samples can be used. The acceptances for the proton dissociation measurement are shown for each mass bin in figure 5.6, and can be seen to be rather flat in the measured range. The differential cross-sections measured in the separate samples are shown in figures 5.7a and 5.7b, and are superimposed in the same plot in figure 5.7c. Final points are obtained from weighted averages of measurements using the two ToF-IA samples, in the manner described in section 5.2.3. The combined points are shown in figure 5.7d, and full details of the measured differential cross-section and its errors are given in table 5.2.

The fractional systematic errors for the measurement of cross-sections in which the proton dissociates are significantly larger than those where the event is elastic at the proton vertex. In the low mass bins, the dominant sources of error are the model dependence, BEMC energy scale uncertainty, start point for the DD process in $M_X$, and the back-

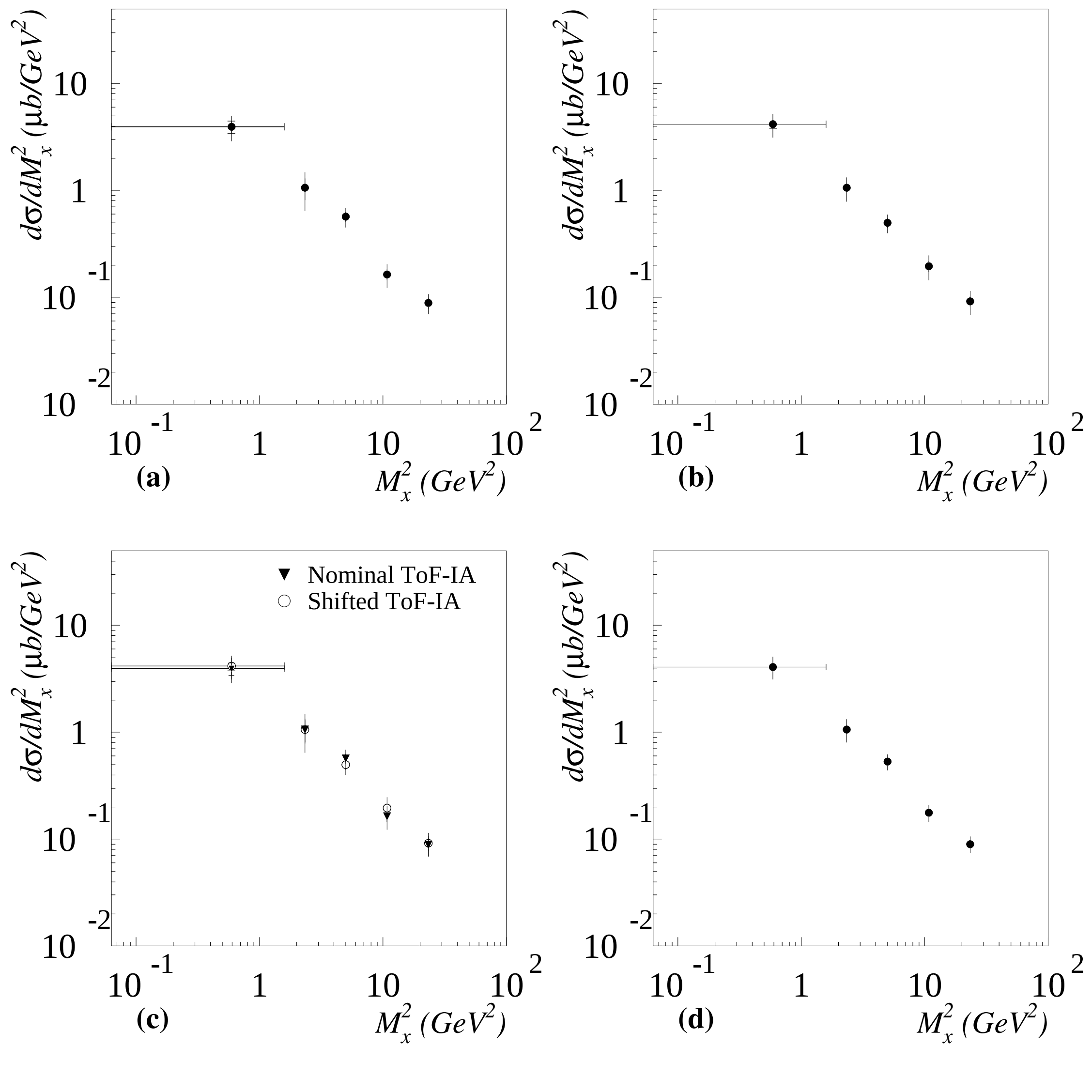


Figure 5.7: *Comparison of points measured for the differential cross-section,* $\frac{d\sigma}{dM_X^2}$*, for the process,* $\gamma p \rightarrow XY$*. a) The nominal vertex ToF-IA sample. b) The shifted vertex ToF-IA sample. c) Points from both samples superimposed. d) Combined points.*

| *BIN* | $M_X^2$ ($\mathrm{GeV}^2$) | *Bin Width* ($\mathrm{GeV}^2$) | $\frac{d\sigma}{dM_X^2}$ ($\mu\mathrm{bGeV}^{-2}$) | *Stat Error* ($\mu\mathrm{bGeV}^{-2}$) | *Sys Error* ($\mu\mathrm{bGeV}^{-2}$) |
|---|---|---|---|---|---|
| 1 | 0.593 | 1.58 | 4.10 | 0.29 | 0.93 |
| 2 | 2.33 | 1.83 | 1.06 | 0.10 | 0.24 |
| 3 | 5.01 | 3.92 | 0.530 | 0.039 | 0.082 |
| 4 | 10.8 | 8.50 | 0.177 | 0.014 | 0.029 |
| 5 | 23.3 | 18.3 | 0.0901 | 0.0074 | 0.0140 |

Table 5.2: *Details of the final points measured, and the statistical and systematic errors for diffractive processes in which the proton dissociates. All points are made from weighted averages of the values obtained with the two ToF-IA samples.*

ground subtractions of other photoproduction processes. At larger masses, the $M_X$ and $t$ dependencies of the Monte Carlo, the model dependence and Monte Carlo statistics give the largest contributions to the error.

## 5.4 Total Diffractive Cross-Sections

From the differential cross-sections, measurements of total cross-sections for diffractive sub-processes may be inferred. The PHOJET and PYTHIA Monte Carlos are used to separate the GD from the EL and the DD from the PD components, and to correct for the unmeasured regions of phase-space. Each correction is made using an average of the PHOJET and PYTHIA models, and a systematic error equal to half of the difference between the two models is assigned.

In the proton-elastic measurement, the corrections required are small. The EL cross-section is obtained from the first $M_X$ bin, after subtracting a fraction, $5.7 \pm 0.5\%$ to account for GD events. The resulting elastic cross-section, defined as discussed in section 4.2, is found to be

$$\sigma^{\gamma p \to Vp}_{W_{\gamma p}=187\mathrm{GeV}} = 18.2 \pm 0.8(stat) \pm 1.9(sys)\ \mu\mathrm{b} \qquad (5.15)$$

The systematic error is obtained by making the full measurement with each systematic shift, and arises principally from the beam-gas background subtraction (6.9%) and the model dependence (5.7%). The measured value for the EL cross-section is consistent with that found in a separate analysis, using the low mass part of the shifted vertex ToF-IA sample [132]. In that analysis, a cross-section for $\gamma p \to \rho^0 p$, is extracted, with a proper treatment of $\omega$ and $\phi$ background, and of interference between resonant $\rho$ production, and the non-resonant process, $\gamma p \to \pi^+\pi^- p$. The value for the resonant elastic $\rho$ cross-section is found to be $13.6 \pm 0.8(stat) \pm 2.4(sys)$ $\mu$b

The GD cross-section is estimated by summing the measured cross-sections from all $M_X$ bins except the first. The fraction, $5.7 \pm 0.5\%$, of the cross-section in the first bin, that is assumed to arise from the GD process, is added. The total cross-section in the measured region is found to be

$$\sigma^{\gamma p \to X p}_{W_{\gamma p}=187\mathrm{GeV}\ ,\ M_X<27.1\mathrm{GeV}} = 17.5 \pm 0.4(stat) \pm 2.4(sys)\ \mu\mathrm{b} \tag{5.16}$$

The statistical errors are given by the sum in quadrature of the statistical errors on each bin. The largest contributions to the systematic error arise from the subtraction of background from other processes (8.0%) and the $M_X$ and $M_Y$ dependences of the Monte Carlos (8.4%).

In order to correct the total cross-section to $\xi < 0.05$, in line with previous measurements, a correction factor of $12.5 \pm 1.5\%$ is applied, to account for the part of the cross-section that lies outside the measured range. The total GD cross-section is then

$$\sigma^{\gamma p \to X p}_{W_{\gamma p}=187\mathrm{GeV}\ ,\ \xi<0.05} = 19.8 \pm 0.4(stat) \pm 2.7(sys)\ \mu\mathrm{b} \tag{5.17}$$

Dividing the measurement into two ranges in $y$ yields variations in the measured value of the EL cross-section that are slightly larger than the statistical error, but are well contained by the overall error. The variations in the value of the GD cross-section are found to be well within the statistical error. This is also the case when the measurement is performed using any of the three separate samples on its own.

The measurement of the differential cross-section where the proton dissociates allows an extraction of the PD cross-section, and a very limited extraction of that for the DD process. By subtracting a quantity $14.2 \pm 1.4\%$ from the cross-section in the first $M_X$ bin, to correct for DD events, the cross-section for PD in the measured $M_Y$ range is found to be

$$\sigma^{\gamma p \to VY}_{W_{\gamma p}=187\mathrm{GeV}\ ,\ M_Y<10\mathrm{GeV}} = 5.5 \pm 0.4(stat) \pm 1.2(sys)\ \mu\mathrm{b} \tag{5.18}$$

The principal sources of systematic error are the model dependence (12.7%), the assumed starting point of the invariant mass spectrum of GD events (12.2%) and the background subtraction from other processes (6.9%). Multiplying this cross-section by a factor, $1.71 \pm 0.28$ in order to correct to $\xi_Y < 0.05$, a value is obtained for the total cross- section for the PD process

$$\sigma^{\gamma p \to VY}_{W_{\gamma p}=187\mathrm{GeV}\ ,\ \xi_Y<0.05} = 9.4 \pm 0.7(stat) \pm 2.8(sys)\ \mu\mathrm{b} \tag{5.19}$$

The sensitivity of this figure to the value of $M_Y$ to which the original measurement is corrected has been investigated, by performing the full measurement, with an initial correction to $M_Y < 6\mathrm{GeV}$. The change to the overall PD cross-section is at the 10% level.

The cross-section for the DD process in the measured range is evaluated in the same way as the GD cross-section is extracted. It is found to be

$$\sigma^{\gamma p \to XY}_{W_{\gamma p}=187\mathrm{GeV}\,,\,M_Y<10\mathrm{GeV}\,,\,M_X<5.8\mathrm{GeV}} = 8.1 \pm 0.3(stat) \pm 0.7(sys)\ \mu\mathrm{b} \tag{5.20}$$

The restriction of the DD measurement to low values of $M_X$ and $M_Y$ ensures that the background subtraction and model dependence systematic errors are small. The dominant sources of error arise from the Monte Carlo $M_X$ and $M_Y$ dependences (5.8%) and the $t$ dependence (4.2%).

Since the DD cross-section is measured in a very limited range of $M_X$ and $M_Y$, any extrapolation to a total cross-section for the process must be heavily model dependent, and should be treated with caution. There is no direct experimental evidence to support the parameterisations that are used by either Monte Carlo, but if the $M_X$ and $M_Y$ dependences are assumed to be approximately correct, the two models are in surprisingly good agreement about the fraction of the total DD cross-section that lies outside the measured range. Since there are significant differences between the two models, this must to some extent be coincidental. If the average of the PHOJET and PYTHIA models is taken to make the extrapolation, then the cross-section in the measured range should be multiplied by a factor $2.7 \pm 0.2$ to obtain a full cross-section for the process bounded by $\xi < 0.05$ and $\xi_Y < 0.05$. The resulting DD cross-section would then be

$$\sigma^{\gamma p \to XY}_{W_{\gamma p}=187\mathrm{GeV}\,,\,\xi<0.05\,,\,\xi_Y<0.05} = 21.8 \pm 0.9(stat) \pm 2.5(sys)\ \mu\mathrm{b} \tag{5.21}$$

though the quoted systematic error does not give a true reflection of the uncertainty. When the measurement is remade, with a correction in the first instance to $M_Y < 6\mathrm{GeV}$, the change in the resulting estimate of the overall DD cross-section changes by approximately 1.5 statistical standard deviations.

## 5.5 Discussion

Although cross-sections for elastic $\rho^0$ and $J/\psi$ photoproduction have previously been measured at HERA [132] [121], the analysis presented here is the first detailed study of diffractive dissociation in the real photon$-$proton system. The main limitation on the precision with which cross-sections for the GD and EL processes have been measured, both here and elsewhere, is the understanding of the proton dissociation background. Experimental conditions dictate that only very limited measurements of the PD and DD cross-sections are possible, but the constraints that have been placed on their sizes here will facilitate a reduction in systematic errors in future analyses.

In [25], total cross-sections for three of the four sub-processes of diffractive photoproduction were extracted, by an entirely different method, but with similar data samples to those used in this measurement. The definition of the EL process was identical to that used here. Dissociative processes were corrected to $\xi < 0.1$ and $\xi_Y < 0.1$, which results in a difference in the measured cross-sections at the 10% level. The EL, GD and PD cross-sections were measured as a function of the DD cross-section, which was assumed to lie in the range, $0 < \sigma_{DD} < 40\mu b$. The estimate of the DD cross-section in this analysis indicates that its value lies in the middle of the range proposed in [25]. If the DD cross-section measured here is assumed, then the EL and GD cross-sections found in the two analyses are consistent at the level of statistical errors. The PD cross-section is larger here, but remains consistent within systematic errors.

The total GD and EL cross-sections measured in this analysis are consistent with those in the previous analysis for most values of $\sigma_{DD}$. The PD cross-section is larger here, and is consistent within full errors only for $\sigma_{DD} \lesssim 26\mu$b.

| *PROCESS* | *EL* | *GD* | *PD* | *DD* |
|---|---|---|---|---|
| *This Analysis* | $18.2 \pm 2.1$ | $19.8 \pm 2.7$ | $9.4 \pm 2.9$ | $21.8 \pm 2.7$ |
| *Previous H1 Analysis* | $17.1 \pm 4.3$ | $21.3 \pm 10.4$ | $7.8 \pm 3.4$ | $18.0 \pm 18.0$ |
| *CKMT* | 17 | 23 | 6 | 14 |
| *SaS* | 16 | 12 | 9 | 12 |
| *GLM* | 17 | 16 | 14 | 14 |

Table 5.3: *Two H1 Measurements of the cross-sections for the four diffractive photoproduction sub-processes, quoted in* $\mu$b *and compared to predictions. The results from this analysis are at* $\langle W_{\gamma p} \rangle = 187$GeV. *Those from the previous analysis [25] , are at* $\langle W_{\gamma p} \rangle = 200$GeV. *The quoted errors for both analyses are the statistical and systematic errors added in quadrature. All figures in the table are scaled to* $\xi < 0.05$ *and* $\xi_Y < 0.05$. *The figures quoted for the PD, and in particular, the DD cross-section, for this analysis are based on measurements in a very limited kinematic range, and rely heavily on Monte Carlo corrections to extrapolate to the full range in* $M_X$ *and* $M_Y$. *The quoted DD figure for the previous H1 measurement was not measured, but assumed.*

Table 5.3 shows a comparison of total cross-section measurements from this analysis with those of [25], and to three Regge inspired phenomenological models, which make varying assumptions for the forms of the differential cross-sections, and for the couplings of the pomeron to external particles. The model of Schuler and Sjöstrand (SaS) [140] is essentially that implemented in PYTHIA, and is described in section 4.3.1, with the differential cross-sections for the four diffractive sub-processes given by equations 4.13– 4.16. The photon couplings to the pomeron are derived from those of the $\rho$, $\omega$ and $\phi$ mesons using the simple VDM. For the $M_X$ and $M_Y$ dependences of the PD, GD and DD processes, a critical pomeron is assumed. Like SaS, Gotsman, Levin and Maor (GLM) [141] derive a prediction for the EL cross-section, via the optical theorem, from Donnachie Landshoff type fits to the total cross-section. For the GD cross-section, the same supercritical pomeron is used as is implied by fits to total and elastic cross-sections. In order to obtain predictions for the remaining sub-processes, the relations,

$$\sigma_{PD} = \frac{2\sigma_{GD}}{3} \tag{5.22}$$

$$\sigma_{DD} = \frac{\sigma_{GD}\ \sigma_{PD}}{\sigma_{EL}} \tag{5.23}$$

are used, both of which arise from the additive quark model. Capella, Kaidalov, Merino and Tran Thanh Van (CKMT) have extended their model of diffractive dissociation in DIS [142] to make predictions for the photoproduction regime. Calculations are explicitly made for each of the four sub-processes, based on a supercritical pomeron with large absorptive corrections.

The EL cross-section measured in this analysis is well reproduced by all three of the models. The two single dissociation cross-sections are less well predicted, and all three models anticipate a value for the DD cross-section which is smaller than that obtained in the current analysis by at least 35%.

A comparison of the differential cross-section, $\gamma p \to Xp$, throughout the measured range in $M_X$ (figure 5.5), to a typical measurement for $pp \to Xp$ (figure 3.9), shows qualitatively a similar behaviour. A strong elastic peak at low $M_X$ is observed, which falls sharply through the resonance region, until the data are well described at large $M_X$ by the triple Regge behaviour, $d\sigma/dM_X^2 \sim 1/M_X^2$. Since $t$ is not measured in this analysis, a detailed study of the data in the framework of the FMSR is not possible. However, the highly significant departure of the data from a $1/M_X^2$ behaviour at low $M_X$ indicates that the effective incoming photon mass of equation 3.39 is finite.

From the $M_X$ dependence in the triple Regge region of the differential cross-section, $\gamma p \to Xp$, an effective $t$ averaged value for the pomeron trajectory was obtained (equation 5.11), and found to be entirely consistent with that expected for the universal soft pomeron from hadron-hadron interactions. Since no hard scales are present in diffractive photoproduction processes, it comes as no surprise that there is no evidence for a harder pomeron, such as that discussed in section 3.5. The measured value for the pomeron intercept is found to be consistent with those extracted from the $W_{\gamma p}$ dependence of the total and exclusive $\rho^0$ photoproduction cross-sections. The value is within $\sim 1\sigma$ of that obtained from the $x_{I\!P}$ dependence of diffractive DIS data [126], though there is a significant difference if ZEUS results [128] are taken into account.

# Chapter 6

# The Forward Muon Trigger

This chapter is concerned with the trigger processor that uses the information from the Forward Muon Detector (FMD), described in section 1.9.1, to provide information about high momentum forward going muons to the first level of the central trigger (CTL1). The hardware implementation of the trigger is first surveyed, and the track-finding algorithms that are used are then described. The current mode of operation of the trigger is explained, and its acceptance is studied using simulations of single muons. A review of physics processes that lead to muons within the identified range of acceptance follows, along with the prospects for making measurements with the FMD.

## 6.1 Overview of the Forward Muon Trigger

The Forward Muon Trigger (FMT) [143] uses the $\theta$ planes of the FMD, to provide a fast decision for the first level trigger. It must discriminate muon tracks originating from $ep$ interactions from an overwhelming level of background, from

- High rapidity proton fragments, both from $ep$, and beam gas interactions.
- Beam halo muons.
- Cosmic muons.
- Synchrotron radiation from the electron beam.
- Muons from $\pi$ or K decays in the main detector.
- Electronic noise.

The requirement that a track should point to the nominal interaction vertex region is sufficient to reduce all sources of background to tolerable levels. Half of the trigger elements sent to CTL1 relate to full tracks, passing through all four $\theta$ planes of the FMD, and the other half are activated by pre-toroid track segments only. If possible, the trigger should provide T0 information, uniquely identifying a muon track with a bunch-crossing. More detailed information is sent to the level 2 and level 3 stages of the central trigger.

Pipelining (section 1.4) is implemented in the FMT by the use of digital shift registers. These are shifted serially, one bit at a time, by a clock that is phase-locked to the HERA RF signal. Buffer registers, which are also strobed with the HERA clock, store the trigger information until a readout instruction arrives, whereupon the pipelines are rewound, and all trigger data are read out for monitoring purposes. A decision from the FMT is required to reach the central trigger within 22 bunch-crossings ($2.1\mu$s) of an interaction. After the flight time of muons from the vertex, drift times in the FMD cells, and unavoidable cable delays have been taken into account, only $\sim 300ns$ remain for the trigger logic. In the FMT, the pipelines are clocked at double the bunch-crossing frequency, in order to increase spatial hit resolution, and to allow for more logical steps in the trigger electronics.

The implementation of the trigger is effected, mainly by the use of two semi-custom Application Specific Integrated Circuits (ASICs) [144], and the hardware is field programmable at all stages of the algorithm. A reconstruction is effectively performed on-line[1], so that only combinations of hits that are consistent with a track originating from the nominal vertex region are accepted[2]. In order to standardise the electronics, all four $\theta$ planes of the FMD are treated identically by the trigger, irrespective of the numbers of cells that they contain. This is achieved by the ORing together of information from the outer cells of the post-toroid planes, and by the presence of null chambers in $\theta 1$.

The input information to the trigger arrives in analogue format from the pre-amplifiers of the FMD. Signals pass through three distinct modules in their processing by the FMT. The first of these is the *Discriminator module*, which is responsible for digitising the signals. The second is called the *Road Finder Module* (RFM), and identifies tracks within a single octant of the FMD. The RFMs contain on-board RAM, so that simulations, and tests of the trigger programming can take place with known input signals. The final stage is the *Final Decision Module* (FDM), where information from different octants is

[1]Philosophically, the track reconstruction method used by the trigger is similar to that used by the off-line reconstruction of FMD information (section 1.9.3). The main restrictions in the case of the trigger are that the $\phi$ layers are not used, and that tracks passing between octants during their flight through the system cannot be triggered.

[2]The trigger may also be programmed to accept tracks from cosmic or beam halo muons. Samples of such tracks, triggered by the FMT have been particularly useful for calibration and acceptance studies, both of the FMD, and of other sub-detectors.

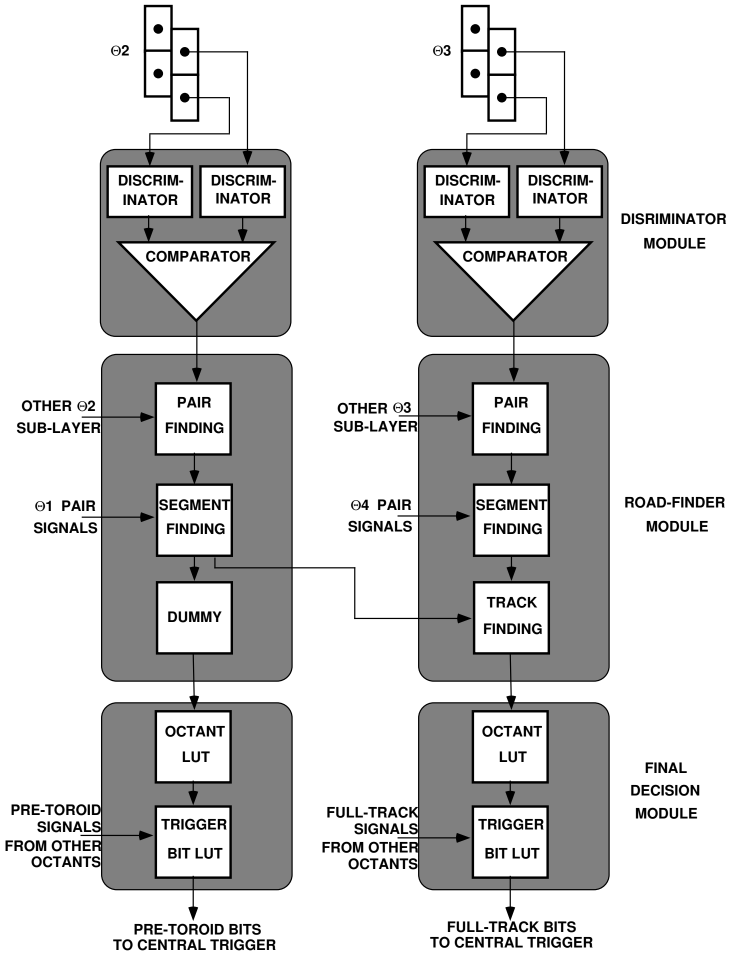


Figure 6.1: *Block diagram of the Forward Muon Trigger.*

combined to produce the final trigger elements that are sent to the level 1 trigger. A block diagram, showing the passage of information through the FMT, is shown in figure 6.1. A brief description of the various logical stages is given here. Fuller details can be found in [145]. The integration of the FMT with the central trigger and data acquisition systems is described in [146].

### 6.1.1 The Discriminator Modules

The analogue input signals to the trigger pass first through the discriminator module, where a single discriminator circuit receives information from two chambers of the FMD that are coupled by a link resistor. An 8-bit programmable threshold determines whether or not a pulse should be considered as a possible track component. The circuit must resolve the ambiguity as to which of the two coupled cells was struck, and produce a digitised signal. This is done by the use of a comparator, which samples the pulses at the two wire ends at a fixed time after rising above threshold, and chooses the bigger. In order to avoid double strobing from messy pulses, the discriminator circuit remains inactive after identifying a hit, until the signals from both wire ends have passed back below threshold. Where a hit has been identified, an output, corresponding to the wire that was struck, emerges from the discriminator circuit in the form of a 48ns digital signal.

The pulse height thresholds are chosen to be as high as possible, without decreasing the efficiency for minimally ionising particles. The best level is chosen by studying cosmic muon rates as a function of threshold [145]. The resolution with which the discriminator circuit is able to determine the start time of a pulse has been investigated by comparing the arrival times of hits in the RFMs to the drift times measured by the $Q-t$ algorithm. With current thresholds, it is found that the discriminator resolution is around 7ns. This is more than sufficient, as the trigger itself operates in time-slices of 48ns.

### 6.1.2 Pair Finding

Finding pairs of hits in the twin planes of a $\theta$ layer, consistent with tracks originating in the vertex region, is the first stage of the track reconstruction algorithm, and takes place in the first of the ASICs, in the RFMs. It is at this stage that the majority of non vertex-pointing background is eliminated, and that the T0 information for the event is extracted. One pair-finding chip takes serial input from the discriminator circuits corresponding to two cells from different sub-planes of a layer, overlapping in their coverage in local $y$, as shown in figure 6.2. A single ASIC therefore services a 6cm region of drift space. Single bit inputs arrive asynchronously from the discriminator modules, and are strobed into the 'X' and 'Y' input registers of the pair-finding chips every 48ns, using a clock derived from the HERA clock. The existing contents of the X and Y registers are shifted by one position at each clock cycle, to accommodate the new bit.

Logically connected to the X and Y registers is a $32 \times 32$ array of AND gates, each of which can be programmed to be active or otherwise, as illustrated with the filled elements labelled 'ASIC Load' in figure 6.2. Where an AND gate is active, and its inputs from the X and Y registers are both high, an output, corresponding to an identified pair, appears on a third 'Z' register.

The path in the array followed by a pair of hits as time passes is similar to that shown with grey shading in figure 6.2, with time increasing from the bottom right to the top left. For a track at normal incidence to the drift cells, such as that shown in the figure,

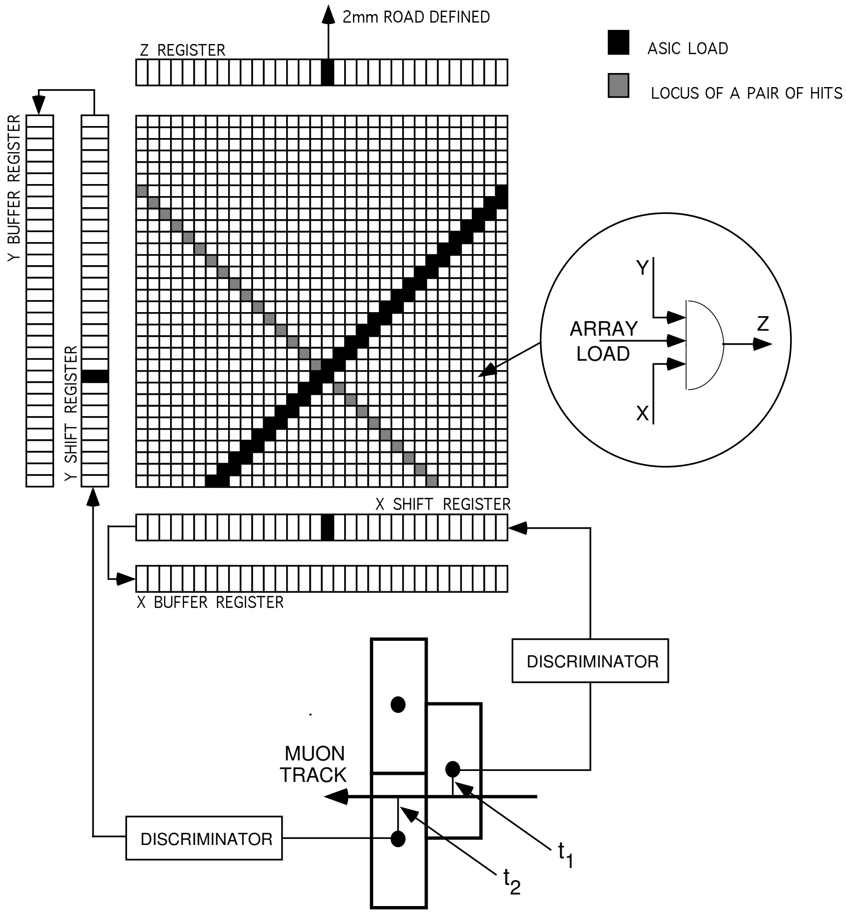


Figure 6.2: *The principal of operation of a pair finding chip.*

the sum of drift times in the two layers is a constant, equal to the maximum drift time.

$$t_1 + t_2 = t_{max} \tag{6.1}$$

A diagonal line in the direction of that shown for the load in the figure is therefore crossed in the same clock cycle by any pair of hits originating from a muon, passing at normal incidence, anywhere through the pair of cells at a particular point in time. If the load is made to be narrow enough, the pair of hits generate an output in the Z register for one clock cycle only. The Z register contents are passed to the later stages of the trigger processor in parallel at each clock cycle. The T0 extraction can therefore be implemented by placing the load diagonal of every T0 chip in the system such that the output occurs in the same clock cycle for any track originating in the vertex region in a given bunch-crossing. Tracks that do not point to the vertex region generally give outputs from T0 chips, but those in different planes occur in different time-slices, and only vertex pointing tracks give correlations at the later stages of the algorithm.

The location of the hit within the 6cm drift space is measured by the quantity, $t_1 - t_2$, which translates to the position in the shift-register reached by by the X signal, when the load condition is satisfied. The location of an entry in the Z register is defined by that in the X register, so that the position of the Z output gives the local $y$ coordinate for the pair, with $\sim$ 2mm resolution.

Pipelining of the data is effected by continuing to strobe the X and Y register contents into buffer registers until the L1Keep signal is returned from CTL1. This occurs a fixed number of bunch crossings after an interaction. When a readout instruction arrives, the pipelines are rewound by the appropriate number of register positions, and the full trigger response is automatically reproduced from the pair finding stage.

### 6.1.3 Segment Finding

After finding pairs of hits within a layer of the FMD, the next stage of the trigger algorithm is to identify track segments in the $\theta$ layers either before or after the toroid. This is done using the second set of ASICs, which are also located in the RFMs.

Once the T0 for an event has been extracted, it is no longer necessary to carry information with the same granularity in the local $y$ coordinate. In order to make correlations between $\theta$ layers on the same side of the toroid, the information from an entire octant of a layer is reduced to 64 bits. This is done by ORing bits from the Z registers of the pair-finding chips, in groups of 8, 16, or the full register, with the highest granularity nearest to the beam-pipe.

Depending on the experimental conditions, either three or four-hit segments can be accepted. Since the single hit efficiency of the system is not perfect, and some of the cells have become inactive with time, the efficiency of the trigger improves substantially when only three hits per segment are required. However, if background conditions are unfavourable and trigger rates become too high, the trigger retains the capacity to tighten its requirements and accept only four hit segments. In order to cater for both possibilities, inputs to the segment finding chips are taken not only from the outputs from the pair finding chips, but also from their inputs. The inputs to the pair finding chips are combined to provide a 32 bit map of the octant along similar lines to the 64 bit map of the pair finding outputs. Information from the same sense wire is passed to the Y register of a pair finding chip as is passed to the X register of an adjacent ASIC. Taking the inputs to alternate chips is therefore sufficient to produce a complete single hit map of the octant, provided that ORs are made of the relevant regions of each X and Y register.

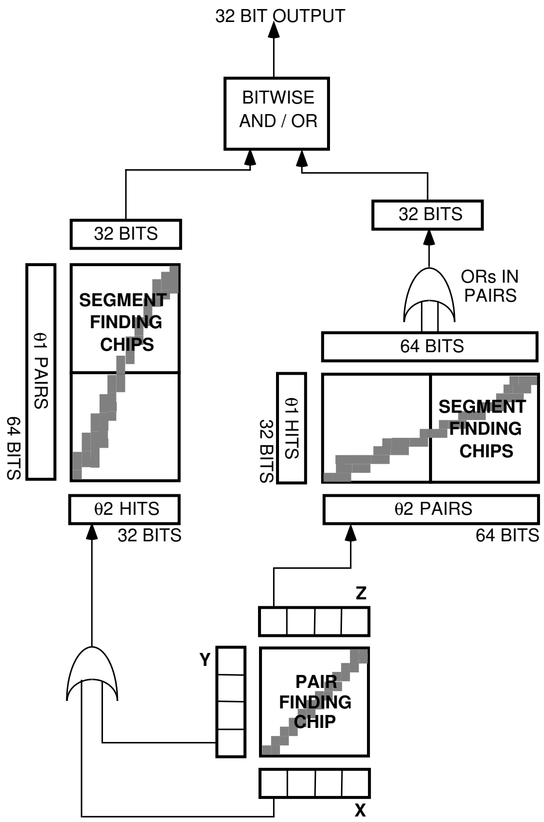


Figure 6.3: *The segment finding stage of the triggering process, illustrated for the case of a single octant of the pre-toroid layers.*

The full algorithm for the case of the pre-toroid layers is illustrated in figure 6.3. A single segment-finding chip combines the single hit information from one $\theta$ layer with the information on pairs from the other. Once again, the chips consist of $32 \times 32$ arrays of programmable AND gates, but this time, they take parallel input at each 48ns clock cycle. Two segment finding chips are needed to perform each correlation, and two correlations must be performed for each pair of planes, to account for the possibility with the three-hit criterion, that the unpaired hit could be in either plane. The choice between three and four-hit segments is implemented by combining the outputs from the two pairs of segment-finding chips either in bitwise ANDs, or in bitwise ORs. The output from the segment finding stage of the algorithm is in the form of a 32 bit map of each octant, describing the presence or absence of a track segment.

### 6.1.4 Track Linking

The final stage of processing in the RFMs is the linking of track segments from before and after the toroid. This is done in much the same way as the segment-finding, and the same ASICs are used. The 32 bit maps of pre and post-toroid segments for an octant are fed, at each 48ns clock cycle, into the two input registers of a single ASIC, which is programmed with the desired load condition. The pre-toroid information is also passed through a 'dummy' chip (figure 6.1), where it is correlated with itself to give an automatic output. At the output stage of the track-linking chips, the resolution is further reduced, and the 32 bits of output from each ASIC are ORed in groups of four, leaving 8 bits in local $y$ per octant. The final output from the RFMs is therefore in the form of two 64 bit maps, covering all octants of the FMD, one describing full tracks, and the other describing pre-toroid segments.

### 6.1.5 The Final Decision Modules

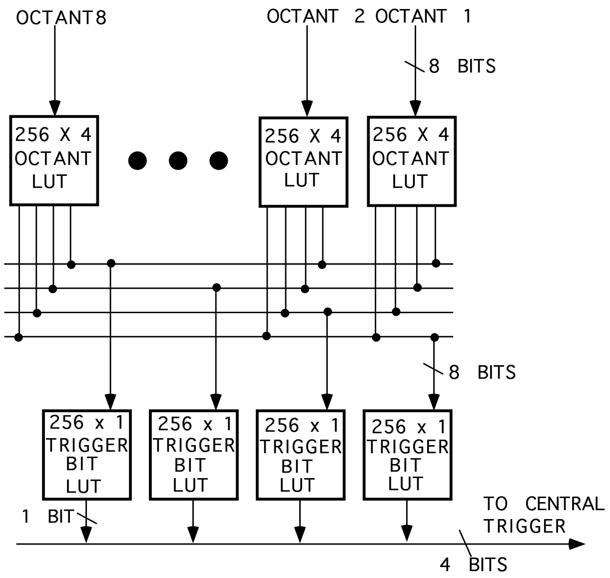


Figure 6.4: *The logical process that takes place in a Final Decision Module.*

Once the data leaves the RFMs, the tracks and pre-toroid segments that have been found for a given bunch-crossing are fully determined. The FDMs merely sort this information, in a programmable manner, according to multiplicity and topology, before the results are sent to the central trigger. The pre-toroid segment signals are sent to one FDM, and those for fully reconstructed tracks to another.

Figure 6.4 illustrates the mode of operation of the FDMs. Two sets of programmable Look Up Tables (LUTs) are used to process the information arriving from the RFMs. The first set of LUTs take the eight bits from a single octant, and give a four bit output. One bit from each of the eight *octant* LUTs is passed to each of the second set of four *trigger bit* LUTs. The trigger bit LUTs produce a single bit output, to be sent to the central trigger. Since the FMT is strobed every 48ns, and the central trigger is clocked every 96ns, some form of cycle combination must take place before the outputs from the trigger bit LUTs are sent to CTL1. The FMT may be programmed to combine pairs of 48ns clock cycles, or to send information from alternate cycles.

## 6.2 Loading the Trigger

### 6.2.1 Philosophy of the Load

The trigger loads described in this section have been used since the beginning of the 1995 run period. They optimise the sensitivity of the system to full muon tracks produced at the vertex with momentum, $p \gtrsim 6$GeV, and for pre-toroid segments with $p \gtrsim 3$GeV, whilst maintaining acceptably low background trigger rates. The trigger is configured to search for three-hit, rather than four-hit segments, and in order to improve the background rejection, the alternate mode of cycle combination is used in the FDMs.

The acceptance of the FMD extends in the forward direction as far as $\theta \simeq 3^{o}$, whereas those of other sub-detectors that are sensitive to forward going muons (the instrumented iron and the forward tracker) reach only as far as $\theta \simeq 7^{o}$. In order to obtain acceptable trigger rates, the level 1 trigger always combines FMT trigger elements with further information from at least one of the central muon system and the forward tracker, before forming the sub-triggers that fire events. This, coupled with the fact that the innermost region of the FMD is subjected to the largest flux of beam-halo and hadronic background, means that the region, $3^{o} \lesssim \theta \lesssim 7^{o}$ of the FMD is of little use for the triggering of muons. As discussed in section 4.5.3, the FMD has been used to tag hadronic activity, in the selection of elastic and diffractive events. The level of activity from this source falls off with increasing distance from the beam-pipe, so that the region of the FMD that is ineffective for muon triggering is ideally suited, instead, to providing a diffractive veto signal to the level 1 trigger.

By reconfiguring the loads of the ASICs that correspond to the low $\theta$ region, the diffractive selection has been implemented at the trigger level, and one of the trigger bits sent to the central trigger describes the presence or absence of steep particle tracks in this region. In conjunction with positive signals from other sub-detector triggers, this *veto* bit can be used in the triggering of events with large rapidity gaps adjacent to a leading proton.

Possibly the most obvious approach to generating the loads for the correlation matrices of the ASICs would be to take samples of simulated muon tracks, originating from the vertex region, and determine which elements of the ASIC loads have to be filled in order to trigger them. However, to perform the task effectively, taking full account of the effects of smearing due to multiple scattering, and closely monitoring the effectiveness of the load for muons at all polar angles, large numbers of simulated muons are necessary. The loads are therefore generated analytically, and smaller samples of simulated muons are used to verify that the efficiency is optimised.

### 6.2.2 Loading the pair-finding chips

The loads for the pair-finding chips are designed to give outputs in the same clock cycle, regardless of the location of the corresponding drift space in the FMD, for any muon that originates from the vertex region at a fixed point in time. In reality, tracks from the vertex region do not arrive at normal incidence, but with polar angle increasing with the local $y$ coordinate. This results in small relative changes in the fixed value of $t_1 + t_2$ from cell to cell, and the load diagonal must be shifted accordingly. This, along with other small corrections to the position of the load diagonal from chip to chip, is detailed in [145]. Apart from the variation in the polar and azimuthal angles at the vertex, the other main factors that influence the path of a muon are

- Smearing in the vertex position.
- Multiple scattering in the main body of H1.
- Multiple scattering in the iron toroid.
- Deflection in the field of the toroid.

The rms in $z$ of the vertex distribution for $ep$ collisions during 1994 and 1995 running was approximately 10cm. Changes from the nominal vertex position at this level have negligible effect on the polar angle of a muon entering a given drift cell, by comparison with the other effects, and so no correction is made. The widths of the pair-finding chip loads are therefore determined by consideration of the other three factors.

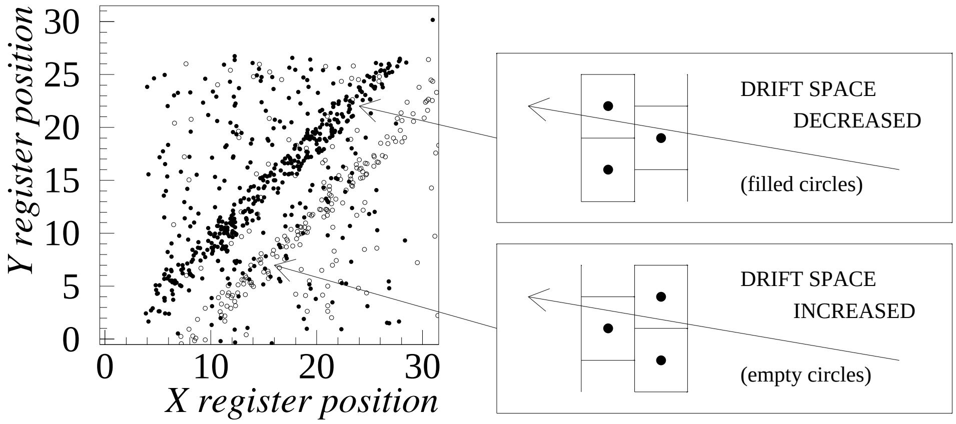


Figure 6.5: *The location in the pair-finding chip correlation matrix of pairs of hits generating outputs, from two chips covering adjacent drift spaces towards the outside of layer, θ2. The load diagonal must be shifted in opposite directions from its central value for the two cases, due to the opposite effects on the sums of drift times occurring in the two different configurations of pairs of cells. The insert shows the orientation of the cells in the two cases.*

A reference position in the correlation matrix of the pair-finding chips, of the main diagonal that is loaded (figure 6.2), is chosen for tracks arriving at normal incidence. But for a constant offset, this defines the sum of drift times in the two cells of a plane covered by a single chip (equation 6.1). For each 6cm drift space, the change, $\delta t$, in the sum of drift times, due to the polar angle of a track originating from the vertex is calculated from

$$\delta t = \pm \frac{\Delta z \, \frac{Y}{z_{plane}}}{v_{drift}} \tag{6.2}$$

where $\Delta z$ ($= 3.42$cm) is the separation of the two sense wires in the $z$ direction, $Y$ is the local coordinate of the centre of the 6cm drift space[3], $z_{plane}$ is the $z$-coordinate of the plane relative to the nominal vertex, $v_{drift}$ is the drift velocity, and a small angle approximation has been used. As illustrated in figure 6.5, the sign of $\delta t$ changes between adjacent drift spaces. The diagonal on which the load is positioned is displaced by the value of $\delta t$, after converting to 48ns clock ticks.

[3]The identification of $Y/z_{plane}$ as the polar angle of incidence of a muon, is only strictly valid at the centre of a cell in the local $X$ coordinate. Away from the centre, the polar angle increases. The effects of this, as well as other factors, such as non-constancy of the drift field, have been studied in [145], and are found to be small by comparison with the effects of multiple scattering and discriminator resolution.

The width of the load for pre-toroid cells is determined by the sum in quadrature of the rms deviations in the sum of drift times, due to multiple scattering, and the finite discriminator resolution. The deflection in track angle due to multiple scattering is approximated to a Gaussian distribution, with rms [147],

$$\sigma(\Delta\theta_{MS}) = \frac{0.78^{o}}{p(GeV)}\sqrt{X}(1 + 0.038\ln X) \tag{6.3}$$

where $p$ is the track momentum, and $X$ is the effective number of radiation lengths of material, through which the particle must pass before reaching the FMD, taken to be 119. As it passes through the main body of H1, a muon track loses an average energy of approximately 3GeV. In using equation 6.3 to estimate the necessary width of the pre-toroid pair-finding ASIC loads, the value of $p$ sets the effective momentum threshold. The smearing in $\theta$ due to multiple scattering is converted to a smearing in $\delta t$, by application of equation 6.2. A load spanning three diagonals is found to be appropriate throughout most of the pre-toroid region.

In passing through the toroid, a track at normal incidence encounters a further 74 radiation lengths of dead material, and loses approximately a further 1.4GeV of energy. When estimating the total smearing to be taken into account due to multiple scattering for the post-toroid pair finding chips, equation 6.3 is used once again, with $X = 193$, and the average value of the momentum chosen to correspond to the desired threshold for full tracks. The deflection in polar angle of a track passing through the field of the toroid follows approximately

$$\Delta\theta = \pm 17.2^{o} \cdot \frac{Bt}{p(GeV)} \tag{6.4}$$

where $B$ is the magnetic field strength, taken to be 1.5T, and $t$ (= 1.2m) is the thickness of the toroid. In devising the loads for the post-toroid pair-finding chips, account is taken of bending in the field for muons of either charge, multiple scattering, and discriminator resolutions. Loads covering either five or six diagonals[4] are found to be necessary.

There is an additional complication that affects the loading of the pair-finding chips, in that an inclined track can occasionally pass on the same side of both sense-wires. This situation is illustrated in figure 6.6a for the extreme case of very sharply angled tracks, passing through a drift space near to the beam-pipe. The figure shows the contents of the $X$ and $Y$ registers of a single pair-finding chip, whenever an event is read out for a certain run. Since most events do not contain a forward going muon, the overwhelming majority of tracks in such events originate from secondary scattering of proton fragments with the

[4]For the outer cells in the post-toroid planes, whose signals are ORed together before entering the trigger system, the load is extended to accept tracks in any of the drift spaces covered.

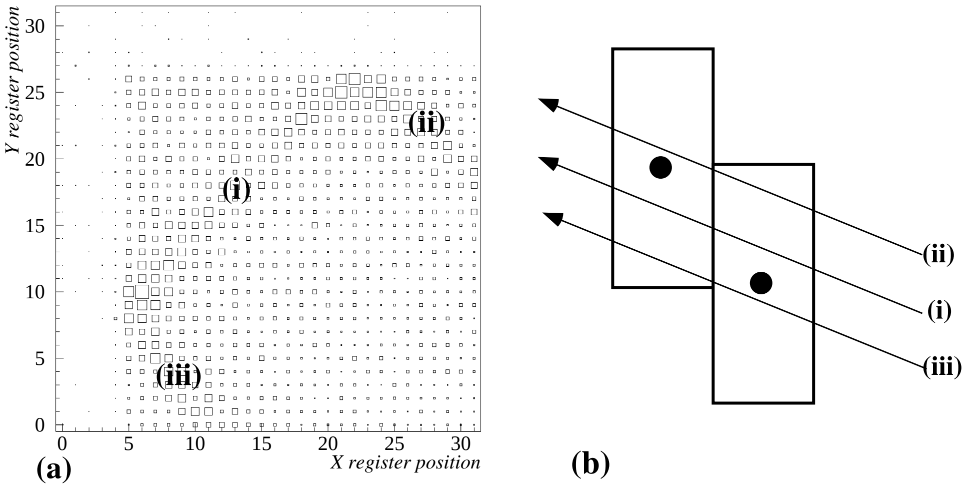


Figure 6.6: *An illustration of the effect on the pair-finding chips, of tracks that pass on the same side of both sense wires. (a) shows the contents of the $X$ and $Y$ registers of a pair-finding chip near to the beam-pipe whenever an event is read out in normal luminosity running. Almost all of the tracks passing through the system under such circumstances have vertices well forward of the nominal. (b) shows the three different types of path taken by tracks through the cell covered by the pair-finding chip. In case, (i), the track passes between the two sense wires, and activity is found in the correlation matrix in the normal region, labelled (i) in (a). Tracks of types (ii) and (iii) in (b) pass on the same side of both sense wires. The sum of drift times is no longer a constant, and the pairs of hits are found in the regions labelled (ii) and (iii) in (a).*

forward beam-pipe, and therefore have very large polar angles (compare the position of the diagonal labelled (i) in figure 6.6a with those in figure 6.5). The three labelled regions of the correlation matrix in figure 6.6a that are the most active, correspond to the three different configurations of tracks shown in figure 6.6b. Although the situation is considerably less drastic for the triggering of muons with shallower polar angles, the same types of configuration can occur. In chips that correspond to drift regions far from the beam-pipe, the load is made similar in shape to that defined by the densely populated regions in figure 6.6a. For tracks that pass on the same side of both sense wires, all timing information is lost, and an output that is several clock cycles long emerges from the pair-finding chips. The T0 for the event must be extracted in other planes.

The innermost six pair-finding chips in the pre-toroid layers of the FMD correspond roughly to the region, $3^{o} < \theta < 7^{o}$, that is to be used to implement the rapidity gap veto trigger. Due to similar considerations to those discussed in section 4.5.3, hadronic activity in the FMD is most efficiently measured by counting pairs of hits. Noise becomes a problem if single hits are used, and reconstruction to the level of four-hit track segments is overkill, and reduces the effectiveness of the veto signal. The current minimum requirement for the veto signal is a single pair of hits found in one of the innermost six chips of $\theta 1$. To implement this criterion, the loads calculated for muon tracks are inverted in the six chips used. This results in triggering on sharply inclined tracks, originating well forward of the vertex region, and as a by-product, also provides a veto against very shallow tracks, with vertex positions well backward of the nominal, consistent with beam-halo muons. No veto signal is sent when a track originating from the vertex region passes through the drift space used for the veto bit. At the segment finding stage of the algorithm, a positive correlation is required between a pair of hits from $\theta 1$ and at least a single hit from $\theta 2$. The highly programmable nature of the trigger processor allows this requirement to be satisfied artificially at each bunch-crossing. The control software configures the innermost chip in $\theta 2$ such that it no longer takes input from the discriminators, but recirculates the contents of the buffer register back into the main register. Two bits, spaced by 32 register positions are placed in the main and buffer $X$ registers, such that there is a single hit signal from the chip at each clock cycle. The $Y$ register also recirculates, but contains no filled bits.

### 6.2.3 Loading the Segment-Finding and Track-Linking Chips

In designing the loads for the remaining two levels of the track-finding algorithm, the only considerations necessary are geometric. Each element of the segment and track finding chips corresponds to a correlation between the local $y$ positions of pairs of hits, or single hits in different $\theta$ layers. The mixture of subtleties of the cell geometry, the ORing of single hit and pair information from the pair-finding chips, along with the tails of multiple scattering distributions, mean that the segment and track-finding ASIC loads have a complex structure. In order to generate the loads, a simple muon track simulation has been devised, so that very large numbers of varying particle tracks can be considered. A typical simulation considers 1 000 tracks of either charge, at each of 2 500 equally spaced polar angles in the range, $0 < \theta < 28.6^{\circ}$. Each track is assigned the same limiting velocity, for which the load is designed. The local $y$ coordinates of each track, as it passes through each $\theta$ layer is calculated, and the elements of the coincidence matrices that would need to be filled in order to trigger the track are recorded. After simulating a large number of tracks, any array element that must be filled to trigger at least a fixed proportion of the entries in that array (currently 0.01%) is filled for the load.

Figure 6.7 illustrates how the simulation works. The vertex is given a Gaussian smearing, with a large standard deviation of 20cm. Each track then takes a straight line path to an

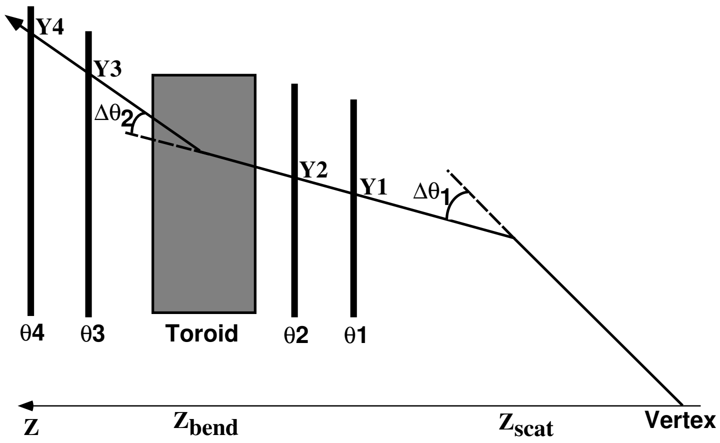


Figure 6.7: *Illustration of the track simulation used in obtaining the loads for the segment and pair-finding chips.*

effective centre for multiple scattering in the main body of H1, given by

$$z_{scat} = \frac{\sum z/X_0}{\sum 1/X_0} = 371cm \tag{6.5}$$

where the numbers of radiation lengths of all components of the detector are taken into account. In reaching $z = z_{scat}$, the track undergoes an energy loss of 0.643GeV, and at $z_{scat}$, its polar angle deviates by a single Gaussian distributed multiple scatter, $\Delta\theta_1$, given by equation 6.3, with X=119. The track continues at the modified polar angle, passing through layers, $\theta 1$ and $\theta 2$ at local $y$ values of $Y1$ and $Y2$, until it reaches the centre in $z$ of the toroid, $z_{bend}$. In reaching this point, a further energy loss of 3.0GeV takes place, and at $z_{bend}$, a multiple scattering is generated, based on 74 radiation lengths. Bending in the magnetic field also changes the polar angle of the track via equation 6.4, and the overall deflection in polar angle at $z_{bend}$ is $\Delta\theta_2$. Finally, the track passes, at its new polar angle, through layers, $\theta 3$ and $\theta 4$, with local $y$ coordinates, $Y3$ and $Y4$.

For the loading of the post-toroid segment finding chips and the track-linking chips, only tracks that remain within the geometrical acceptance of the FMD in all four $\theta$ layers are considered. In loading the pre-toroid segment-finding chips, the track need only be contained by the system for the two layers before the toroid.

The diffractive part of the load is implemented by filling all elements of the segment-finding chips that correspond to correlations between pair signals from any of the first six pair-finding chips in $\theta 1$, and the artificially placed hit in the first chip in $\theta 2$. The corresponding region in the segment-finding chips that correlate single hits in $\theta 1$ with pairs in $\theta 2$ is left empty. With a three-hit segment requirement, only pairs of hits in the inner layers of $\theta 1$ can then give a veto.

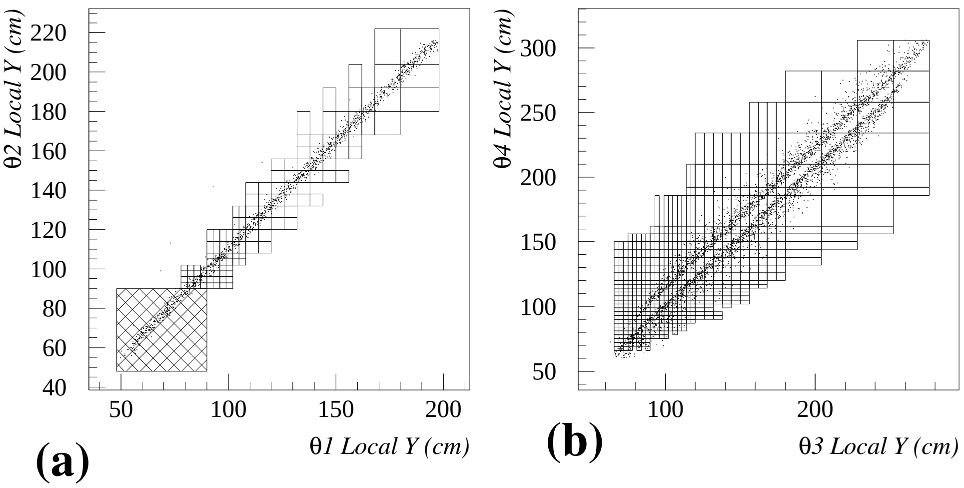


Figure 6.8: *A test of the segment-finding chip loads. (a) Scatter plot for simulated tracks in the momentum range,* $5 < p < 7\mathrm{GeV}$*, giving at least a reconstructed pre-toroid segment in the FMD, showing the value of local* $y$ *at which they pass through plane,* $\theta 2$ *against the position in* $\theta 1$*. Superimposed on the plot are boxes, showing the regions in local* $y$ *in the two planes corresponding to the elements of the array that are filled in the load. The cross-hatched box shows the region covered by the diffractive veto bit. (b) As (a), but for tracks simulated in the range,* $p < 10\mathrm{GeV}$*, that give a fully reconstructed track in the FMD, and showing the correlation between* $\theta 4$ *and* $\theta 3$ *local* $y$ *values.*

Figure 6.8 shows a comparison of the loads generated by the method described, with samples of simulated single muons that have passed through the full H1 simulation, including that of the FMD. In figure 6.8a, the correlation is shown for fully simulated muons in the momentum range, $5 < p < 7\mathrm{GeV}$, between the values of $Y1$ and $Y2$. The superimposed boxes show the region covered by the current ASIC loads, including the part that is sacrificed to the rapidity gap veto. Figure 6.8b shows the correlation between $Y3$ and $Y4$ for the post-toroid segment-finding ASICs, for muons passing through all four $\theta$ layers, with $p < 10\mathrm{GeV}$. Two bands are clearly visible, corresponding to muons of either charge, and the load is considerably broader. The load of the final track-linking chip is equally broad.

### 6.2.4 Final Trigger Definitions

The final definitions of the trigger bits that are sent to the central trigger by the FMT are determined by the contents of the LUTs in the FDMs. Table 6.1 shows how they are currently defined.

| *TRIGGER BIT* | *DEFINITION* |
|---|---|
| 1 | Diffractive veto signal |
| 2 | Pre-toroid, muon T0 |
| 3 | Pre-toroid, $\geq 2$ muons in the same octant |
| 4 | Pre-toroid, $\geq 2$ muons in different octants |
| 5 | Post-toroid, muon T0 |
| 6 | Post-toroid, dimuon in opposite octants |
| 7 | Post-toroid, $\geq 2$ muons in the same octant |
| 8 | Post-toroid, $\geq 2$ muons in different octants |

Table 6.1: *The current definitions of the eight Forward Muon Trigger elements.*

The rapidity gap veto has been combined with trigger elements from the trackers and calorimetry, to make sub-triggers for diffractive events in which there is no tagged electron. The pre-toroid muon T0 bit is combined with information from the z-vertex, forward tracker, and Front End Cap instrumented iron triggers, to provide a low threshold sub-trigger for $J/\psi$ events, decaying to muon pairs. The post-toroid muon T0 bit is used with various combinations of similar detectors, to give higher threshold sub-triggers that are more stable against fluctuations in background. It is also set in coincidence with Barrel and Backward End Cap instrumented iron triggers, to provide a global dimuon sub-trigger throughout the detector. The post-toroid dimuon trigger elements have some acceptance for $J/\psi$ physics, and are very effective for the triggering of leptonic decays of heavier states. They are used with different combinations of instrumented iron, forward tracker and z-vertex triggers, such that some redundancy is retained. The single muon post-toroid trigger element is also used, in coincidence with Veto Wall signals, as a beam-halo monitor sub-trigger.

## 6.3 Acceptance of the Load

Various techniques have been used to study the acceptance of the FMT trigger elements. The ideal method would be to use any available redundancy of the detector, and extract FMT efficiencies from samples of $ep$ events that lead to forward going final state muons, but which were triggered by different detector components. However, the overall $ep$ cross-section for muon production is small, and due to the very large background rates, almost all of the sub-detector triggers that are sensitive to muons in the forward direction, including the FMT, are always placed in coincidence when constructing sub-triggers. In

1995, there were no sub-triggers that specifically searched for forward muons that did not include the FMT. In a study [148] of 1995 data, which contains by far the largest numbers of high quality FMD tracks, a sample of events with two reconstructed muons anywhere in H1, at least one of which is constrained to be in the FMD, and where the invariant mass of the dimuon pair is broadly compatible with that of a $J/\psi$ ($1 < m_{\mu^+\mu^-} < 5$GeV), 251 events were selected. Of these, 137 were triggered *only* by sub-triggers involving the FMT. Until much larger samples become available, measurements of the acceptance of the FMT must be extracted from simulations.

The simulation of the FMT [148] uses the loads that have been devised for luminosity running, and contains a full implementation of the digital part of the trigger (the RFM and FDM stages). Information on muon tracks, after simulation through the FMD is available to the trigger simulation in the $Q-t$ format. Since the pulse height information in the FMD simulation is not yet fully reliable, the FMT discriminator threshold in the simulation is set to be low. However, as the thresholds for luminosity running have been carefully tuned, using data, to accept minimum ionising particles [145], this should have only marginal effect on the efficiency measurements. The time of arrival in the pair-finding chip registers is extracted from the $Q-t$ time information, after simulation of the smearing due to finite time resolution of the discriminators.

### 6.3.1 Efficiency of the Rapidity Gap Veto Bit

Various samples have been used to study the effectiveness of the FMT rapidity gap veto bit. Some of the results are presented in figure 6.9. The rejection efficiency, as a function of $M_Y$, for diffractive events in which the proton dissociates (types PD and DD) is extracted in simulations using events generated by PHOJET and PYTHIA. The results are shown in figure 6.9a. The behaviour, as a function of $M_Y$, is observed to be similar to that of the off-line forward muon rapidity gap cut (figure 4.9a), with a threshold behaviour, reaching a plateau at $M_Y \simeq 5$GeV. The fact that only a very limited region of the FMD is used by the trigger for the rapidity gap veto decreases the rejection efficiency by only $\sim 10\%$ at all values of $M_Y$. The overall rejection efficiency of the veto trigger bit for each photoproduction sub-process is shown in table 6.2. There is a very good rejection efficiency for non-diffractive events, approximately 50% efficiency for diffractive events in which the proton dissociates, and almost no incursion on the signal for diffractive events in which the proton remains intact. Differences between the two Monte Carlos, as to the details of final state energy flow at large rapidity lead to discrepancies at the 10% level in the efficiencies extracted with the two models.

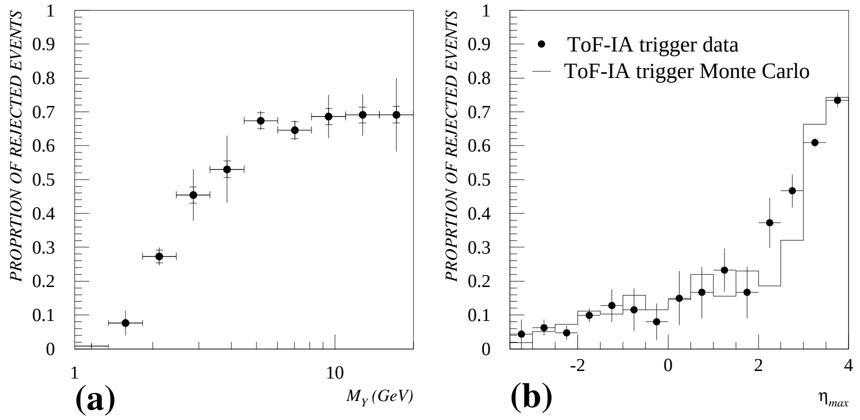


Figure 6.9: *Results of studies of the efficiency of the FMT rapidity gap veto bit. (a) The efficiency, from simulations using the PHOJET and PYTHIA Monte Carlos, for diffractive events with a dissociating proton, as a function of the dissociating proton mass, $M_Y$. The points shown are the averages of those obtained using the two models. The inner error bars are statistical, and the outer error bars are the statistical errors added in quadrature with a model dependence error, estimated from the difference between the PHOJET and PYTHIA predictions. (b) The rejection efficiency as a function of $\eta_{max}$, measured in the nominal vertex ToF-IA data sample, compared to an average of PHOJET and PYTHIA predictions. The sample, and the cuts applied, are described in chapter 4.*

For the veto bit at least, comparisons with data are possible. Figure 6.9b shows the rejection efficiency as a function of $\eta_{max}$, for events in the nominal vertex ToF-IA sample used in chapters 4 and 5, with the cuts described in section 4.4.3. Compared to the data is the rejection efficiency predicted by an average of the PHOJET and PYTHIA models, after identical cuts, and with relative fractions of each photoproduction sub-process, as expressed in equation 5.6. The agreement between Monte Carlo and data is good, particularly in the uppermost bin of $\eta_{max}$, which contains most of the non-diffractive data. Similar levels of agreement are found when the rejection efficiency is made using data samples from other photoproduction triggers. This would indicate that, at least as regards sharply inclined tracks arising from secondary hadrons, the simulation of the trigger works well.

The rapidity gap veto bit is effective in the rejection of proton beam-gas events, since the collision of an 820GeV proton with another hadron at rest inevitably yields large track multiplicities at high rapidity. In order to investigate the rejection efficiency of the veto trigger element for proton beam-gas background, a sample of events, triggered

| *MODEL* | *ND* | *GD* | *PD* | *DD* | *EL* |
|---|---|---|---|---|---|
| *PHOJET* | $80.1 \pm 0.5$ | $2.6 \pm 0.2$ | $49.5 \pm 1.2$ | $53.3 \pm 1.0$ | $0.0 \pm 0.0$ |
| *PYTHIA* | $69.5 \pm 0.4$ | $2.9 \pm 0.3$ | $53.8 \pm 1.9$ | $47.6 \pm 1.7$ | $0.0 \pm 0.0$ |

Table 6.2: *Measurement of the overall rejection efficiency of the FMT veto bit for each photoproduction sub-process, using the PHOJET and PYTHIA Monte Carlos. No cuts are applied, with the exception of the restriction, $0.3 < y < 0.5$. The names given to each sub-process are the same as those used in chapters 4 and 5. All results are quoted as percentages and the errors are statistical.*

predominantly by minimum bias photoproduction triggers, but from proton pilot bunches is studied. The overall rejection efficiency for all beam-gas events in the sample was found to be $55.8 \pm 1.4\%$ [5].

Events at values of $Q^2$ in the approximate range, $0.01 < Q^2 < 2\mathrm{GeV}^2$, in which neither the luminosity electron tagger, nor the electromagnetic calorimetry in the main detector has any acceptance, must be triggered on the basis of the hadronic final state. The absence of a tagged electron in such events leads to very large backgrounds from proton beam-gas processes, and unless large values of $p_T$ are required for final state particles, trigger rates are prohibitively high. The largest use of the rapidity gap veto bit is likely to be in obtaining samples of diffractive events in which no final state electron is visible in the detector. Analyses of such samples are likely to be very revealing, as the $Q^2$ range covered is that in which the transfer from the photoproduction to the DIS regimes takes place. An estimate of the efficiency of the veto trigger bit for such processes has been obtained, using a class of events that were triggered on the basis of high $p_T$ particles in the central tracker and LAr calorimeter, and for which no final state electron is reconstructed. Use of the FMT veto bit in combination with the untagged triggers, would reduce the sample size in the non-diffractive region of large $\eta_{max}$ by $\sim 70\%$. This figure increases to $\sim 80\%$ if the FToF-IA trigger (section 1.8) is also used as a forward veto component. Application of a forward veto at the level 1 trigger level can therefore reduce trigger rates substantially, and ultimately, can lead to a reduction in the criteria required for triggering events without a tagged final state electron.

[5]This figure is smaller than the rejection efficiency for non-diffractive events for two reasons. Firstly, the bulk of obvious beam-gas events are removed by the level 4 trigger, and do not reach data tapes. Dead-time can be improved if these events are rejected at level 1 instead. The second reason is that proton beam-gas events can also be diffractive, and can contain large rapidity gaps in the region of acceptance of the veto.

### 6.3.2 Single Muon Acceptance

Acceptances for muons are estimated by studying samples of single muon tracks, passed through the full detector simulation, including that of the FMD and FMT. 35 000 positively charged, and 35 000 negatively charged muons are generated, in the momentum range, $2.5 < p < 50$GeV, with the highest statistics for the lowest momentum tracks, and with a uniform distribution in polar angle, $2 < \theta < 20^{o}$. The simulation of the FMD contains all of the dead regions between the active drift spaces, and inactive cells are removed[6]. Single hit efficiencies for minimally ionising particles have been studied using independently triggered beam-halo data, and found to be approximately 98%. A random 2% of hits are therefore removed. All coordinates of hits are smeared to represent the resolution. Misalignments of the chambers are not implemented in the simulation, but within the established limits, are not expected to affect the results as far as triggering is concerned.

Despite the presence of dead cells, the acceptance is found to be rather flat in azimuth, and a parameterisation as a function of momentum and polar angle only is possible. Figure 6.10a shows the measured acceptance, in bins of momentum, $p$, and polar angle, $\theta$, for the FMT pre-toroid single muon trigger element, for positively charged muons. There is a relatively smooth plateau of efficiency at the level of around 95%, for $p \gtrsim 5$GeV and $8 < \theta < 16^{o}$. Outside this region, the efficiency falls off fairly rapidly. To parameterise the acceptance, *sigmoid* functions are used, describing the efficiency as a function of $\theta$ once the momentum plateau is reached, and as a function of momentum for the $\theta$ plateau. The form of the parameterisation is

$$f(x) = \frac{\mathcal{A}}{1 + e^{-\frac{(x - x_0)}{x_1}}} \tag{6.6}$$

where $x$ may be either the momentum or the polar angle. The parameters, $\mathcal{A}$, $x_0$ and $x_1$ are determined in fits. $\mathcal{A}$ represents the efficiency of the plateau region, $x_0$ is the value of $x$ at which the efficiency is half that of the plateau, and $x_1$ describes the speed at which the rise at threshold occurs. Figure 6.10b shows the result of a sigmoid fit to the efficiency as a function of momentum, taking only muons in the range of polar angle, $9 < \theta < 15^{o}$. Figure 6.10c shows the fit to the rising edge of the efficiency in $\theta$ for $p > 10$GeV. Figure 6.10d shows the fit as a function of $20^{o} - \theta$, parameterising the falling edge of the $\theta$ distribution, in the same range of momentum. The full parameterisation of the single muon acceptance, as a function both of momentum and of polar angle, is obtained separately for positive and negatively charged muons for both the pre-toroid and

[6]The cells that are dead are determined by monitoring the level of activity over a large number of luminosity runs. For 1995, 27 pairs of FMD cells were found to be inactive.

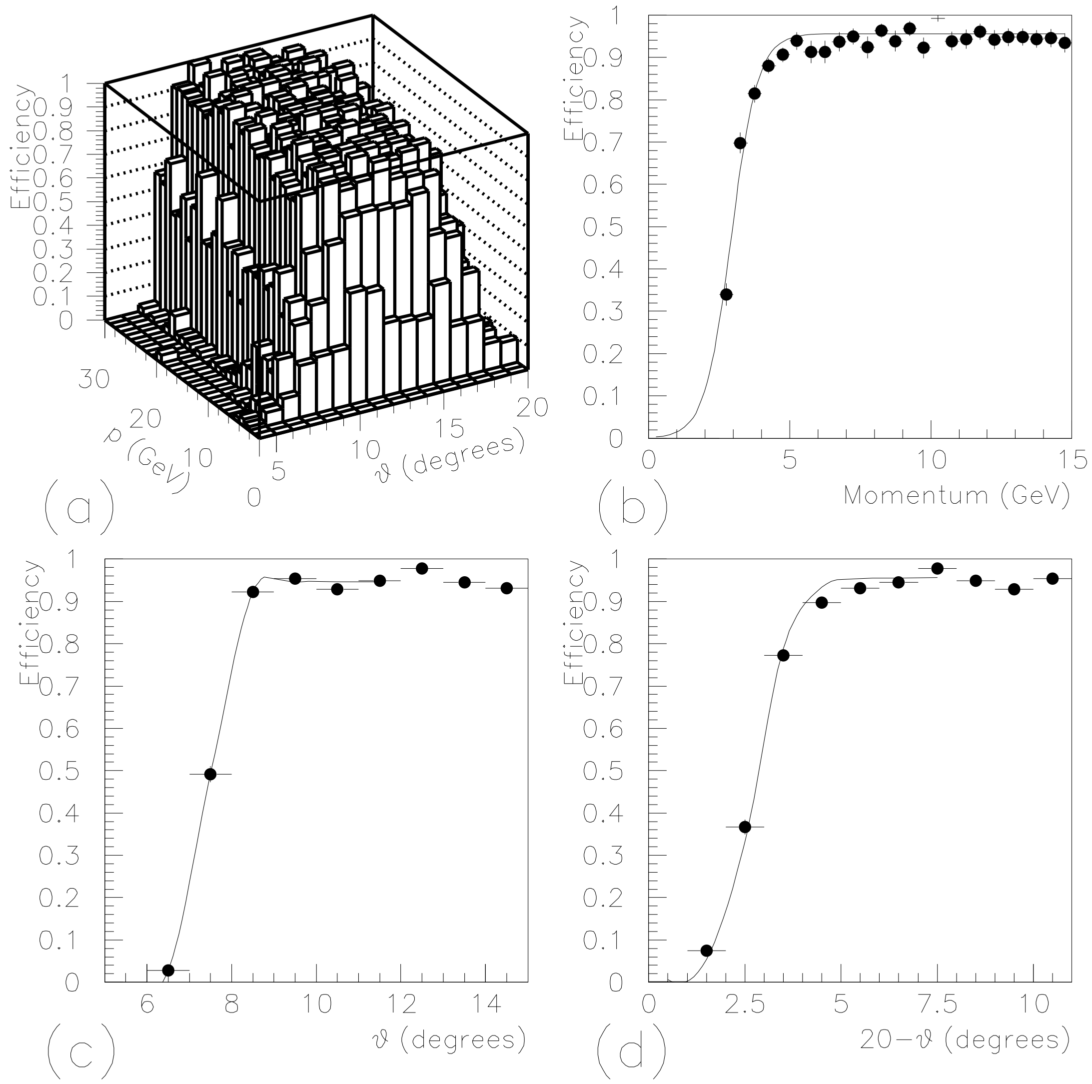


Figure 6.10: *Parameterisation of the acceptance of the pre-toroid FMT trigger bit for positively charged muons, from studies of simulated single muons. (a) The efficiency in bins of momentum and polar angle. (b) Sigmoid fit to the efficiency as a function of momentum, for $9^{\circ} < \theta < 15^{\circ}$. (c) Sigmoid fit to the rising edge of the efficiency as a function of $\theta$, for $p > 10\mathrm{GeV}$. (d) Sigmoid fit to the falling edge of the efficiency as a function of $20^{\circ} - \theta$, for $p > 10\mathrm{GeV}$.*

full-track triggers, and takes the form

$$\epsilon(p,\theta) = \mathcal{A} \cdot \frac{1}{1+e^{-\frac{(p-p_0)}{p_1}}} \cdot \frac{1}{1+e^{-\frac{(\theta-\theta_0)}{\theta_1}}} \tag{6.7}$$

where the value for $\mathcal{A}$ is taken from the momentum fits, the rising edge $\theta$ parameterisation is used for $\theta < 13^{\rm o}$, and the falling edge parameterisation is used for $\theta > 13^{\rm o}$. Similar results to those shown in figure 6.10 are obtained for negative muons with the pre-toroid trigger bit. For the post-toroid trigger bit, the efficiency on the plateau drops slightly, and the momentum threshold rises considerably. A summary of all parameters extracted from the fits is given in table 6.3.

| *PARAMETER* | *PRE-TOROID* $\mu^+$ | *PRE-TOROID* $\mu^-$ | *FULL-TRACKS* $\mu^+$ | *FULL TRACKS* $\mu^-$ |
|---|---|---|---|---|
| $\mathcal{A}$ | 0.96 | 0.95 | 0.94 | 0.92 |
| $p_0$ | 2.93 | 2.94 | 6.25 | 5.63 |
| $p_1$ | 0.47 | 0.55 | 0.49 | 0.61 |
| *Rising* $\theta_0$ | 7.48 | 7.49 | 7.47 | 7.48 |
| *Rising* $\theta_1$ | 0.28 | 0.29 | 0.28 | 0.28 |
| *Falling* $\theta_0$ | 17.21 | 17.11 | 17.20 | 17.20 |
| *Falling* $\theta_1$ | 0.46 | 0.46 | 0.49 | 0.48 |

Table 6.3: *Values obtained from fits to sigmoid functions, and used in the parameterisation of single muon efficiencies. $\mathcal{A}$ describes the efficiency of the plateau region. $p_0$ and $p_1$ describe the momentum threshold and speed with which the rise at threshold takes place, respectively. The values of $\theta_0$ are the polar angle thresholds for the rising and falling theta distributions, and those of $\theta_1$ are the speed with which the rise at threshold in $\theta$ takes place.*

The source of the remaining inefficiency in the plateau region has been investigated, by running the simulation under varying conditions. If all of the FMT ASICs are fully loaded, corresponding to the maximum possible acceptance of the trigger, then the efficiencies improve by only $1-2\%$. If the simulation is performed without any dead cells, the improvement is at a similar level. The remaining inefficiencies are caused primarily by the dead regions between drift cells, and the tails of the multiple scattering distributions, that deviate a small fraction of tracks nominally within the plateau region, out of the acceptance of the FMD.

## 6.4 Measurements with Forward Muons

A number of processes occurring in $ep$ and $\gamma p$ interactions at HERA can give rise to high momentum forward going muons within the acceptance of the FMD. In this section, the

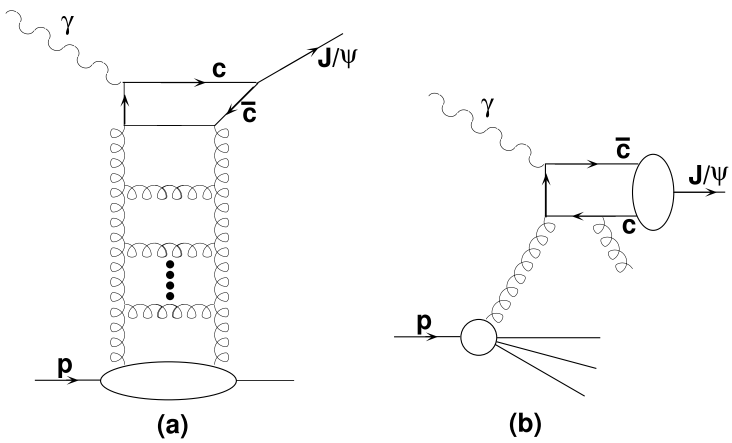


Figure 6.11: *Perturbatively calculable $J/\psi$ production diagrams. (a) Elastic production in the model of Ryskin. (b) The photon-gluon fusion process, in the colour singlet model.*

capacity of the forward muon system to make useful measurements of a subset of such processes is studied, using simulations. Monte Carlo event generators are used to obtain distributions in momentum and polar angle of muons produced in the interactions, before simulation through the detector. The generator level information is then convoluted with the acceptance parameterisation for single muons (section 6.3.2). Whilst the parameterisation method inevitably results in some loss in detail, the alternative of running the full detector simulation for each event is highly computer-time intensive, and with the present level of understanding, is probably unjustified. The validity of the parameterisation method has, however, been checked by performing a full simulation of the muon tracks for one of the Monte Carlo models studied, and comparing results obtained with the full simulation to those obtained by the parameterisation method. The agreement in the calculated efficiencies was always found to be good at the 5% level, which is less than the present level of statistical errors.

### 6.4.1 Elastic $J/\psi$ Production

The photoproduction of $J/\psi$ mesons will be the largest area of interest in the use of the FMD to make measurements. By comparison with other processes yielding forward muons, cross-sections are large. The physics interest is sustained by the fact that $J/\psi$ production, by various mechanisms, is sensitive to the gluon distribution of the proton. The elastic process, $\gamma p \to J/\psi\ p$, additionally provides information on the $\gamma - J/\psi$ coupling, and tests the ideas of the VDM with large vector meson masses. A final motivation is that elastic $J/\psi$ production is an ideal arena in which to study the interplay between hard and soft diffractive dynamics (see section 3.5). Models based on non-perturbative diffractive exchange [105] and the VDM have been applied to elastic $J/\psi$ production, and are successful in describing low energy data. Perturbative models, such as that of Ryskin [122], based on the exchange of gluon ladders between the proton and a charm quark, calculated in LLA($Q^2$), find the elastic cross-section to be proportional to the square of the proton gluon density. The production mechanism in the Ryskin model is illustrated in figure 6.11a. If perturbative QCD models are successful in describing the elastic $J/\psi$ cross-section, then the study of the process may turn out to be one of the cleanest ways to investigate the rôle of absorptive corrections, and gluon saturation (section 2.2.3) in the proton.

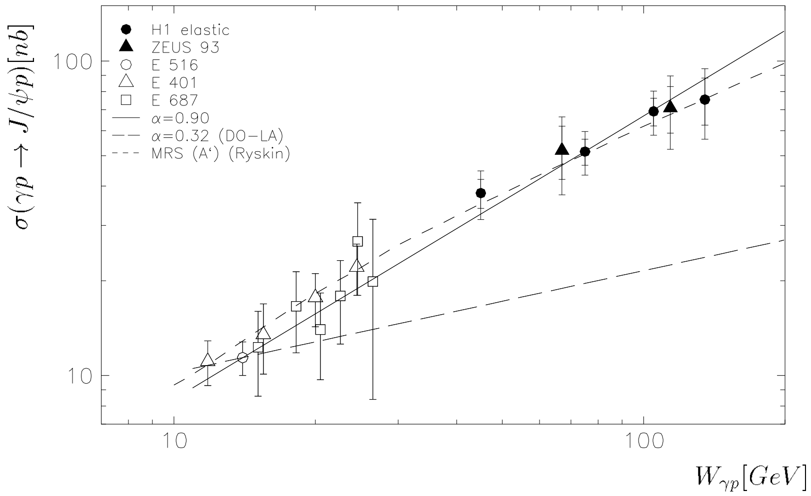


Figure 6.12: *Summary of measurements of the elastic $J/\psi$ cross-section as a function of $\gamma p$ centre of mass energy. Points are shown from H1, ZEUS, and fixed target experiments, and compared to Regge parameterisations with a soft pomeron (long dashed line), a harder pomeron with $\alpha_{I\!P}(0) = 0.225$ (solid line), and the Ryskin model, including higher order corrections, using parameterisations of the gluon distribution based on HERA measurement (short dashed line). The plot is taken from [121] .*

Figure 6.12 shows recent HERA measurements [121] [120] of the elastic $J/\psi$ cross-section, differential in $W_{\gamma p}$, along with lower energy measurements from fixed target experiments [149]. If all of the data shown are fitted to extract an effective pomeron intercept via equation 3.20, then one obtains $\bar{\alpha}_{I\!P} = 1.23 \pm 0.02$. If the HERA data alone are fitted, the value is found to be $\bar{\alpha}_{I\!P} = 1.17 \pm 0.03$. Additional information from HERA at low $W_{\gamma p}$, will enable the more precise determination of this quantity, and investigations of the presence or absence of shrinkage (section 3.2.4). The experimentally measured dependence on $\gamma p$ centre of mass energy can be reproduced by the Ryskin model if a gluon density in the low $x$ regime, strongly rising with decreasing $x$, is assumed.

The acceptance of the FMT for triggering muons from the decay, $J/\psi \to \mu^+\mu^-$ (Branching ratio $5.97 \pm 0.25\%$), of elastically produced $J/\psi$s, has been studied at vanishing $Q^2$, using the Monte Carlo generators, DIFFVM [150] and EPJPSI [151]. Both models are based on soft diffractive exchange in the $\gamma p$ system, with $\alpha_{I\!P}(0) \sim 1.08$.

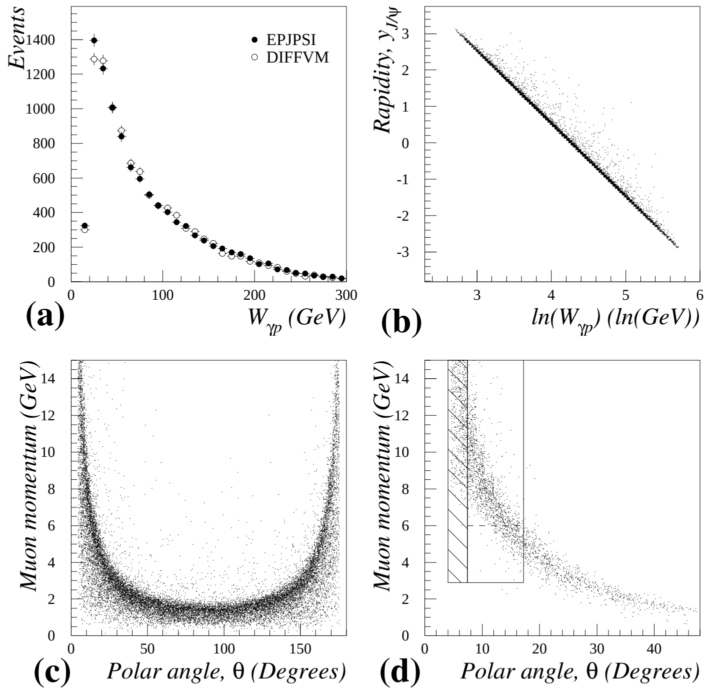


Figure 6.13: *(a) The $W_{\gamma p}$ distribution at the generator level of two Monte Carlo files describing elastic $J/\psi$ production in Donnachie-Landshoff type models. (b) The laboratory rapidity of the $J/\psi$ plotted against $\ln W_{\gamma p}$ for the EPJPSI Monte Carlo. (c) The momentum plotted against the polar angle for both muons arising from the decay of the $J/\psi$ in the EPJPSI Monte Carlo. (d) The same plot as (c), but restricted to the range $10 < W_{\gamma p} < 30\mathrm{GeV}$. The approximate region of acceptance of the FMT, as calculated in the single muon study, is superimposed. The full line represents the acceptance of the pre-toroid trigger, and the dashed line shows the acceptance for validated tracks. The region filled with a striped pattern represents that used for the rapidity gap veto.*

Figure 6.13a shows the distribution in $\gamma p$ centre of mass energy in the two models, which is essentially a relatively flat cross-section, convoluted with a $y$ dependent photon flux factor. The rapidity of the $J/\psi$ produced is logarithmically correlated to $W_{\gamma p}$ via equation 4.21. Figure 6.13b shows this correlation for the case of the EPJPSI Monte Carlo. $J/\psi$ mesons produced at the lowest values of $W_{\gamma p}$ are boosted most strongly in the forward direction relative to the laboratory frame. The decay angular distribution of the elastically photoproduced $J/\psi$ has been shown [121] to be consistent with complete transverse polarisation of the $J/\psi$. Figure 6.13c is a scatter plot, based on EPJPSI at the generator level, showing the polar angles and laboratory momenta of muons from the $J/\psi$ decay, assuming a decay distribution in the $J/\psi$ rest frame, $\frac{d\sigma}{d\cos\theta^\star} \sim 1+\cos^2\theta^\star$, where $\theta^\star$ is measured relative to the $J/\psi$ direction. Both because of the boost of the $J/\psi$ meson, and because of the angular distribution of its decay, elastic $J/\psi$ production at low $W_{\gamma p}$ is expected to give rise to high momentum forward going muons. Figure 6.13d shows the subset of muon tracks in figure 6.13c for which $10 < W_{\gamma p} < 30$GeV. The approximate region of acceptance of the FMT with the current ASIC loads is superimposed. It is clear that the trigger is capable of being very efficient for the detection of the muons from the decays of $J/\psi$ mesons at low $W_{\gamma p}$.

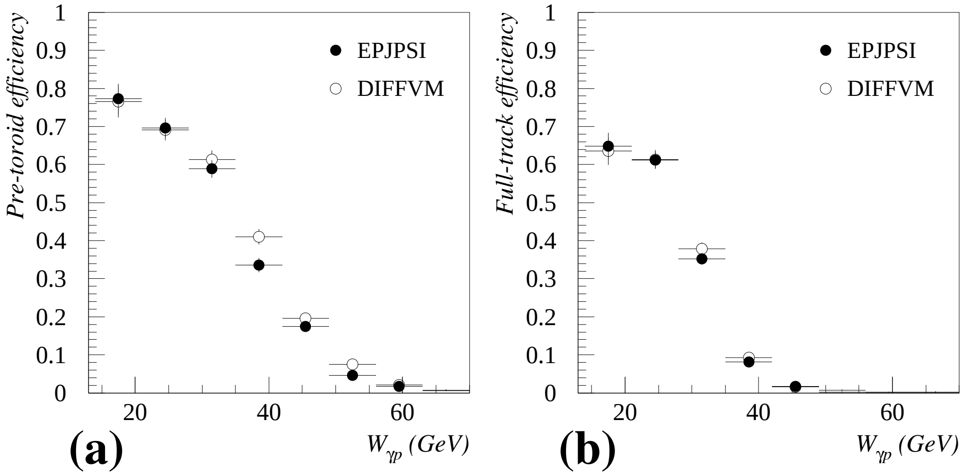


Figure 6.14: *Efficiency of the FMT for the triggering of elastic $J/\psi \to \mu^+\mu^-$ events, calculated using the parameterisation described in the text, assuming a soft pomeron, and plotted as a function of the $\gamma p$ centre of mass energy. (a) The pre-toroid muon T0 trigger bit. (b) The full-track muon T0 trigger bit.*

Figure 6.14 shows the efficiency of the FMT pre-toroid and full-track muon T0 trigger bits, for the detection of at least one of the muons arising from $J/\psi$ decays, in the elastic process, using the parameterisation described in section 6.3.2. The efficiency is best at the lowest values of $W_{\gamma p}$, and falls off, due to the upper polar angle, and lower momentum limits in the FMT acceptance, with increasing $W_{\gamma p}$. Comparison of figure 6.14 with figure 6.12 shows that an elastic $J/\psi$ measurement using the FMD can provide a data point in the region currently covered only by fixed target experiments, and can help to increase the precision on the measurement of the power of $W_{\gamma p}$ with which the cross-section rises. If cross-checks with previous H1 measurements made in similar $W_{\gamma p}$ ranges are to be performed, the importance of the pre-toroid trigger is apparent.

### 6.4.2 Inelastic $J/\psi$ production

Inelastic $J/\psi$ production can take place, either as a direct, or as a resolved photon interaction. The direct case corresponds to the photon-gluon fusion process, $\gamma g \rightarrow c\bar{c}$, which, as discussed in section 2.2.5, provides a method of measuring the gluon distribution of the proton. Fixed target experiments [152] have used $J/\psi$ production by the photon-gluon fusion process for this purpose. The variable,

$$z = \frac{p \,.\, J/\psi}{p \,.\, \gamma} \tag{6.8}$$

where particle symbols have been used to denote their four-vectors, measures the elasticity of the process. At very large values, $z \simeq 1$, all of the photon momentum is transferred to the $J/\psi$, and the process is elastic. Inelastic processes in which the photon interacts directly, yield larger values of $z$ than those in which only part of the photon momentum enters the hard sub-process. With good reconstruction, a rather pure sample of directly produced inelastic $J/\psi$ events may be obtained by selecting events with $0.4 \lesssim z \lesssim 0.9$ [153].

The Colour Singlet Model (CSM) [154], in which the colour octet $c\bar{c}$ system, produced in photon-gluon fusion, reverts to an $S$-wave colour-singlet state by emission of a single gluon, is used to describe the process. The diagram for the CSM model is shown in figure 6.11b. Since $\alpha_s(m_c) \sim 0.2$, the full diagram, including the gluon emission, can be treated perturbatively in QCD. The large charm quark mass also means that the $J/\psi$ may be treated to reasonable approximation as a non-relativistic system. The original CSM ignores the $J/\psi$ binding energy, and ascribes half of its mass and 4-momentum to each of the charm quarks. Since the $J/\psi$ is treated as an $S$-wave system, the wavefunction at the origin fixes the normalisation. The CSM in leading order of QCD provides a good description of the $z$ and $p_T$ distributions of the process, although a 'K'-factor of 2–5, attributed to higher order corrections, is required for a proper normalisation. The cross-section depends linearly on the proton gluon density, via

$$\frac{d\sigma}{dxdt} = G(x, \mu^2)\,\frac{d\hat{\sigma}}{d\hat{t}} \tag{6.9}$$

where $\mu^2$ is a mass factorisation scale, and $d\hat{\sigma}/d\hat{t}$ is a parton cross-section, calculable to leading order in QCD.

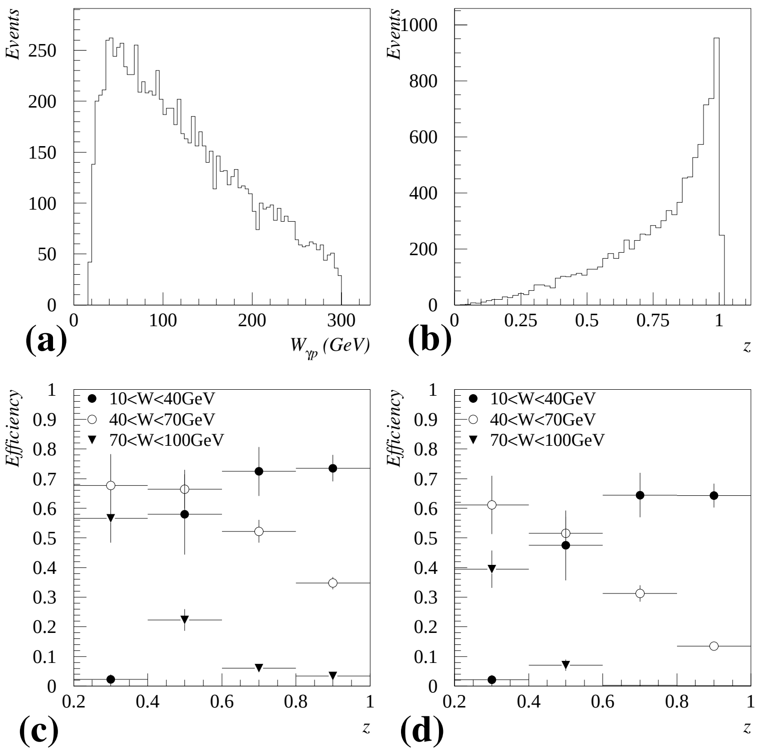


Figure 6.15: *(a) The generated $W_{\gamma p}$ distribution from the EPJPSI Monte Carlo, for $J/\psi$ production by photon-gluon fusion. (b) The generated $z$ distribution for the EPJPSI Monte Carlo. (c) The efficiency of the FMT pre-toroid T0 trigger bit for the photon-gluon fusion process, as calculated using the single muon parameterisation. The efficiency is shown as a function of $z$, for different ranges in $W_{\gamma p}$. (d) As (c), but for the full-track FMT trigger bit.*

The CSM, with some relativistic corrections, is implemented in the EPJPSI Monte Carlo for the direct photon-gluon fusion process. Figures 6.15a and 6.15b show the expected $W_{\gamma p}$ and $z$ distributions respectively, using parameterisations of the gluon structure function based on HERA measurement. Any inelasticity of the production process can only result in the $J/\psi$ being boosted further forwards in the laboratory frame than is the case for the elastic process at the same $W_{\gamma p}$. The efficiencies of the FMT pre-toroid and full-track muon T0 trigger bits are shown in figures 6.15c and 6.15d. There is a band of good acceptance in the $W_{\gamma p} - z$ plane, such that the FMT is most efficient at high $z$ and low $W_{\gamma p}$, or at low $z$ and high $W_{\gamma p}$.

Apart from the value of $z$, elastic and inelastic $J/\psi$ processes can be distinguished using track multiplicity and topology. The FMT alone is able to provide an effective trigger for the elastic process, by requiring both that a muon should be identified, and that the rapidity gap veto should not be set. In the EPJPSI simulation of photon-gluon fusion events, 75% of events giving a single muon trigger, also set the rapidity gap veto. A trigger explicitly searching for boson-gluon fusion events would require further track and calorimetry triggers, other than those for muon tracks, in the main body of H1.

### 6.4.3 Other Processes

Apart from the elastic and photon-gluon fusion mechanisms described in the previous two sections, a number of other processes can lead to the production at HERA of $J/\psi$ mesons. The diffractive process in which a $J/\psi$ is produced elastically and the proton dissociates produces forward muons with similar distributions to those in the fully elastic case, and has similar cross-section [121]. There is also the possibility of $J/\psi$ production as part of the final state, $X$, in diffractive dissociation processes at all $Q^2$. At HERA energies, a signal for $J/\psi$ production via resolved inelastic processes ($q\bar{q} \to c\bar{c}$ and $gg \to c\bar{c}$ at the parton level) should also be visible.

The cross-section for the production of pairs of charmed hadrons is estimated to be as high as 1$\mu$b [155], arising mainly from photon-gluon fusion processes, without subsequent conversion to a $J/\psi$, and from resolved processes. Semi-leptonic decays of charmed particles can lead to muons within the acceptance of the FMD. Open charm provides further channels in which to investigate the gluon density of the proton, and with such a large cross-section, searches for rare decays of $D$ mesons may be possible.

Since the $b$-quark mass is $\sim$ 5GeV, perturbative QCD in low order is unquestionably valid for studies in the $b$ sector, making them theoretically less complicated than is the case for charm physics. All of the charm production mechanisms discussed also apply to bottom quarks, though the photon-gluon fusion process is expected to be dominant. The large mass of the $b$ quark results in cross-sections typically lower by two orders of magnitude than those for charm production, and with poor signal to background ratios, HERA is not expected to be competitive as a $b$ factory.

Various electroweak processes yield forward going muons at high momentum. The FMD is well located for the detection of muons arising from the decays of electroweak gauge bosons, and heavy exotic states, produced in $\gamma p$ and $ep$ interactions. For example, in the production of the weak gauge bosons via the processes, $\gamma q_i \to Z^0 q_i$, and $\gamma q_i \to W^{\pm} q_j$, the heavy state is strongly boosted forwards in the laboratory frame, the decay muons have very large momenta, and may lie within the angular acceptance of the FMD. Preliminary acceptance studies of the efficiency of the FMT for the muon decay channel of the $Z^0$ (Branching ratio $3.34 \pm 0.04\%$), for the above production mechanism, using the PYTHIA [134] Monte Carlo and the single muon parameterisation, give a result of $39 \pm 1(stat)\%$ [7]. Since only one muon can be produced in the decays of $W$ bosons, the efficiency is smaller than that for the detection of $Z$ bosons. The FMT load was found, in the simulation, to be $16 \pm 1(stat)\%$ efficient for detection of the muon from the decay $W \to \mu\nu_\mu$. However the larger branching ratio ($10.5 \pm 1.9\%$) means that the overall efficiency for the $W$ production process studied is better than that for the $Z$. Cross-sections for weak gauge boson production are small, and large amounts of luminosity are required before any detailed study can realistically be made, but when statistics allow, the FMD will be essential to measurements.

A final class of events for which the FMD may prove useful, are those containing photon-photon interactions. A photon density associated with a quark, and generated by the splitting, $q \to q\gamma$, can be calculated in QED, and convoluted with quark density functions, leads to an effective photon density for the proton that is strongly peaked at low $Q^2$ [156]. The beam electron can interact with the nearly real photon flux associated with the photon, by Compton scattering, or DIS. The process, $\gamma\gamma \to \mu^+\mu^-$ is estimated [156] to have a cross-section of approximately 100nb, and with full track reconstruction of the event, provides an alternative method of measuring $F_2(x, Q^2)$.

## 6.5 Conclusions

The FMD has been fully operational as a component of H1 since the first days of data taking, and the FMT was installed at the beginning of the 1993 run. Since that time, extensive monitoring has indicated that the trigger processor works to its specifications. The method by which the trigger is loaded has developed over the three years since its implementation. Simulation studies in this chapter indicate that the load is efficient, whilst being effective in the removal of background by the use of vertex pointing criteria. The acceptance for single muons is found to be high in the region, $7.5 \lesssim \theta \lesssim 17.2^o$, with momentum thresholds of approximately 2.9GeV for pre-toroid segments, and 6.0GeV for fully validated tracks. The region, $3^o \lesssim \theta \lesssim 7^o$ is used to provide a rapidity gap veto signal, which has been shown to be approximately 75% efficient for the rejection of non-diffractive and proton beam-gas events at the level 1 stage of the trigger.

The principal potential use of the FMD has been identified as the study of elastic and

[7] The efficiencies of the pre-toroid, and full-track trigger bits are within 1%, since the track momenta are always sufficiently high for the track to be only slightly deviated in the toroid.

inelastic $J/\psi$ production at low $W_{\gamma p}$. The detector and trigger are believed to be well enough understood to produce measurements of these processes using 1995 data[8]. With larger integrated luminosity in the future, a number of other processes giving rise to muons within the acceptance limits of the system are also expected to become accessible in the longer term.

[8]Low overall luminosities in 1993, and problems with synchrotron radiation in 1994 have prevented measurements in previous years.

# References


[1] S.Glashow, Nucl. Phys. **B8**(1961) 579.
S.Weinberg, Phys. Rev. Lett. **19**(1967) 1264.

[2] R.Hofstander, Rev. Mod. Phys. **28**(1956) 214.

[3] W.Panofsky,E.Alton, Phys. Rev. **110**(1958) 1155.

[4] M.Breidenbach et al., Phys. Rev. Lett. **23**(1969) 935.

[5] W.Albrecht, Nucl. Phys. **B13**(1969) 1.

[6] H1 Collaboration, DESY **93-103**. To be published in NIM.

[7] EMC Collaboration, Phys. Lett. **B206**(1988) 364.
EMC Collaboration, Nucl. Phys. **B328**(1989) 1.

[8] K.Coulter et al., HERMES Collaboration. DESY/PRC **90/1**(1990).

[9] A.Sokolov,I.Ternov, Sov. Phys. Dokl. **8**(1964) 1203.

[10] *The VMEbus Specification.* IEEE Standard **1014**.

[11] E.Elsen, *The H1 Trigger and Data Acquisition.* Proc. of the 'International Symposium on Electronic Instrumentation in Physics', Dubna, May 1991. H1 Internal Note **93-262**.
F.Sefkow et al., *Experience with the First Level Trigger of H1.* Proc. of the 1994 IEEE Nuclear Science Symposium, Norfolk, Virginia. H1 Internal Note **94-407**.

[12] W.Haynes, *Experiences at HERA with the H1 Data Acquisition System.* Proc. of 'Computing in High Energy Physics 1992', Annecy, France. DESY **92-129**.

[13] W.Hildesheim,M.Seidel, *An investigation into the Radiation Damage of the Silicon Detectors of the H1-PLUG calorimeter within the HERA environment.* DESY **95-139**.

[14] H1 Calorimeter Group, NIM. **A336**(1993) 460.

[15] H1 BEMC Calorimeter Group, DESY **95-177**. Submitted to NIM.

[16] H1 Collaboration, *Technical Proposal to Upgrade the Backward Scattering region of the H1 Detector.* PRC **93/02**.

[17] J.Bürger et al., NIM. **A279**(1989) 217.

[18] T.Wolff et al., NIM. **A323**(1992) 537.

[19] S.Egli et al., NIM. **A283**(1989) 487.

[20] K.Müller et al., NIM. **A312**(1992) 457.

[21] S.Burke et al., RAL **95-037**. DESY **95-132**.

[22] R.Eichler et al., *The first level MWPC trigger for the H1 detector.* H1 Internal Note **87-61**.

[23] S.Eichenberger et al., NIM. **A323**(1992) 532.

[24] L.Suszycki, *Proc. of the HERA Workshop,* p.505, October 1987, ed. R.Peccei

[25] H1 Collaboration, Z.Phys. **C69**(1995) 27.

[26] H1 Collaboration, Z. Phys. **C66**(1995) 529.

[27] H.Bethe,W.Heitler, Proc. Roy. Soc. **A146**(1934) 83.

[28] S.Levonian, *H1LUMI - A Fast Simulation Package for the H1 Luminosity System.* H1 Internal Note **93-287**.

[29] J.Heatherington et al., *Studies on ToF FTDC data.* H1 Internal Note **93-307**.

[30] J.Heatherington et al., *Analysis of FToF TDC data.* H1 Internal Note **94-362**.

[31] J.Tutas, *A Level 1 Trigger from the Limited Streamer Tube system.* H1 Internal Note **91-185**.
H.Itterbeck et al., *Improvement of the Trigger Timing of the H1 Digital Muon System.* H1 Internal Note **95-427**.

[32] H.Cronstrom et al., NIM. **A340**(1994) 304.

[33] A.Mehta, *Measurement of the Diffractive Proton Structure Function and Calibration of the Forward Muon Detector at H1.* Ph.D. thesis, University of Manchester (1994).

[34] J.P.Sutton, *The H1 Forward Muon Spectrometer at the HERA Collider.* Ph.D. thesis, University of Manchester (1993).

[35] A.Mehta, *Investigation of the Drift Velocity of the Forward Muon Drift Chambers of the H1 Detector.* Diploma Thesis, University of Manchester (1992).

[36] C.Hilton, *Forward Muon Detection in H1 and Hadronic Energy Flow in DIS.* Ph.D. thesis, University of Manchester (1993).

[37] H.Phillips, *Track Reconstruction in the Forward Muon Subdetector and Investigations Concerning the Photon Remnant in the H1 Detector at HERA.* Ph.D thesis, University of Birningham (1993).

[38] L.West, *Private Communication.*

[39] Proc. of Workshop *Physics at HERA.* Vol. 2, October 1991. ed. W.Buchmüller,G.Ingelman.

[40] H1 Collaboration, Phys. Lett. **B324**(1994) 176.

[41] C.Itzykson,J.Zuber, *Quantum Field Theory.* McGraw-Hill (1985).
F.Halzen,A.Martin, *Quarks and Leptons.* John Wiley (1984).

[42] C.Callan,D.Gross, Phys. Rev. Lett. **22**(1969) 156.

[43] A.Cooper-Sarkar et al., Proc. of Workshop *Physics at HERA.* p.155 October 1991, ed. W.Buchmüller,G.Ingelman.

[44] M.Krasny et al., Proc. of Workshop *Physics at HERA.* p.171 October 1991, ed. W.Buchmüller,G.Ingelman.

[45] C.Callan,D.Gross, Phys. Rev. Lett. **21**(1968) 311.

[46] G.Altarelli,G.Martinelli, Phys. Lett. **B76**(1978) 89.

[47] H1 Collaboration, Nucl. Phys. **B439**(1995) 471.

[48] J.Friedman,H.Kendall, Ann. Rev. Nuc. Sci. **22**(1972) 203.

[49] J.Bjorken, Phys. Rev. **163**(1967) 1767.

[50] R.Feynman, Phys. Rev. Lett. **23**(1969) 1415.
J.Bjorken,E.Paschos, Phys. Rev. **185**(1969) 1975.

[51] H1 Collaboration, Phys. Lett. **B346**(1995) 415.

[52] J.Kuti,V.Weisskopf, Phys. Rev. **D4**(1971) 3418.

[53] D.Gross,F.Wilczek, Phys. Rev. **D9**(1974) 980.

[54] NMC Collaboration, Phys. lett. **B295**(1992) 159.
BCDMS Collaboration, Phys. Lett. **B223**(1989) 485.

[55] V.Gribov et al., Sov. J. Nucl. Phys. **15**(1972) 438.
G.Alterelli,G.Parisi, Nucl. Phys. **B126**(1977) 298.

[56] A.Martin,R.Roberts,J.Stirling, Phys. Lett. **B306**(1993) 145.

[57] M.Glück,E.Reya,A.Vogt, Phys. Lett. **B306**(1993) 391.

[58] R.Ball,S.Forte, Phys. Lett. **B335**(1994) 77.
A.De Rujula et al., Phys. Rev. **D10**(1974) 1649.

[59] H1 Collaboration, Phys. Lett. **B354**(1995) 494.

[60] E.Kuraev,L.Lipatov,V.Fadin, Sov. Phys. JETP. **44**(1976) 443.
Y.Balitsky,L.Lipatov, Sov. J. Nucl. Phys. **28**(1978) 822.

[61] J.Collins,P.Landshoff, Phys. Lett. **B276**(1992) 196.

[62] L.Gribov,E.Levin,M.Ryskin, Phys. Rep. **100**(1983) 1.

[63] A.Müller, J. Phys. **G19**(1993) 1463.

[64] E.Levin,M.Ryskin, Phys. Rep. **189**(1990) 267.
A.Mueller, Nucl. Phys. B(Proc Suppl) **C18**(1990) 125.

[65] V.Gribov, Sov. Phys. JETP. **30**(1969) 709.

[66] J.Bjorken,J.Kogut, Phys. Rev. **D8**(1973) 1341.

[67] H.Abramowicz et al., Phys. Lett. **B269**(1991) 465.

[68] G.Schuler, Proc. of Workshop *Physics at HERA.* p.461, October 1991, ed. W.Buchmüller,G.Ingelman.

[69] ZEUS Collaboration, Phys. Lett. **B356**(1995) 601.

[70] NMC Collaboration, Z. Phys. **C51**(1991) 387.
E665 Collaboration, Phys. Rev. Lett. **68**(1992) 3266.

[71] H1 Collaboration, Phys. Lett. **B358**(1995) 412.

[72] V.Del Duca,S.J.Brodsky,P.Hoyer, Phys. Rev. **D46**(1992) 931.

[73] K.Prytz, Phys. Lett. **B311**(1993) 286.

[74] H1 Collaboration, Nucl. Phys. **B449**(1995) 3.

[75] H1 Collaboration, Phys. lett. **B356**(1995) 118.

[76] R.Van Dyke, Atomic Physics 9(1984) **53** (Plenum Press).

[77] J.Bailey et al., Nucl. Phys. **B150**(1979) 1.

[78] F.Murphy,D.Yount, Scientific American, July 1971, 94.

[79] E665 Collaboration, Z. Phys. **C67**(1995) 403.

[80] T.Bauer et al., Rev. Mod. Phys. **50**(1978) 261.

[81] J.J.Sakurai, Ann. Phys. **11**(1960) 1.

[82] J.Busenitz et al., Phys. Rev. **D40**(1989) 1.

[83] J.J.Sakurai,D.Schildknecht, Phys. Lett. **B40**(1972) 121.

[84] M.Greko, Nucl. Phys. **B63**(1973) 398.

[85] E.Lohrmann, Proc. of Workshop *Physics at HERA.* p.519, October 1991, ed. W.Buchmüller,G.Ingelman.

[86] H.Lipkin, Nucl. Phys. **B78**(1974) 381.

[87] PLUTO Collaboration, Phys. Lett. **B142**(1984) 111.

[88] H1 Collaboration, Nucl. Phys. **B445**(1995) 195.

[89] K.Goulianos, Phys. Rep. **101**(1983) 169.

[90] UA8 Collaboration, Phys. Lett. **B211**(1988) 239.
UA8 Collaboration, Phys. Lett. **B297**(1992) 417.

[91] H1 Collaboration, Nucl. Phys. **B435**(1995) 3.

[92] P.Collins, *An Introduction to Regge Theory and High Energy Physics.* CUP (1977).
P.Collins,A.Martin, *Hadron Interactions.* Adam Hilger (1984).

[93] T.Regge, Nuovo Cimento **14**(1959) 951.
T.Regge, Nuovo Cimento **18**(1960) 947.

[94] H.Yukawa, Proc. Phys. Math. Soc. Japan **17**(1935) 48.

[95] J.Jackson, Rev. Mod. Phys. **37**(1965) 484.

[96] G.Chew,S.Frautschi,S.Mandelstam, Phys. Rev. **126**(1962) 1202.

[97] D.Perkins, *Introduction to High Energy Physics.* Second Ed. AWP (1982).
I.R.Kenyon, *Elementary Particle Physics.* RKP (1987).

[98] R.Eden et al., *The Analytic S-Matrix.* CUP (1966).

[99] A.Barnes et al., Phys. Rev. Lett. **37**(1976) 76.

[100] A.Irving,R.Worden, Phys. Rep. **C34**(1977) 118.

[101] I.Pomerančuk, Sov. Phys. JETP. **7**(1958) 499.

[102] A.Donachie,P.Landshoff, Nucl. Phys. **B231**(1983) 189.

[103] WA91 Collaboration, Phys. Lett. **B234**(1994) 509.

[104] P.Landshoff, *The two Pomerons*, University of Cambridge Preprint, **HEP-PH-9410250**.

[105] A.Donnachie,P.Landshoff, Phys. Lett. **B296**(1992) 227.

[106] M.Froissart, Phys. Rev. **123**(1961) 1053.

[107] R608 Collaboration, Phys. Lett. **B163**(1985) 267.

[108] R.Feynman, Phys. Rev. Lett. **23**(1969) 1415.

[109] A.Mueller, Phys. Rev. **D2**(1970) 2963.

[110] A.Kaidalov, Phys. Rep. **50**(1979) 157.

[111] CHLM Collaboration, Nucl. Phys. **B108**(1976) 1.

[112] T.Chapin et al., Phys. Rev. **D31**(1985) 17.

[113] CHLM Collaboration, Nucl. Phys. **B72**(1974) 376.

[114] R.Cool et al., Phys. Rev. **47**(1981) 701.

[115] UA4 collaboration, Phys. lett. **B186**(1987) 227.

[116] A.Sanda, Phys. Rev. **D6**(1972) 280.

[117] Y.Akimov et al., Phys. Rev. **D14**(1976) 3148.

[118] ZEUS Collaboration, DESY **95-193**. To be published in Z. Phys. C.

[119] L.Lipatov, Sov. Phys. JETP. **63**(1986) 904.

[120] ZEUS Collaboration, Phys. Lett. **B350**(1995) 120.

[121] H1 Collaboration, DESY **96-037**. To be published in Nucl. Phys. B.

[122] M.Ryskin, Zeit Phys **C57**(1993) 89.

[123] H1 Collaboration, DESY **96-023**. To be published in Nucl. Phys. B.

[124] ZEUS Collaboration, Phys. Lett. **B315**(1993) 481.
H1 Collaboration, Nucl. Phys. **B429**(1994) 377.

[125] *Proposal for a Forward Proton Spectrometer for H1* PRC **94-03**. H1 Internal Note **94-381**.

[126] H1 Collaboration, Phys. lett. **B348**(1995) 681.

[127] A.Donnachie,P.Landshoff, Phys. Lett. **B191**(1987) 309.
G.Ingelman,P.Schlein, Phys. Lett. **B152**(1985) 256.

[128] ZEUS Collaboration, DESY **96-018**, DESY **95-093**. Accepted by Z. Phys. C.

[129] J.Phillips, *Private Communication.*
T.Gehrmann,W.Stirling, DTP **95-26**(1995).
A.Capella et al., LPTHE Orsay **95-33**(1995).

[130] J.Bjorken, *Rapidity Gaps in Deep Inelastic Scattering.* Talk presented at ITEP, Moscow, October 1995. **SLAC-PUB-7096**.

[131] W.Buchmüller, Phys. Lett. **B353**(1995) 335.

[132] H1 Collaboration, DESY **95-251**. To be published in Nucl Phys B.

[133] R.Engel, Zeit Phys **C66**(1995) 203.

[134] H.Bengtsson,T.Sjöstrand, Comp Phys Commun **46**(1987) 43.

[135] UA5 Collaboration, Z. Phys. **C33**(1986) 175.

[136] D.Amati,A.Stanghellini,S.Fubini, Nuovo Cimento **26**(1962) 896.

[137] G.Ingelman, Proc. of the Workshop *Physics at HERA.* p.1336, October 1991, ed. W.Buchmüller,G.Ingelman.

[138] C.Weizsäcker, Z. Phys. **88**(1934) 612.
E.Williams, Phys. Rev. **45**(1934) 729.

[139] S.Frixione et al., Phys. Lett. **B319**(1993) 339.

[140] G.Schuler,T.Sjöstrand, Nucl. Phys. **B407**(1993) 539.

[141] E.Gotsman,E.Levin,U.Maor, Phys. Lett. **B347**(1995) 424.

[142] A.Capella,A.Kaidalov,C.Merino,J.Tran Thanh Van, Phys. Lett. **B343**(1995) 403.

[143] T.Ahmed at al., NIM. **A364**(1995) 456.

[144] RAL Microelectronics Group, *Specification for T0 ASIC*, RAL No. **114** (1991).
RAL Microelectronics Group, *Specification for Track-Finding ASIC*, RAL No **115** (1991).

[145] P.Newman, *First Experiences with the Forward Muon Trigger for the H1 Detector at HERA.* Mid-term report, University of Birmingham (1994).

[146] G.Noyes, *A first level Forward Muon Trigger for the H1 Experiment at HERA.* Ph.D thesis, University of Birmingham (1993).

[147] V.Highland, NIM **129**(1975) 497. NIM. **161**(1979) 171.

[148] J.P.Sutton, *Private Communication.*

[149] E687 Collaboration, Phys. Lett. **B316**(1993) 197.
E401 Collaboration, Phys. Rev. Lett. **48**(1982) 73.
FTPS Collaboration, Phys. Rev. Lett. **52**(1984) 795.

[150] B.List, *Diffractive $J/\psi$ Production in Electron-Proton Collisions at HERA.* Diploma Thesis, Techn. Univ. of Berlin (1993) H1 Internal Note **93-319**.

[151] H.Jung et al., Z. Phys. **C60**(1993) 721.

[152] EMC Collaboration, Z. Phys. **C56**(1992) 21.
NA-14 Collaboration, Z. Phys. **C33**(1987) 505.
NMC Collaboration, Phys. Lett. **B258**(1991) 493.

[153] H.Jung,G.Schuler,J.Terron, Proc. of Workshop *Physics at HERA.* p.712, October 1991, ed. W.Buchmüller,G.Ingelman.

[154] E.Berger,D.Jones, Phys. Rev. **D23**(1981) 1521.

[155] A.Ali,D.Wyler, Proc. of Workshop *Physics at HERA.* 669, October 1991, ed. W.Buchmüller,G.Ingelman.

[156] G.Levman,Proc. of Workshop *Physics at HERA.* 623, October 1991, ed. W.Buchmüller,G.Ingelman.

# Acknowledgements

There are a number of people who's patient help over the past three years I wish to acknowledge. Firstly, my supervisor, John Garvey has been entirely supportive throughout the course of my PhD. I would like to thank him for allowing me the freedom to pursue the research topics that interested me most, and for his wisdom in occasionally encouraging me to be interested in the right research topics! The other Birmingham academics involved in H1, John Dowell and Ian Kenyon have been equally willing to lend a hand and to give positive advice and guidance.

At Birmingham and DESY I have spent a period in excess of two years working mainly on the implementation, smooth running, and monitoring of the Forward Muon Trigger, a responsibility that I have shared with Paul Sutton. I found Paul to be a most amenable person with whom to work, and a physicist of some considerable ability. I wish him the very best of luck with the trigger and its potential uses in the future.

It was in discussions with Gerhard Knies that I began to develop some sort of a feel for HERA physics in general, and diffractive physics in particular. I worked closely with Gerhard on the development of triggers for diffractive photoproduction, and on an off-line diffractive event selection. His flamboyant and easy going style was a breath of fresh air in a physics community that is often guilty of taking itself too seriously [1].

For the final few months at DESY I was fortunate enough to be an incumbent of Building 10b, and it is here that I feel I learned most rapidly about experimental physics. To say that being in close proximity to John Dainton, Julian Phillips, and Andrew Mehta was stimulating would be an understatement. I would like to acknowledge the encouragement and advice offered to me by John during this period, as well as his help in introducing me to the dreaded 'Reggeography'. It is from Julian and Andrew that I have learned most about how to go about doing a piece of analysis. Working with Andrew allowed me to learn good technique very quickly, and I thank him for his patience, and readiness to answer questions.

Inevitably, there are lots of other people who have helped me in less obvious ways to produce the work in this thesis. I learned much of what I know about the Forward Muon Trigger from Gareth Noyes, and others (Phill Biddulph, John Dowdell, Eric Eisenhandler, Joe Foster, Chris Hilton, Lee West) were always happy to offer technical advice with forward muon matters. As well as doing much of the early work on the data and Monte

[1] I can think of few other academics who could ever be found at a party at my St Pauli abode, engrossed for hours in a conversation on Modern Political Theory with a punk-rocker with a particularly impressive mohikan hair-style.

Carlo used in this work, Andrej Rostotsev and Alexander Fedotov have straightened me out on a number of points of photoproduction physics.

In a wider sense, there are very many people whose friendship has been an inspiration throughout the past three years. To all the people with whom I have shared houses in these relatively nomadic times (Graham Wilkes, Dave Kant, Phil Kaziewicz, Sean Willard, Andrew Mehta, Eram Rizvi, Paul Davies, Chris Nolan and Whirlitzer von Trippenhof), my thanks for your company. For older friendships, and for staying in touch [2], thanks and respect to Jason Petch, Carl Petersen, Mat Roberts and Mat Zoid. For making life pleasant both socially and at work, thanks also to Vicki Hudgson, Tim Nicholls, Stuart Robertson, Paul Thompson and Alison Wright. Finally, for immeasurable support during the past three years as ever, my most profound thanks to my family.

*One has to take the first steps of adopting a stance that is simply one of critical intelligence towards everything one reads .... and discover the assumptions that underlie it. Then analyse those assumptions and restate the account of the facts in terms that really are true to the facts .... Once one does that, I think the world becomes rather clear.*

Noam Chomsky - Institute professor of Linguistics, Massachusetts Institute of Technology, and long-time political activist. Chronicles of Dissent (AK Press 1992)

*We delight in physics pain.*

William Shakespeare - (Macbeth II iii 56)

[2] Impressive, given the frightening level of disorganisation of all concerned.